Influence of adhesion between the main cement phases on the mechanical behaviour of hydrated cement paste

Sela Hoeun

MEMOIRE DE DOCTORAT DE

L'ECOLE CENTRALE DE NANTES

ECOLE DOCTORALE N° 602
Sciences de l'Ingénierie et des Systèmes
Spécialité : *Génie Civil*

Par
Sela HOEUN

Influence de l'adhésion entre les principales phases cimentaires sur le comportement mécanique de la pâte de ciment hydratée

Projet de recherche doctoral présenté et soutenu à l'École Centrale de Nantes, le 22 Décembre 2023
Unité de recherche : UMR 6183 - Institut de Recherche en Génie Civil et Mécanique (GeM)
UR 3913 - Laboratoire de Génie Civil et Génie Mécanique (LGCGM)

Rapporteurs avant soutenance :

Ali ZAOUI	Professeur des Universités, Université de Lille
Tulio HONORIO	Ingénieur de Recherche, CEA Paris-Saclay

Composition du Jury :

Président :	Sébastien RÉMOND	Professeur des Universités, Université d'Orléans
Examinateurs :	Ali ZAOUI	Professeur des Universités, Université de Lille
	Syed Yasir ALAM	Maître de Conférences – HDR, École Centrale de Nantes
	Julien SANAHUJA	Ingénieur de Recherche, EDF R&D
	Tulio HONORIO	Ingénieur de Recherche, CEA Paris-Saclay

Directeur de recherches doctorales : Fabrice BERNARD	Maître de Conférences – HDR, INSA de Rennes
Co-dir. de recherches doctorales : Frédéric GRONDIN	Professeur des Universités, Ecole Centrale de Nantes
Co-enc.de recherches doctorales : Siham KAMALI-BERNARD	Professeure des Universités, INSA de Rennes

Acknowledgements

First and foremost, I would like to express my deepest gratitude to my supervisors, Dr. Fabrice BERNARD, Prof. Frédéric GRONDIN and Prof. Siham KAMALI-BERNARD who have guided, motivated and encouraged me to do the right thing even when the road got tough. Especially, thank you so much for providing me such a great opportunity to work with you. Thank for your valuable time on many hours of discussion and meeting. I whole-heartedly appreciate for your great advices and supports toward the success of this PhD study.

I am very grateful to Prof. Ali ZAOUI, Prof. Sébastien RÉMOND, Dr. Syed Yasir ALAM, Dr. Tulio Honorio and Dr. Julien Sanahuja for accepting being the reporters and examiners of my dissertation presentations. Thank you for spending your valuable time to read, question and give feedback, which allow me to reflect and foresee my future research. In addition, I would like to show my gratitude again to Dr. Syed Yasir ALAM who gave me not only many great advices and suggestions but also encouragement. You have spent your valuable time to give me an opportunity to explore more on the application of Discrete Element Method via PFC. Next; I would like to thank Dr. Laurent PÉDESSEAU and Dr. Syed Yasir ALAM for being my thesis monitoring committee since the first year of my PhD. Furthermore, I would like to express my appreciation to Dr. Jérôme CLAVERIE for his guidance at the beginning of the journey with Molecular Dynamics simulations via LAMMPS.

I also wish to pay my sincere regards to Laboratoire de Génie Civil et Génie Mécanique (LGCGM), Université de Rennes, INSA Rennes and Institut de Recherche en Génie Civil et Mécanique (GeM), Nantes Université, École Centrale de Nantes for financial support. Without their support, I would not have an opportunity to work in this project. Moreover, I would like to recognize the invaluable assistance to my colleagues, Jinane Murr and Marinelle EL KHOURY. I also wish to thank all people who I have met during this PhD journey such as Pisey KEO, Piseth HENG, Theany TO, Khundadino LENG, Sokvisal MOM, Yeakleang MUY, Try MENG, Davin SANG, Sounean HENG, Lynita SAROU, Rithymarady HORM, Thaileng OENG, Vanthet OUCH, Vathana PHANG, Bunpo EAR, Pengzhi WANG, Elodie PIOLET, Mickael Le VERN, Siddhartha Harsha OMMI, Julien BOMBERAULT and many others for being around. Thank you for your advice, suggestion, support, motivation and encouragement.

Last but not least, I would like to express my special thank toward my beloved parents, Sophat SOU, Bunthoeun SIEK, Narin HOK and Maty SRUN for their encouragement and

motivation during my PhD study and their support for my study since I was a child. Without their support, I would not be who I am today. Next, I would like to thank my wonderful wife, Rathanaraingsey HOK who always supports, motivates, encourages and loves who I am. I would like to say that I really love you my sweetheart and thank you so much. I also thank my brothers and sisters, Sophanith HOEUN, Dorasy HOK, Phearom UN and Pongvanthorn NARIN. Lastly, I was not present when you breathed your last (my grandparents) since I was here researching. However, I do possess the most vivid memories a grandchild can conjure.

Finally, I would like to mention that it would not be possible to complete my PhD thesis without their tremendous support and encouragement in the past few years. They have always been my inspiration to improve myself and to achieve my dream. Therefore, I dedicate this work to them.

Abstract

This PhD thesis focuses on the multi-scale modelling of the mechanical properties of cementitious materials. The aim of this PhD thesis is to obtain the mechanical properties of hydrated cement paste phases at the nano-scale using Molecular Dynamics (MD) simulations. Mechanical properties of hardened cement paste at the micro-scale were then calculated with homogenization scheme and Discrete Element Method (DEM). Indeed, properties obtained at the lower scale are considered as the input data at the upper scale. At the nano-scale, tensile test and shear test were performed with main hydrated cement paste phases (i.e., calcium-silicate-hydrates, portlandite and ettringite) using MD simulations. Combination of two different main phases of hydrated cement paste was called cement paste composite in this study. Different sizes, strain rates, configurations of spacing and orientations of cement paste composites were studied for sensitive analysis. As a result, mechanical properties at the nano-scale were obtained. Another approach to obtain Young's modulus and Poisson ratio was done via Voigt-Reuss-Hill (VRH) approximation. With homogenization scheme (i.e., Mori-Tanaka scheme), Young's modulus and Poisson's ratio of a simplified hardened cement paste were calculated. Finally, DEM simulation was done with tensile test of a simplified hardened cement paste by taking into account the mechanical properties at the nano-scale. This PhD thesis contributes to create the bridge of achieving the transition from the molecular scale to the continuous microscopic scale.

Keywords: Multi-scale modelling, hydrated cement paste, Voigt-Reuss-Hill, homogenization, Molecular Dynamics, Discrete Element Method

Résumé

Cette thèse de doctorat porte sur la modélisation multi-échelle des propriétés mécaniques des matériaux cimentaires. L'objectif est d'obtenir les propriétés mécaniques des phases de pâte de ciment hydratées à l'échelle nanométrique à l'aide de simulations de Dynamique Moléculaire (DM). Les propriétés mécaniques de la pâte de ciment durcie à l'échelle microscopique ont ensuite été calculées à l'aide d'une méthode d'homogénéisation et de la méthode des éléments discrets (MED). En effet, les propriétés obtenues à l'échelle inférieure sont considérées comme les données d'entrée à l'échelle supérieure. À l'échelle nanométrique, des tests de traction et de cisaillement ont été réalisés avec les principales phases de pâte de ciment hydratées (i.e., les hydrates de silicate de calcium, la portlandite et l'ettringite) à l'aide de simulations DM. La combinaison de deux phases principales différentes de pâte de ciment hydratée a été appelée pâte de ciment composite dans cette étude. Différentes tailles, vitesses de déformation, configurations d'espacement et orientations de composites de pâte de ciment ont été étudiées pour une analyse sensible. En conséquence, des propriétés mécaniques à l'échelle nanométrique ont été obtenues. Une autre approche pour obtenir le module de Young et le coefficient de Poisson a été réalisée via l'approximation de Voigt-Reuss-Hill (VRH). Avec la méthode d'homogénéisation (i.e., Mori-Tanaka), le module d'Young et le coefficient de Poisson d'une pâte de ciment durcie simplifiée ont été calculés. Enfin, une simulation MED a été réalisée avec un essai de traction d'une pâte de ciment durcie simplifiée en prenant en compte les propriétés mécaniques à l'échelle nanométrique. Cette thèse de doctorat contribue à créer le pont permettant de réaliser la transition de l'échelle moléculaire à l'échelle microscopique continue.

Mots clés : Modélisation multi-échelle, Pâte de ciment hydratée, Voigt-Reuss-Hill, homogénéisation, Dynamique Moléculaire, Méthode Eléments Discrets

Contents

List of Figures

List of Figures

List of Figures

List of Figures

List of Tables

List of Tables

Introduction

General introduction

Cementitious materials are by far the most used materials that are characterized by a heterogeneous composition on several scales. Due to this complex structure, the behaviour of concrete and especially its cracking remain relatively controlled. Concrete is composed of aggregates (a particulate phase) and cement matrix (a binding phase) as a complex composite. Consequently, cement matrix influences the mechanical properties of concrete [1,2]. Cement paste is a porous multiscale substance with various physical properties at varying length scales [3]. Calcium-silicate-hydrates (C-S-H) representing up to 50% of the volume is the major component of hardened hydrated cement paste [2]. In hydrated Portland cement paste, another considerable phase is portlandite (CH). For pastes of typical Portland cements cured for 3-12 months, the portlandite content found by thermal methods or QXDA is typically 15-25%, referred to the ignited mass [4]. In addition, another hydration product of Portland cement, slag and super-sulphated cements but not only, is ettringite (AFt) which is an important phase to be considered particularly in durability aspects [5].

In order to simulate accurately the behaviour of the concrete, it is important to develop the finest possible modelling of the cement paste and to ascend to the overall behaviour of the cement-based composite material. The chemistry and fineness of the cement, quantity of water, ratio of additives and admixtures, mixing method, and temperature have a significant impact on the paste's properties. Therefore, any attempt to simulate concrete without accounting for the heterogeneity of the cement paste requires systematic calibration of the latter's mechanical properties, for instance by experimental tests. This hinders the advancement of novel concrete made from industrial by-product (i.e., green-concrete).

Problems

The multi-scale modelling requires the mechanical properties of different phases of hydrated cement paste. One of the method to obtain these properties is using nano-indentation experiments [6]. Nonetheless, values obtained by nano-indentation tests could intrigue question. Hence, it leads to obtain these properties by other method, in particular, numerical simulations (i.e., Molecular Dynamics (MD) simulations at the nano-scale). The material

parameters are not required for MD simulations. Nevertheless, hypothesis of force field is needed for simulations at the nano-scale. On the other hand, macro-scale fracture is originated from the breakage of interatomic bonds at the nano-scale. The characterization of the nanoscale structure of cement-based materials and breakthroughs in computational materials science have made it possible for scientists and engineers to well understand and design concrete, as well as to increase its durability and performance. In civil engineering, numerous analytical and/or numerical modelling works taking heterogeneity into account have thus been gradually published [1,6–14]. It is now necessary to grasp the adhesion properties between different hydrated cement paste phases and to consider them at the microstructure scale of the cement paste. It is indeed the rupture of the adhesion between these phases which is responsible for damage of the material and the micro-cracking even more than the rupture of the phases themselves (inter-phase and not intra-phase ruptures) [15–18]. There are many problems related to micro-cracking simulations at the nano-scale. For example, the durability of the concrete is reduced by the micro-cracking. The storage of nuclear or gas could leak and cause the problem because of micro-cracking. Thus, it is interesting to study the micro-cracking using MD simulations at nano-scale, which is related to interatomic potential between atoms.

Objectives

The two main objectives of this PhD thesis are as follows: (1) obtain the mechanical properties of interphases of the main cement paste phases, for example by mean of modelling via MD simulations and (2) use results obtained from MD simulations as inputs in the scale of hardened cement paste (i.e., micro-scale) by mean of homogenization scheme and Discrete Element Method (DEM). This PhD thesis subject may make it possible to create the bridge of achieving the transition from the molecular scale to the continuous microscopic scale.

Manuscript organization

The contents of this PhD thesis were arranged as the following chapters. **Chapter 1** describes the mechanical properties calculation of the hydrated cement paste phases using tensile test via MD simulations at the nano-scale. It focuses on the tensile test of the main hydrated cement paste phases as follows: (a) C-S-H (I) supercells, (b) CH supercells and (c) AFt supercells. **Chapter 2** shows one of the main objective in this work, which is the methodology on how to obtain the mechanical properties of main hydrated cement paste composites using MD simulations. Those composites are presented as follows: (a) C-S-H (I)/C-S-H (I), (b) C-S-H (I)/CH, (c) C-S-H (I)/AFt and (d) AFt/CH. **Chapter 3** discusses a similar contents as previous

chapter, but they were done with shear test of the hydrated cement paste phases using MD simulations. Shear modulus and peak stress of hydrated cement phases composites could be observed in this chapter. **Chapter 4** presents another work related to MD simulations. This chapter focuses on the methodology to obtain the elastic constants of nano-scale hydrated cement paste composites using MD simulations. Many topics could be found as follows: elastic constant calculation via MD simulations and Young's modulus and Poisson's ratio calculation via Voigt-Reuss-Hill approximation. **Chapter 5** discusses on the application of results obtained by MD simulations. On the one hand, the first part concentrates on the calculation of the mechanical properties of a simplified hardened cement paste using homogenization scheme, i.e., Mori-Tanaka scheme. On the other hand, those results were taken into account in micro-scale simulation, i.e., DEM simulation. The last part of this manuscript includes general conclusion and perspective. Conclusion discusses all main chapters in their respective paragraph. Finally, perspective will be drawn based on the limitation and what areas required to improve in the future.

1 Tensile test of hydrated cement paste phases

1.1 Background

This chapter deals primarily with the mechanical properties calculation of hydrated cement paste phases using molecular dynamics (MD) simulations at the nano-scale. As outlined in the introduction, mechanical properties of different phases of hydrated cement paste are required for the multi-scale modelling. The results obtained in this chapter could be served as the input in the upper-scale, i.e., microscale of cement-based materials. Three main hydrated cement paste phases have been chosen to study. Those phases are calcium-silicate-hydrates (C-S-H), portlandite (CH) and ettringite (AFt). Tensile test was applied on the supercells of these phases in order to obtain the stress-strain curves. Different force fields, strain rate and sizes of the supercells were investigated. Young's modulus, peak stress and peak strain could be deduced from the stress-strain curves. This chapter was arranged as follows: (1.2) materials and methods, (1.3) tensile test of portlandite, (1.4) tensile test of ettringite, (1.5) tensile test of calcium-silicate-hydrates and (1.6) in summary.

1.2 Numerical methods

1.2.1 Main hydrated cement phases

Hydration of Portland cement creates different hydration products including amorphous or poorly crystalline C-S-H and coarsely CH. For example, from a case of 14 months saturated old Portland cement paste with water-to-cement (w/c) ratio of 0.5, Taylor [4] calculated volume percentages based on the phase composition to be: C-S-H = 48.7%, CH = 13.9%, AFt = 3.6%, Alite = 1%, Belite = 0.6%, Ferrite = 1%, AFm = 11.1%, Hydrogarnet = 2.2%, Hydrotalcite = 1.8%, insoluble residue = 1%, and pores = 16%. In relation to the volume percentages of phase composition, three primary phases were selected to study (i.e., C-S-H, CH and AFt).

The formation of CH always occurs in conjunction with the hydration of C_3S or C_2S. In the hydration of C_3S paste, the majority of CH precipitates as portlandite crystals, some of which can reach tens of micrometres in diameter [19]. Unit cell of portlandite (CH) was modelled following Desgranges et al. [20] as shown in **Figure 1.1** with the chemical formula: $Ca(OH)_2$ and cell angles $(\alpha, \beta, \gamma) = (90^o, 90^o, 120^o)$. Cell length are $(a, b, c) = (3.589\ \text{Å}, 3.589\ \text{Å},$

4.911 Å). White balls are Ca atoms, lime balls are H atoms, and purple balls are O atoms. The structure of the crystal is trigonal in the $P\bar{3}m1$ space group. **Table 1.1** shows the structural refinement for portlandite model. OVITO (Open Visualization Tool) [21] was used for the visualization of all simulations.

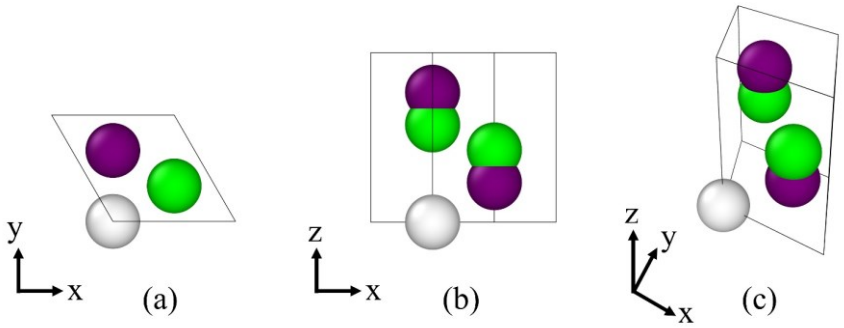

Figure 1.1 Unit cell of portlandite (CH): (a) xy-plane, (b) xz-plane and (c) perspective view.

Table 1.1 Structural refinement for portlandite model of one harmonic site for H atom (thermal parameters are given in $Å^2 \times 10^{-4}$) [20].

Room temperature		
	z_O	-0.2337(1)
	z_H	-0.4256(1)
Ca	u_{11}	42(1)
	u_{33}	145(2)
O	u_{11}	82(1)
	u_{33}	106(2)
H	u_{11}	510(5)
	u_{33}	157(3)
R		0.028
wR		0.029
Independent reflections	211	

The general formula for ettringite is $[Ca_3(Al,Fe)(OH)_6]X_3 \cdot xH_2O$, where X is a formula unit for a doubly charged anion. Ettringite is a member of the large group of AFt phases. At the nanometre scale, ettringite is composed of columns of the chemical formula $[Ca_3Al(OH)_6 \cdot 12H_2O]^{26-}$ that are parallel to the c-axis, with $3SO_4^{2-}$ and H_2O molecules in the channels in between [19]. Unit cell of ettringite (AFt) at 23 ºC was modelled following Goetz-

Neunhoeffer and Neubauer [22] with the chemical formula: $Ca_6[Al_2(SO_4)_3(OH)_{12}]\cdot 26H_2O$, cell angles $(\alpha, \beta, \gamma) = (90^o, 90^o, 120^o)$ and cell length $(a, b, c) = (11.229\ \text{Å}, 11.229\ \text{Å}, 21.478\ \text{Å})$ as illustrated by **Figure 1.2**. Grey balls are Al atoms, magenta balls are Ca atoms, cyan balls are H atoms, brown balls are O atoms, and black balls are S atoms. The structure of the crystal is trigonal in the P31c space group. **Table 1.2** presents the fractional atomic coordinates of revised ettringite structure.

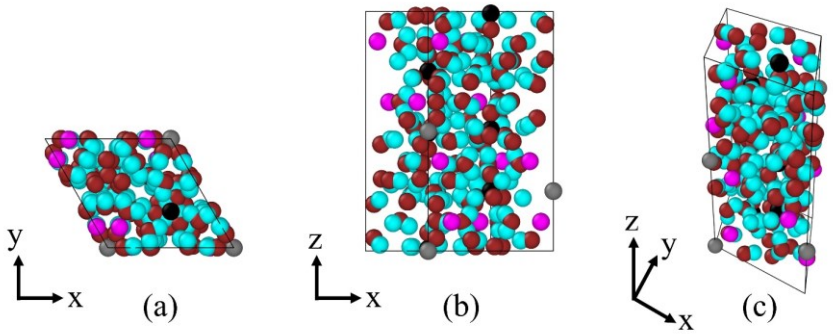

Figure 1.2 Unit cell of ettringite (AFt): (a) xy-plane, (b) xz-plane and (c) perspective view.

Table 1.2 Fractional atomic coordinates of revised ettringite structure from Rietveld refinement results (e.s.d. in brackets of refined positions) [22].

Site	x	y	z	Site	x	y	z
Al1	0.000	0.000	0.000	O9	0.265(2)	0.406(2)	0.622(2)
Al2	0.000	0.000	0.250	H9a	0.293(2)	0.476(2)	0.654(2)
Ca1	0.002(1)	0.813(1)	0.875(2)	H9b	0.295(2)	0.456(0)	0.584(2)
Ca2	0.993(1)	0.184(1)	0.122(2)	O10	0.789(2)	0.624(2)	0.362(2)
O1	0.997(4)	0.122(3)	0.945(2)	H10a	0.754(2)	0.556(2)	0.330(2)
H1	0.985(4)	0.192(3)	0.966(2)	H10b	0.764(2)	0.573(2)	0.400(2)
O2	0.002(5)	0.869(3)	0.054(2)	O11	0.266(3)	0.408(3)	0.126(2)
H2	0.019(5)	0.810(3)	0.026(2)	H11a	0.337(3)	0.388(3)	0.116(2)
O3	0.999(3)	0.128(3)	0.801(2)	H11b	0.291(3)	0.492(3)	0.104(2)
H3	0.990(3)	0.200(3)	0.778(3)	O12	0.752(2)	0.598(3)	0.865(2)
O4	0.003(3)	0.871(3)	0.196(2)	H12a	0.699(2)	0.639(3)	0.877(2)
H4	0.006(3)	0.791(3)	0.213(2)	H12b	0.687(2)	0.502(3)	0.860(2)
O5	0.994(5)	0.342(4)	0.046(3)	O13	0.3333	0.6667	0.425(2)
H5a	0.060(5)	0.405(4)	0.017(3)	O14	0.3333	0.6667	0.819(2)
H5b	0.920(5)	0.362(4)	0.044(3)	O15	0.3333	0.6667	0.076(2)
O6	0.018(4)	0.684(3)	0.957(2)	O16	0.1950	0.6280	0.519(2)
H6a	0.936(4)	0.599(3)	0.965(2)	O17	0.1950	0.6200	0.724(2)
H6b	0.091(4)	0.666(3)	0.965(2)	O18	0.1920	0.5850	0.982(2)
O7	0.003(4)	0.340(3)	0.206(2)	O19	0.227(3)	0.685(3)	0.243(3)
H7a	0.078(4)	0.401(3)	0.232(2)	H19a	0.325(3)	0.728(3)	0.239(3)
H7b	0.923(4)	0.334(3)	0.221(2)	H19b	0.200(3)	0.727(3)	0.211(3)
O8	0.990(4)	0.630(2)	0.795(2)	S1	0.3333	0.6667	0.492(2)
H8a	0.918(4)	0.536(2)	0.793(2)	S2	0.3333	0.6667	0.751(2)
H8b	0.073(4)	0.627(2)	0.792(2)	S3	0.3333	0.6667	0.009(3)

Amorphous or nearly amorphous C-S-H products are referred as the 'C-S-H phase.' At room temperature, hydration of C_3S produces C-S-H phase, which appears to be structurally related to the crystalline phases of 1.1 nm tobermorite and jennite as well as to the weakly crystalline substances C-S-H (I) and C-S-H (II) [19]. The structure of the semi-crystalline phase C-S-H (I), which can be made by mixing sodium silicate solutions with calcium salt solutions or by reacting calcium hydroxide with hydrous silica, is comparable to that of tobermorite at short-range length scale. It can be made with a Ca/Si molar ratio of between about 0.8 and 1.5. Similar

in short-range structure to jennite, the phase C-S-H (II) may be created by hydrating C_3S or β-C_2S in excess water and repeatedly draining the liquid to reduce the CaO/SiO_2 ratio in the system [19]. The C-S-H phases is generally amorphous with no long-range order. Based on the ratio of Ca/Si, C-S-H phase can be grouped into calcium-rich and into silicon-rich forms and can also be grouped into C-S-H (I) with Ca/Si ratio of 0.6-1.5 and C-S-H (II) with Ca/Si ratio of 1.5-2.0. C-S-H structures are most often modelled as jennite-like and as tobermorite-like systems (i.e., tobermorite 9, 11 and 14 Å) and/or with distorted semi-crystalline variations of them. Both C-S-H (I) and C-S-H (II) structures resemble tobermorite with the exception of which some silicon oxygen tetrahedrons in their silicon chain are partially lost or deformed and hence form some plurality of dimmers. Model of C-S-H is not known yet because of a lot of factors include water/Ca ratio, Ca/Si ratio, Q_n ratio, chemical composition, density, etc. C-S-H phase with averaged Ca/Si ratio of about 1.7 is found in ordinary hardened cement paste. It is also an important binding phase [23]. In the thesis of Fu [24], he developed C-S-H cell starting from tobermorite 11 A and obtained first amorphous tobermorite whose long range is distorted.

Unit cell of 11 Å tobermorite was obtained from work of Fu et al. [23]. It has chemical formula: $Ca_8Si_{12}O_{28}(OH)_8{\cdot}4H_2O$, cell angles $(\alpha, \beta, \gamma) = (90^o, 90^o, 123.49^o)$ and cell length $(a, b, c) = (6.69\ \text{Å}, 7.39\ \text{Å}, 22.779\ \text{Å})$. The structure of the crystal is monoclinic in the $P2_1$ space group. C-S-H was modelled based on Hamid [25] as can be seen in **Figure 1.3**. Green balls are Ca atoms, yellow balls are Si atoms, red balls are O atoms, and blue balls are H atoms. **Table 1.3** presents atom coordinates of 11 Å natural tobermorite. Fu et al. developed C-S-H (I) initially from 11 Å tobermorite with annealing process. Following the same procedure, we obtained C-S-H (I) with calcium-to-silicon (Ca/Si) ratio of 0.67. All colours of the balls remain the same in this study unless mentioned otherwise.

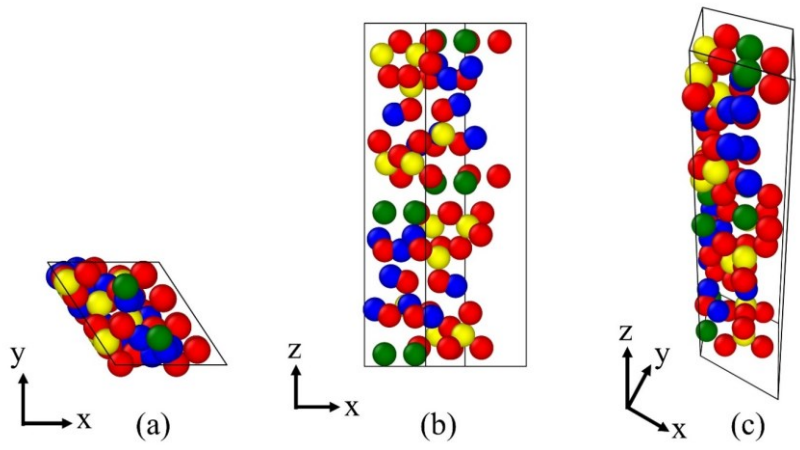

Figure 1.3 Unit cell of 11 Å tobermorite: (a) xy-plane, (b) xz-plane and (c) perspective view.

Table 1.3 Atom coordinates of 11 Å natural tobermorite in space group $P2_1$ (Ca denote with $^+$) are statistically distributed [25].

	x	y	z		x	y	z
Ca(1)	0.75	0.75	0	Ca(4)	0.75	0.25	0.413
Ca(2)	0.75	0.25	0	$^+$)Ca(5)	0.506	0.38	0.198
Ca(3)	0.75	0.75	0.413	$^+$)Ca(6)	0.506	0.88	0.198
Si(1)	0.25	0.287	0.056	Si(4)	0.25	0.207	0.373
Si(2)	0.25	0.707	0.056	Si(5)	0.084	0.417	0.282
Si(3)	0.068	0.909	0.141	Si(6)	0.25	0.787	0.373
O(1)	0.25	0.17	0.12	O(10)	0.25	0.0	0.348
O(2)	0.015	0.137	0.0189	O(11)	0.015	0.122	0.4108
O(3)	0.484	0.372	0.0189	O(12)	0.484	0.357	0.4108
O(4)	0.25	0.50	0.077	O(13)	0.25	0.335	0.31
O(5)	0.015	0.622	0.0189	OH/O(14)	0.1	0.425	0.213
O(6)	0.484	0.856	0.0189	O(15)	0.25	0.645	0.31
O(7)	0.25	0.83	0.12	O(16)	0.015	0.638	0.4108
OH/O(8)	0.068	0.909	0.211	O(17)	0.484	0.872	0.4108
O/OH(9)	-0.18	0.785	0.113	O/OH(18)	-0.175	0.288	0.306
$H_2O(1)$	0.75	0.75	0.303	$H_2O(2)$	0.75	0.25	0.11

1.2.2 Adhesion between main cement phases

Bonnaud et al. [26] have studied on the interaction grand potential between C-S-H nanoparticles at the molecular level. To study mean forces between C-S-H nanoparticles for defined physical environments, particle orientations, particle compositions, and particle volume fraction, they employed grand canonical Monte Carlo simulations. Since C-S-H particles are anisotropic in crystallography and in geometry, interaction forces among particles may be different depending on relative particle orientation. Therefore, mechanical properties of cement pastes could be affected by such differences. To account for this effect, they have constructed 3 different particle-pair configurations. While configuration A represents two interacting particles aligned in parallel, configuration B represents two interaction particles maintain the same opposing surface, but particle 2 is rotated in plane by 123.58^o around the z-axis in respect to particle 1. On the other hand, configuration C represents a configuration where particle 2 is

rotated by 88.52° around the x-axis in respect to particle 1 as shown in **Figure 1.4**, where water molecules are removed for clarity, red and yellow sticks represents silica chains, grey spheres represent calcium ions in the molecular structure (Ca) and calcium counterions (C_w). They found the minima of mean forces (often refer to adhesion force with the absolute value) of configuration A, B and C as -24.34 nN, -1.97 nN and -11.53 nN, respectively. Using a mean force integration method to obtain interaction grand potentials make it possible to use it in mesoscale simulations, which could describe cementitious materials at coarser length scales. Moreover, they found that both the aspect ratio and crystallographic misorientation of interacting particles affect strongly the cohesion between nanoparticles.

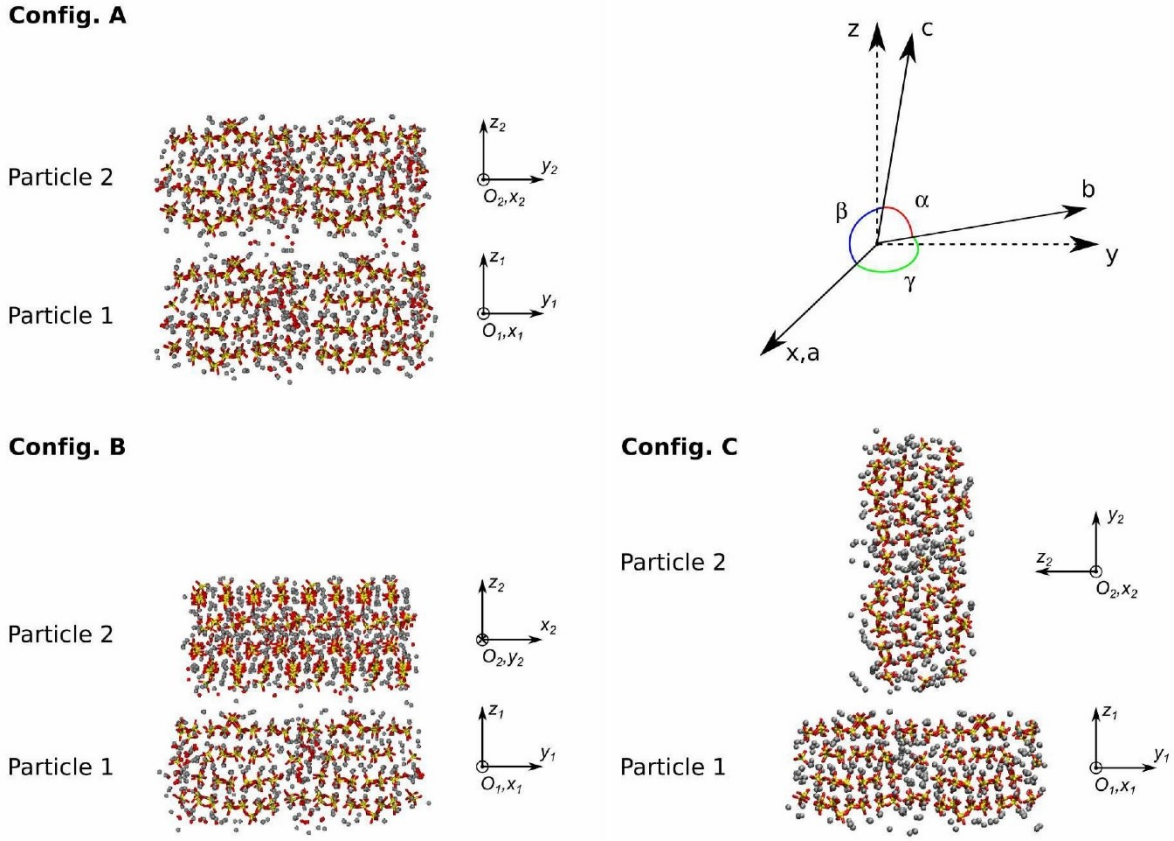

Figure 1.4 Three distinct configurations of C-S-H particle pairs used to calculate interaction grand potential at the molecular level **[26]**.

In the work of Liang [27], the fracture and mechanical properties of C-S-H and CH composite by reactive molecular dynamics simulations were investigated. The results show that C-S-H/CH composite has the lowest Young's modulus and tensile strength, just followed by C-S-H and CH. Moreover, crack could weaken the mechanical properties. The results also show that the fracture toughness of cement does not depend on size and can be viewed as the intrinsic attribute. Within the C-S-H phase and near the interface, crack mainly propagates as a result of

the weak H bonds in the interlayer region of C-S-H. Bonnaud et al. [3] and Liang [24] used different method to obtain the adhesion properties. While Bonnaud et al. increase distance between 2 C-S-H particles in order to obtain potential energy or adhesion force, Liang applied tensile test along the weakest direction (z-direction) to the C-S-H/CH composite.

The main purpose of Ioannidou [3] is to have a modelling approach, which is able to connect structure and mechanics of C-S-H at the mesoscale from early stages of hydration up to the hardened cement paste. Since the structure of cement is amorphous and develops over a range of length scales under conditions of out-of-equilibrium, it is the origin of complexity in cement, especially in C-S-H. This problem has high significances in the mechanical properties of cement as well as in the durability and stability of buildings.

The effective interaction of two spherical C-S-H particles in the mesoscale approach of Ioannidou et al. [28] is defined as a combining of a short-range generalized Lennard-Jones (LJ) attraction and a long-range Yukawa repulsion:

$$V(r) = 4\varepsilon\left[\left(\frac{\sigma}{r}\right)^{2\gamma} - \left(\frac{\sigma}{r}\right)^{\gamma}\right] + A\frac{e^{-\kappa r}}{r} \tag{1.1}$$

where ε and A quantify the relative strength of the attractive, σ is the diameter of particles, r is inter-particle distance, γ is the exponent in the generalized LJ interaction, and κ is the inverse screening length.

Bonnaud et al. [26] also obtained fitting parameters with **Eq. (1.2)** from results of mean force integration which are used to model their interaction grand potentials as shown in **Table 1.4**.

$$U_{ij}(D_{ij}) = 4\varepsilon_{ij}\left[\left(\frac{\sigma_{ij}}{D_{ij}}\right)^{2\alpha} - \left(\frac{\sigma_{ij}}{D_{ij}}\right)^{\alpha}\right] + \psi_{ij}\sigma_{ij}\frac{\exp(-\sigma_{ij}(D_{ij}/\sigma_{ij} - 1)/\lambda_{D,ij})}{D_{ij}} \tag{1.2}$$

where σ_{ij} is the distance for which $U_{ij}(\sigma_{ij}) = 0$, ε_{ij} is the potential well-depth, α is the exponent in the generalized Lennard-Jones potential, ψ_{ij} is the energy of the Yukawa potential term when particle pairs are in contact ($D_{ij} = \sigma_{ij}$), $\lambda_{D,ij}$ is the Debye screening length. As could be seen, interaction grand potentials expression used in Bonnaud et al. is quite similar to the one used in Ioannidou which $A = \psi_{ij}\sigma_{ij}\exp(\sigma_{ij}/\lambda_{D,ij})$ and $\kappa = 1/\lambda_{D,ij}$.

Table 1.4 Fitting parameter obtained from mean force integration used to model their interaction grand potential [26].

Configuration	ε_{ij} × 10³ (kJ/mol)	σ_{ij} (nm)	α	ψ_{ij} × 10³ (kJ/mol)	$\lambda_{D,ij}$ (nm)
A	140.91	2.02	7.24	179.34	1.13
B	48.49	2.23	13.01	47.81	1.70
C	32.63	3.56	13.93	23.59	1.42

Masoero et al. [29] have described a polydisperse colloidal model of the C-S-H get at length scales between 1 and 100 nm. They have shown that results from modelling at the molecular scale can be translated into inputs of the interaction potential, which could predict mechanical properties and structural features at the larger scale of the gel. They used the single-well pairwise interaction potential:

$$U_{ij}(r_{ij}) = 4\varepsilon(\sigma_i, \sigma_j)\left[\left(\frac{\bar{\sigma}_{ij}}{r_{ij}}\right)^{2\alpha} - \left(\frac{\bar{\sigma}_{ij}}{r_{ij}}\right)^{\alpha}\right] \tag{1.3}$$

where r_{ij} is the inter-particle distance, ε is the well depth between two particles with different size σ_i and σ_j, and α controls how narrow the potential well is, $\bar{\sigma}_{ij} = (\sigma_i + \sigma_j)/2$.

For the study of Sekkal et al. [30], they analyse the technical connection between (001) montmorillonite and (104) calcite surfaces at the atomic level and also the conditions to obtain a stable assembly. Results demonstrate that the elastic energy of calcite to ensure good adhesion at the interface in the x direction is lower than the elastic energy of clay. In contrast, the elastic energy of clays provides the energy for the accommodation to calcite in the y direction. Moreover, they have also evaluated adhesion energy (E_{ad}) and work of separation (W_{sep}):

$$\begin{aligned} E_{ad} &= \gamma_c + \gamma_a - \gamma_{c/a} \\ W_{sep} &= E_{ad}/(2A) \end{aligned} \tag{1.4}$$

where γ_c and γ_a is the surface free energy of calcite and clay, $\gamma_{c/a}$ is the interfacial energy of calcite/clay assembly, and A is the area of the contact surface.

Late on, Sekkal and Zaoui [31] studied on the enhancing of the interface bond strength of cement nanocomposite with carbonate nanostructure. They intended to study the interfacial strength as well as the adhesion contact between calcite and C-S-H surface. By applying longitudinal and lateral strain on both surfaces, it shows that the elastic energy of calcite to

ensure accommodation at the interface is higher than the one obtained for C-S-H and the distance of 1 Å is the best choice to achieve a good adhesion between (001) C-S-H and (104) calcite surfaces. Furthermore, the presence of water molecules at the interface absorbs the excess energy and consequently, contributes to the stabilization of the interface. They also calculated the energy of adhesion (E_{ad}) and work of separation (W_{sep}) following **Eq. (1.4)**.

1.2.3 Molecular Dynamics simulations

MD is a computer simulation technique for analysing physical movement of atoms and molecules. Atoms and molecules can interact for a time period, giving insight into dynamic 'evolution' of the system. In the most common version, the atoms and molecules trajectories are determined by numerically solving Newton's equation of motion in a system of interacting particles. The interatomic force and its potential energy are often calculated using the interatomic potential or the mechanical force field of the molecular [32].

1.2.4 Large-scale Atomic/Molecular Massively Parallel Simulator

Large-scale Atomic/Molecular Massively Parallel Simulator (LAMMPS) focus on material modelling using a classical molecular dynamic code. It can be used for soft matter, solid-state materials, and coarse-grained or mesoscopic systems to model atoms as a parallel particle simulator at continuum, meso or atomic scale. Moreover, it can also run with a single processors or in parallel to save time using message-passing techniques and a spatial-decomposition of simulation domain. It is an open source code which distributed by Sandia National Laboratories, a US department of energy laboratory under the terms of GPL. In order to compute their motion, Newton's equations are integrated to calculate their motion while each of N atoms or molecules in the simulation is considered as a point mass. A variety of microscopic and macroscopic information can be extracted such as structural or conformational properties, phases diagrams and transport coefficients. In a potential energy functional for the system from which individual force equations for each atom are derived, it contains the physics of model. Since only vectors of atom information are stored, MD simulations do not typically take large space on memory. The simulations are memory intensive in two domains which are the number of timesteps and the number of atoms. Angstrom is the length scale of atomic coordinate and many thousands or millions of atoms must usually be simulated to approach even the sub-micron scale in three dimensions. Plus, the timestep size is constrained by the demand that the vibrational motion of the atoms be accurately tracked in solids and liquids. As a result, timestep is limited to

femtosecond scale and so tens of hundreds of thousands of timestep are required to simulate even picoseconds of 'real' time [32].

1.2.5 Introduction of force field

Force field is very important in the MD simulation and there are multiple force fields. For instance, ClayFF force field which is a classical molecular dynamics and ReaxFF force field which is a reactive molecular dynamics. For ClayFF force field, it works with CH and C-S-H, whereas ReaxFF force field works with CH, C-S-H and AFt. In order to run ClayFF force field in LAMMPS, bonds between atoms are created at the beginning of the simulation. ReaxFF force field does not required to create bonds between atoms at the beginning of the simulation. Hence, it fits to model composite between main cement paste phases, in particular, interaction at interface to represent adhesion. However, ReaxFF is time consuming compared to ClayFF.

1.2.5.1 ReaxFF force field

Van Duin et al. [33] developed ReaxFF force field for hydrocarbons, which is a force field for reactive systems in order to make practical molecular dynamics simulations of large scale reactive chemical systems. On the one hand, ReaxFF force field uses a general relationship between bond order and bond distance. On the other hand, ReaxFF force field uses a general relationship between bond order and bond energy, which leads to proper dissociation of bonds to separated atoms. Other valence terms that present in force field (torsion and angle) are defined in terms of the same bond orders. Thus, all these terms go to zero smoothly as bond break. Moreover, in order to describe non-bond interactions between all atoms (no exclusions), Morse (van der Waals) and Coulomb potentials are also included in ReaxFF force field. From reactions of small molecules plus geometry data and heat of formation for a number of stable hydrocarbon compounds and quantum chemical calculations on bond dissociation, the parameters were derived. The classical force fields are unable to describe the chemical reactions, which will be initiated because of large deformations. This matter has been taken into account in the study of Hajilar and Shafei [34] through reactive molecular dynamics simulations using ReaxFF force field. The harmonic bonds of classical MD is substituted by the bond orders and energies based on interatomic distances. With this approach, it is capable of capture the bond breakage and formation while the bond interactions are permitted to decay smoothly to zero. For all atoms in the system by a screened taper function, van der Waals and non-bonded Columbic interactions are calculated. The charged equilibrium (Q_{Eq}) method determines atomic charges and need to be updated at every timestep.

1 Tensile test of hydrated cement paste phases

The system energy of ReaxFF force field could be written as shown as follows [33]:

$$E_{system} = E_{bond} + E_{over} + E_{under} + E_{val} + E_{pen} + E_{tors} + E_{conj} + E_{vdWaals} + E_{Coulomb} \quad (1.5)$$

where E_{bond} represents the bond energy, E_{over} and E_{under} the energy penalty for over- and under-coordination of atoms, E_{val}, E_{pen}, E_{tors}, E_{conj}, $E_{vdWaals}$ and $E_{Coulomb}$ the valence angle, penalty, torsion, conjugation, Van der Waals and Coulomb energy, respectively.

Bond energies are calculated from the corrected bond order BO_{ij} [33]:

$$E_{bond} = -D_e \cdot BO_{ij} \cdot \exp\left[p_{be,1}\left(1 - BO_{ij}^{p_{be,2}}\right)\right] \quad (1.6)$$

where D_e, $p_{be,1}$ and $p_{be,2}$ are bond parameters (**Table 1.5**).

Table 1.5 Bond parameter parameters [33].

Bond	D_e (kcal/mol)	$p_{be,1}$ (–)	$p_{be,1}$ (–)
C–C	145.2	0.318	0.65
C–H	183.8	-0.454	12.80
H–H	168.4	-0.310	10.25

The energy penalty (E_{over}) on the system for an over-coordinated atom $(\Delta_i > 0)$ immediately vanishes to zero for under coordinated systems $(\Delta_i < 0)$ and it is defined by [33]:

$$E_{over} = p_{over} \cdot \Delta_i \cdot \left(\frac{1}{1 + \exp(\lambda_6 \cdot \Delta_i)}\right) \quad (1.7)$$

where p_{over} represents the atom parameter (see **Table 1.6**), Δ_i the degree of deviation of the sum of corrected bond order around an atomic centre from the valence of atom i and λ_6 = -8.90 the general parameter of over-coordination energy.

Table 1.6 Atom parameters [33].

	Bond radii	Under/over-coordination		Coulomb parameters
Units	r_o (Å)	p_{over} (kcal/mol)	p_{under} (kcal/mol)	γ (Å)
C	1.399	52.2	29.4	0.69
H	0.656	117.5		0.37

To take into account the energy contribution for the resonance of the π-electron between attached under-coordinated atomic centres, the following equation is used for an under-coordinated atom ($\Delta_i < 0$) [33]:

$$E_{under} = -p_{under} \cdot \frac{1 - \exp(\lambda_7 \cdot \Delta_i)}{1 + \exp(-\lambda_8 \cdot \Delta_i)} \cdot f_6\left(BO_{ij,\pi}, \Delta_j\right)$$
$$f_6\left(BO_{ij,\pi}, \Delta_j\right) = \frac{1}{1 + \lambda_9 \cdot \exp\left(\lambda_{10} \cdot \sum_{j=1}^{neighbors(i)} \Delta_j \cdot BO_{ij,\pi}\right)} \quad (1.8)$$

where p_{under} represents the atom parameter (**Table 1.6**), Δ_i and Δ_j the degree of deviation of the sum of corrected bond order around an atomic centre from the valence of atom i and j, λ_7 = 1.94, λ_8 = -3.47, λ_9 = 5.79 and λ_{10} = 12.38 the general parameter of under-coordination energy and $BO_{ij,\pi}$ the bond order with π-bond character.

To get energy contribution from valence angle terms vanishes to zero as bond order in the valence angle goes to zero, the following definition is used for an under-coordination atom ($\Delta_i, 0$) [33]:

$$E_{val} = f_7(BO_{ij}) \cdot f_7(BO_{jk}) \cdot f_8(\Delta_j) \cdot \left\{k_a - k_a \exp\left[-k_b\left(\Theta_0 - \Theta_{ijk}\right)^2\right]\right\} \quad (1.9)$$

where $f_7(BO)$ represents the term to ensure the valence angle energy contribution vanishes smoothly during bond dissociation, $f_8(\Delta_j)$ the term to deal with the effects of over/under-coordination in central atom j on valence angle energy, k_a and k_b the valence angle parameters and Θ_{ijk} and Θ_0 the valence angle and its equilibrium value, respectively (**Table 1.7**).

Table 1.7 Valence angle parameters [33].

Valence angle units	$\Theta_{o,o}$ (degree)	k_a (kcal/mol)	k_b (kcal/rad)²
C–C–C	71.31	35.4	1.37
C–C–H	71.56	29.65	5.29
H–C–H	69.94	17.37	1.00
C–H–C	0	28.5	6.00
H–H–C	0	0	6.00
H–H–H	0	27.9	6.00

1 Tensile test of hydrated cement paste phases

Effects of over/under-coordination in central atom *j* on the penalty energy is defined by [33]:

$$E_{pen} = \lambda_{19} \cdot f_9(\Delta_j) \cdot \exp\left[-\lambda_{20} \cdot \left(BO_{ij} - 2\right)^2\right] \cdot \exp\left[-\lambda_{20} \cdot \left(BO_{jk} - 2\right)^2\right] \tag{1.10}$$

$$f_9(\Delta_j) = \frac{2 + \exp(-\lambda_{21} \cdot \Delta_j)}{1 + \exp(-\lambda_{21} \cdot \Delta_j) + \exp(\lambda_{22} \cdot \Delta_j)}$$

where λ_{19} = 36.0, λ_{20} = 7.98, λ_{21} = 0.40, λ_{22} = 4.00 are general parameters of penalty energy.

To insure that dependence of the energy of torsion angle ω_{ijkl} accounts properly for $BO \rightarrow$ 0 and for BO greater than 1, the following equation is used [33]:

$$E_{tors} = f_{10}(BO_{ij}, BO_{jk}, BO_{kl}) \cdot \sin\Theta_{ijk} \cdot \sin\Theta_{jkl} \left[\frac{1}{2} V_2 \cdot \exp\left\{p_t \left(BO_{jk} - 3 + f_{11}(\Delta_j, \Delta_k)\right)^2\right\} \cdot \left(1 - \cos 2\omega_{ijkl}\right) + \frac{1}{2} V_3 \cdot \left(1 + \cos 3\omega_{ijkl}\right)\right] \tag{1.11}$$

where V_2-cosine term depends on the bond order of the central bond BO_{jk}. $\sin\Theta_{ijk} \cdot \sin\Theta_{jkl}$ is the valence-angle-dependent term to insure that the torsion energy contribution vanishes when either of the two valence angles Θ_{ijk} or Θ_{jkl} approaches π. $f_{10}(BO_{ij}, BO_{jk}, BO_{kl})$ is the term to reduce the influence of BO_{jk} on the V_2-term. $f_{11}(\Delta_j, \Delta_k)$ is the term to describes the smooth vanishing of the torsion energy contribution (**Table 1.8**).

Table 1.8 Torsion and conjugation parameters [33].

Torsion angle	V_2 (kcal/mol)	V_3 (kcal/mol)	p_t
C–C–C–C	21.7	0.00	-2.42
C–C–C–H	30.5	0.58	-2.84
H–C–C–H	26.5	0.37	-2.33

Now, it is possible to describe contribution of conjugation effects to molecular energy [33]:

$$E_{conj} = f_{12}(BO_{ij}, BO_{jk}, BO_{kl}) \cdot \lambda_{26} \cdot [1 + (\cos^2 \omega_{ijkl} - 1) \cdot \sin \Theta_{ijk} \cdot \sin \Theta_{jkl}]$$

$$f_{12}(BO_{ij}, BO_{jk}, BO_{kl}) = \exp\left[-\lambda_{27} \cdot \left(BO_{ij} - 1\frac{1}{2}\right)^2\right] \cdot \exp\left[-\lambda_{27} \cdot \left(BO_{jk} - 1\frac{1}{2}\right)^2\right] \cdot \exp\left[-\lambda_{27} \cdot \left(BO_{kl} - 1\frac{1}{2}\right)^2\right] \quad (1.12)$$

where λ_{26} = -1.14 and λ_{27} = 2.17 are the general parameters of conjugation energy.

A distance-corrected Morse-potential is used to account for van der Waals interactions [33]:

$$E_{vdWaals} = D_{ij} \cdot \left\{\exp\left[\alpha_{ij} \cdot \left(1 - \frac{f_{13}(r_{ij})}{r_{vdWaals}}\right)\right] - 2 \cdot \exp\left[\frac{1}{2} \cdot \alpha_{ij} \cdot \left(1 - \frac{f_{13}(r_{ij})}{r_{vdWaals}}\right)\right]\right\}$$

$$f_{13}(r_{ij}) = \left[r_{ij}^{\lambda_{28}} + \left(\frac{1}{\gamma_w}\right)^{\lambda_{28}}\right]^{1/\lambda_{28}} \quad (1.13)$$

$$r_{ij} = 1/2(r_i + r_j)$$

where $\lambda_{28} = 1.69$ represents the general parameter of van der Waals energy and $f_{13}(r_{ij})$ a shield interaction. Arithmetic combination rules are used for all van der Waals parameters (**Table 1.6** and **Table 1.9**).

Table 1.9 Van der Waals parameters [33].

Atom units	$r_{vdwaals}$ (Å)	D (kcal/mol)	α	γ_w (Å)
C	3.912	0.0862	10.71	1.41
H	3.649	0.0194	10.06	5.36

Coulomb interactions are taken into account between all atom pairs. A shield Coulomb potential is used to adjust orbital overlap between atoms at close distances [33].

$$E_{Coulomb} = C \cdot \frac{q_i \cdot q_j}{\left[r_{ij}^3 + \left(1/\gamma_{ij}\right)^3\right]^{1/3}} \tag{1.14}$$

where q_i and q_j are the atomic charges, γ_{ij} could be found in **Table 1.6**.

1.2.5.1 ClayFF force field

Molecular simulations on computer have become very helpful in giving an atomistic perspective on behaviour and structure of clay minerals. In the paper of Cygan et al. [35], they demonstrate an alternative approach to develop a general force field for molecular simulation of hydrated crystalline compounds and their interfaces with fluid phases. ClayFF is based on a non-bonded (ionic) description of the metal-oxygen interactions, which is associated with hydrated phases. Within this force field framework, all atoms are described as point charges and are allowed to complete translational freedom. Metal-oxygen interactions are based on a simple Lennard-Jones (12-6) potential combining with electrostatics. Their results show that ClayFF has a good promise to employ in a widely adaptable and broadly effective force field for simulations of molecular of fluid interfaces with clays and other clay-related phases, as well as other inorganic materials defined by complex, disordered, and ill-determined composition and structure.

The total energy has contribution from Coulombic interactions, van der Waals interaction, bond stretch and angle bend interactions [35]:

$$E_{total} = E_{Coulomb} + E_{vdWaals} + E_{bond\ stretch} + E_{angle\ bend} \tag{1.15}$$

where $E_{Coulomb}$, $E_{vdWaals}$, $E_{bond\ stretch}$ and $E_{angle\ bend}$ are Coulombic, van der Waals, bond stretch, and angle bend energy, respectively.

The Coulombic energy is inversely proportional to the distance of separation r_{ij}:

$$E_{Coulomb} = \frac{e^2}{4\pi\epsilon_0} \sum_{i \neq j} \frac{q_i q_j}{r_{ij}} \tag{1.16}$$

where q_i and q_j are the partial charges, e is the charge of electron, and ϵ_0 is the dielectric permittivity of vacuum (8.85419×10^{-12} F/m).

The van der Waals energy term includes the attractive dispersion energy, and the short-range repulsion associated with the rise of energy as two atoms approach each other:

$$E_{vdWaals} = \sum_{i \neq j} D_{o,ij} \left[\left(\frac{R_{o,ij}}{r_{ij}} \right)^{12} - 2 \left(\frac{R_{o,ij}}{r_{ij}} \right)^{6} \right] \tag{1.17}$$

where $D_{o,ij}$ and $R_{o,ij}$ are empirical parameters derived from fitting of the model (**Table 1.10**).

Table 1.10 Non-bond parameters for ClayFF force field [35].

Species	Symbol	Charge (e)	D_o (kcal/mol)	R_o (Å)
Water hydrogen	h*	0.4100		
Hydroxyl hydrogen	ho	0.4250		
Water oxygen	o*	-0.8200	0.1554	3.5532
Hydroxyl oxygen	oh	-0.9500	0.1554	3.5532
Bridging oxygen	ob	-1.0500	0.1554	3.5532
Bridging oxygen with octahedral substitution	obos	-1.1808	0.1554	3.5532
Bridging oxygen with tetrahedral substitution	obts	-1.1688	0.1554	3.5532
Bridging oxygen with double substitution	obss	-1.2996	0.1554	3.5532
Hydroxyl oxygen with substitution	ohs	-1.0808	0.1554	3.5532
Tetrahedral silicon	st	2.1000	1.8405×10^{-6}	3.7064
Octahedral aluminium	ao	1.5750	1.3298×10^{-6}	4.7943
Tetrahedral aluminium	at	1.5750	1.8405×10^{-6}	3.7064
Octahedral magnesium	mgo	1.3600	9.0298×10^{-7}	5.9090
Hydroxide magnesium	mgh	1.0500	9.0298×10^{-7}	5.9090
Octahedral calcium	cao	1.3600	5.0298×10^{-6}	6.2484
Hydroxide calcium	cah	1.0500	5.0298×10^{-6}	6.2484
Octahedral iron	feo	1.5750	9.0298×10^{-6}	5.5070
Octahedral lithium	lio	0.5250	9.0298×10^{-6}	4.7257
Aqueous sodium ion	Na	1.0	0.1301	2.6378
Aqueous potassium ion	K	1.0	0.1000	3.7423
Aqueous caesium ion	Cs	1.0	0.1000	4.3002
Aqueous calcium ion	Ca	2.0	0.1000	3.2237
Aqueous barium ion	Ba	2.0	0.0470	4.2840
Aqueous chloride ion	Cl	-1.0	0.1001	4.9388

1 Tensile test of hydrated cement paste phases

The interaction parameters between the unlike atoms are calculated according to the arithmetic mean rule for the distance parameter R_o, and the geometric mean rule for the energy parameter, D_o:

$$R_{o,ij} = \frac{1}{2}\left(R_{o,i} + R_{o,j}\right)$$
$$D_{o,ij} = \sqrt{D_{o,i}D_{o,j}} \tag{1.18}$$

The bond stretch and angle bend energy of the hydroxyl bond are described by a simple harmonic term:

$$E_{bond\ stretch\ ij} = k_1\left(r_{ij} - r_o\right)^2$$
$$E_{angle\ bend\ ij} = k_2\left(\theta_{ijj} - \theta_o\right)^2 \tag{1.19}$$

where k_1 and k_2 are the force constant (**Table 1.11**). θ_{ijk} is the bond angle for the metal-oxygen-hydrogen. r_0 and θ_0 represent equilibrium bond length and equilibrium bond angle, respectively.

Table 1.11 Bond parameters for ClayFF force field [35].

Bond stretch			
Species i	Species j	k_1 (kcal/mol Å²)	r_o (Å)
o*	h*	554.1349	1.0000
oh	ho	554.1349	1.0000
ohs	ho	554.1349	1.0000

Angle bend				
Species i	Species j	Species k	k_1 (kcal/mol rad²)	θ_o (deg)
h*	o*	h*	45.7696	109.47
Metal	oh	ho	30.0	109.47
Metal	ohs	ho	30.0	109.47

1.3 Tensile test of portlandite (CH)

1.3.1 Method

As can be seen in **Sub-section 1.2.5**, there are two force fields that can be used with CH. Therefore, MD simulations were performed with both force field to see the differences. In order to perform the tensile test on CH supercells, CH unit cell was replicated in x-, y- and z-directions to get a larger cell called supercell. Hence, we got the supercells of CH with difference sizes. In the case of simulations with ClayFF force field, there are three different sizes such as 4 × 4 × 4, 7 × 7 × 7 and 10 × 10 × 10 in x-, y- and z-directions (**Figure 1.5**), where lime balls are Ca atoms, white balls are H atoms, and red balls are O atoms. In the case of simulations with ReaxFF force field, the only difference is the biggest supercell (i.e., 9 × 10 × 14) as shown in **Figure 1.6**, where white balls are Ca atoms, lime balls are H atoms, and purple balls are O atoms. These supercells were changed from trigonal supercells to orthogonal supercells in order to acquire the independent results to each direction. All MD simulations were done in real units, three dimensions (3D) and periodic boundary condition (PPP). A software called LAMMPS was used to run all simulations. These supercells were relaxed in NPT ensemble with temperature of 300 K and pressure of 0 atm in all three directions. Timestep of these simulations was 0.25 fs. Tensile test along z-direction was applied with varying strain rates from 10^{-3} fs^{-1} to 10^{-6} fs^{-1} after energy minimization and relaxation in NPT ensemble for 100 ps in the case of ClayFF force field. Since 100 ps relaxation consumed a lot of time especially with ReaxFF force field, 50 ps relaxation was used in the case of ReaxFF force field. The results had only a small difference, but it saved time. Different sizes and strain rates were done to study the sensitive analysis. Deformations were applied along z-direction coupled with relaxation in x- and y-directions. Final strain is 0.5 and 1.0 for ClayFF and ReaxFF force fields, respectively.

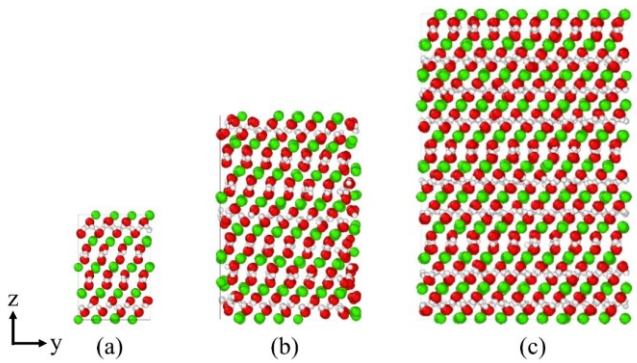

Figure 1.5 CH supercells in yz-plane with ClayFF force field: (a) 4 × 4 × 4, (b) 7 × 7 × 7 and (c) 10 × 10 × 10 in x-, y- and z-directions.

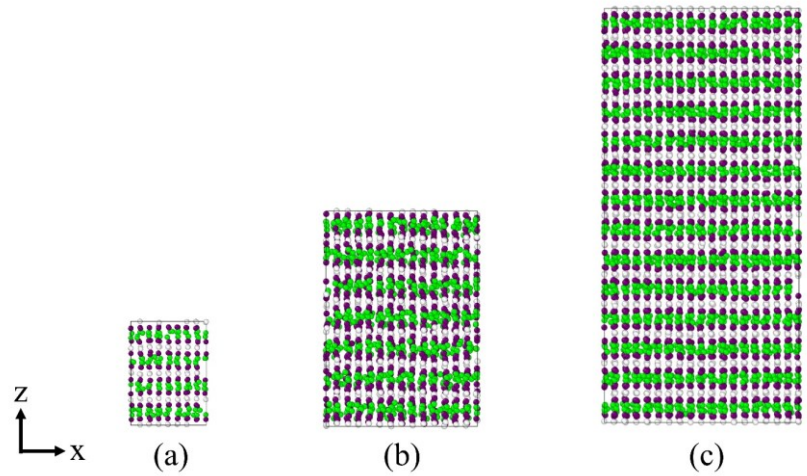

Figure 1.6 CH supercells in xz-plane with ReaxFF force field: (a) 4 × 4 × 4, (b) 7 × 7 × 7 and (c) 9 × 10 × 14 in x-, y- and z-directions.

Simulations were run on computer with the following specifications: Dell OptiPlex 5060, Intel® Core™ i7-8700T with CPU of 2.4 GHz (12 CPUs) and memory of 8192 MB. CPU ranging was from 2 to 8 cores. The relaxation of supercells with NPT ensemble for 100 ps were done only once.

1.3.2 Results and Discussion

Young's modulus, peak stress and peak strain of CH were calculated. Using the method described above, stress-strain curves of different sizes, strain rates and force fields were obtained. Results are divided into two parts as follows: CH cuboid shape supercells with ClayFF force field, CH cuboid and cube shape supercells with ReaxFF force field.

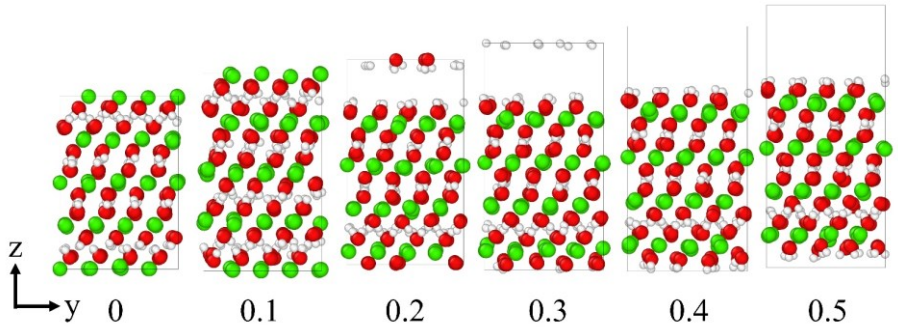

Figure 1.7 Direct tension in z-direction in yz-plane after relaxation to 50% strain of 4 × 4 × 4 CH supercell with ClayFF force field and strain rate of 10^{-5} fs^{-1}.

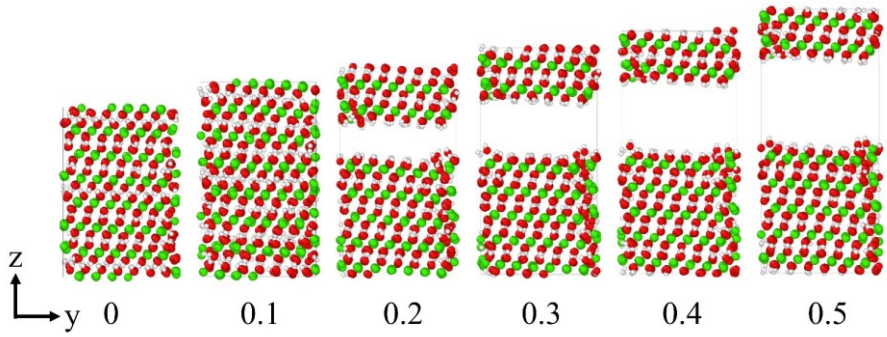

Figure 1.8 Direct tension in z-direction in yz-plane after relaxation to 50% strain of 7 × 7 × 7 CH supercell with ClayFF force field and strain rate of 10^{-5} fs^{-1}.

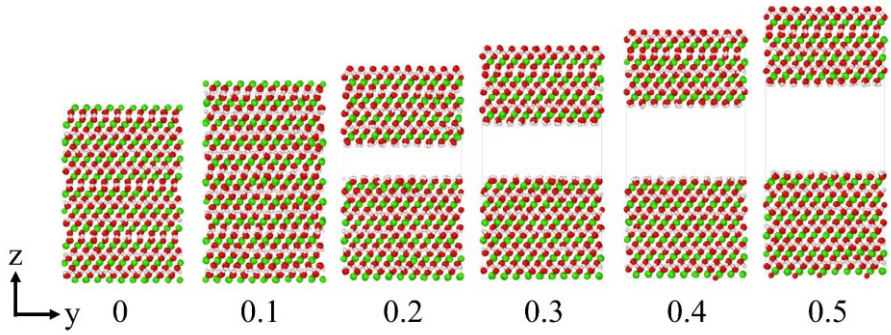

Figure 1.9 Direct tension in z-direction in yz-plane after relaxation to 50% strain of 10 × 10 × 10 CH supercell with ClayFF force field and strain rate of 10^{-5} fs^{-1}.

In the case of CH cuboid shape supercells with ClayFF force field, **Figure 1.7** - **Figure 1.9** illustrate the direct tensile evolution after relaxation to 50% strain of 4 × 4 × 4, 7 × 7 × 7 and 10 × 10 × 10 supercells with strain rate of 10^{-5} fs^{-1}. It can be seen that the rupture was initiated between the H atoms. Stress-strain curves of these supercells with different strain rates can be observed in **Figure 1.10**. Stress returns to the value of around 0 GPa immediately after reaching the peak stress for the cases of 10^{-5} fs^{-1} and 10^{-6} fs^{-1} strain rates. This means that the behaviour seems to be more brittle with smaller strain rate. Also, strain rate has an effect on the stress-strain curve. Bigger strain rate makes bigger oscillation. Sizes of supercell also contributed to a change in oscillation of stress-strain curve. For ClayFF force field, strain rate of 10^{-6} fs^{-1} and size of 10 × 10 × 10 supercell were chosen on the basis of stress-strain curves. Strain rate of 10^{-6} fs^{-1} have a similar peak stress and peak strain compared to strain rate of 10^{-5} fs^{-1}, but it has less oscillation. Size of 10 × 10 × 10 supercell also provides stress-strain curves with less oscillation compared to size of 4 × 4 × 4 and 7 × 7 × 7 supercells.

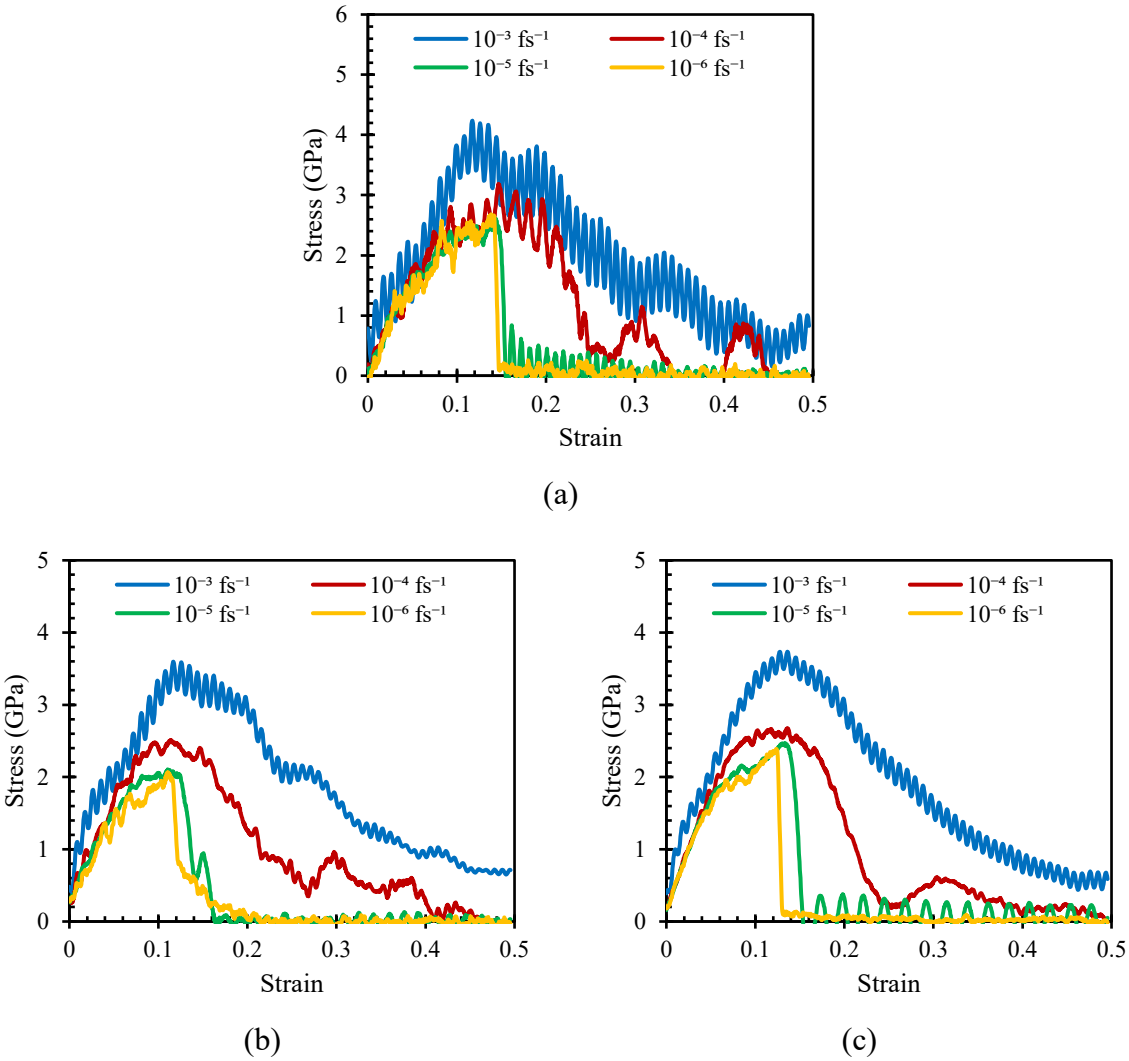

Figure 1.10 Stress-strain curves with three different sizes of CH cuboid shape supercells (ClayFF force field): (a) 4 × 4 × 4 CH supercell, (b) 7 × 7 × 7 CH supercell and (c) 10 × 10 × 10 CH supercell.

The results of peak stress, peak strain and Young's modulus are summarized in **Table 1.12**. These results help us determining which size of supercell and strain rate should be considered to investigate. As can be seen, Young's modulus obtained with 10 × 10 × 10 supercell has similar values despite the different strain rates. In conclusion, we would favour 10 × 10 × 10 supercell with strain rate of 10^{-6} fs^{-1}. For this case, Young's modulus was found to be 33.3 GPa. This result is very close to the other results of the literature with the value of 32.8 GPa [36] and 35.2 GPa [17].

Table 1.12 Peak strain, peak stress, running time and file size of CH cuboid shape supercell with ClayFF force field along z-direction.

Size (x × y × z)	Strain rate (fs^{-1})	Peak strain	Peak stress (GPa)	Young's modulus (GPa)	Running time (hr:min)	File size (MB)
4 × 4 × 4	10^{-3}	0.12	4.24	23.2	0:01	57
	10^{-4}	0.15	3.19	36.6	0:01	45
	10^{-5}	0.14	2.63	33.9	0:01	45
	10^{-6}	0.14	2.68	40.8	0:01	45
7 × 7 × 7	10^{-3}	0.12	3.60	46.9	0:01	301
	10^{-4}	0.11	2.51	29.8	0:01	238
	10^{-5}	0.11	2.11	27.7	0:02	238
	10^{-6}	0.11	2.06	22.1	0:07	238
10 × 10 × 10	10^{-3}	0.13	3.74	35.2	0:05	878
	10^{-4}	0.14	2.68	33.2	0:06	694
	10^{-5}	0.13	2.47	33.0	0:10	693
	10^{-6}	0.12	2.39	33.3	0:32	693

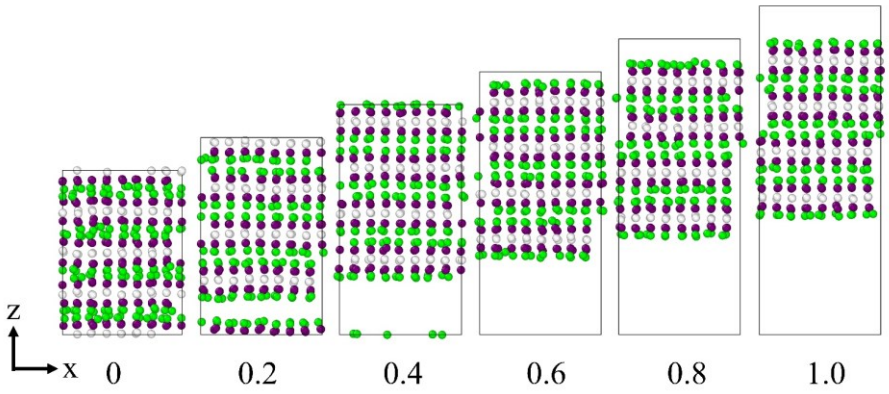

Figure 1.11 Direct tension in z-direction in xz-plane after relaxation to 100% strain of 4 × 4 × 4 CH supercell with ReaxFF force field and strain rate of 10^{-5} fs^{-1}.

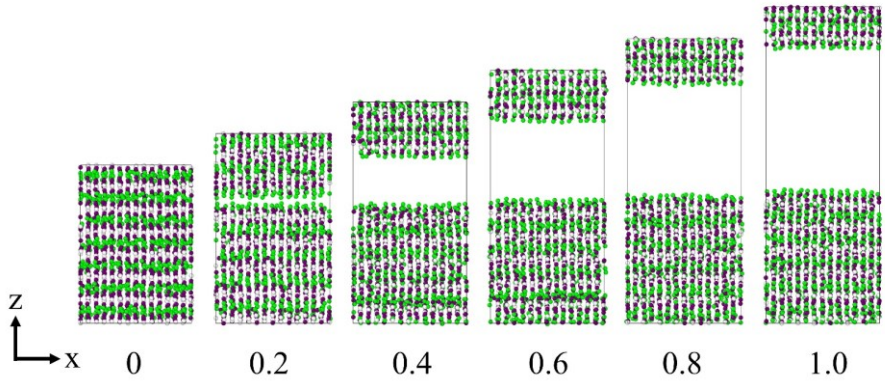

Figure 1.12 Direct tension in z-direction in xz-plane after relaxation to 100% strain of 7 × 7 × 7 CH supercell with ReaxFF force field and strain rate of 10^{-5} fs^{-1}.

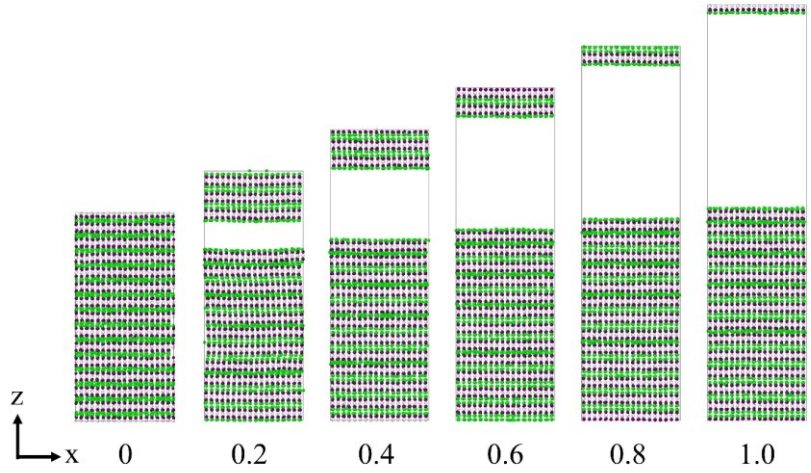

Figure 1.13 Direct tension in z-direction in xz-plane after relaxation to 100% strain of 9 × 10 × 14 CH supercell with ReaxFF force field and strain rate of 10^{-5} fs^{-1}.

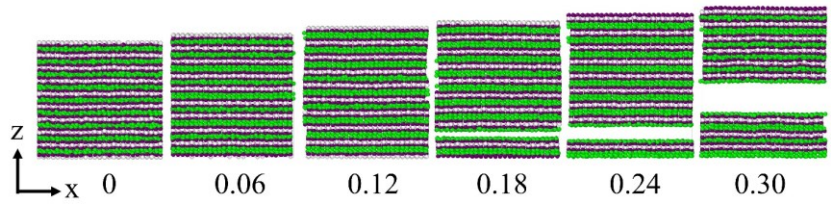

Figure 1.14 Direct tension in z-direction in xz-plane after relaxation to 30% strain of 13 × 16 × 9 CH supercell with ReaxFF force field and strain rate of 10^{-6} fs^{-1}.

In the case of CH supercells with ReaxFF force field, **Figure 1.11 - Figure 1.14** illustrate the direct tensile evolution after relaxation to 30% and 100% strain of 4 × 4 × 4, 7 × 7 × 7, 9 × 10 × 14 and 13 × 16 × 9 supercells with strain rate of 10^{-5} fs^{-1} and 10^{-6} fs^{-1}. It can be seen that the rupture was also initiated between the H atoms. Stress-strain curves of these supercells with

different strain rates can be observed in **Figure 1.15**. Stress returns to the value of around 0 GPa immediately after reaching the peak stress for the cases of 10^{-6} fs^{-1} strain rates except for the size of 7 × 7 × 7 supercell. This means that behaviour of stress-strain curves seems to be more brittle with smaller strain rate. Strain rate also has an effect on the stress-strain curve. Bigger strain rate makes bigger oscillation. Sizes of supercell also contributed to a change in oscillation of stress-strain curve. For ReaxFF force field, strain rate of 10^{-6} fs^{-1} and the size of 9 × 10 × 14 supercell were chosen on the basis of stress-strain curves. Size of 9 × 10 × 14 supercell also provides stress-strain curves with less oscillation compared to size of 4 × 4 × 4, 7 × 7 × 7 and 13 × 16 × 9 supercells. Strain rate of 10^{-6} fs^{-1} has a similar peak stress and peak strain compared to strain rate of 10^{-5} fs^{-1}, but it has less oscillation. The stress-strain curves obtained have more oscillation compared to results obtained with ClayFF force field because ReaxFF force field parameters, which was developed for ettringite (AFt) by Liu et al. [37], may not be an ideal for CH phase. However, this ReaxFF force field parameters include all types of atoms that we need for the study of the other two phases (i.e., C-S-H (I) and AFt). Future work should therefore include the development of ReaxFF force field that will be optimized for all the hydrated cement paste phases.

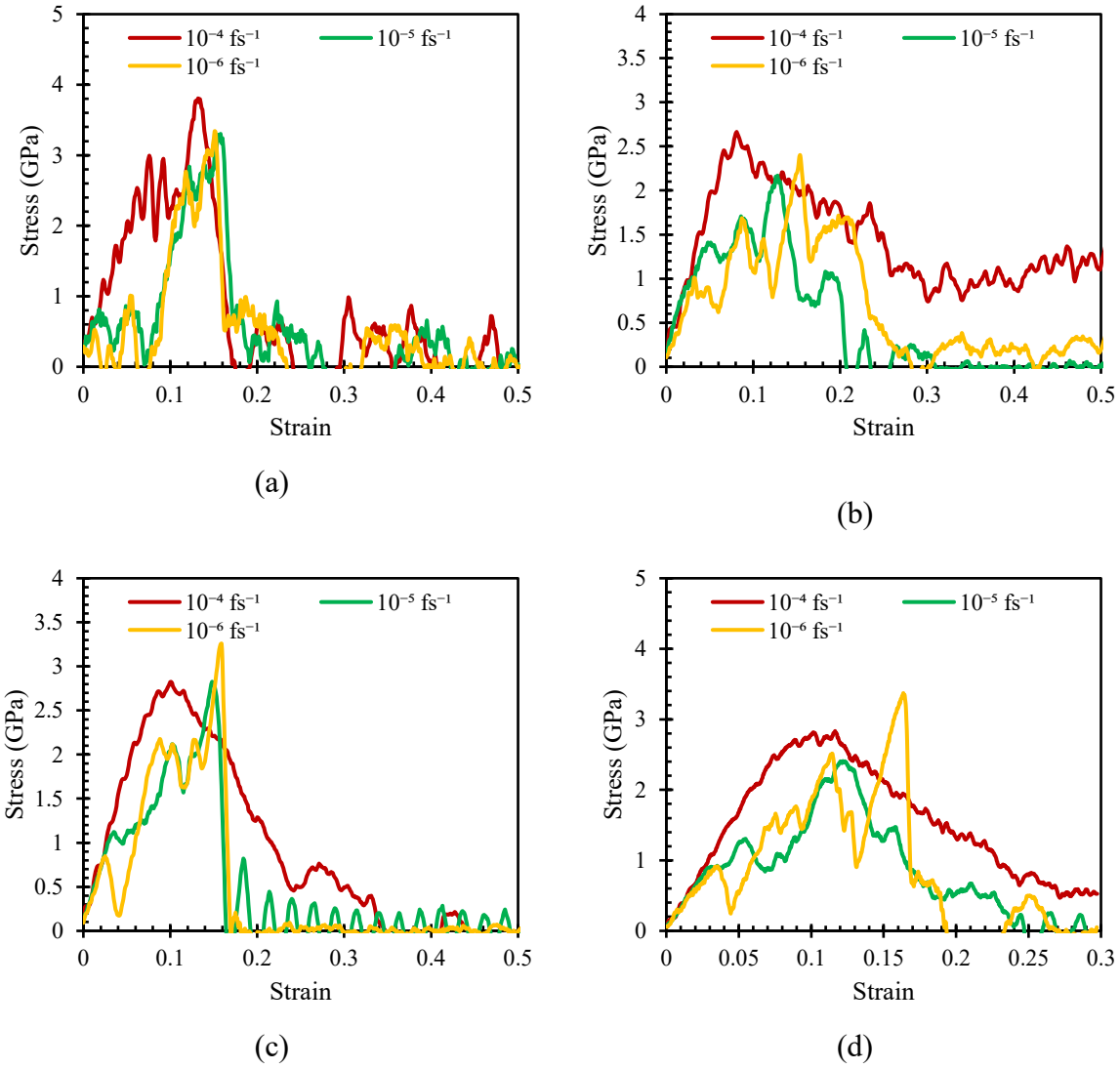

Figure 1.15 Stress-strain curve with different size of CH supercells (ReaxFF force field): (a) 4 × 4 × 4, (b) 7 × 7 × 7, (c) 9 × 10 × 14 and (d) 13 × 16 × 9.

Results of peak stress, peak strain and Young's modulus are summarized in **Table 1.13**. These results help us determining which size of supercell and strain rate should be considered to investigate. Young's modulus obtained with 9 × 10 × 14 and 13 × 16 × 9 supercell are quite close to each other even though the strain rate were different. They are also close to the results obtained by ClayFF force field with the biggest supercell. In conclusion, we would favour either 9 × 10 × 14 or 13 × 16 × 9 supercells with strain rate of 10^{-6} fs^{-1}. Young's modulus was found to be 33.9 GPa and 33.1 GPa, which is close to the other results with the value of 32.8 GPa [36] and 35.2 GPa [17].

Table 1.13 Peak strain, peak stress, running time and file size of CH supercells with ReaxFF force field along z-direction.

Size (x × y × z)	Strain rate (fs^{-1})	Peak strain	Peak stress (GPa)	Young's modulus	Running time (hr:min)	File size (MB)
4 × 4 × 4	10^{-4}	0.13	3.81	33.4	2:38	7
	10^{-5}	0.16	3.30	28.2	3:12	6
	10^{-6}	0.15	3.34	94.5	34:31	9
7 × 7 × 7	10^{-4}	0.08	2.67	31.3	6:05	37
	10^{-5}	0.13	2.17	25.6	9:36	36
	10^{-6}	0.15	2.40	29.3	72:56	37
9 × 10 × 14	10^{-4}	0.10	2.82	34.7	15:38	125
	10^{-5}	0.15	2.83	31.0	27:00	125
	10^{-6}	0.16	3.26	33.9	179:59	125
13 × 16 × 9	10^{-4}	0.12	2.83	34.3	0:22	155
	10^{-5}	0.12	2.41	29.9	3:53	155
	10^{-6}	0.16	3.37	33.1	37:05	155

1.4 Tensile test of ettringite (AFt)

1.4.1 Method

Adapted from **Section 1.3**, AFt unit cell was replicated in x-, y- and z-directions to get a larger cell called supercell to perform the tensile test on AFt supercells. Hence, we got the supercells of AFt with difference sizes. In the case of cuboid shape supercell, there are three difference sizes such as 1 × 1 × 1, 2 × 2 × 2 and 3 × 3 × 3 in x-, y- and z-directions. In the case of cube shape supercell, there is only one size of supercell (i.e., 4 × 5 × 2). These supercells were changed from trigonal supercells to orthogonal supercells in order to acquire the independent results to each direction. Since ReaxFF force field can be used with AFt, this force field was used for these simulations. All MD simulations were in real units, three dimensions (3D) and periodic boundary condition (PPP). These supercells were relaxed in NPT ensemble with temperature of 300 K and pressure of 0 atm in all three directions. Timestep of these simulations was 0.25 fs. Tensile test along z-direction was applied with varying strain rates from 10^{-4} fs^{-1} to 10^{-7} fs^{-1} after energy minimization and relaxation in NPT ensemble for 50 ps. Different sizes and strain rates were done to study the sensitive analysis. Deformations were applied along z-direction coupled with relaxation in x- and y-directions. The final strain is 0.2 and 0.3 for cuboid and cube shape supercells, respectively.

1 Tensile test of hydrated cement paste phases

For cuboid shape supercells, the computer specifications that was used to run all simulations were: Dell Precision 7280, Intel Core Xeon Gold with CPU of 2.2 GHz (56 processors) and memory of 64 GB. We used the CPU ranging from 8 to 24 cores.

For cube shape supercells, visualization cores were used because LAMMPS packages was dependent on graphics libraries. Here are the computer specifications that were used to run all simulations: supercomputer called "Liger", 12-core Intel Xeon (Haswell) E5-2680v3 processors with 252 compute nodes (24 cores per node) and 14 visualization nodes (28 GPUs and 24 cores per node) and 36 608 GB compute memory. The visualization GPUs ranging was from 8 to 24 cores.

1.4.2 Results and Discussion

Using the method described above, we obtained stress-strain curves of different sizes and strain rates. Results are divided into two parts as follows: AFt cuboid shape supercells and AFt cube shape supercells.

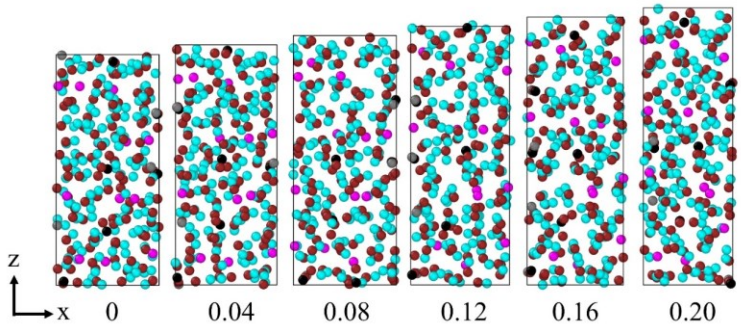

Figure 1.16 Direct tension in z-direction in xz-plane after relaxation to 20% strain of 1 × 1 × 1 AFt supercell with ReaxFF force field and strain rate of 10^{-6} fs^{-1}.

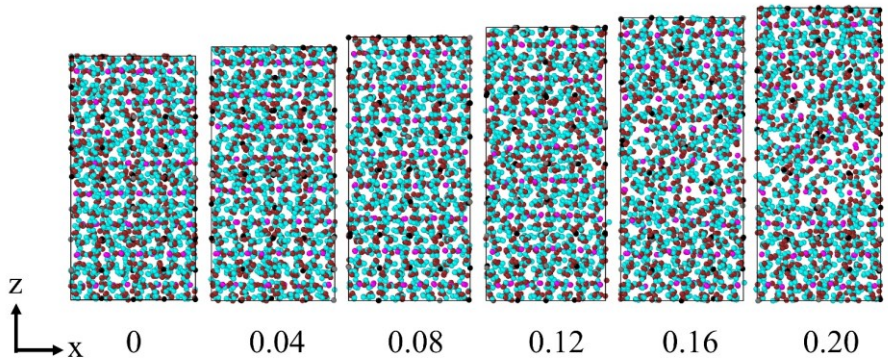

Figure 1.17 Direct tension in z-direction in xz-plane after relaxation to 20% strain of 2 × 2 × 2 AFt supercell with ReaxFF force field and strain rate of 10^{-6} fs^{-1}.

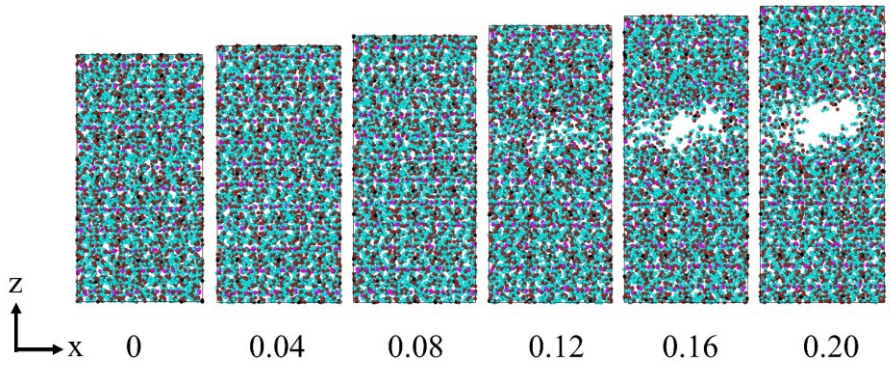

Figure 1.18 Direct tension in z-direction in xz-plane after relaxation to 20% strain of 3 × 3 × 3 AFt supercell with ReaxFF force field and strain rate of 10^{-6} fs^{-1}.

In the case of AFt cuboid shape supercells with ReaxFF force field, **Figure 1.16 - Figure 1.18** illustrate the direct tensile evolution of AFt cuboid shape supercells after relaxation to 20% strain of 1 × 1 × 1, 2 × 2 × 2 and 3 × 3 × 3 supercells with strain rate of 10^{-6} fs^{-1}. A complete rupture was not shown because the strain was stopped at 20%. Running longer would take more time. Especially, the full curves of strain rate 10^{-6} fs^{-1} was already obtained. Stress-strain curves of these supercells with different strain rates can be observed in **Figure 1.19**. In the case of 1 × 1 × 1 supercell, stress-strain curves have remarkable oscillations, which is not usable. Nonetheless, 2 × 2 × 2 and 3 × 3 × 3 supercells provide better results. The behaviour seems to be more brittle with smaller strain rate. Strain rate has an effect on the stress-strain curve. They gave smaller peak stress and peak strain with smaller strain rate, but strain rate did not contribute much to a change in oscillation. However, sizes of supercell contributed to a change in oscillation of stress-strain curve. In order to see the effect of strain rate on peak stress and peak strain, strain rate of 10^{-7} fs^{-1} was run with 2 × 2 × 2 supercell. This size of supercell was chosen because of time consuming compared with 3 × 3 × 3 supercell. As shown in **Figure 1.19b**, they have similar peak stress and peak strain for strain rate of 10^{-6} fs^{-1} and 10^{-7} fs^{-1}. Strain rate of 10^{-6} fs^{-1} and size of 3 × 3 × 3 supercell were chosen on the basis of stress-strain curves. Strain rate of 10^{-6} fs^{-1} have a similar peak stress and peak strain compared to strain rate of 10^{-7} fs^{-1}, but it consumes less time. Size of 3 × 3 × 3 supercell provides stress-strain curves with less oscillation compared to size of 1 × 1 × 1 and 2 × 2 × 2 supercells.

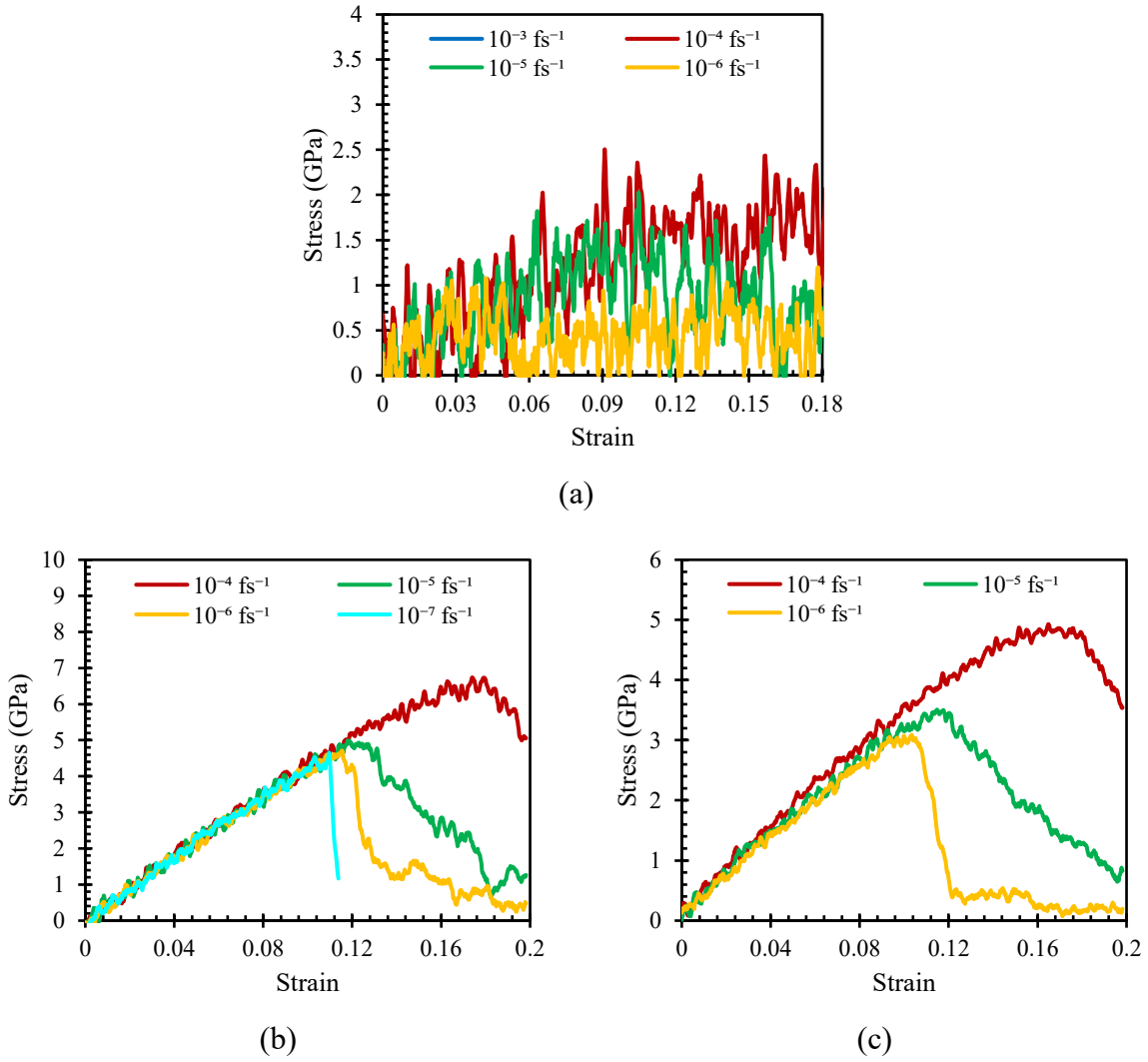

Figure 1.19 Stress-strain curves with three different sizes of AFt cuboid shape supercells (ReaxFF force field): (a) 1 × 1 × 1 AFt supercell, (b) 2 × 2 × 2 AFt supercell and (c) 3 × 3 × 3 AFt supercell.

Results of peak stress, peak strain and Young's modulus are summarized in **Table 1.14**. These results help us determining which size of supercell and strain rate should be considered to investigate. For 2 × 2 × 2 and 3 × 3 × 3 supercells, Young's modulus are close to each other despite different strain rates. However, size of supercell did affect the peak stress and peak strain. Hence, Young's modulus also decreased when size of supercell increased. In conclusion, we would favour 3 × 3 × 3 supercell with strain rate of 10^{-6} fs^{-1}. For this case, Young's modulus was found to be 33.8 GPa, which is close to the other results with the value of 33.1 GPa [38] and 28.3 GPa [39].

Table 1.14 Peak strain, peak stress, running time and file size of AFt cuboid shape supercell with ReaxFF force field along z-direction.

Size (x × y × z)	Strain rate (fs^{-1})	Peak strain	Peak stress (GPa)	Young' modulus (GPa)	Running time (hr:min)	File size (MB)
1 × 1 × 1	10^{-4}	0.09	2.51	16.2	4:07	9
	10^{-5}	0.11	2.03	12.0	1:00	9
	10^{-6}	0.14	1.20	4.2	10:17	9
2 × 2 × 2	10^{-4}	0.17	6.74	44.0	4:55	72
	10^{-5}	0.12	4.99	45.3	1:34	72
	10^{-6}	0.12	4.71	42.1	14:56	72
	10^{-7}	0.11	4.65	44.9	72:00	17
3 × 3 × 3	10^{-4}	0.17	4.93	35.3	9:55	325
	10^{-5}	0.12	3.51	33.6	3:03	325
	10^{-6}	0.10	3.09	33.8	27:25	325

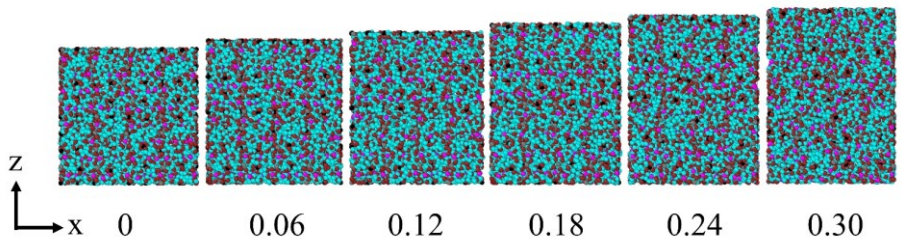

Figure 1.20 Direct tension in z-direction in xz-plane after relaxation to 30% strain of 4 × 5 × 2 AFt supercell with ReaxFF force field and strain rate of 10^{-4} fs^{-1}.

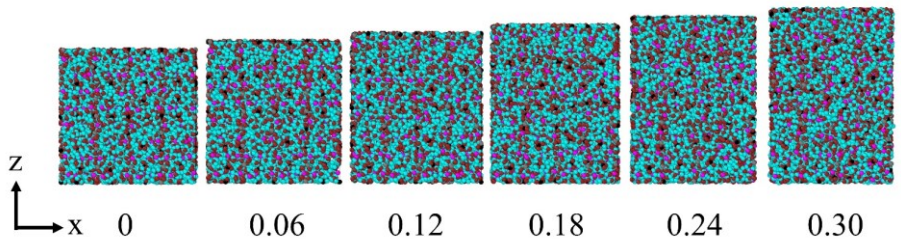

Figure 1.21 Direct tension in z-direction in xz-plane after relaxation to 30% strain of 4 × 5 × 2 AFt supercell with ReaxFF force field and strain rate of 10^{-5} fs^{-1}.

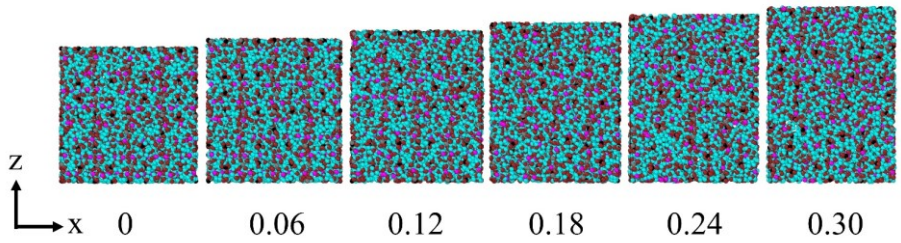

Figure 1.22 Direct tension in z-direction in xz-plane after relaxation to 30% strain of 4 × 5 × 2 AFt supercell with ReaxFF force field and strain rate of 10^{-6} fs^{-1}.

In the case of AFt cube shape supercells with ReaxFF force field, **Figure 1.19 - Figure 1.22** illustrate the direct tensile evolution after relaxation to 30% strain of 4 × 5 × 2 supercell with strain rate of 10^{-4} fs^{-1} to 10^{-6} fs^{-1}. In fact, rupture already occurred, but it is difficult to see because it was not a complete rupture. Stress-strain curves of this supercell with different strain rates can be observed in **Figure 1.23**. The behaviour seems to be more brittle with smaller strain rate. Strain rate has an effect on the stress-strain curve. They gave smaller peak stress and peak strain with smaller strain rate, but strain rate did not contribute much to a change in oscillation. In order to see the effect of strain rate on peak stress and peak strain, strain rate of 10^{-7} fs^{-1} was run. As can be seen, they have similar peak stress and peak strain for strain rate of 10^{-6} fs^{-1} and 10^{-7} fs^{-1}. Strain rate of 10^{-6} fs^{-1} was chosen on the basis of stress-strain curves. Strain rate of 10^{-6} fs^{-1} have a similar peak stress and peak strain compared to strain rate of 10^{-7} fs^{-1}, but it consumes less time.

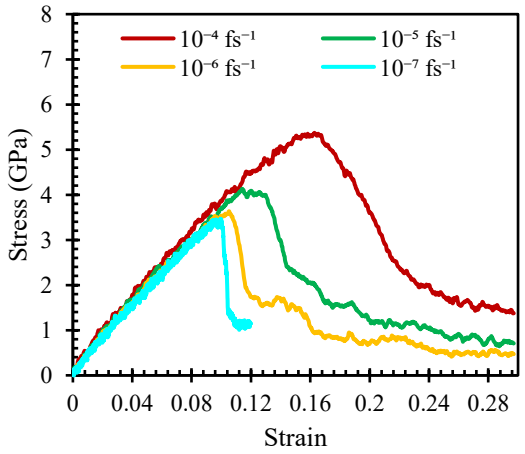

Figure 1.23 Stress-strain curves with different strain rates of AFt cube shape supercells (ReaxFF force field) of 4 × 5 × 2 AFt supercell.

Results of peak stress, peak strain and Young's modulus are summarized in **Table 1.15.** These results help us determining which size of supercell and strain rate should be considered

to investigate. Young's moduli are similar to each other despite the different strain rates. In conclusion, we would favour strain rate of 10^{-6} fs^{-1} in the case of cube shape supercell. For this case, Young's modulus was found to be 37.1 GPa, which is similar to the other results with the value of 33.1 GPa [38] and 28.3 GPa [39].

Table 1.15 Peak strain, peak stress, running time and file size of AFt cube shape supercell with ReaxFF force field along z-direction.

Size (x × y × z)	Strain rate (fs^{-1})	Peak strain	Peak stress (GPa)	Young's modulus (GPa)	Running time (hr:min)	File size (MB)
4 × 5 × 2	10^{-4}	0.16	5.37	37.8	0:30	172
	10^{-5}	0.11	4.13	38.2	5:04	172
	10^{-6}	0.11	3.63	37.1	50:22	172
	10^{-7}	0.10	3.47	36.7	125:12	756

As can be observed in **Figure 1.24**, stress-strain curves of 3 × 3 × 3 AFt supercell (cuboid shape) and 4 × 5 × 2 AFt supercell (cube shape) are quite similar. Therefore, Young's modulus and peak stress have similar values too. To conclude, either cuboid or cube shape could be used for the simulation to obtain its mechanical properties.

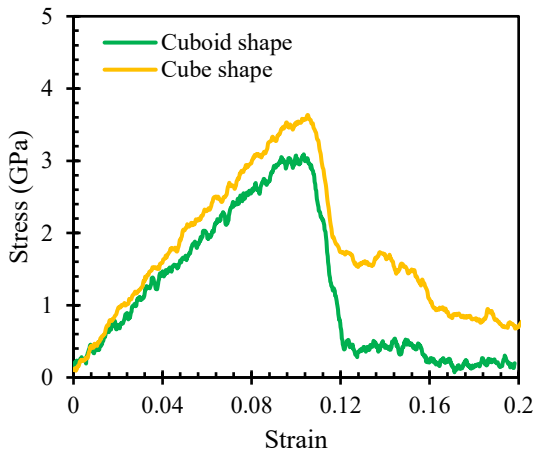

Figure 1.24 Stress-strain curves of AFt cuboid and cube shape supercells with strain rate of 10^{-6} fs^{-1}.

1.5 Tensile test of calcium-silicate-hydrates (C-S-H (I))

1.5.1 Method

Similar to **Section 1.3**, C-S-H (I) unit cell was replicated in x-, y- and z-directions to get a larger cell called supercell to perform the tensile test on C-S-H (I) supercells. Hence, we got the supercells of C-S-H (I) with difference sizes. In the case of cuboid shape supercell, there are three difference sizes such as 2 × 2 × 2, 3 × 3 × 3 and 5 × 5 × 3 in x-, y- and z-directions. In the case of cube shape supercell, there is only one size of supercell (i.e., 7 × 8 × 2). These supercells were changed from monoclinic supercells to orthogonal supercells in order to acquire the independent results to each direction. All MD simulations were done in real units, three dimensions (3D) and periodic boundary condition (PPP). Since ReaxFF force field can be used with C-S-H (I), this force field was utilized in these simulations. Fu et al. [23] developed C-S-H (I) initially from 11 Å tobermorite with annealing process. Following the same procedure, we obtained C-S-H (I) with calcium-to-silicon (Ca/Si) ratio of 0.67. These annealing supercells were then relaxed in NPT ensemble with temperature of 300 K and pressure of 0 atm in all three directions. Timestep of these simulations was 0.25 fs except in the case of 2.5×10^{-5} fs^{-1} and 2.5×10^{-6} fs^{-1} strain rates. Since running steps and timestep defined strain rate and relaxation duration, simulations were run with strain rates of 2.5×10^{-5} fs^{-1} and 2.5×10^{-6} fs^{-1} and relaxed for 20 ps. For other cases, tensile test along z-direction was applied with varying strain rates from 10^{-4} fs^{-1} to 10^{-6} fs^{-1} after energy minimization and relaxation in NPT ensemble for 50 ps. Different sizes and strain rates were done to study the sensitive analysis. Deformations were applied along z-direction coupled with relaxation in x- and y-directions. The final strain is 1.0 for both cuboid and cube shape supercells.

In the case of cuboid shape supercell, the computer specifications that were used to run all simulations were: Dell OptiPlex 5060, Intel® Core™ i7-8700T with CPU of 2.4 GHz (12 CPUs) and memory of 8192 MB. We used 8 cores of CPU.

In the case of cube shape supercell, we used either 24 or 48 visualization cores. Here are the computer specifications that were used to run all simulations: supercomputer called “Liger”, 12-core Intel Xeon (Haswell) E5-2680v3 processors with 252 compute nodes (24 cores per node) and 14 visualization nodes (28 GPUs and 24 cores per node) and 36 608 GB compute memory.

1.5.2 Results and Discussion

Results are divided into two parts as follows: C-S-H (I) cuboid shape supercells and C-S-H (I) cube shape supercells. Stress-strain curves from tensile tests were analysed.

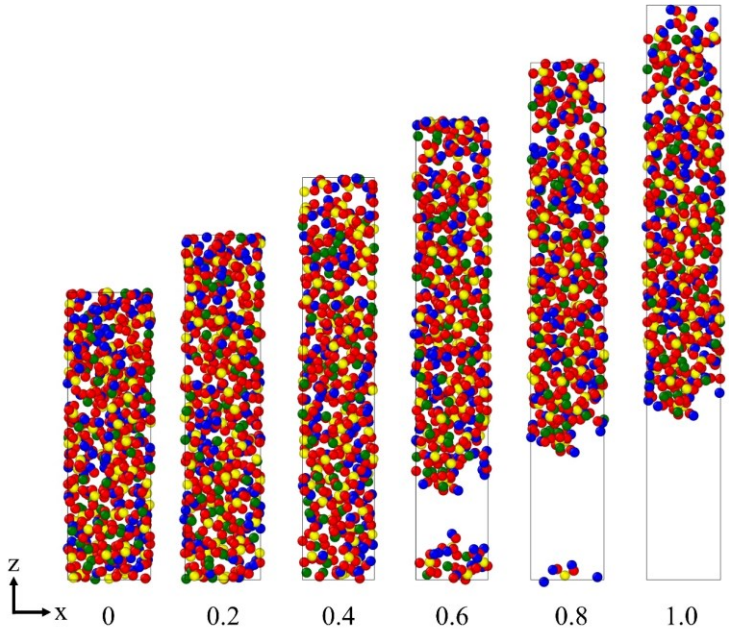

Figure 1.25 Direct tension in z-direction in xz-plane after relaxation to 100% strain of 2 × 2 × 2 C-S-H (I) supercell with ReaxFF force field and strain rate of 2.5×10^{-6} fs^{-1}.

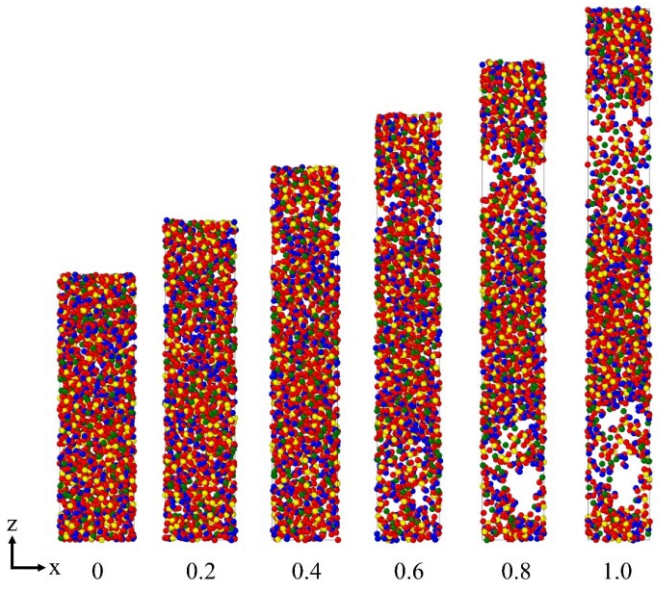

Figure 1.26 Direct tension in z-direction in xz-plane after relaxation to 100% strain of 3 × 3 × 3 C-S-H (I) supercell with ReaxFF force field and strain rate of 2.5×10^{-6} fs^{-1}.

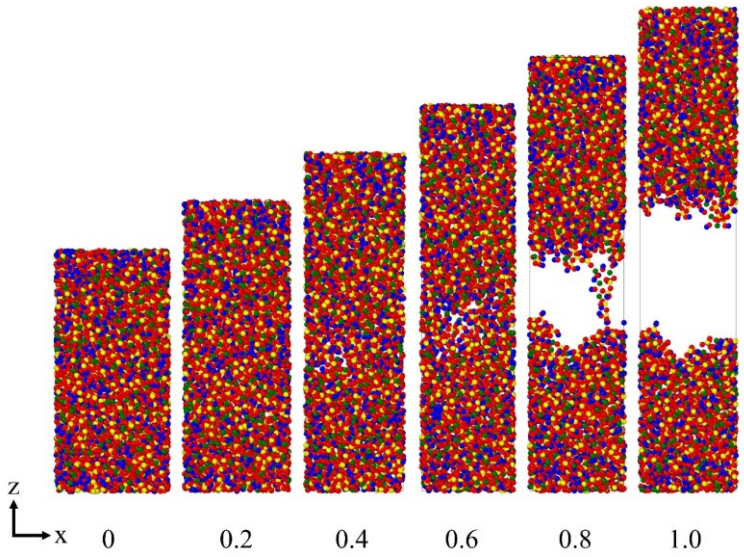

Figure 1.27 Direct tension in z-direction in xz-plane after relaxation to 100% strain of 5 × 5 × 3 C-S-H (I) supercell with ReaxFF force field and strain rate of 2.5×10^{-6} fs^{-1}.

In the case of C-S-H (I) cuboid shape supercells with ReaxFF force field, **Figure 1.25 - Figure 1.27** illustrate the direct tensile evolution after relaxation to 100% strain of 2 × 2 × 2, 3 × 3 × 3 and 5 × 5 × 3 supercells with strain rate of 2.5×10^{-6} fs^{-1}. All the rupture appeared nearly at the end of supercells except 5 × 5 × 3 with strain rate of 2.5×10^{-6} fs^{-1}. Stress-strain curves of these supercells with different strain rates can be observed in **Figure 1.28**. The behaviour seems to be ductile except 3 × 3 × 3 supercell. Strain rate has a negligible effect on the oscillation, but smaller strain rate gave smaller peak stress. However, sizes of supercell contributed to a change in oscillation of stress-strain curve. Strain rate of 2.5×10^{-6} fs^{-1} and size of 5 × 5 × 3 supercell were chosen on the basis of stress-strain curves and tensile evolution.

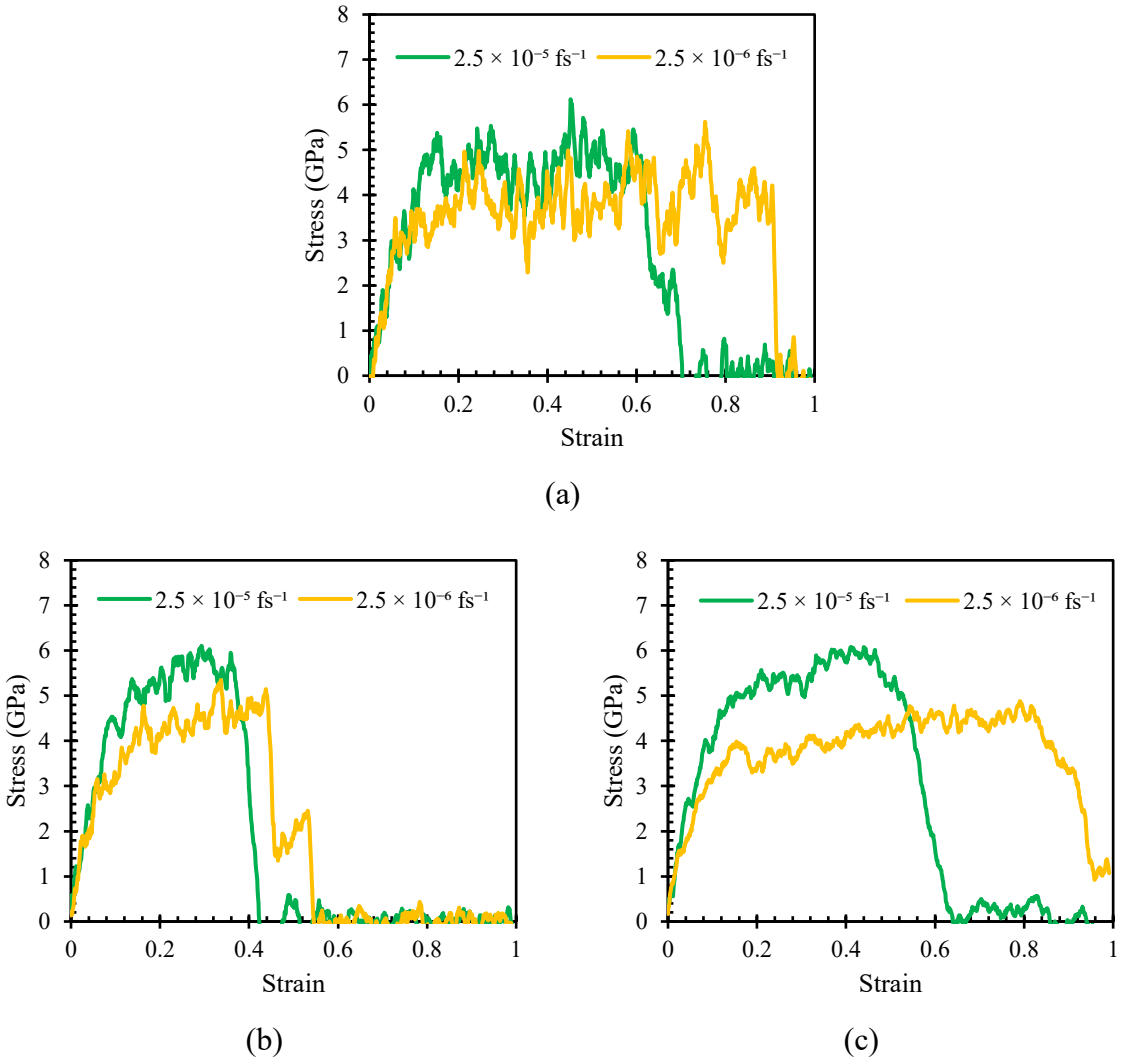

Figure 1.28 Stress-strain curves of C-S-H (I) cuboid shape supercells with ReaxFF force field: (a) 2 × 2 × 2 C-S-H (I) supercell, (b) 3 × 3 × 3 C-S-H (I) supercell and (c) 5 × 5 × 3 C-S-H (I) supercell.

Results of peak stress, peak strain and Young's modulus are summarized in **Table 1.16**. Young's moduli are quite similar to each other despite the size of supercell and strain rate. In conclusion, we would favour 5 × 5 × 3 supercell with strain rate of 2.5 × 10^{-6} fs^{-1}. For this case, Young's modulus was found to be 56.0 GPa, which is in good agreement with results of Fu et al. [23] (i.e., 55 GPa in z-direction).

Table 1.16 Peak strain, peak stress, running time and file size of C-S-H (I) cuboid shape supercell with ReaxFF force field along z-direction.

Size (x × y × z)	Strain rate (fs^{-1})	Peak strain	Peak stress (GPa)	Young's modulus (GPa)	Running time (hr:min)	File size (MB)
2 × 2 × 2	2.5×10^{-5}	0.45	6.12	55.2	11:18	72
	2.5×10^{-6}	0.75	5.63	55.6	5:47	72
3 × 3 × 3	2.5×10^{-5}	0.29	6.11	55.9	24:24	210
	2.5×10^{-6}	0.34	5.35	54.7	11:41	210
5 × 5 × 3	2.5 × 10-5	0.41	6.08	54.9	47:50	665
	2.5 × 10-6	0.79	4.88	56.0	22:59	665

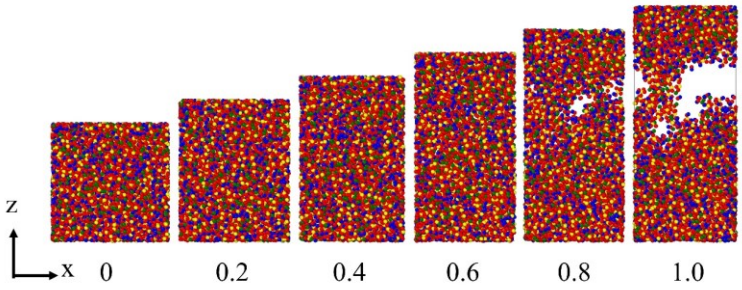

Figure 1.29 Direct tension in z-direction in xz-plane after relaxation to 100% strain of 7 × 8 × 2 C-S-H (I) supercell with ReaxFF force field and strain rate of 10^{-4} fs^{-1}.

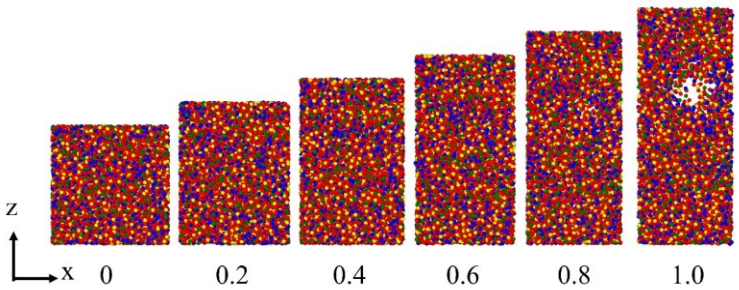

Figure 1.30 Direct tension in z-direction in xz-plane after relaxation to 100% strain of 7 × 8 × 2 C-S-H (I) supercell with ReaxFF force field and strain rate of 10^{-5} fs^{-1}.

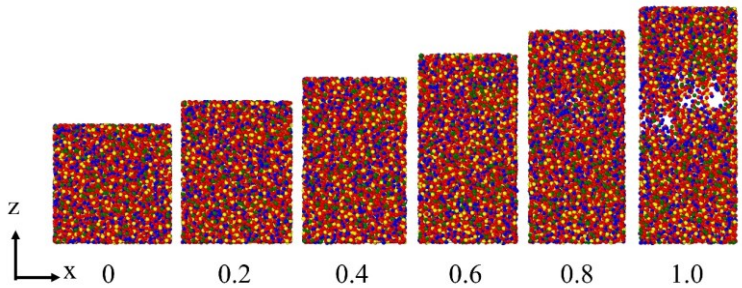

Figure 1.31 Direct tension in z-direction in xz-plane after relaxation to 100% strain of 7 × 8 × 2 C-S-H (I) supercell with ReaxFF force field and strain rate of 10^{-6} fs^{-1}.

In the case of C-S-H (I) cube shape supercells with ReaxFF force field, **Figure 1.29 - Figure 1.31** illustrate the direct tensile evolution of C-S-H (I) cube shape supercells after relaxation to 100% strain of 7 × 8 × 2 supercell with strain rate of 10^{-4} fs^{-1} to 10^{-6} fs^{-1}. All the rupture appeared almost at the middle of the supercell. Stress-strain curves of this supercell with different strain rates can be observed in **Figure 1.32**. The behaviour seems to be ductile. Strain rate has a negligible effect on the oscillation, but smaller strain rate gave smaller peak stress. Strain rate of 10^{-6} fs^{-1} was chosen on the basis of stress-strain curves.

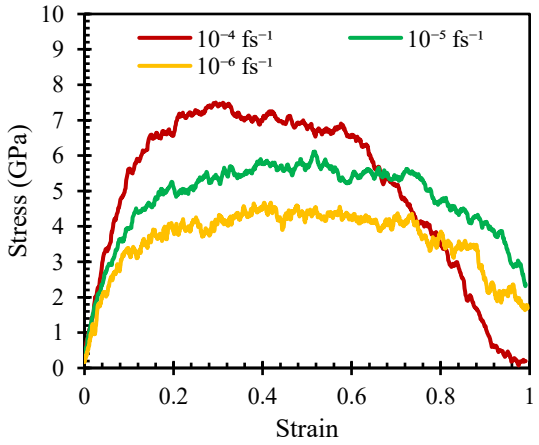

Figure 1.32 Stress-strain curves with three different strain rates of C-S-H (I) cube shape supercells (ReaxFF force field) of 7 × 8 × 2 C-S-H (I) supercell.

Results of peak stress, peak strain and Young's modulus are summarized in **Table 1.17**. In conclusion, we would favour strain rate of 10^{-6} fs^{-1}. For this case, Young's modulus was found to be 56.4 GPa, which is in good agreement with results of Fu et al. [23] (i.e., 55 GPa in z-direction).

Table 1.17 Peak strain, peak stress, running time and file size of C-S-H (I) cube shape supercell with ReaxFF force field along z-direction.

Size (x × y × z)	Strain rate (fs^{-1})	Peak strain	Peak stress (GPa)	Young's modulus (GPa)	Running time (hr:min)	File size (MB)
7 × 8 × 2	10^{-4}	0.31	7.49	56.9	1:13	151
	10^{-5}	0.52	6.11	55.0	12:05	151
	10^{-6}	0.40	4.67	56.4	76:55	393

As can be observed in **Figure 1.33**, stress-strain curves of 5 × 5 × 3 C-S-H (I) supercell (cuboid shape) with strain rate of 2.5 × 10^{-6} fs^{-1} and 7 × 8 × 2 C-S-H (I) supercell (cube shape) with strain rate of 10^{-6} fs^{-1} are quite similar. Therefore, Young's modulus and peak stress have similar values too. To conclude, either cuboid or cube shape could be used for the simulation to obtain its mechanical properties.

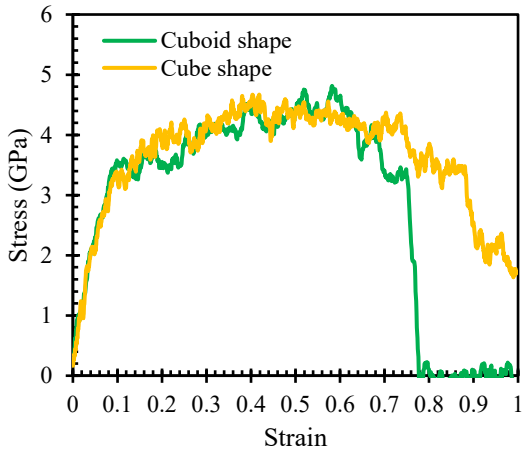

Figure 1.33 Stress-strain curves of C-S-H (I) cuboid and cube shape supercells.

1.6 In summary

This chapter investigates the mechanical properties of three main hydrated cement phases, i.e., C-S-H (I), CH and AFt. Results of Young's modulus, peak stress and peak strain have been deduced from the stress-strain curves obtained from tensile test via MD simulations. Results are divided into two parts: cuboid shape and cube shape supercells. Strain rate, force field, size of supercells have effect on the stress-strain curves. They could lead to smaller or bigger oscillation, the behaviour as brittle or ductile, and smaller or bigger values of peak stress and peak strain. Since we used ReaxFF force field developed for AFt by Liu et al. [37], it may not be able to give the best results. Nevertheless, this ReaxFF force field parameters include all

types of atoms that we need for the study of all the main hydrated cement paste phases. In summary, we would like to favour the ReaxFF force field with strain rate of 10^{-6} fs^{-1} and the following sizes in x-, y- and z-directions as follows: 9 × 10 × 14 and 13 × 16 × 9 CH supercells, 3 × 3 × 3 and 4 × 5 × 2 AFt supercells and 5 × 5 × 3 and 7 × 8 × 2 C-S-H (I) supercells. Young's modulus and peak stress of these phases can be used in upper-scale simulation in **Chapter 5**. These choices of sizes will be served to simulate the tensile test of composites composed of these three main phases in the next chapter.

2 Tensile test of cement paste phase composites

2.1 Background

This chapter focuses primarily on the mechanical properties calculation of hydrated cement phase composites using molecular dynamics (MD) simulations at the nano-scale. Mechanical properties of different phase composites are required for the multi-scale modelling. The results obtained in this chapter could be served as the input in the upper-scale, i.e., microscale of cement-based materials. We used MD simulations with ReaxFF force field to investigate the mechanical properties of these composites. Three main hydrated cement phases have been chosen to study. Those phases are C-S-H (I), CH and AFt. Hence, different phases put together are called "composite" and they consist of: (a) C-S-H (I)/C-S-H (I) composite, (b) C-S-H (I)/CH composite, (c) C-S-H (I)/AFt composite and (d) AFt/CH composite. Three different orientations and configurations of spacing were imposed on these composites. Tensile test was performed on these composites with strain rate of 10^{-6} fs^{-1}. There are two different cases: (a) cuboid shape and (b) cube shape supercells composites. Stress-strain curves were then obtained. Young's modulus, peak stress and peak strain were deduced from these stress-strain curves. The contents of this chapter were placed as the following order: (2.2) tensile test of C-S-H (I)/C-S-H (I) composite, (2.3) tensile test of C-S-H (I)/CH composite, (2.4) tensile test of C-S-H (I)/AFt composite, (2.5) tensile test of AFt/CH composite and (2.6) in summary.

2.2 Tensile test of C-S-H (I)/C-S-H (I) composite

2.2.1 Method

In the work of Liang [27], mechanical and fracture properties of CH and C-S-H composite were investigated. In order to get believable results, CH and C-S-H unit cells were extended along x-, y, and z-directions. Supercells were then relaxed with NPT ensemble at temperature of 300 K and pressure of 0 Pa at x-, y- and z-directions. Relaxed supercells were put together with about 3 Å gap. C-S-H/CH composite was relaxed once again with NPT ensemble.

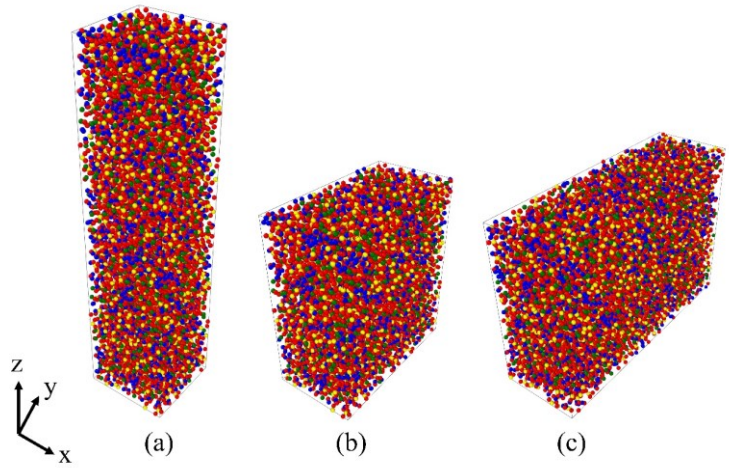

Figure 2.1 Orientations of C-S-H (I)/C-S-H (I) composite: (a) in z-direction, (b) in y-direction, and (c) counterclockwise rotated in y-direction (Cuboid shape supercells).

Similar to the methodology proposed by Liang [27], unit cell of C-S-H (I) was replicated in x-, y-, and z-directions. Size of supercells were chosen to ensure that all chosen phases (i.e., CH, AFt, C-S-H (I)) have similar size in all three dimensions. Since AFt unit cell has the biggest size in all three dimensions, size of AFt supercell was used as the reference. Hence, it was easier to replicate other phases to have approximately the same size.

C-S-H (I) unit cell was replicated 5 × 5 × 3 and 7 × 8 × 2 in x-, y- and z-directions in the case of cuboid and cube shapes, respectively. These supercells were changed from monoclinic supercells to orthogonal supercells in order to acquire the independent results to each direction. All MD simulations were done with ReaxFF force field in real units, three dimensions (3D) and periodic boundary condition (PPP). These supercells were relaxed in NPT ensemble with temperature of 300 K and pressure of 0 atm in all three directions for 50 ps.

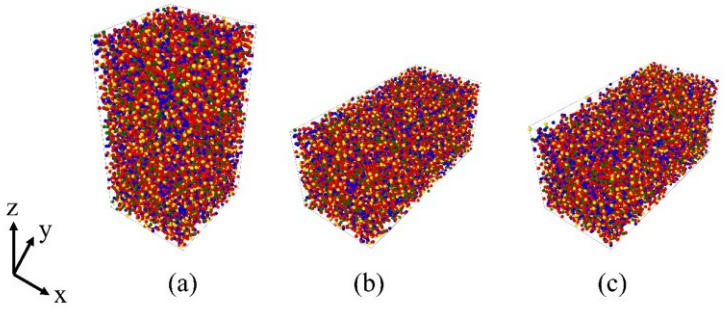

Figure 2.2 Orientations of C-S-H (I)/C-S-H (I) composite: (a) in z-direction, (b) in y-direction, and (c) counterclockwise rotated in y-direction (Cube shape supercells).

Bonnaud et al. [26] investigated three different orientations of C-S-H particle pairs in order to study the interaction grand potential at the molecular level. These orientations were chosen

to consider the effect of: (a) anisotropy in crystallography and geometry of C-S-H particles, and (b) different interaction forces among particles related to orientation. Moreover, other particle was moved at various inter-particle distance to calculate the interaction grand potentials. Different inter-particle distances related to the minimum interaction grand potential minima were found. Therefore, three different orientations were chosen in this study as follows: (a) C-S-H (I) supercell on top of C-S-H (I) supercell in z-direction, (b) C-S-H (I) supercell on the side of C-S-H (I) supercell in y-direction, and (c) counterclockwise rotated C-S-H (I) supercell around x-axis on the side of C-S-H (I) supercell in y-direction. **Figure 2.1** and **Figure 2.2** show the different orientations in the case of cuboid and cube shape supercells, respectively. Additionally, 1 Å vacuum, 3.1 Å water and 6.2 Å water spacing were placed between supercells. Zhu et al. [40] chose SPC/E water model to investigate the properties of hydrated surface of C-S-H through MD simulations with ReaxFF force field. Subsequently, SPC/E water model was used in this study. Relaxed supercells were put together with these different spacing in-between. C-S-H (I)/C-S-H (I) composite was relaxed once again with NPT ensemble for another 50 ps. It should be noted that C-S-H (I) supercell of counterclockwise rotated in y-direction was replicated 5 × 11 × 3 in x-, y- and z-directions to have a similar dimension in z-direction. This procedure was only applied in the case of cuboid shape composite because they did not have similar size along y- and z-directions. These supercells were counterclockwise rotated around x-axis in yz-plane. Bottom of these supercells were placed to the side of C-S-H (I) supercell. Timestep of these simulations was 0.25 fs. Different sizes and strain rates were done to study the sensitive analysis. Deformations were applied along z-direction coupled with relaxation in x- and y-directions. As can be seen in **Figure 2.3**, strain rate has an effect on stress-strain curves. Strain rate of 10^{-4} fs^{-1} gives high values of peak stress and peak strain compared to other strain rates. On the other hand, strain rate of 10^{-5} fs^{-1} has noticeable global oscillation after reaching peak stress. Strain rates of 10^{-6} fs^{-1} and 10^{-7} fs^{-1} provides similar curves as well as peak stress and peak strain. Therefore, strain rates of 10^{-6} fs^{-1} was chosen for tensile test along z-direction because it consume less time compared with strain rates of 10^{-7} fs^{-1}. Final strain is comprised in between 20% and 100%.

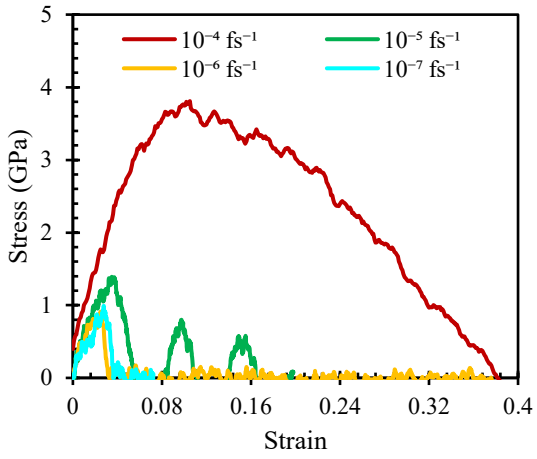

Figure 2.3 Sensitivity analysis of stress-strain curves with different strain rates of C-S-H (I)/C-S-H (I) composite (Cuboid shape supercells) in the case of 3.1 Å water spacing.

Either 24 or 48 visualization cores were used. Here are the computer specifications that were used to run all simulations: supercomputer called "Liger", 12-core Intel Xeon (Haswell) E5-2680v3 processors with 252 compute nodes (24 cores per node) and 14 visualization nodes (28 GPUs and 24 cores per node) and 36 608 GB compute memory.

2.2.2 Results and Discussion

The purpose was to obtain the mechanical properties (i.e., Young's modulus, peak stress and peak strain) of C-S-H (I)/C-S-H (I) composite using MD simulations. Using the method described above, stress-strain curves were obtained with different orientations and configurations of spacing. Results are divided into two parts as follows: C-S-H (I)/C-S-H (I) composite cuboid shape supercells and C-S-H (I)/C-S-H (I) composite cube shape supercells.

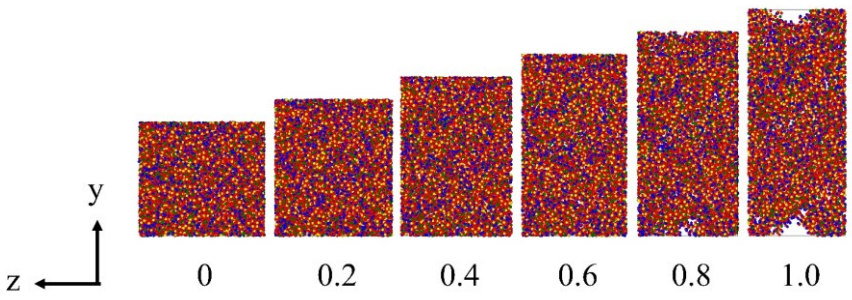

Figure 2.4 Direct tension of C-S-H (I)/vacuum (1 Å)/C-S-H (I) composite in y-direction (Cuboid shape supercells).

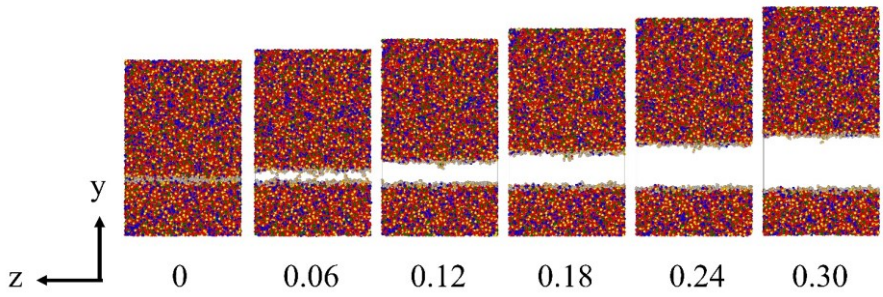

Figure 2.5 Direct tension of C-S-H (I)/H_2O (3.1 Å)/C-S-H (I) composite counterclockwise rotated in y-direction (Cuboid shape supercells).

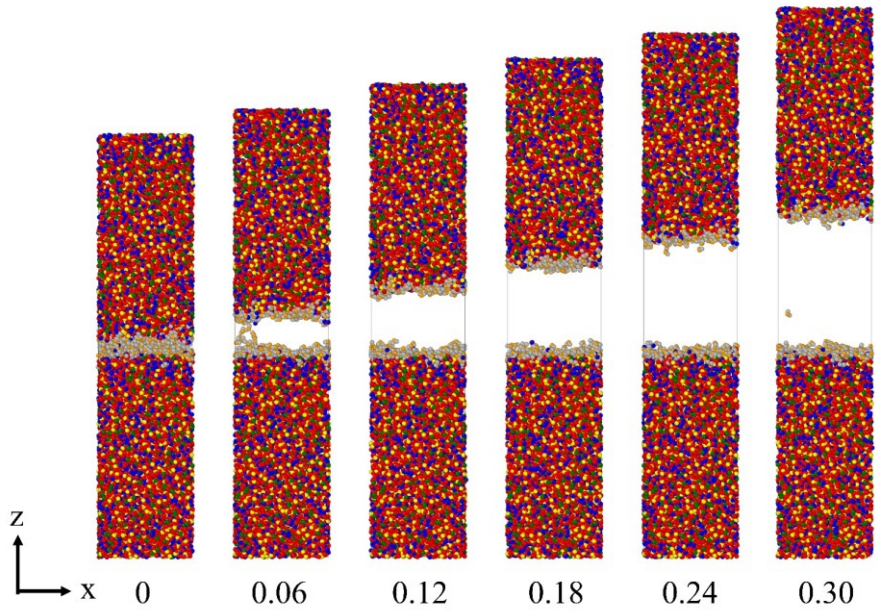

Figure 2.6 Direct tension of C-S-H (I)/H_2O (6.2 Å)/C-S-H (I) composite in z-direction (Cuboid shape supercells).

In the case of C-S-H (I)/C-S-H (I) composite cuboid shape supercells with ReaxFF force field, **Figure 2.4 - Figure 2.6** illustrate the direct tensile evolution of C-S-H (I)/C-S-H (I) composite after relaxation to 100% and 30% strain with different orientations and configurations of spacing. All simulations were run with strain rate of 10^{-6} fs^{-1}. All rupture appeared at the interface of composites. This means that vacuum and water spacing made the interaction between main hydrated cement phases weaker and initiated the rupture. Stress-strain curves of C-S-H (I)/C-S-H (I) composite cuboid shape supercells with different orientations and configurations of spacing can be observed in **Figure 2.7**. In the case of 1 Å vacuum spacing, the behaviour seems to be ductile, especially in y-direction. In fact, for this spacing, the stress-strain curves of C-S-H (I) supercell alone are re-obtained. In the case of water spacing, the

behaviour seems to be brittle. It appears that the bigger the spacing, the bigger the oscillation can be observed. Results indicate that orientations of two supercells and configurations of different spacing affected the stress-strain curves of C-S-H (I)/C-S-H (I) composite cuboid shape supercells. As can be seen, 1 Å vacuum spacing gave the highest peak stress and peak strain which correspond to the results obtained on C-S-H (I) supercells. In contrast, 6.2 Å water spacing gave the lowest peak stress and peak strain. Results of peak stress, peak strain, running time and file size are summarized in **Table 2.1**.

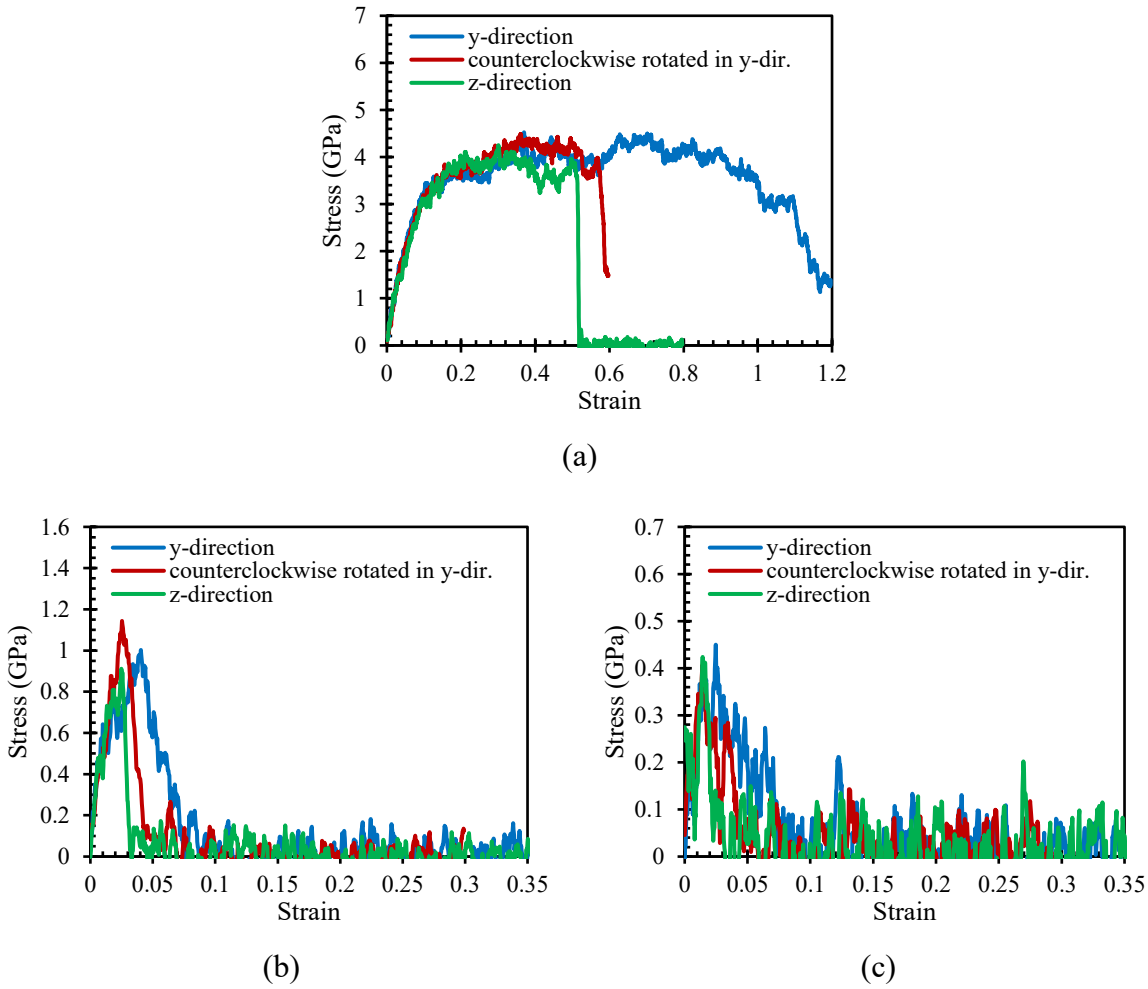

Figure 2.7 Stress-strain curves with three orientations of C-S-H (I)/C-S-H (I) composite (Cuboid shape supercells): (a) 1 Å vacuum spacing, (b) 3.1 Å water spacing and (c) 6.2 Å water spacing.

Table 2.1 Peak strain, peak stress, running time and file size of C-S-H (I)/C-S-H (I) composite (Cuboid shape supercells).

Orientation	Spacing	Peak strain	Peak stress (GPa)	Running time (hr:min)	File size (MB)
y-direction	1 Å vacuum	0.37	4.53	184:34	622
	3.1 Å water	0.04	1.00	72:00	276
	6.2 Å water	0.03	0.45	72:00	316
Counterclockwise rotated in y-direction	1 Å vacuum	0.36	4.49	74:02	980
	3.1 Å water	0.03	1.14	72:00	470
	6.2 Å water	0.01	0.41	72:00	468
z-direction	1 Å vacuum	0.30	4.25	137:14	456
	3.1 Å water	0.03	0.91	72:00	247
	6.2 Å water	0.01	0.42	72:00	255

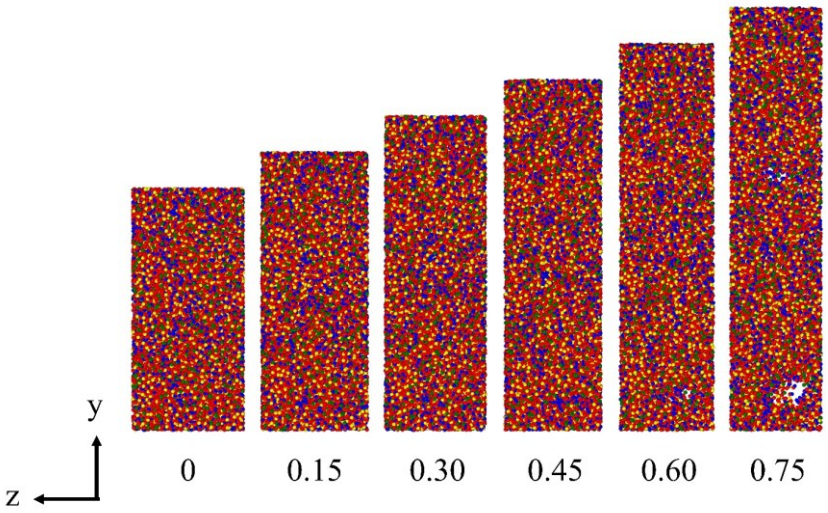

Figure 2.8 Direct tension of C-S-H (I)/vacuum (1 Å)/C-S-H (I) composite in y-direction (Cube shape supercells).

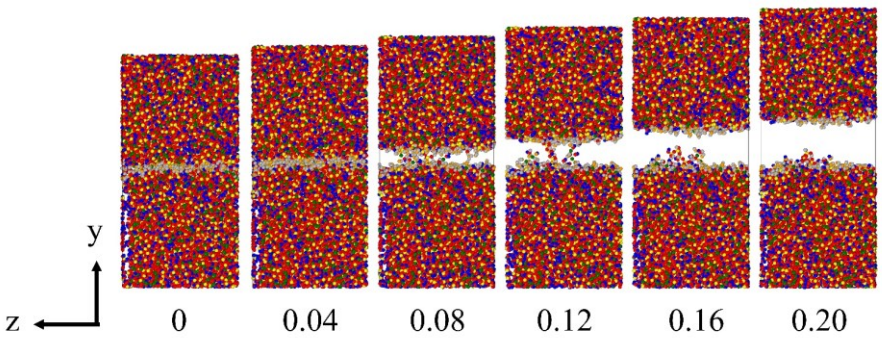

Figure 2.9 Direct tension of C-S-H (I)/H_2O (3.1 Å)/C-S-H (I) composite counterclockwise rotated in y-direction (Cube shape supercells).

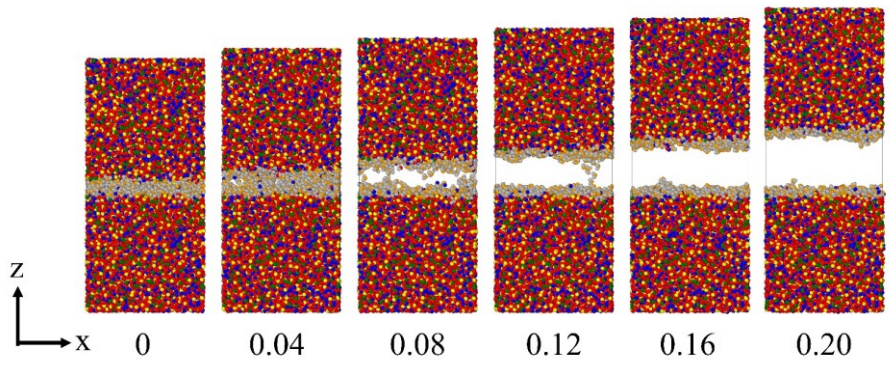

Figure 2.10 Direct tension of C-S-H (I)/H_2O (6.2 Å)/C-S-H (I) composite in z-direction (Cube shape supercells).

In the case of C-S-H (I)/C-S-H (I) composite cube shape supercells with ReaxFF force field, **Figure 2.8 - Figure 2.10** illustrate the direct tensile evolution of C-S-H (I)/C-S-H (I) composite after relaxation to 75% and 20% strain with different orientations and configurations of spacing. All simulations were run with strain rate of 10^{-6} fs^{-1}. All rupture appeared at the interface of composites. This means that vacuum and water spacing made the interaction between main hydrated cement phases weaker and initiated the rupture. Stress-strain curves of C-S-H (I)/C-S-H (I) composite cube shape supercells with different orientations and configurations of spacing can be observed in **Figure 2.11**. In the case of 1 Å vacuum spacing, the behaviour seems to be ductile, especially in y-direction and counterclockwise rotated in y-direction. In fact, for this spacing, the stress-strain curves of C-S-H (I) supercell alone are re-obtained. In the case of water spacing, the behaviour seems to be brittle. It appears that the bigger the spacing, the bigger the oscillation can be observed. Results indicate that orientations of two supercells and configurations of different spacing affected the stress-strain curves of C-S-H (I)/C-S-H (I) composite cube shape supercells. However, unlike the C-S-H (I)/C-S-H (I) composite cuboid shape supercells, orientations of C-S-H (I)/C-S-H (I) composite cube shape supercells did not affect much the stress-strain curves except in the case of 3.1 Å water spacing. As can be seen, 1 Å vacuum spacing gave the highest peak stress and peak strain which correspond to the results obtained on C-S-H (I) supercells. In contrast, 6.2 Å water spacing gave the lowest peak stress and peak strain. Results of peak stress, peak strain, running time and file size are summarized in **Table 2.2**.

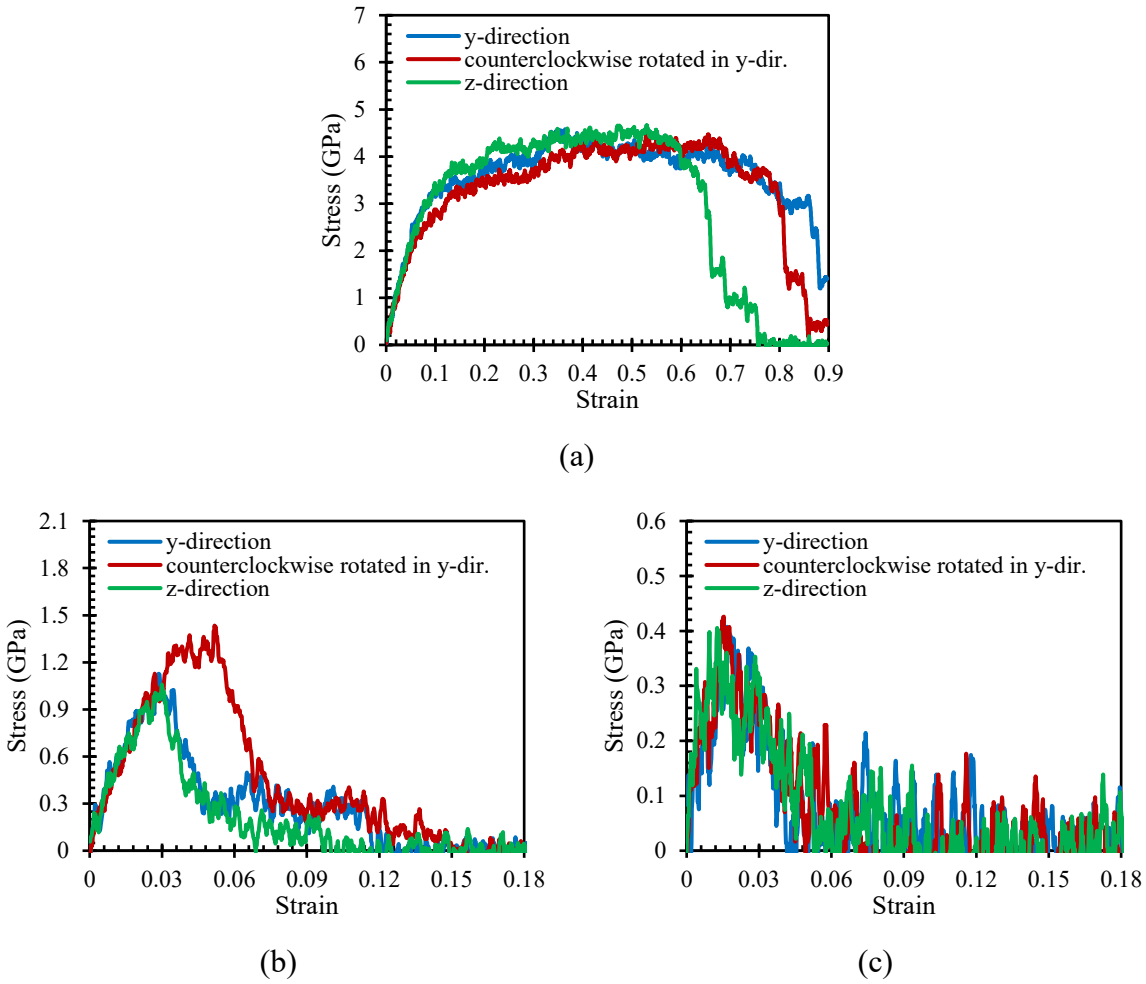

Figure 2.11 Stress-strain curves with three orientations of C-S-H (I)/C-S-H (I) composite (Cube shape supercells): (a) 1 Å vacuum spacing, (b) 3.1 Å water spacing and (c) 6.2 Å water spacing.

Table 2.2 Peak strain, peak stress, running time and file size of C-S-H (I)/C-S-H (I) composite (Cube shape supercells).

Orientation	Spacing	Peak strain	Peak stress (GPa)	Running time (hr:min)	File size (MB)
y-direction	1 Å vacuum	0.35	4.57	107:53	903
	3.1 Å water	0.03	1.13	45:05	406
	6.2 Å water	0.02	0.41	46:28	397
Counterclockwise rotated in y-direction	1 Å vacuum	0.66	4.47	109:03	903
	3.1 Å water	0.05	1.43	43:44	457
	6.2 Å water	0.02	0.43	45:32	457
z-direction	1 Å vacuum	0.53	4.66	114:17	903
	3.1 Å water	0.03	1.06	44:30	423
	6.2 Å water	0.01	0.41	43:43	420

2 Tensile test of cement paste phase composites

The Young's modulus is deduced from the stress-strain curves on the linear elastic part. **Figure 2.12** illustrates Young's modulus of different orientation and configurations of spacing. C-S-H (I)/C-S-H (I) composite cuboid and cube shape supercells are shown on the left and on the right, respectively. The values of Young's modulus obtained are quite similar despite the different shapes. The average Young's modulus of three different orientations is summarized in **Table 2.3**. In the case of 1 Å vacuum spacing, Young's modulus was found to be 37.4 GPa and 38.9 GPa for C-S-H (I)/C-S-H (I) composite cuboid and cube shape supercells, respectively. When 3.1 Å water spacing was placed in between the supercells, Young's modulus increased to 48.7 GPa and 47.7 GPa, respectively. Finally, Young's modulus were found to be 47.8 GPa and 45.8 GPa, respectively. This means that it slightly decreased the values in the case of 6.2 Å water spacing. The values of Young's modulus might be compared to the result obtained by Bonnaud et al. [26] with mean value of 40.1 GPa between different orientations. The procedure of Bonnaud et al. is different from this study. They derived the pair potentials by the combination of grand canonical Monte Carlo simulations and the mean force integration method.

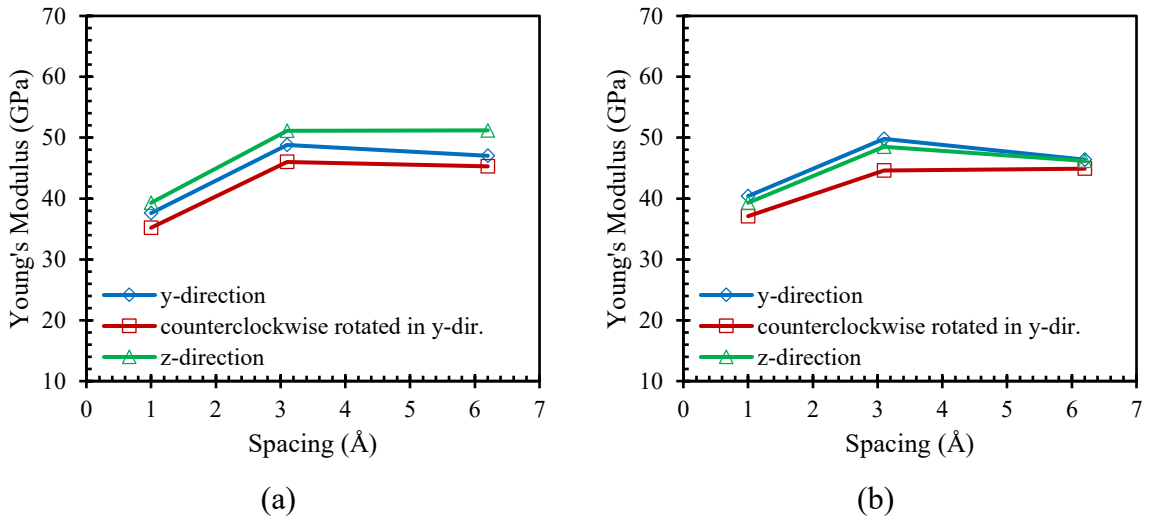

Figure 2.12 Curves of Young's modulus and spacing between supercells with three orientations of C-S-H (I)/C-S-H (I) composite: (a) cuboid shape supercells and (b) cube shape supercells.

Table 2.3 Mean Young's modulus of three orientations of C-S-H (I)/C-S-H (I) composite.

Composite	Shape	Spacing	E (GPa)
C-S-H (I)/C-S-H (I)	Cuboid	1 Å vacuum	37.4
		3.1 Å water	48.7
		6.2 Å water	47.8
C-S-H (I)/C-S-H (I)	Cube	1 Å vacuum	38.9
		3.1 Å water	47.7
		6.2 Å water	45.8

2.3 Tensile test of C-S-H (I)/CH composite

2.3.1 Method

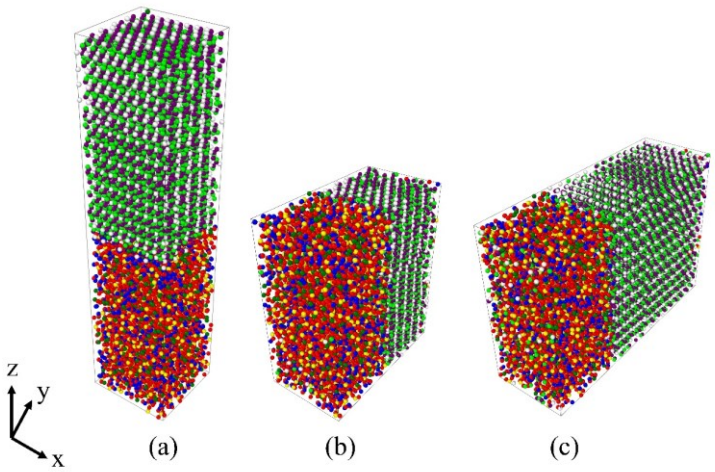

Figure 2.13 Orientations of C-S-H (I)/CH composite: (a) in z-direction, (b) in y-direction, and (c) counterclockwise rotated in y-direction (Cuboid shape supercells).

Similar to the methodology in **Section 2.2**, unit cells of C-S-H (I) and CH were replicated in x-, y-, and z-directions. Size of supercells were chosen to ensure that all chosen phases (i.e., CH, AFt, C-S-H (I)) have similar size in all three dimensions. Since AFt unit cell has the biggest size in all three dimensions, size of AFt supercell was used as the reference. Hence, it was easier to replicate other phases to have approximately the same size.

C-S-H (I) unit cell was replicated 5 × 5 × 3 and 7 × 8 × 2 in x-, y- and z-directions in the case of cuboid and cube shapes, respectively. CH unit cell was replicated 9 × 10 × 14 and 13 × 16 × 9 in x-, y- and z-directions in the case of cuboid and cube shapes, respectively. C-S-H (I) and CH supercells were changed from monoclinic and trigonal supercells to orthogonal supercells in order to acquire the independent results to each direction. All MD simulations

were done with ReaxFF force field in real units, three dimensions (3D) and periodic boundary condition (PPP). These supercells were relaxed in NPT ensemble with temperature of 300 K and pressure of 0 atm in all three directions for 50 ps.

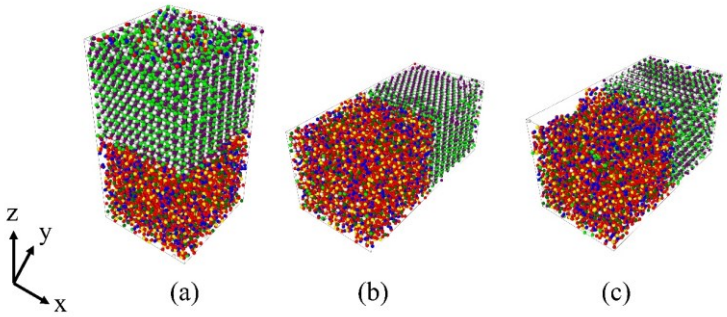

Figure 2.14 Orientations of C-S-H (I)/CH composite: (a) in z-direction, (b) in y-direction, and (c) counterclockwise rotated in y-direction (Cube shape supercells).

Three different orientations were chosen in this study as follows: (a) CH supercell on top of C-S-H (I) supercell in z-direction, (b) CH supercell on the side of C-S-H (I) supercell in y-direction, and (c) counterclockwise rotated CH supercell around x-axis on the side of C-S-H (I) supercell in y-direction. **Figure 2.13** and **Figure 2.14** show the different orientations in the case of cuboid and cube shape supercells, respectively. Additionally, 1 Å vacuum, 3.1 Å water and 6.2 Å water spacing were placed between supercells. Relaxed supercells were put together with these different spacing in-between. C-S-H (I)/CH composite was relaxed once again with NPT ensemble for another 50 ps. It should be noted that CH supercell of counterclockwise rotated in y-direction was replicated 9 × 22 × 14 in x-, y- and z-directions to have a similar dimension in z-direction. This procedure was only applied in the case of cuboid shape composite because they did not have similar size along y- and z-directions. These supercells were counterclockwise rotated around x-axis in yz-plane. Bottom of these supercells were placed to the side of C-S-H (I) supercell. Timestep of these simulations was 0.25 fs. Different sizes and strain rates were done to study the sensitive analysis. Deformations were applied along z-direction coupled with relaxation in x- and y-directions. As can be seen in **Figure 2.15**, strain rate has an effect on stress-strain curves. Strain rate of 10^{-4} fs^{-1} gives high values of peak stress and peak strain compared to other strain rates. On the other hand, strain rate of 10^{-5} fs^{-1} has small global oscillation after reaching peak stress. Strain rates of 10^{-6} fs^{-1} and 10^{-7} fs^{-1} provides similar peak stress and peak strain. Therefore, strain rates of 10^{-6} fs^{-1} was chosen for tensile test along z-direction because it consumes less time compared with strain rates of 10^{-7} fs^{-1}. Final strain is comprised in between 15% to 50%.

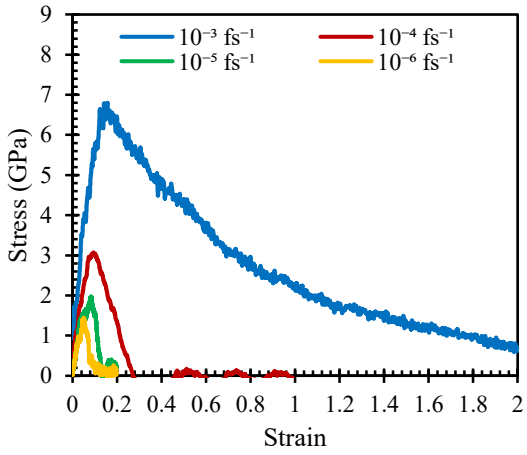

Figure 2.15 Sensitivity analysis of stress-strain curves with different strain rates of C-S-H (I)/CH composite (Cuboid shape supercells) of 3.1 Å water spacing.

For the simulations of C-S-H (I)/CH composite cuboid shape supercells, the computer specifications used were: Dell Precision 7280, Intel Core Xeon Gold with CPU of 2.2 GHz (56 processors) and memory of 64 GB. We used the CPU ranging from 16 to 24 cores.

For the simulations of C-S-H (I)/CH composite cube shape supercells, 24 visualization cores were used. The computer specifications used to run all simulations were: supercomputer called "Liger", 12-core Intel Xeon (Haswell) E5-2680v3 processors with 252 compute nodes (24 cores per node) and 14 visualization nodes (28 GPUs and 24 cores per node) and 36 608 GB compute memory.

2.3.2 Results and Discussion

Using the method described above, stress-strain curves were obtained with different orientations and configurations of spacing. Results are divided into two parts as follows: C-S-H (I)/CH composite cuboid shape supercells and C-S-H (I)/CH composite cube shape supercells.

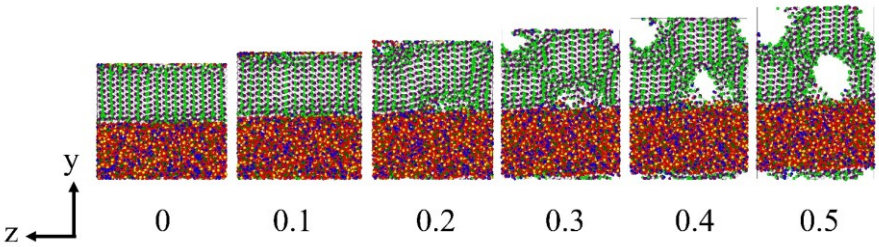

Figure 2.16 Direct tension of C-S-H (I)/vacuum (1 Å)/CH composite in y-direction (Cuboid shape supercells).

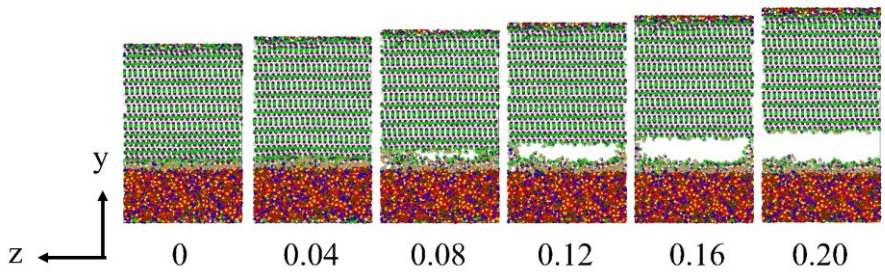

Figure 2.17 Direct tension of C-S-H (I)/H_2O (3.1 Å)/CH composite counterclockwise rotated in y-direction (Cuboid shape supercells).

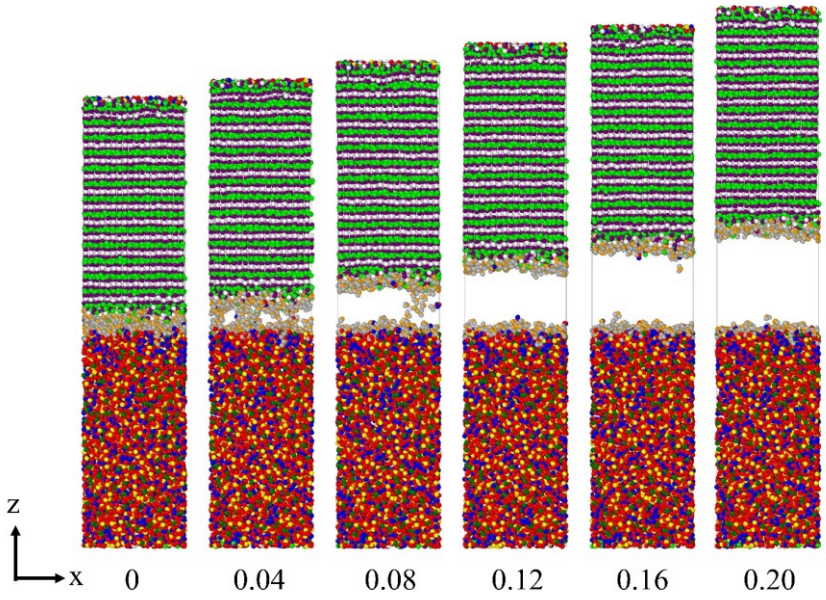

Figure 2.18 Direct tension of C-S-H (I)/H_2O (6.2 Å)/CH composite in z-direction (Cuboid shape supercells).

In the case of C-S-H (I)/CH composite cuboid shape supercells with ReaxFF force field, **Figure 2.16 - Figure 2.18** illustrate the direct tensile evolution of C-S-H (I)/CH composite after relaxation to 50% and 20% strain with different orientations and configurations of spacing. All the simulations were run with strain rate of 10^{-6} fs^{-1}. All rupture appeared at the interface of composite indicating that vacuum and water spacing made the interaction between main hydrated cement phases weaker and initiated the rupture. Stress-strain curves of C-S-H (I)/CH composite cuboid shape supercells with different orientations and configurations of spacing can be observed in **Figure 2.19**. In the case of 1 Å vacuum spacing, the behaviour seems to be brittle except in y-direction. For orientation in y-direction, it also gave a bigger peak stress and peak strain compared to the other orientations. It indicates that this orientation provided a better interaction at the interface between C-S-H (I) and CH supercells. In the case of 3.1 Å water

spacing, behaviour seems to be slightly more ductile. In the case of 6.2 Å water spacing, the behaviour seems to be brittle. It appears that the bigger the spacing, the bigger the oscillation can be observed. Results indicate that orientations of two supercells and configurations of different spacing affected the stress-strain curves of C-S-H (I)/CH composite cuboid shape supercells. As can be seen, 1 Å vacuum spacing gave the highest peak stress and peak strain. In contrast, 6.2 Å water spacing gave the lowest peak stress and peak strain. Results of peak stress, peak strain, running time and file size are summarized in **Table 2.4**.

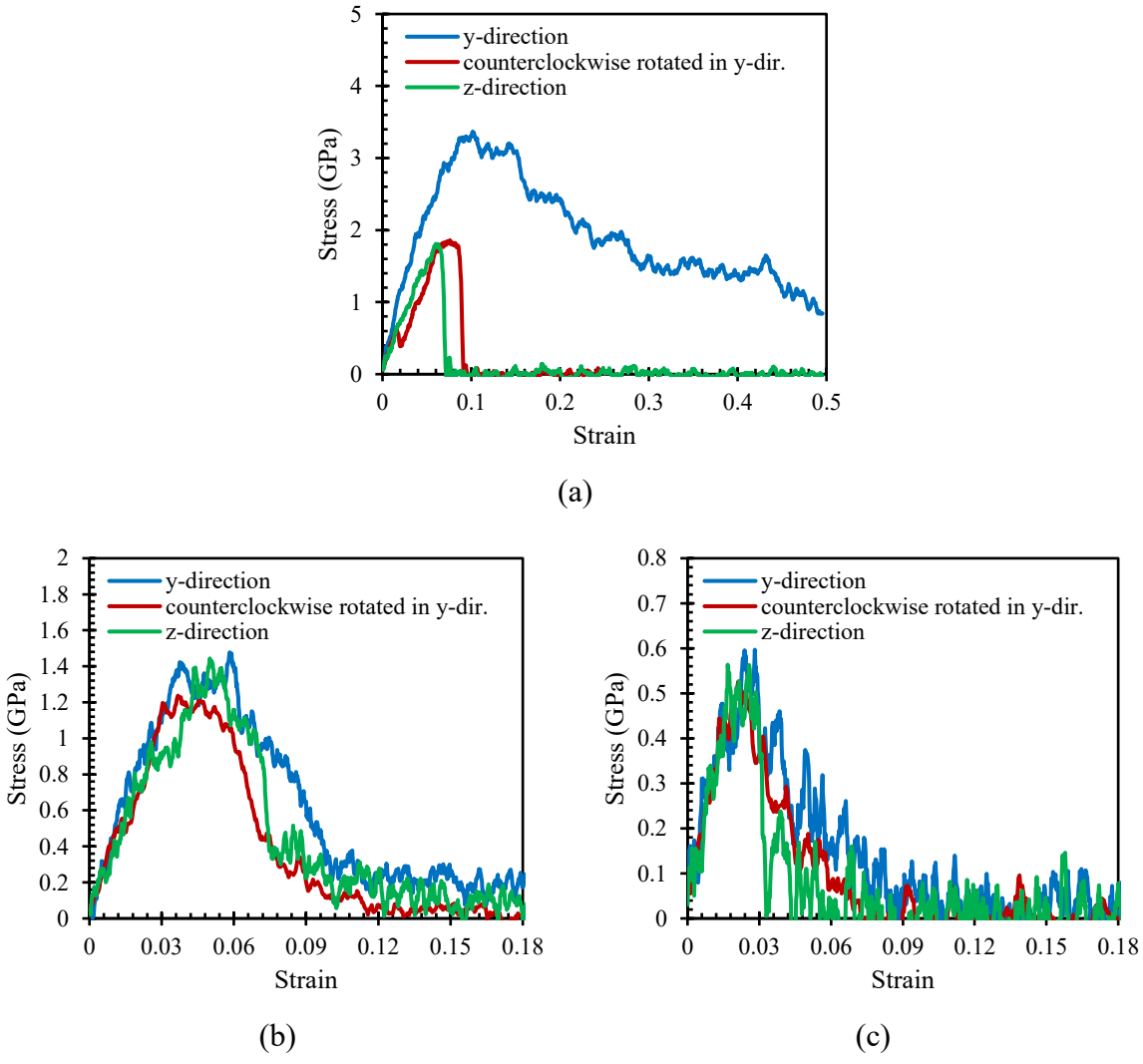

Figure 2.19 Stress-strain curves with three orientations of C-S-H (I)/CH composite (Cuboid shape supercells): (a) 1 Å vacuum spacing, (b) 3.1 Å water spacing and (c) 6.2 Å water spacing.

Table 2.4 Peak strain, peak stress, running time and file size of C-S-H (I)/CH composite (Cuboid shape supercells).

Orientation	Spacing	Peak strain	Peak stress (GPa)	Running time (hr:min)	File size (MB)
y-direction	1 Å vacuum	0.10	3.37	95:25	293
	3.1 Å water	0.06	1.48	46:12	271
	6.2 Å water	0.03	0.60	49:55	273
Counterclockwise rotated in y-direction	1 Å vacuum	0.08	1.86	72:00	334
	3.1 Å water	0.04	1.24	72:00	345
	6.2 Å water	0.02	0.53	72:00	372
z-direction	1 Å vacuum	0.06	1.81	118:38	259
	3.1 Å water	0.05	1.44	47:21	243
	6.2 Å water	0.03	0.56	51:04	249

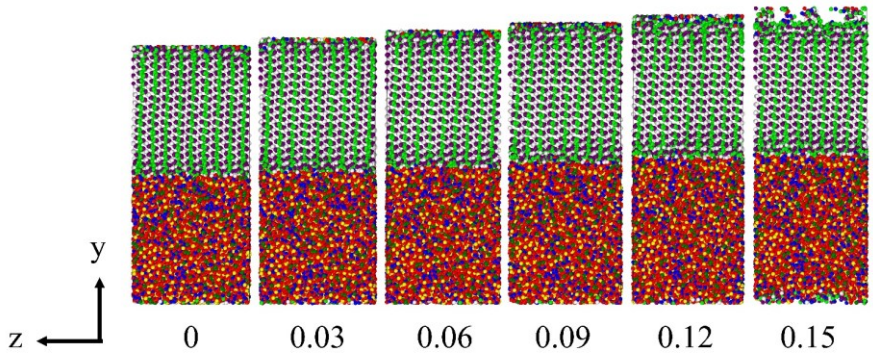

Figure 2.20 Direct tension of C-S-H (I)/vacuum (1 Å)/CH composite in y-direction (Cube shape supercells).

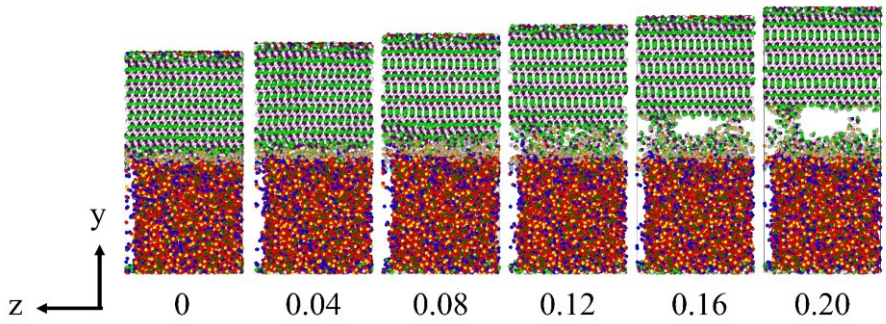

Figure 2.21 Direct tension of C-S-H (I)/H_2O (3.1 Å)/CH composite counterclockwise rotated in y-direction (Cube shape supercells).

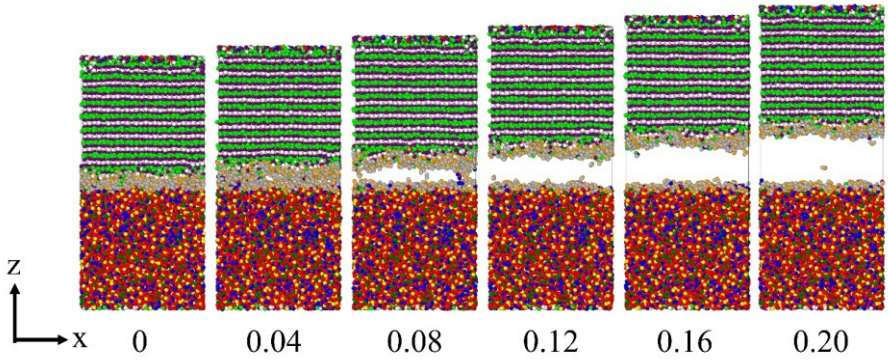

Figure 2.22 Direct tension of C-S-H (I)/H_2O (6.2 Å)/CH composite in z-direction (Cube shape supercells).

In the case of C-S-H (I)/CH composite cube shape supercells with ReaxFF force field, **Figure 2.20 - Figure 2.22** illustrate the direct tensile evolution of C-S-H (I)/CH composite after relaxation to 15% and 20% strain with different orientations and configurations of spacing. All simulations were run with strain rate of 10^{-6} fs^{-1}. All rupture appeared at the interface of composite indicating that vacuum and water spacing made the interaction between main hydrated cement phases weaker and initiated the rupture. Stress-strain curves of C-S-H (I)/CH composite cube shape supercells with different orientations and configurations of spacing can be observed in **Figure 2.23**. In the case of 1 Å vacuum spacing, the behaviour seems to be ductile. For orientation in y-direction, it also gave a bigger peak stress and peak strain compared to the other orientations. It indicates that this orientation provided a better interaction at the interface between C-S-H (I) and CH supercells. In the case of 3.1 Å water spacing, the behaviour seems to be ductile too. In the case of 6.2 Å water spacing, the behaviour seems to be more brittle compared to the smaller spacing. It appears that the bigger the spacing, the bigger the oscillation can be observed. Results indicate that orientations of two supercells and configurations of different spacing affected the stress-strain curves of C-S-H (I)/CH composite cube shape supercells. As can be seen, 1 Å vacuum spacing gave the highest peak stress and peak strain. In contrast, 6.2 Å water spacing gave the lowest peak stress and peak strain. Results of peak stress, peak strain, running time and file size are summarized in **Table 2.5**.

2 *Tensile test of cement paste phase composites*

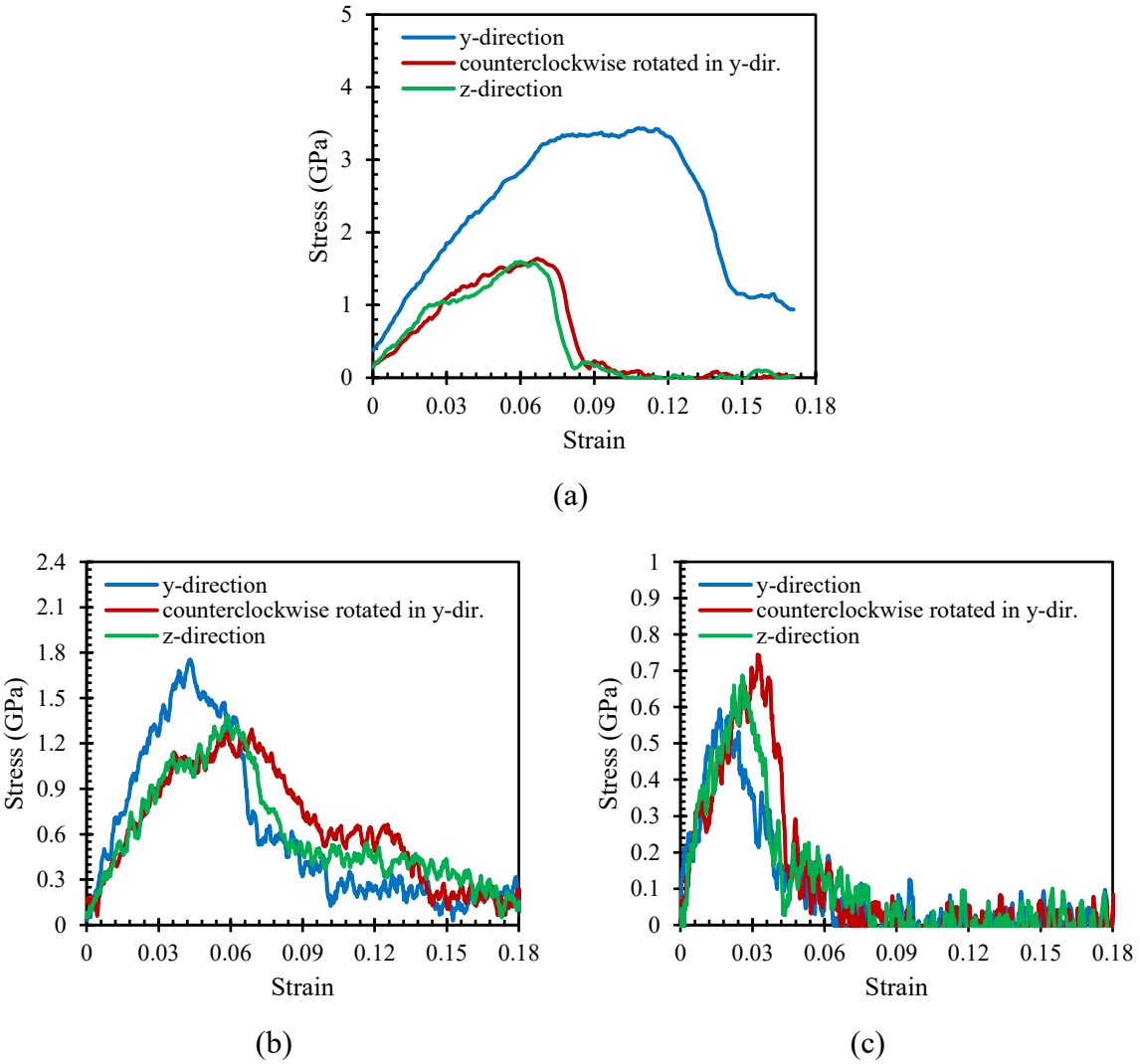

Figure 2.23 Stress-strain curves with three orientations of C-S-H (I)/CH composite (Cube shape supercells): (a) 1 Å vacuum spacing, (b) 3.1 Å water spacing and (c) 6.2 Å water spacing.

Table 2.5 Peak strain, peak stress, running time and file size of C-S-H (I)/CH composite (Cube shape supercells).

Orientation	Spacing	Peak strain	Peak stress (GPa)	Running time (hr:min)	File size (MB)
y-direction	1 Å vacuum	0.11	3.44	72:00	173
	3.1 Å water	0.04	1.75	47:54	462
	6.2 Å water	0.02	0.59	49:46	481
Counterclockwise rotated in y-direction	1 Å vacuum	0.07	1.64	72:00	173
	3.1 Å water	0.07	1.29	45:36	420
	6.2 Å water	0.03	0.74	48:12	434
z-direction	1 Å vacuum	0.06	1.60	72:00	177
	3.1 Å water	0.06	1.39	44:39	413
	6.2 Å water	0.03	0.69	48:13	428

Figure 2.24 illustrates Young's modulus of different orientation and configurations of spacing. C-S-H (I)/CH composite cuboid and cube shape supercells are shown on the left and on the right, respectively. The values of Young's modulus obtained are not identical between the different shapes. However, the values of Young's modulus are similar in some cases. The average Young's modulus of three different orientations is summarized in **Table 2.6**. In the case of 1 Å vacuum spacing, Young's modulus was found to be 37.7 GPa and 37.3 GPa for C-S-H (I)/CH composite cuboid and cube shape supercells, respectively. They are quite similar. When 3.1 Å water spacing was placed in between the supercells, Young's modulus increased to 40 GPa in the case of cuboid shape. Nevertheless, it decreased to 35.2 GPa in the case of cube shape. Finally, Young's modulus were found to be 28.9 GPa and 39.1 GPa in the case of cuboid and cube shapes, respectively. This means that the initial was decreased and the latter was increased in the case of 6.2 Å water spacing. To the authors' knowledge, C-S-H (I)/CH composite modelled with MD simulation was only done by Liang [27]. The values of Young's modulus might be compared to the result obtained by Liang with value of 40 GPa for a similar spacing. The procedure is quite similar from this study. Liang placed CH phase about 3 Å on top of C-S-H phase and derived the Young's modulus from the stress-strain curve of the uniaxial tensile test.

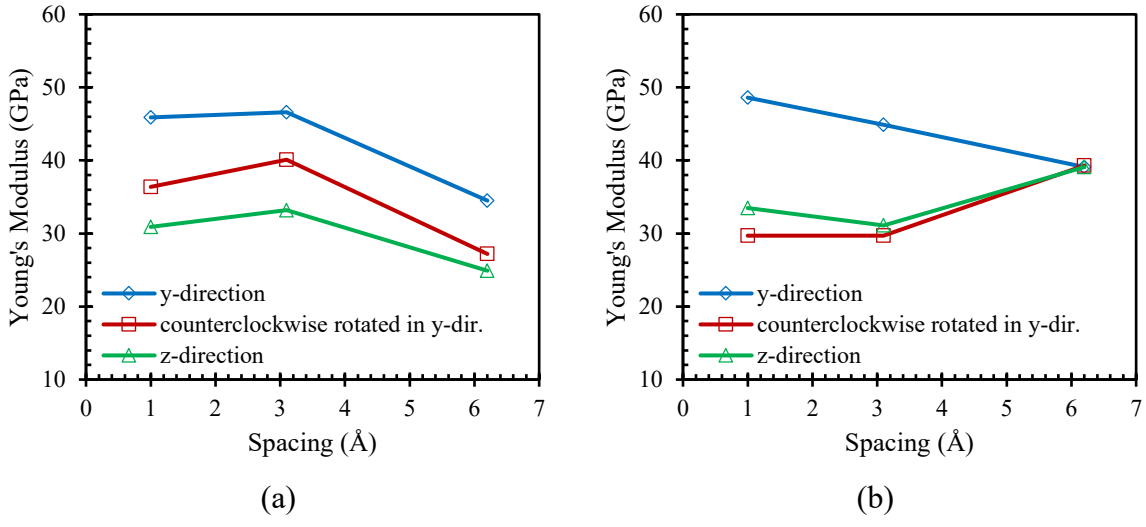

Figure 2.24 Curves of Young's modulus and spacing between supercells with three orientations of C-S-H (I)/CH composite: (a) cuboid shape supercells and (b) cube shape supercells.

Table 2.6 Mean Young's modulus of three orientations of C-S-H (I)/CH composite.

Composite	Shape	Spacing	E (GPa)
C-S-H (I)/CH	Cuboid	1 Å vacuum	37.7
		3.1 Å water	40.0
		6.2 Å water	28.9
C-S-H (I)/CH	Cube	1 Å vacuum	37.3
		3.1 Å water	35.2
		6.2 Å water	39.1

2.4 Tensile test of C-S-H (I)/AFt composite

2.4.1 Method

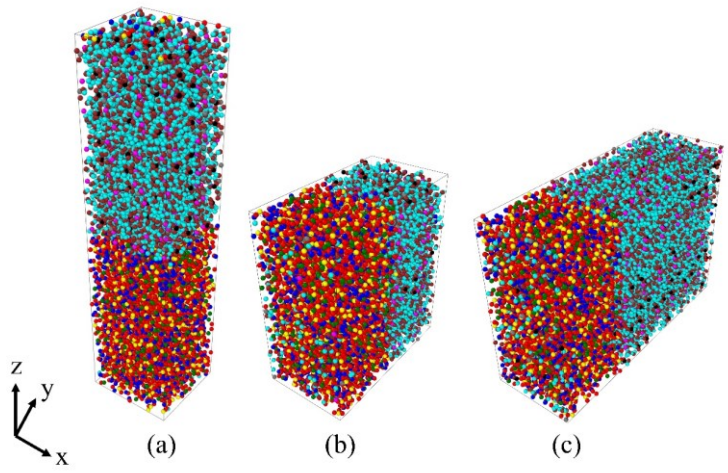

Figure 2.25 Orientations of C-S-H (I)/AFt composite: (a) in z-direction, (b) in y-direction, and (c) counterclockwise rotated in y-direction (Cuboid shape supercells).

The methodology is similar to **Section 2.2**, unit cells of C-S-H (I) and AFt were replicated in x-, y-, and z-directions. Size of supercells were chosen to ensure that all chosen phases (i.e., CH, AFt, C-S-H (I)) have similar size in all three dimensions. Since AFt unit cell has the biggest size in all three dimensions, size of AFt supercell was used as the reference. Hence, it was easier to replicate other phases to have approximately the same size.

C-S-H (I) unit cell was replicated 5 × 5 × 3 and 7 × 8 × 2 in x-, y- and z-directions in the case of cuboid and cube shapes, respectively. AFt unit cell was replicated 3 × 3 × 3 and 4 × 5 × 2 in x-, y- and z-directions in the case of cuboid and cube shapes, respectively. C-S-H (I) and AFt supercells were changed from monoclinic and trigonal supercells to orthogonal supercells in order to acquire the independent results to each direction. All MD simulations were done

with ReaxFF force field in real units, three dimensions (3D) and periodic boundary condition (PPP). These supercells were relaxed in NPT ensemble with temperature of 300 K and pressure of 0 atm in all three directions for 50 ps.

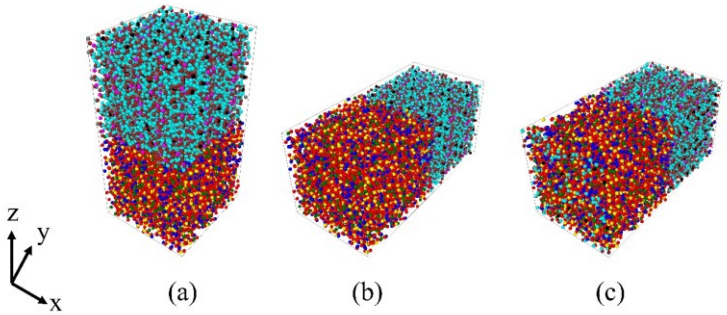

Figure 2.26 Orientations of C-S-H (I)/AFt composite: (a) in z-direction, (b) in y-direction, and (c) counterclockwise rotated in y-direction (Cube shape supercells).

Three different orientations were chosen as follows: (a) AFt supercell on top of C-S-H (I) supercell in z-direction, (b) AFt supercell on the side of C-S-H (I) supercell in y-direction, and (c) counterclockwise rotated AFt supercell around x-axis on the side of C-S-H (I) supercell in y-direction. **Figure 2.25** and **Figure 2.26** show the different orientations in the case of cuboid and cube shape supercells, respectively. Additionally, 1 Å vacuum, 3.1 Å water and 6.2 Å water spacing were placed between supercells. Relaxed supercells were put together with these different spacing in-between. C-S-H (I)/AFt composite was relaxed once again with NPT ensemble for another 50 ps. It should be noted that AFt supercell of counterclockwise rotated in y-direction was replicated 3 × 7 × 3 in x-, y- and z-directions to have a similar dimension in z-direction. This procedure was only applied in the case of cuboid shape composite because they did not have similar size along y- and z-directions. These supercells were counterclockwise rotated around x-axis in yz-plane. Bottom of these supercells were placed to the side of C-S-H (I) supercell. Timestep of these simulations was 0.25 fs. Different sizes and strain rates were done to study the sensitive analysis. Deformations were applied along z-direction coupled with relaxation in x- and y-directions. As can be seen in **Figure 2.27**, strain rate has an effect on stress-strain strain curves. Strain rate of 10^{-4} fs^{-1} gives high values of peak stress and peak strain compared to other strain rates. On the other hand, strain rate of 10^{-5} fs^{-1} has a noticeable global oscillation after reaching peak stress. Strain rates of 10^{-6} fs^{-1} and 10^{-7} fs^{-1} provides similar curves as well as peak stress and peak strain. Therefore, strain rates of 10^{-6} fs^{-1} was chosen for tensile test along z-direction because it consume less time compared with strain rates of 10^{-7} fs^{-1}. Final strain is comprised in between 15% to 40%.

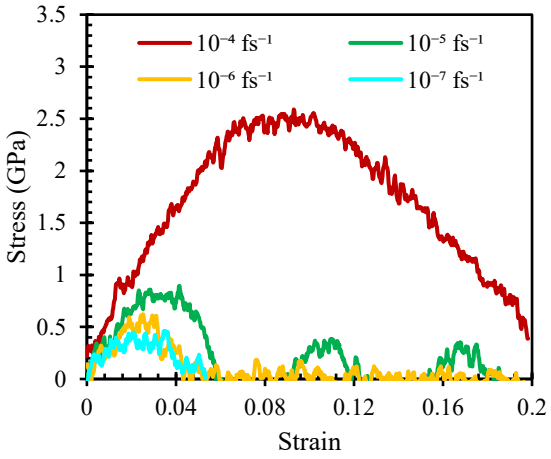

Figure 2.27 Sensitivity analysis of stress-strain curves with different strain rates of C-S-H (I)/AFt composite (Cuboid shape supercells) of 3.1 Å water spacing.

For C-S-H (I)/AFt composite cuboid shape supercell, here are the computer specifications that were used to run simulations: Dell Precision 7280, Intel Core Xeon Gold with CPU of 2.2 GHz (56 processors) and memory of 64 GB. We used either 8 or 24 cores of CPU.

For the simulation of C-S-H (I)/AFt composite cube shape supercells, either 24 or 48 visualization cores were used. The computer specifications were: supercomputer called "Liger", 12-core Intel Xeon (Haswell) E5-2680v3 processors with 252 compute nodes (24 cores per node) and 14 visualization nodes (28 GPUs and 24 cores per node) and 36 608 GB compute memory.

2.4.2 Results and Discussion

The mechanical properties of C-S-H (I)/AFt composite have been obtained after calculating the stress-strain curves with different orientations and configurations of spacing. Results are divided into two parts as follows: C-S-H (I)/AFt composite cuboid shape supercells and C-S-H (I)/AFt composite cube shape supercells.

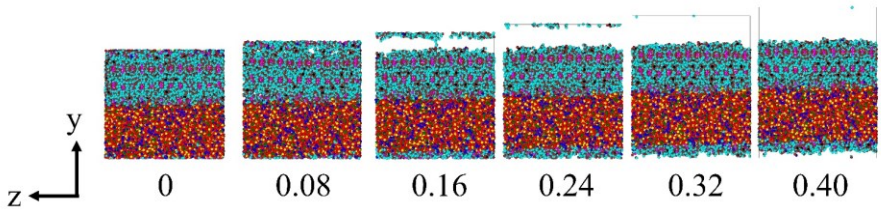

Figure 2.28 Direct tension of C-S-H (I)/vacuum (1 Å)/AFt composite in y-direction (Cuboid shape supercells).

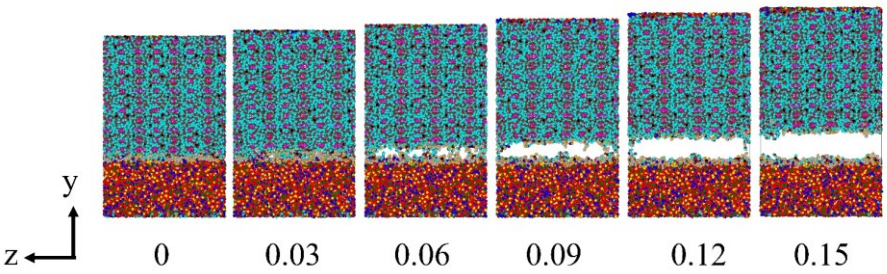

Figure 2.29 Direct tension of C-S-H (I)/H_2O (3.1 Å)/AFt composite counterclockwise rotated in y-direction (Cuboid shape supercells).

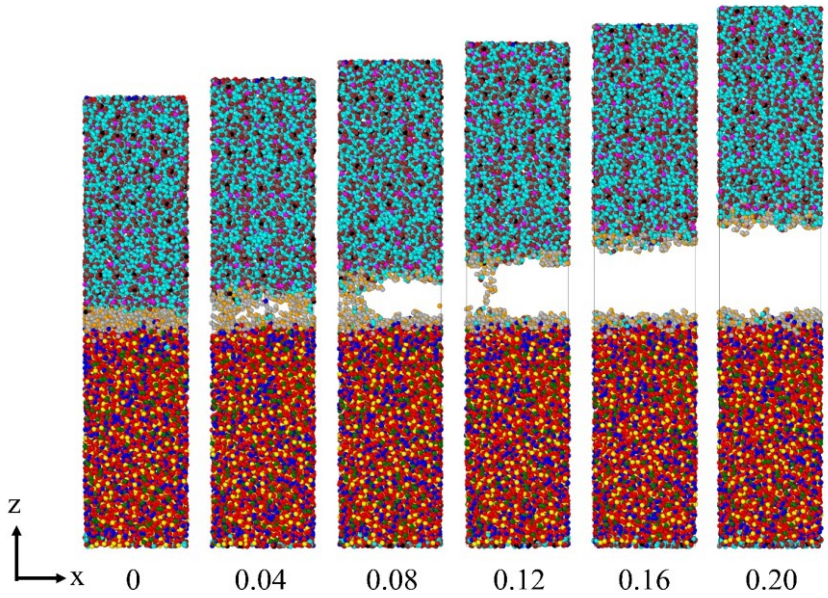

Figure 2.30 Direct tension of C-S-H (I)/H_2O (6.2 Å)/AFt composite in z-direction (Cuboid shape supercells).

In the case of C-S-H (I)/AFt composite cuboid shape supercells with ReaxFF force field, **Figure 2.28 - Figure 2.30** illustrate the direct tensile evolution of C-S-H (I)/AFt composite after relaxation to 40%, 15% and 20% strain with different orientations and configurations of spacing. All simulations were run with strain rate of 10^{-6} fs^{-1}. All rupture appeared at the interface of composite indicating that vacuum and water spacing made the interaction between main hydrated cement phases weaker and initiated the rupture. Stress-strain curves of C-S-H (I)/AFt composite cuboid shape supercells with different orientations and configurations of spacing can be observed in **Figure 2.31**. In the case of 1 Å vacuum spacing, the behaviour seems to be ductile. For the orientation in y-direction, stress-strain curve provided a smaller peak stress compared to other orientations. This suggests that this orientation had the lowest interaction at the interface between C-S-H (I) and AFt supercells. In the case of 3.1 Å water

spacing, the behaviour seems to be ductile too. However, with 3.1 Å water spacing added at the interface, it made a better interaction at the interface for the orientation in y-direction. As a result, it provided a bigger peak stress and peak strain compared to other orientations. A similar behaviour was found in the case of 6.2 Å water spacing. It appears that the bigger the spacing, the bigger the oscillation can be observed. Results indicate that orientations of two supercells and configurations of different spacing affected the stress-strain curves of C-S-H (I)/AFt composite cuboid shape supercells. As can be seen, 1 Å vacuum spacing gave the highest peak stress and peak strain. In contrast, 6.2 Å water spacing gave the lowest peak stress and peak strain. Results of peak stress, peak strain, running time and file size are summarized in **Table 2.7**.

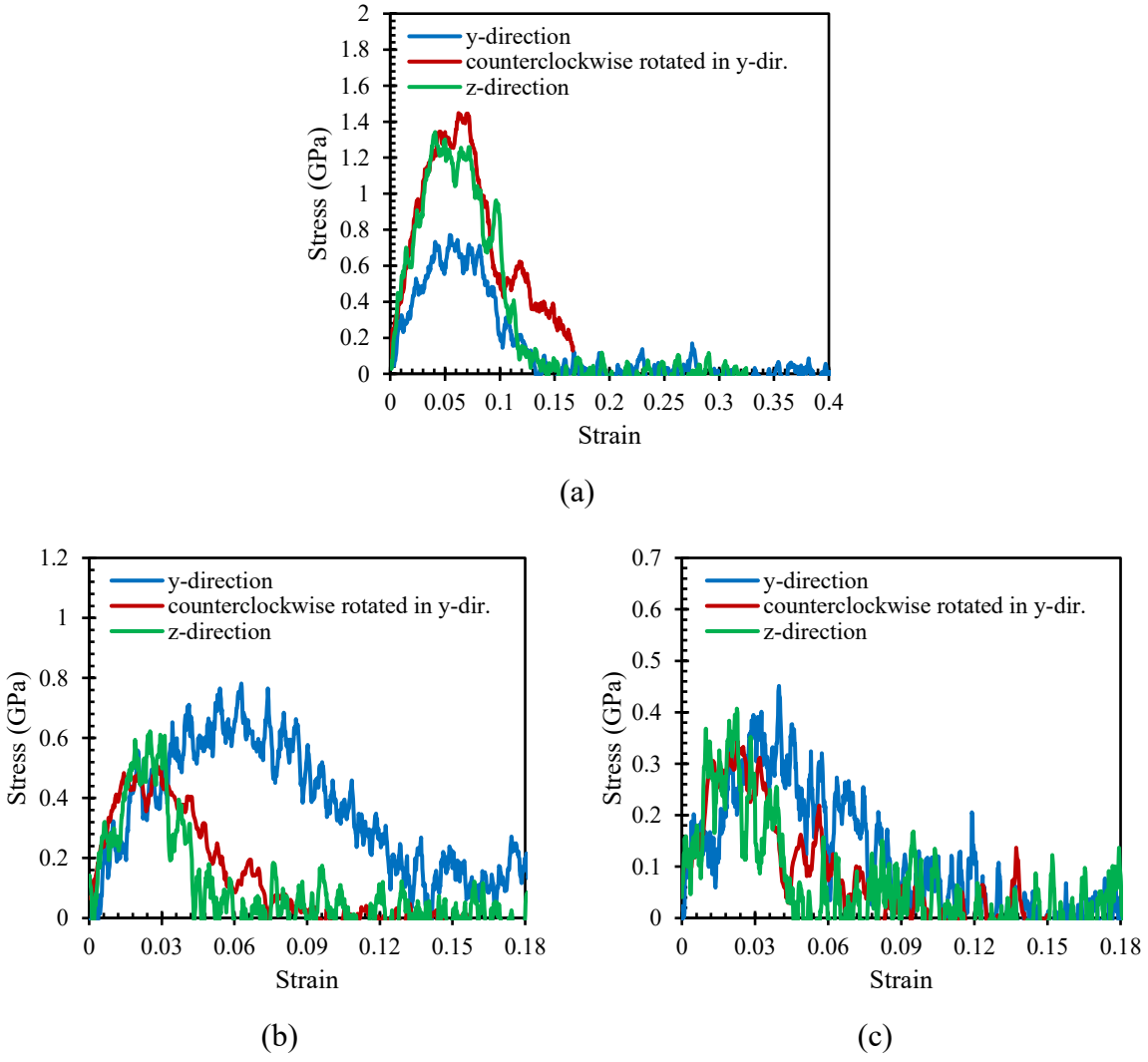

Figure 2.31 Stress-strain curves with three orientations of C-S-H (I)/AFt composite (Cuboid shape supercells): (a) 1 Å vacuum spacing, (b) 3.1 Å water spacing and (c) 6.2 Å water spacing.

Table 2.7 Peak strain, peak stress, running time and file size of C-S-H (I)/AFt composite (Cuboid shape supercells).

Orientation	Spacing	Peak strain	Peak stress (GPa)	Running time (hr:min)	File size (MB)
y-direction	1 Å vacuum	0.06	0.77	149:47	226
	3.1 Å water	0.06	0.78	89:33	313
	6.2 Å water	0.04	0.45	95:25	344
Counterclockwise rotated in y-direction	1 Å vacuum	0.07	1.45	72:00	324
	3.1 Å water	0.03	0.52	72:00	317
	6.2 Å water	0.02	0.35	72:00	447
z-direction	1 Å vacuum	0.04	1.34	147:47	187
	3.1 Å water	0.03	0.62	102:59	271
	6.2 Å water	0.02	0.41	105:59	277

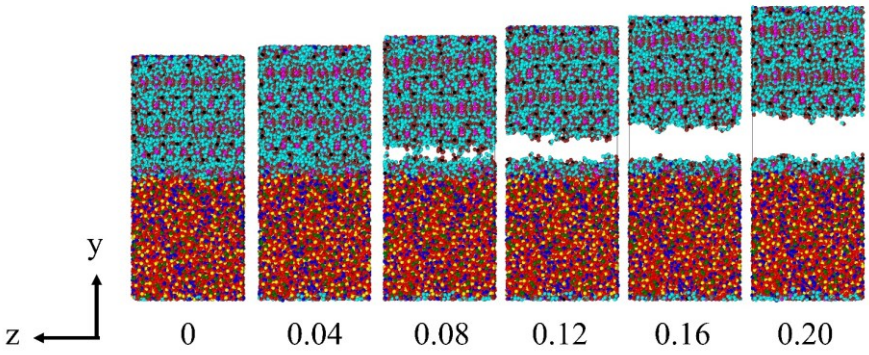

Figure 2.32 Direct tension of C-S-H (I)/vacuum (1 Å)/AFt composite in y-direction (Cube shape supercells).

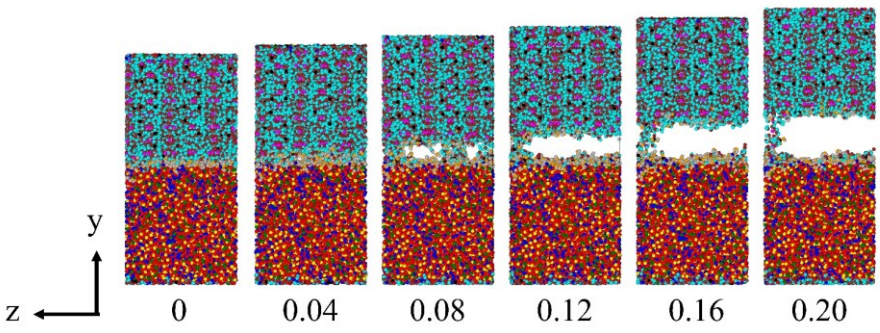

Figure 2.33 Direct tension of C-S-H (I)/H_2O (3.1 Å)/AFt composite counterclockwise rotated in y-direction (Cube shape supercells).

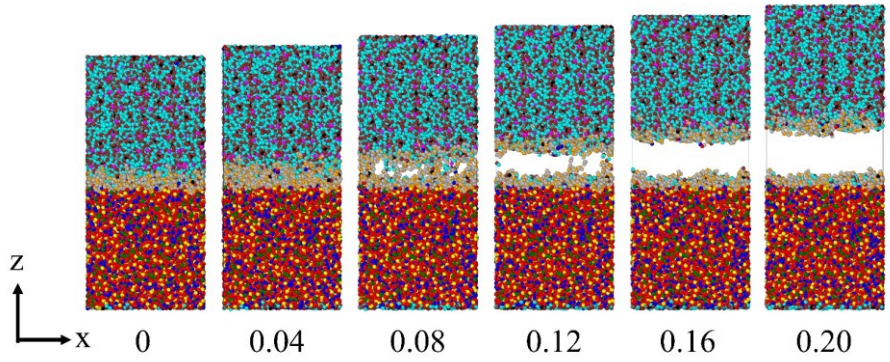

Figure 2.34 Direct tension of C-S-H (I)/H_2O (6.2 Å)/AFt composite in z-direction (Cube shape supercells).

In the case of C-S-H (I)/AFt composite cube shape supercells with ReaxFF force field, **Figure 2.32 - Figure 2.34** illustrate the direct tensile evolution of C-S-H (I)/AFt composite after relaxation to 20% strain with different orientations and configurations of spacing. All simulations were run with strain rate of 10^{-6} fs^{-1}. All rupture appeared at the interface of composite except for 1 Å vacuum spacing, but it was also originated quite close to the interface between C-S-H (I) and AFt supercells. It is likely that water spacing made the interaction between main hydrated cement phases weaker and initiated the rupture. Stress-strain curves of C-S-H (I)/AFt composite cube shape supercells with different orientations and configurations of spacing can be observed in **Figure 2.31**. In the case of 1 Å vacuum spacing, the behaviour seems to be ductile. It seems that the interaction at the interface in y-direction provided a lower peak stress compared to other orientations. In the case of 3.1 Å water spacing, the behaviour seems to be also ductile. However, the interaction at the interface in y-direction appears to be better which gave a slightly bigger peak stress and peak strain compared to other orientations. A similar behaviour could be observed in the case of 6.2 Å water spacing. It appears that the bigger the spacing, the bigger the oscillation can be observed. Results indicate that orientations of two supercells and configurations of different spacing affected the stress-strain curves of C-S-H (I)/AFt composite cube shape supercells. As can be seen, 1 Å vacuum spacing gave the highest peak stress and peak strain. In contrast, 6.2 Å water spacing gave the lowest peak stress and peak strain. Results of peak stress, peak strain, running time and file size are summarized in **Table 2.8**.

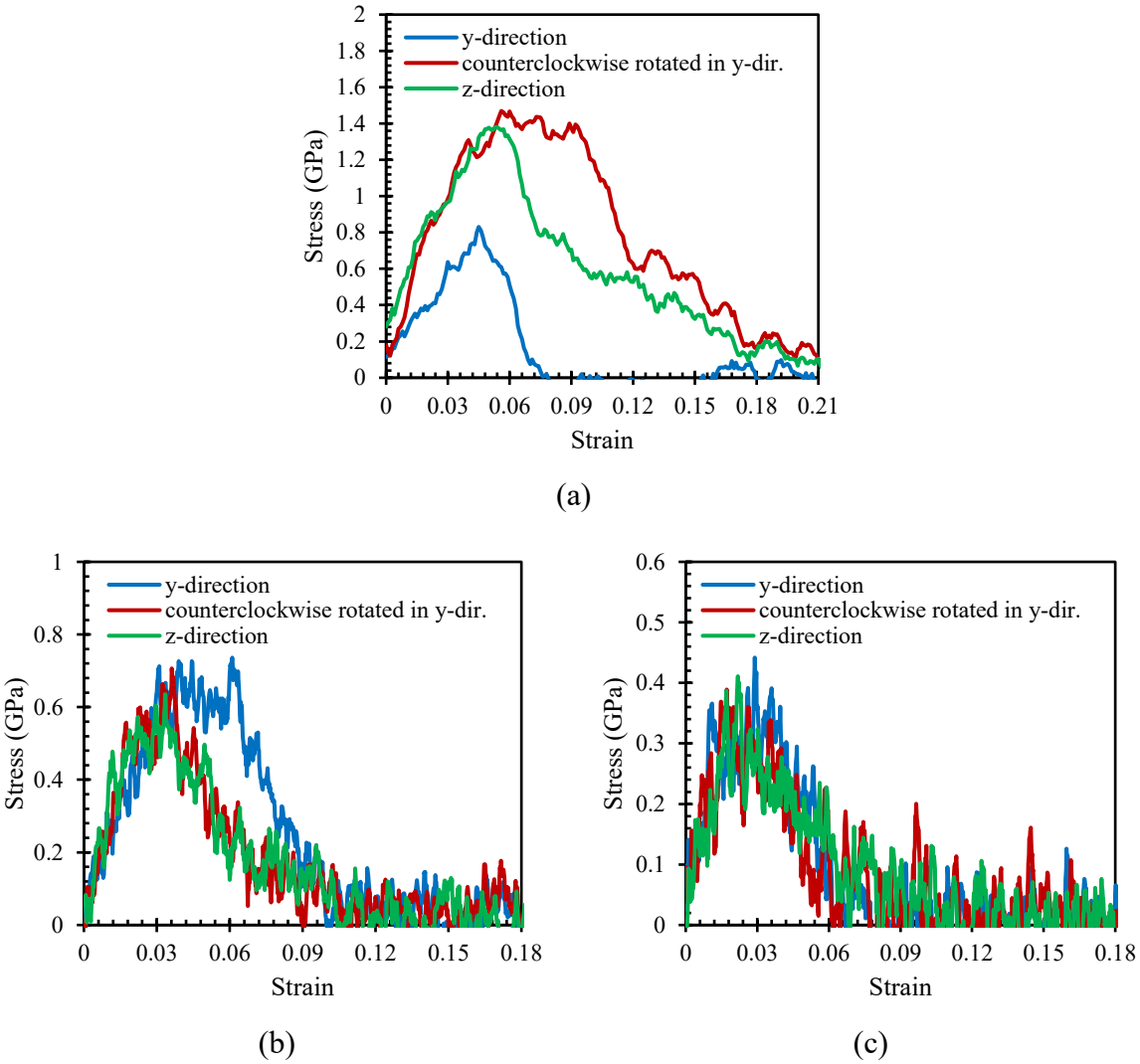

Figure 2.35 Stress-strain curves with three orientations of C-S-H (I)/AFt composite (Cube shape supercells): (a) 1 Å vacuum spacing, (b) 3.1 Å water spacing and (c) 6.2 Å water spacing.

Table 2.8 Peak strain, peak stress, running time and file size of C-S-H (I)/AFt composite (Cube shape supercells).

Orientation	Spacing	Peak strain	Peak stress (GPa)	Running time (hr:min)	File size (MB)
y-direction	1 Å vacuum	0.05	0.83	72:00	195
	3.1 Å water	0.06	0.74	59:46	463
	6.2 Å water	0.03	0.44	64:11	487
Counterclockwise rotated in y-direction	1 Å vacuum	0.06	1.47	72:00	198
	3.1 Å water	0.04	0.71	37:20	337
	6.2 Å water	0.02	0.39	65:27	513
z-direction	1 Å vacuum	0.05	1.38	72:00	265
	3.1 Å water	0.03	0.63	57:55	549
	6.2 Å water	0.02	0.41	60:07	531

2 Tensile test of cement paste phase composites

Figure 2.36 illustrates Young's modulus of different orientation and configurations of spacing deduced from the stress-strain curves. C-S-H (I)/AFt composite cuboid and cube shape supercells are shown on the left and on the right, respectively. The values of Young's modulus are quite similar in some cases. The average Young's modulus of three different orientations is summarized in **Table 2.9**. In the case of 1 Å vacuum spacing, Young's modulus was found to be 37.2 GPa and 27.6 GPa for C-S-H (I)/AFt composite cuboid and cube shape supercells, respectively. They are quite different because results obtained by cube shape in y-direction were lower than results of cuboid shape. When 3.1 Å water spacing was placed in between the supercells, Young's modulus increased to 38.7 GPa and 31.8 GPa, respectively. Finally, Young's modulus were found to be 22.5 GPa and 22.8 GPa in the case of cuboid and cube shapes, respectively. This means that they were decreased in the case of 6.2 Å water spacing. The average values in this case are similar. To the authors' knowledge, C-S-H (I)/AFt composite modelled with MD simulation was never done before. For the first time, Young's modulus of C-S-H (I)/AFt composite has been calculated. As a result, no literature value has been found for a sake of comparison.

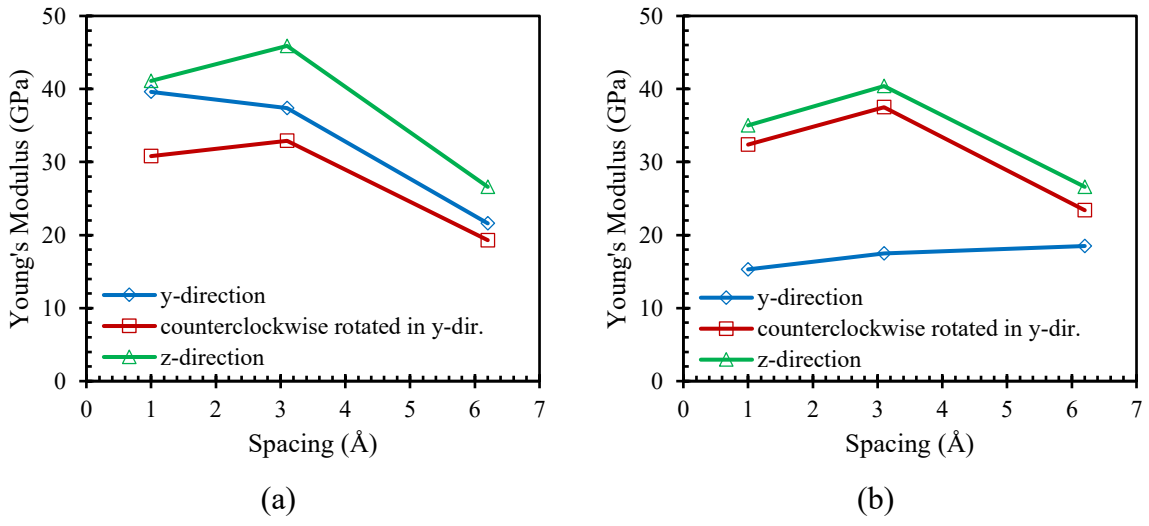

Figure 2.36 Curves of Young's modulus and spacing between supercells with three orientations of C-S-H (I)/AFt composite: (a) cuboid shape supercells and (b) cube shape supercells.

Table 2.9 Mean Young's modulus of three orientations of C-S-H (I)/AFt composite.

Composite	Shape	Spacing	E (GPa)
C-S-H (I)/AFt	Cuboid	1 Å vacuum	37.2
		3.1 Å water	38.7
		6.2 Å water	22.5
C-S-H (I)/AFt	Cube	1 Å vacuum	27.6
		3.1 Å water	31.8
		6.2 Å water	22.8

2.5 Tensile test of AFt/CH composite

2.5.1 Method

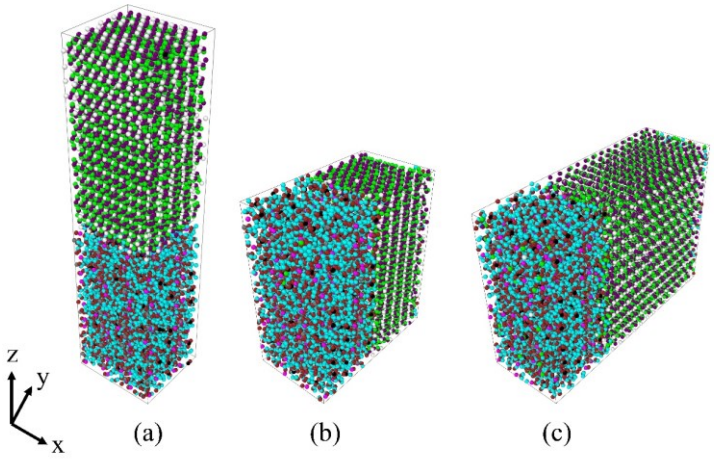

Figure 2.37 Orientations of AFt /CH composite: (a) in z-direction, (b) in y-direction, and (c) counterclockwise rotated in y-direction (Cuboid shape supercells).

Adapted from **Section 2.2**, unit cells of AFt and CH were replicated in x-, y-, and z-directions. Size of supercells were chosen to ensure that all chosen phases (i.e., CH, AFt, C-S-H (I)) have similar size in all three dimensions. Since AFt unit cell has the biggest size in all three dimensions, size of AFt supercell was used as the reference. Hence, it was easier to replicate other phases to have approximately the same size.

AFt unit cell was replicated 3 × 3 × 3 and 4 × 5 × 2 in x-, y- and z-directions in the case of cuboid and cube shapes, respectively. CH unit cell was respectively replicated 9 × 10 × 14 and 13 × 16 × 9 in x-, y- and z-directions in the case of cuboid and cube shapes. These supercells were changed from trigonal supercells to orthogonal supercells in order to acquire the independent results to each direction. All MD simulations were done with ReaxFF force field

in real units, three dimensions (3D) and periodic boundary condition (PPP). These supercells were relaxed in the NPT ensemble with temperature of 300 K and pressure of 0 atm in all three directions for 50 ps.

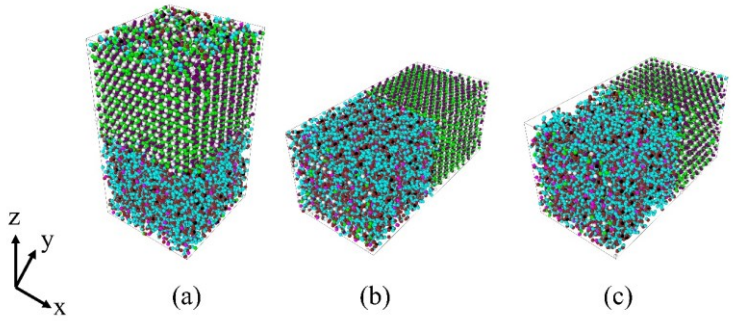

Figure 2.38 Orientations of AFt /CH composite: (a) in z-direction, (b) in y-direction, and (c) counterclockwise rotated in y-direction (Cube shape supercells).

Three different orientations were chosen as follows: (a) CH supercell on top of AFt supercell in z-direction, (b) CH supercell on the side of AFt supercell in y-direction, and (c) counterclockwise rotated CH supercell around x-axis on the side of AFt supercell in y-direction. **Figure 2.37** and **Figure 2.38** show the different orientations in the case of cuboid and cube shape supercells, respectively. Additionally, 1 Å vacuum, 3.1 Å water and 6.2 Å water spacing were placed between supercells in our study. Relaxed supercells were put together with these different spacing in-between. AFt/CH composite was relaxed once again with NPT ensemble for another 50 ps. It should be noted that CH supercell of counterclockwise rotated in y-direction was replicated 9 × 22 × 14 in x-, y- and z-directions to have a similar dimension in z-direction. This procedure was only applied in the case of cuboid shape composite because they did not have similar size along y- and z-directions. These supercells were counterclockwise rotated around x-axis in yz-plane. Bottom of these supercells were placed to the side of AFt supercell. Timestep of these simulations was 0.25 fs. Deformations were applied along z-direction coupled with relaxation in x- and y-directions. Final strain is comprised in between 20% to 50%.

For the simulations of AFt/CH composite cuboid shape supercells, 48 visualization cores were used. The computer specifications were as follows: supercomputer called “Liger”, 12-core Intel Xeon (Haswell) E5-2680v3 processors with 252 compute nodes (24 cores per node) and 14 visualization nodes (28 GPUs and 24 cores per node) and 36 608 GB compute memory.

For the simulations of AFt/CH composite cube shape supercells, we used 48 visualization cores. Here are the computer specifications that were used to run all simulations: supercomputer called “Liger”, 12-core Intel Xeon (Haswell) E5-2680v3 processors with 252 compute nodes

(24 cores per node) and 14 visualization nodes (28 GPUs and 24 cores per node) and 36 608 GB compute memory.

2.5.2 Results and Discussion

Using the method described above, we obtained stress-strain curves with different orientations and configurations of spacing. Results are divided into two parts as follows: AFt/CH composite cuboid shape supercells and AFt/CH composite cube shape supercells.

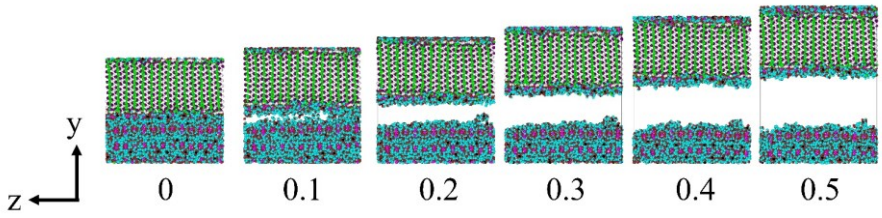

Figure 2.39 Direct tension of AFt/vacuum (1 Å)/CH composite in y-direction (Cuboid shape supercells).

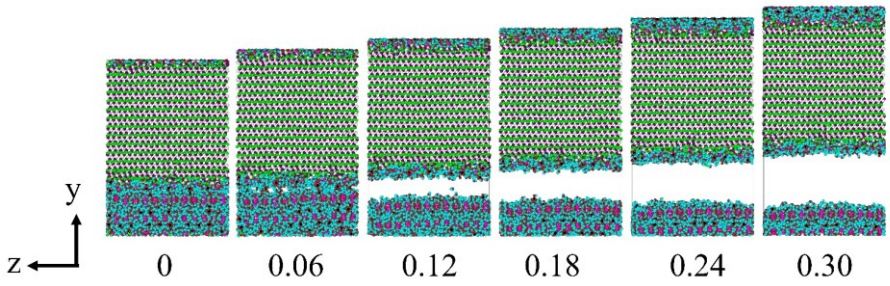

Figure 2.40 Direct tension of AFt/vacuum (1 Å)/CH composite counterclockwise rotated in y-direction (Cuboid shape supercells).

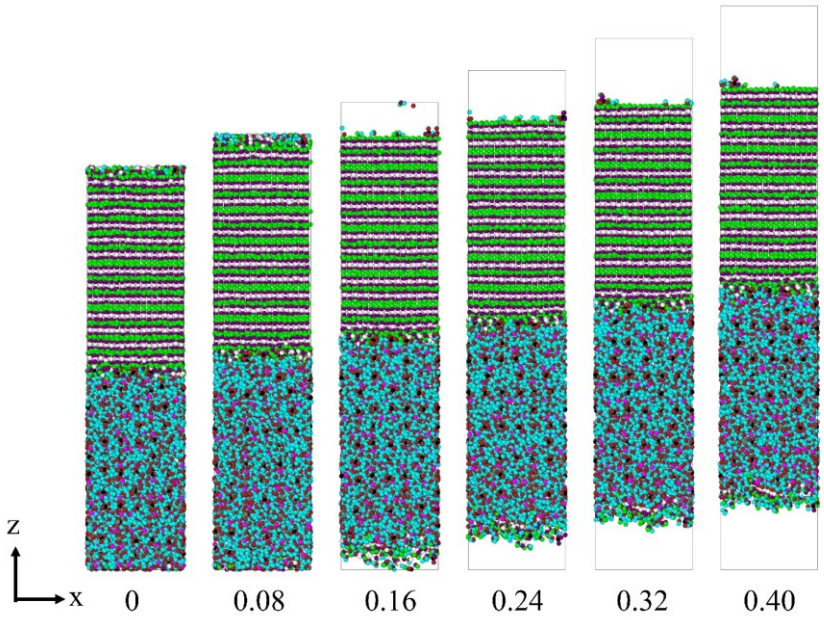

Figure 2.41 Direct tension of AFt/vacuum (1 Å)/CH composite in z-direction (Cuboid shape supercells).

In the case of AFt/CH composite cuboid shape supercells with ReaxFF force field, **Figure 2.39 - Figure 2.41** illustrate the direct tensile evolution of AFt/CH composite after relaxation to 50%, 30% and 40% strain with different orientations. All simulations were run with strain rate of 10^{-6} fs^{-1}. All rupture appeared quite close to the interface of composite except for the orientation in z-direction. It seems that the interaction of the layer in the AFt supercell was weaker than the interaction of the interface in the case of orientations in y-direction and counterclockwise rotated in y-direction. However, the interaction of the layer in the CH supercell was weaker than the interaction of interface in the case of orientation in z-direction. Since there is not water spacing imposed in this composite cuboid shape supercells, the rupture was not originated at the interface of the composite. Stress-strain curves of AFt/CH composite cuboid shape supercells with different orientations and configurations of spacing can be observed in **Figure 2.42**. In the case of 1 Å vacuum spacing, the behaviour seems to be ductile except in z-direction. However, orientation in z-direction gave a bigger value of peak stress and peak strain. Results indicate that orientations of two supercells affects the stress-strain curves of AFt/CH composite cuboid shape supercells. Results of peak stress, peak strain, running time and file size are summarized in **Table 2.10**.

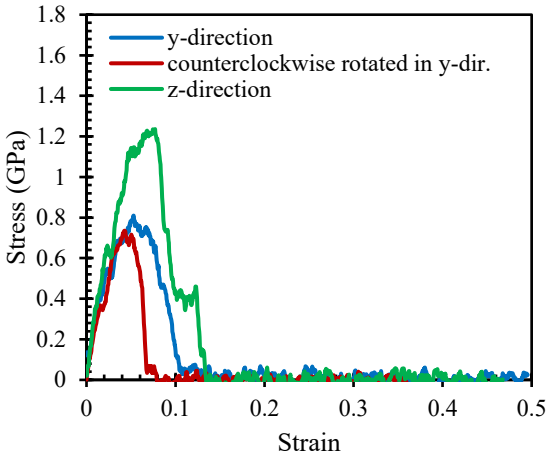

Figure 2.42 Stress-strain curves with three orientations of AFt/CH composite (Cuboid shape supercells) of 1 Å vacuum spacing.

Table 2.10 Peak strain, peak stress, running time and file size of AFt/CH composite (Cuboid shape supercells).

Orientation	Spacing	Peak strain	Peak stress (GPa)	Running time (hr:min)	File size (MB)
y-direction	1 Å vacuum	0.05	0.81	71:17	307
Counterclockwise rotated in y-direction	1 Å vacuum	0.04	0.74	72:00	418
z-direction	1 Å vacuum	0.08	1.24	72:00	296

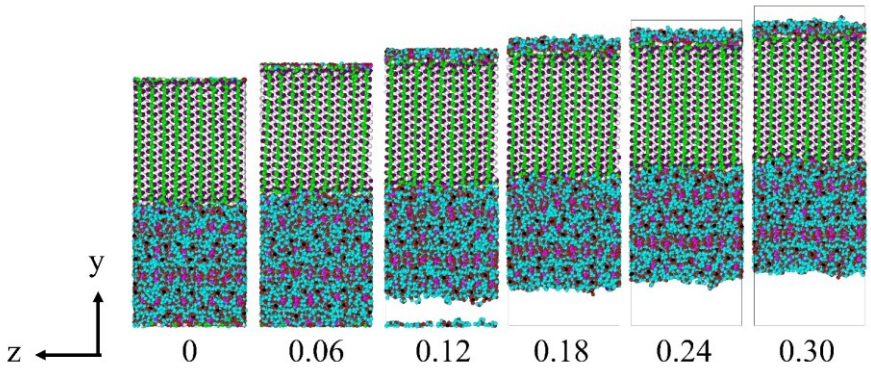

Figure 2.43 Direct tension of AFt/vacuum (1 Å)/CH composite in y-direction (Cube shape supercells).

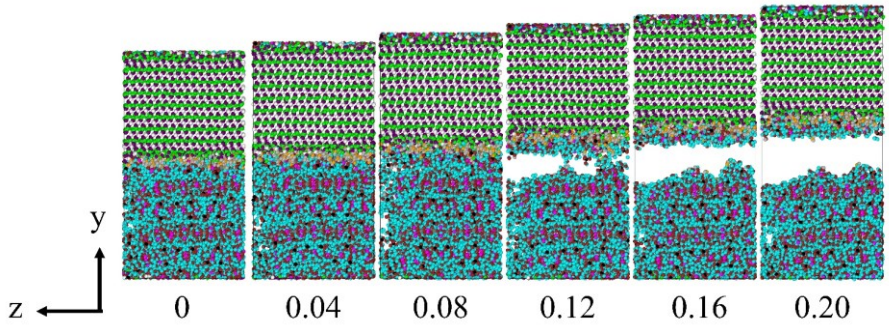

Figure 2.44 Direct tension of AFt/H_2O (3.1 Å)/CH composite counterclockwise rotated in y-direction (Cube shape supercells).

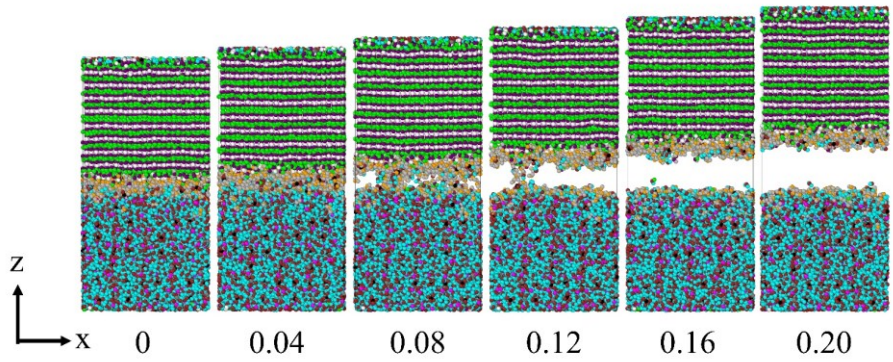

Figure 2.45 Direct tension of AFt/H_2O (6.2 Å)/CH composite in z-direction (Cube shape supercells).

In the case of AFt/CH composite cube shape supercells with ReaxFF force field, **Figure 2.43 - Figure 2.45** illustrate the direct tensile evolution of AFt/CH composite after relaxation to 30% and 20% strain with different orientations and configurations of spacing. All simulations were run with strain rate of 10^{-6} fs^{-1}. All rupture appeared at the interface of composite. This means that water spacing made the interaction between main hydrated cement phases weaker and initiated the rupture. Moreover, the interaction in the layer of AFt tends to be weaker than the interaction at the interface in the case of 1 Å vacuum spacing. Stress-strain curves of AFt/CH composite cube shape supercells with different orientations and configurations of spacing can be observed in **Figure 2.46**. In the case of 1 Å vacuum spacing, the behaviour seems to be ductile. The orientation in z-direction gave the highest peak stress compared to the other orientations. Similar behaviour could be observed in the case of 3.1 Å water spacing. In the case of 6.2 Å water spacing, the behaviour seems to be ductile too. Furthermore, orientation of counterclockwise rotated in y-direction tends to give a slightly bigger peak stress and peak strain. It appears that the bigger the spacing, the bigger the oscillation can be observed. Results indicate that orientations of two supercells and configurations of different spacing affected the

stress-strain curves of AFt/CH composite cube shape supercells. As can be seen, 1 Å vacuum spacing gave the highest peak stress and peak strain. In contrast, 6.2 Å water spacing gave the lowest peak stress and peak strain. Results of peak stress, peak strain, running time and file size are summarized in **Table 2.11**.

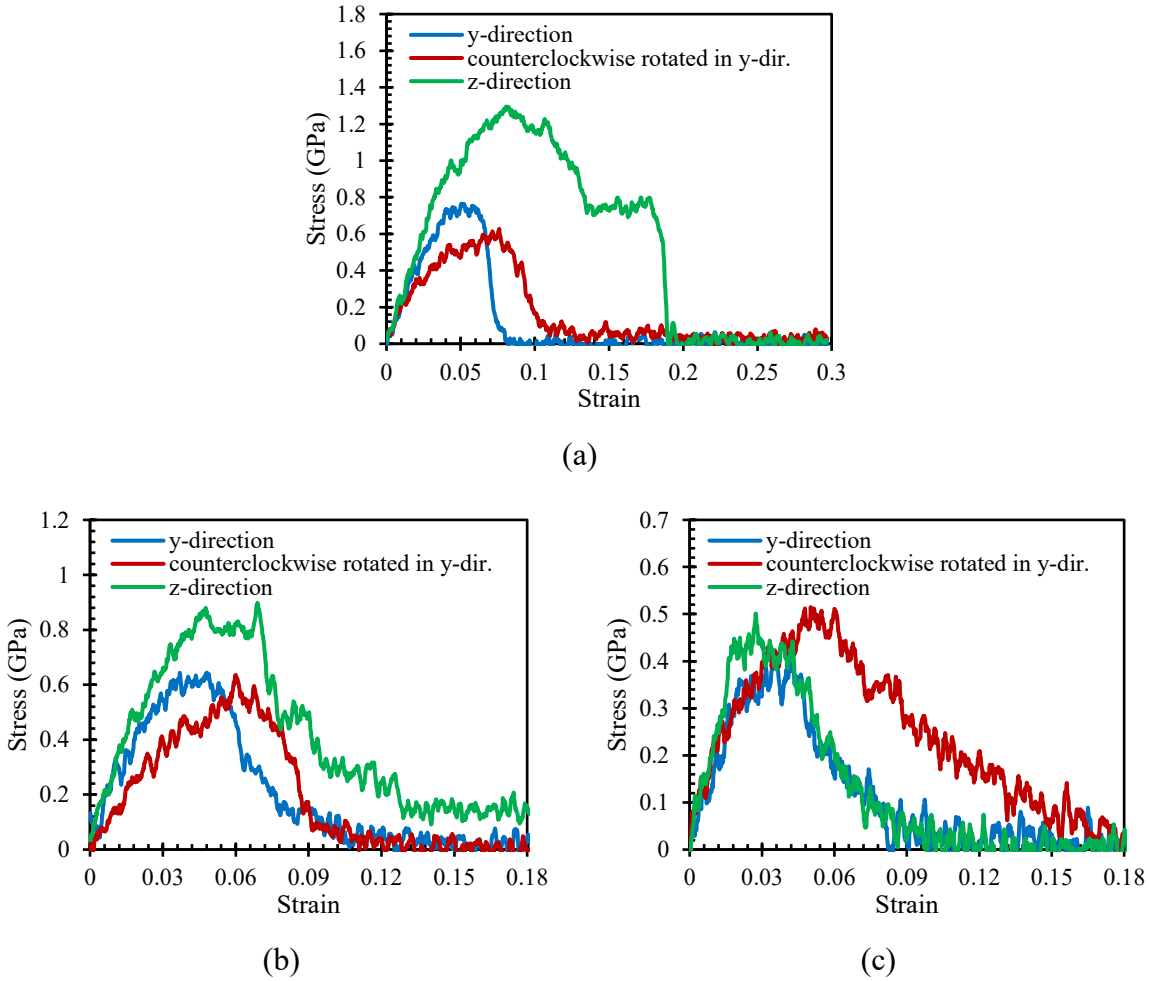

Figure 2.46 Stress-strain curves with three orientations of AFt/CH composite (Cube shape supercells): (a) 1 Å vacuum spacing, (b) 3.1 Å water spacing and (c) 6.2 Å water spacing.

Table 2.11 Peak strain, peak stress, running time and file size of AFt/CH composite (Cube shape supercells).

Orientation	Spacing	Peak strain	Peak stress (GPa)	Running time (hr:min)	File size (MB)
y-direction	1 Å vacuum	0.05	0.76	54:13	329
	3.1 Å water	0.05	0.64	36:23	343
	6.2 Å water	0.04	0.42	36:56	354
Counterclockwise rotated in y-direction	1 Å vacuum	0.08	0.63	54:13	329
	3.1 Å water	0.06	0.64	35:46	344
	6.2 Å water	0.05	0.52	35:40	354
z-direction	1 Å vacuum	0.08	1.30	49:27	329
	3.1 Å water	0.07	0.90	35:33	345
	6.2 Å water	0.03	0.50	36:04	357

Figure 2.36 illustrates Young's modulus of different orientation and configurations of spacing obtained from the stress-strain curves. AFt/CH composite cuboid and cube shape supercells are shown on the left and on the right, respectively. As mentioned before, only one configuration of spacing was done in the case of cuboid shape. The average Young's modulus of three different orientations is summarized in **Table 2.9**. In the case of 1 Å vacuum spacing, Young's modulus was found to be 23.7 GPa and 19.5 GPa for AFt/CH composite cuboid and cube shape supercells, respectively. They are quite similar. When 3.1 Å water spacing was placed in between the supercells, Young's modulus remained quite the same with the value of 19.2 GPa. Finally, Young's modulus were found to be 15.3 GPa in the case of cube shape. This means that it was decreased in the case of 6.2 Å water spacing. To the authors' knowledge, AFt/CH composite modelled with MD simulation was never done before. For the first time, Young's modulus of AFt/CH composite has been calculated. As a result, no literature value has been found for a sake of comparison.

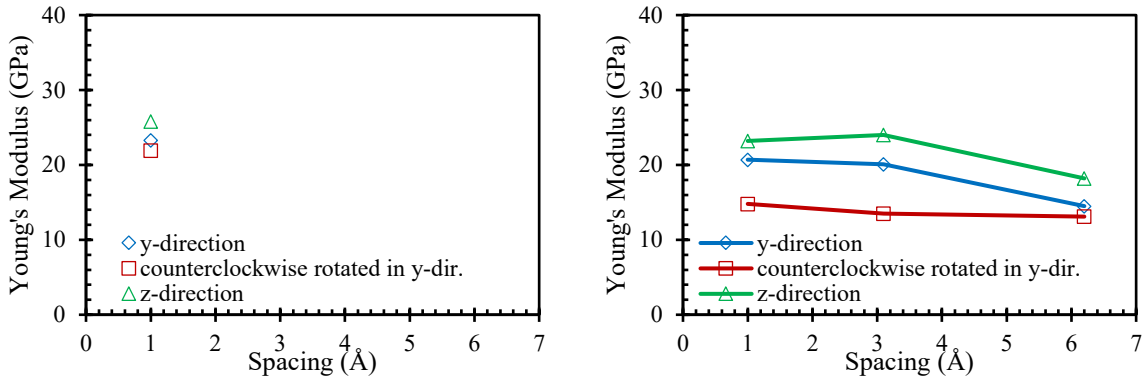

Figure 2.47 Curves of Young's modulus and spacing between supercells with three orientations of AFt/CH composite: (a) cuboid shape supercells and (b) cube shape supercells.

Table 2.12 Mean Young's modulus of three orientations of AFt/CH composite.

Composite	Shape	Spacing	E (GPa)
AFt/CH	Cuboid	1 Å vacuum	23.7
AFt/CH	Cube	1 Å vacuum	19.5
		3.1 Å water	19.2
		6.2 Å water	15.3

2.6 In summary

This chapter focuses on the mechanical properties of different main hydrated cement paste composites, i.e., C-S-H (I)/C-S-H (I) composite, C-S-H (I)/CH composite, C-S-H (I)/AFt composite and AFt/CH composite. The objective was concentrated on the adhesion between the different phases of the hydrated cement paste. The rupture of the adhesion between these phases causes the micro-cracking and damage of material even more than the rupture of the phases themselves. By means of reactive molecular dynamics simulations, the adhesion between the phases was taken into account with ReaxFF force field. Different cases of tensile test were performed consisting of three different orientations and three different configurations of spacing with strain rate of 10^{-6} fs^{-1}. Simulations included two different sizes called cuboid shape and cube shape supercells composites. Results indicate that stress-strain curves were affected by orientations and configurations of spacing as well as the cuboid shape and cube shape supercells composites. Brittle or ductile behaviour, more or less oscillation, and bigger or smaller peak stress can be observed for different cases. These results can be served in the upper-scale simulation in **Chapter 5**. In the next chapter, shear test were performed on the main hydrated cement paste phases in order to obtain the shear properties.

3 Shear test of hydrated cement paste phases

3.1 Background

As could be seen in the previous chapter, tensile test simulations were performed on the main hydrated cement phases and mechanical properties were then obtained. In this chapter, shear behaviour of these main hydrated cement paste phases were obtained via shear test using MD simulations. Similar to **Chapter 2**, different cases were imposed consisting of different orientations and configurations of spacing. ReaxFF force field was used for all simulations. Only cube shape supercells composites were performed under shear test. With stress-strain curved obtained from MD simulations, shear modulus, peak stress and peak strain were calculated. This chapter was written with the following order: (3.2) shear test of CH and AFt supercells, (3.3) shear test of C-S-H (I)/C-S-H (I) composite, (3.4) shear test of C-S-H (I)/CH composite, (3.5) shear test of C-S-H (I)/AFt composite, (3.6) shear test of AFt/CH composite and (3.7) in summary.

3.2 Shear test of CH and AFt supercells

3.2.1 Method

Similar to the methodology in **Chapter 2**, ReaxFF force field was used for both CH and AFt supercells and all procedures are the same except for the deformation direction. For tensile test, the deformation direction was in z-directions. However, it was in xz-plane for shear test. CH and AFt were replicated 13 × 16 × 9 and 4 × 5 ×2 in x-, y- and z-direction, respectively. These supercells were then changed from trigonal supercells to orthogonal supercells in order to acquire the independent results to each direction. All MD simulations were done with timestep of 0.25 fs in real units, three dimension (3D) and periodic boundary condition (PPP). A software called LAMMPS was used to run all simulations. These supercell were relaxed in NPT ensemble with temperature of 300 K and pressure of 0 atom in all three directions. Shear test in xz-plane was performed with strain rate of 10^{-6} fs^{-1} after energy minimization and relaxation in NPT ensemble for 50 ps. Shear deformation was applied in xz-plane coupled with relaxation in other directions. The final strain is 0.16 and 0.12 for CH and AFt supercells, respectively.

3 Shear test of hydrated cement paste phases

Simulations were run on computer with the following specifications: Dell Latitude 5410, Intel® Core™ i5-10210U with CPU of 1.60 GHz and memory of 8192 MB. The CPU ranging was from 4 to 8 cores.

3.2.2 Results and discussion

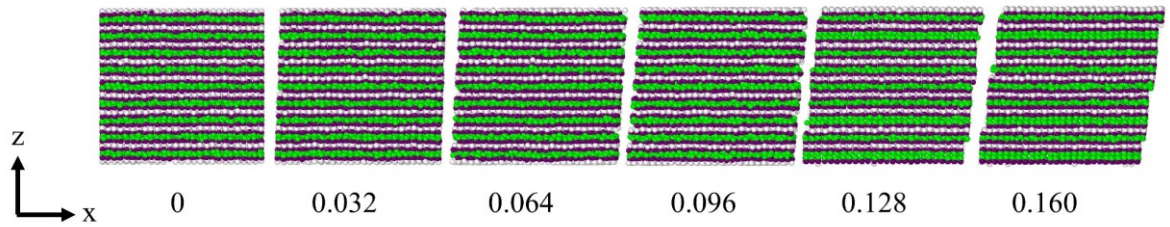

Figure 3.1 Shear test of CH supercell in xz-plane.

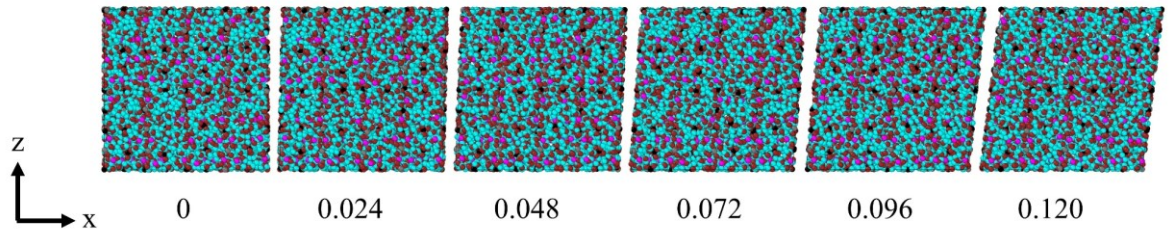

Figure 3.2 Shear test of AFt supercell in xz-plane.

Figure 3.1 and **Figure 3.2** show the shear evolution after relaxation to 16% and 12% of CH and AFt supercells, respectively. Stress-strain curves of CH and AFt supercells could be seen in **Figure 3.3**. Shear modulus, peak stress and peak strain of CH deduced from the stress-strain curves are summarized in **Table 3.1**. Peak stress of AFt supercell is higher than the one of CH supercell. Shear modulus of AFt supercell is also slightly higher than the one of CH supercell. To the authors' knowledge, shear test with CH and AFt supercells modelled with MD simulation was never done before. For the first time, shear modulus of CH and AFt supercells have been calculated. As a result, no literature value has been found for a sake of comparison.

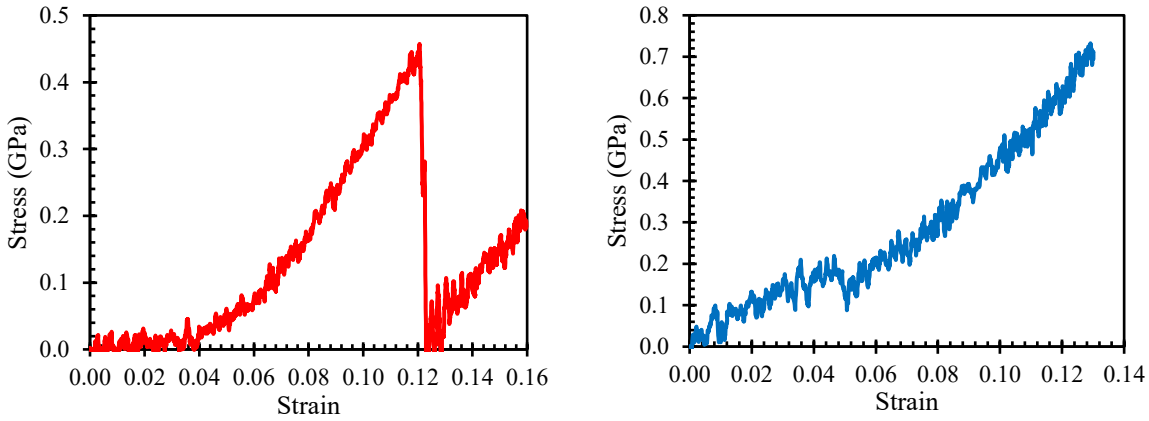

Figure 3.3 Stress-strain curves in xz-plane: (a) CH supercell and (b) AFt supercell.

Table 3.1 Peak strain, peak stress, shear modulus and file size of CH and AFt supercells.

Phase	Direction	Peak strain	Peak stress (GPa)	Shear modulus (GPa)	File size (MB)
CH	xz-plane	0.12	0.46	4.6	3574
AFt	xz-plane	0.13	0.73	5.4	3123

3.3 Shear test of C-S-H (I)/C-S-H (I) composite

3.3.1 Method

Similar to the methodology in **Chapter 3**, unit cell of C-S-H (I) was replicated in x-, y-, and z-directions. Size of supercells were chosen to ensure that all chosen phases (i.e., CH, AFt, C-S-H (I)) have similar size in all three dimensions. Since AFt unit cell has the biggest size in all three dimensions, size of AFt supercell was used as the reference. Hence, it was easier to replicate other phases to have approximately the same size.

C-S-H (I) unit cell was replicated 7 × 8 × 2 in x-, y- and z-directions and only cube shape was used for shear test. These supercells were changed from monoclinic supercells to orthogonal supercells in order to acquire the independent results to each direction. All MD simulations were done with ReaxFF force field in real units, three dimensions (3D) and periodic boundary condition (PPP). These supercells were relaxed in NPT ensemble with temperature of 300 K and pressure of 0 atm in all three directions for 50 ps.

Three different orientations were chosen in this study as follows: (a) C-S-H (I) supercell on top of C-S-H (I) supercell in z-direction, (b) C-S-H (I) supercell on the side of C-S-H (I) supercell in y-direction, and (c) counterclockwise rotated C-S-H (I) supercell around x-axis on

the side of C-S-H (I) supercell in y-direction. Additionally, 1 Å vacuum, 3.1 Å water and 6.2 Å water spacing were placed between supercells. SPC/E water model was used in this study. Relaxed supercells were put together with these different spacing in-between. C-S-H (I)/C-S-H (I) composite was relaxed once again with NPT ensemble for another 50 ps. These supercells were counterclockwise rotated around x-axis in yz-plane. Bottom of these supercells were placed to the side of C-S-H (I) supercell. Timestep of these simulations was 0.25 fs. Shear deformations were applied in either xy- or xz-planes coupled with relaxation in other directions. Final strain is comprised in between 20% to 25%.

For all simulations, 24 visualization cores were used. Here are the computer specifications that were used to run all simulations: supercomputer called "Liger", 12-core Intel Xeon (Haswell) E5-2680v3 processors with 252 compute nodes (24 cores per node) and 14 visualization nodes (28 GPUs and 24 cores per node) and 36 608 GB compute memory.

3.3.2 Results and Discussion

The purpose was to obtain the mechanical properties (i.e., shear modulus, peak stress and peak strain) of C-S-H (I)/C-S-H (I) composite using MD simulations. Using the method described above, stress-strain curves were obtained with different orientations and configurations of spacing.

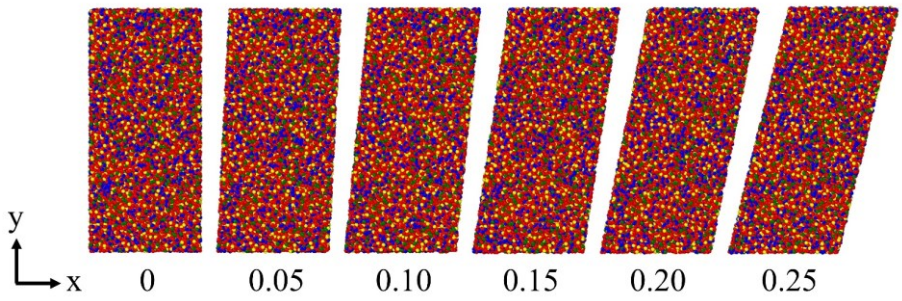

Figure 3.4 Shear test in xy-plane of C-S-H (I)/vacuum (1 Å)/C-S-H (I) composite in y-direction.

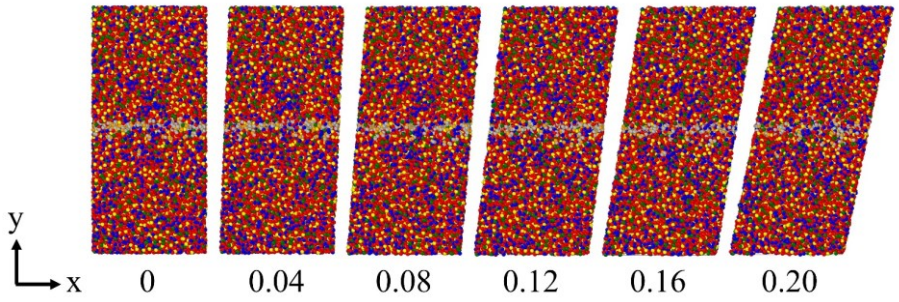

Figure 3.5 Shear test in xy-plane of C-S-H (I)/H_2O (3.1 Å)/C-S-H (I) composite counterclockwise rotated in y-direction.

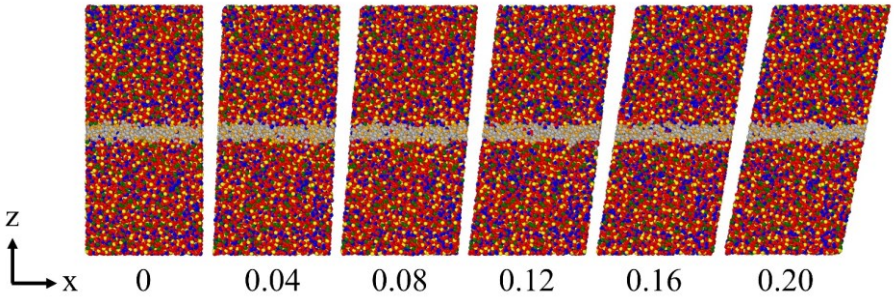

Figure 3.6 Shear test in xz-plane of C-S-H (I)/H_2O (6.2 Å)/C-S-H (I) composite in z-direction.

Figure 2.8 - Figure 2.10 illustrate the shear evolution of C-S-H (I)/C-S-H (I) composite after relaxation to 25% and 20% strain with different orientations and configurations of spacing. All simulations were run with strain rate of 10^{-6} fs^{-1}. Stress-strain curves of C-S-H (I)/C-S-H (I) composite with different orientations and configurations of spacing can be observed in **Figure 2.11**. It should be noted that shear test performed using deform method by LAMMPS simulation could not provide the full curve with the post peak stress-strain curve. The reason is that after shear deformation strain reaches 25%, the simulation box will be flip to the other side. Hence, it gives the negative value of strain. In the case of 1 Å vacuum spacing, the oscillation seems to be less than the bigger water spacing. Peak stress and peak strain are quite similar despite the different of orientations. In the case of water spacing, the values of peak stress and peak strain are quite different. Results indicate that orientations of two supercells and configurations of different spacing affected the stress-strain curves of C-S-H (I)/C-S-H (I) composite. As can be seen, 1 Å vacuum spacing gave the highest peak stress and peak strain. In contrast, 6.2 Å water spacing gave the lowest peak stress and peak strain. Results of peak stress, peak strain, running time and file size are summarized in **Table 2.2**.

3 Shear test of hydrated cement paste phases

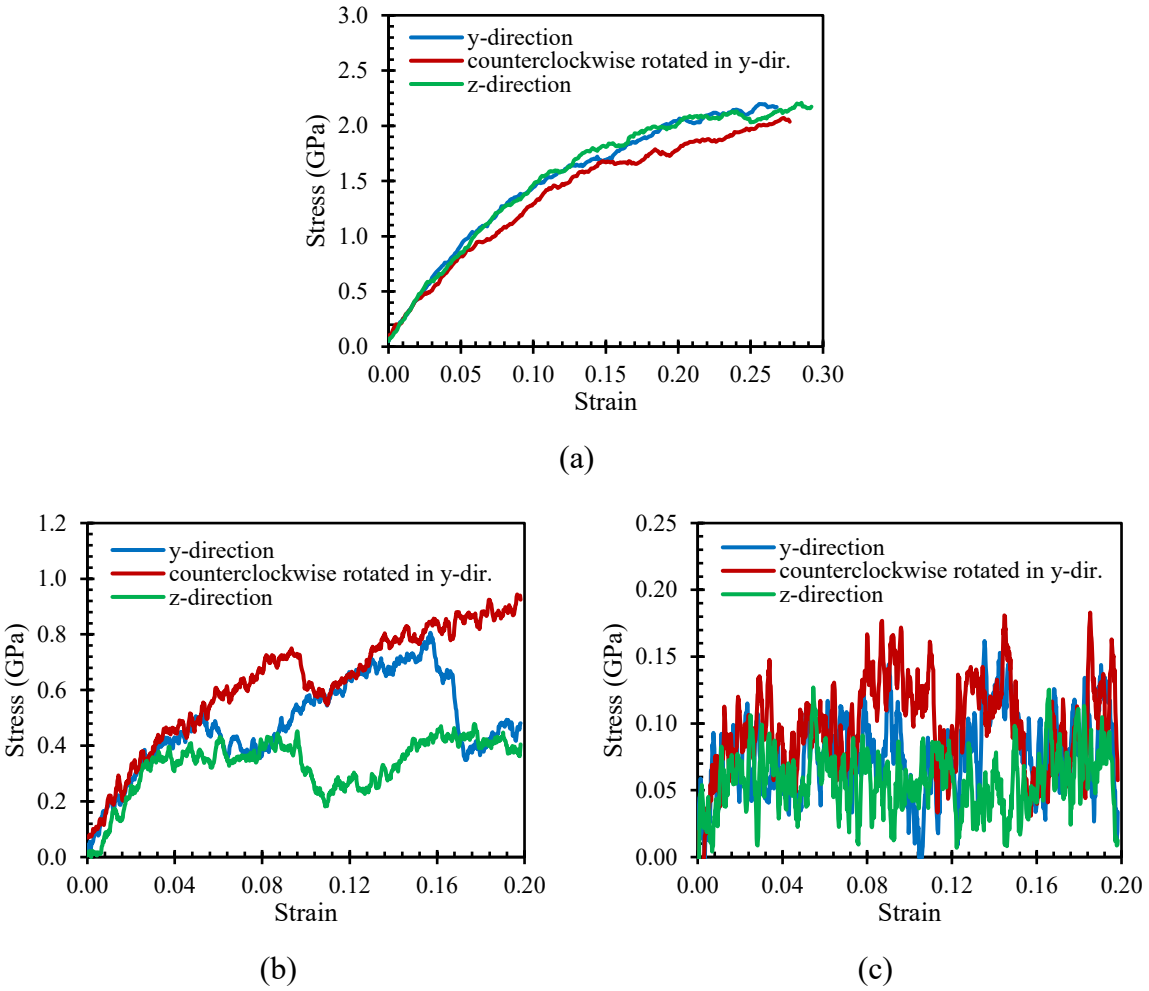

Figure 3.7 Stress-strain curves of shear tests with three orientations of C-S-H (I)/C-S-H (I) composite: (a) 1 Å vacuum spacing, (b) 3.1 Å water spacing and (c) 6.2 Å water spacing.

Table 3.2 Peak strain, peak stress, running time and file size of C-S-H (I)/C-S-H (I) composite.

Orientation	Spacing	Peak strain	Peak stress (GPa)	Running time (hr:min)	File size (MB)
y-direction	1 Å vacuum	0.26	2.20	72:00	183
	3.1 Å water	0.16	0.81	43:35	406
	6.2 Å water	0.14	0.16	45:24	450
Counterclockwise rotated in y-direction	1 Å vacuum	0.27	2.07	72:00	211
	3.1 Å water	0.20	0.94	41:53	457
	6.2 Å water	0.19	0.18	43:19	457
z-direction	1 Å vacuum	0.29	2.21	72:00	186
	3.1 Å water	0.18	0.48	42:51	423
	6.2 Å water	0.06	0.13	44:50	420

Shear modulus is deduced from the stress-strain curves on the linear elastic part. **Figure 2.12** illustrates shear modulus of different orientation and configurations of spacing. The values of shear modulus obtained are quite similar despite the different orientations. The average shear modulus of three different orientations is summarized in **Table 2.3**. In the case of 1 Å vacuum spacing, shear modulus was found to be 14 GPa. When 3.1 Å and 6.2 Å water spacing were placed in between the supercells, shear modulus decreased to 10.6 GPa and 5.8 GPa, respectively. This means that the bigger the spacing is the lower the values of shear modulus. The values of peak stress might be compared to the result obtained by Fan and Yang [41] with the value of about 0.56 ± 0.14 GPa for a similar water spacing. The procedure of Fan and Yang is different from this study. They fixed the bottom atoms and moved the top atoms along the interface with a constant loading rate of 0.08 Å/ps. They derived the interfacial shear strength of C-S-H globules interface from the average value of stress with 0.5 Å, 1.0 Å, 1.5 Å and 2.0 Å water layer thickness.

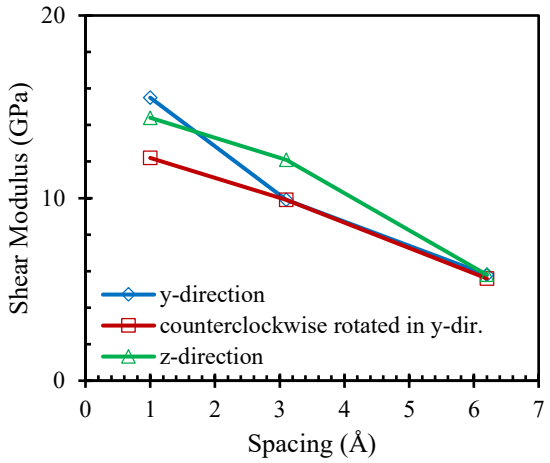

Figure 3.8 Curves of shear modulus and spacing between supercells with three orientations of C-S-H (I)/C-S-H (I) composite.

Table 3.3 Mean shear modulus of three orientations of C-S-H (I)/C-S-H (I) composite.

Composite	Shape	Spacing	G (GPa)
C-S-H (I)/C-S-H (I)	Cube	1 Å vacuum	14.0
		3.1 Å water	10.6
		6.2 Å water	5.8

3.4 Shear test of C-S-H (I)/CH composite

3.4.1 Method

Similar to the methodology in **Section 2.2**, unit cells of C-S-H (I) and CH were replicated in x-, y-, and z-directions. C-S-H (I) and CH unit cells were replicated 7 × 8 × 2 and 13 × 16 × 9 in x-, y- and z-directions, respectively. C-S-H (I) and CH supercells were changed from monoclinic and trigonal supercells to orthogonal supercells in order to acquire independent results to each direction. All MD simulations were done with ReaxFF force field in real units, three dimensions (3D) and periodic boundary condition (PPP). These supercells were relaxed in NPT ensemble with temperature of 300 K and pressure of 0 atm in three directions for 50 ps.

Three different orientations were chosen in this study as follows: (a) CH supercell on top of C-S-H (I) supercell in z-direction, (b) CH supercell on the side of C-S-H (I) supercell in y-direction, and (c) counterclockwise rotated CH supercell around x-axis on the side of C-S-H (I) supercell in y-direction. Additionally, 1 Å vacuum, 3.1 Å water and 6.2 Å water spacing were placed between supercells. Relaxed supercells were put together with these different spacing in-between. C-S-H (I)/CH composite was relaxed once again with NPT ensemble for another 50 ps. These supercells were counterclockwise rotated around x-axis in yz-plane. Bottom of these supercells were placed to the side of C-S-H (I) supercell. Timestep of these simulations was 0.25 fs. Shear deformations were applied in either xy- or xz-planes coupled with relaxation in other directions. Final strain is comprised in between 20% to 25%.

For all simulations, 24 visualization cores were used. The computer specifications used to run all simulations were: supercomputer called “Liger”, 12-core Intel Xeon (Haswell) E5-2680v3 processors with 252 compute nodes (24 cores per node) and 14 visualization nodes (28 GPUs and 24 cores per node) and 36 608 GB compute memory.

3.4.2 Results and Discussion

Using the method described above, stress-strain curves were obtained with different orientations and configurations of spacing.

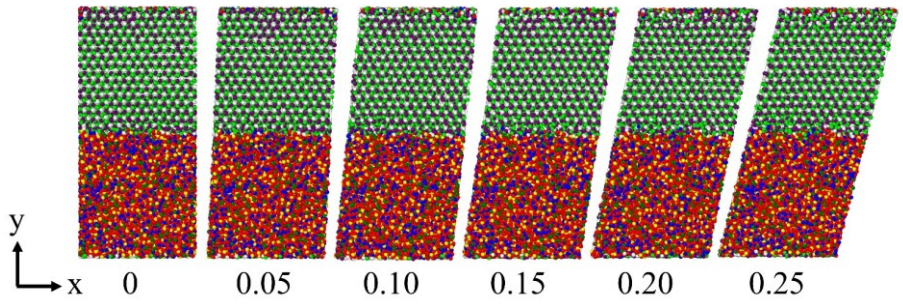

Figure 3.9 Shear test in xy-plane of C-S-H (I)/vacuum (1 Å)/CH composite in y-direction.

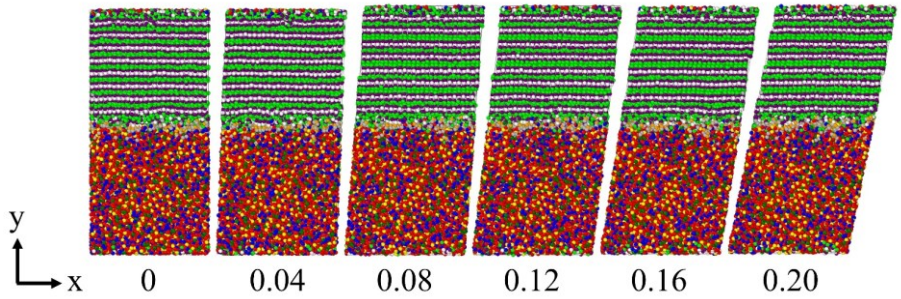

Figure 3.10 Shear test in xy-plane of C-S-H (I)/H_2O (3.1 Å)/CH composite in y-direction.

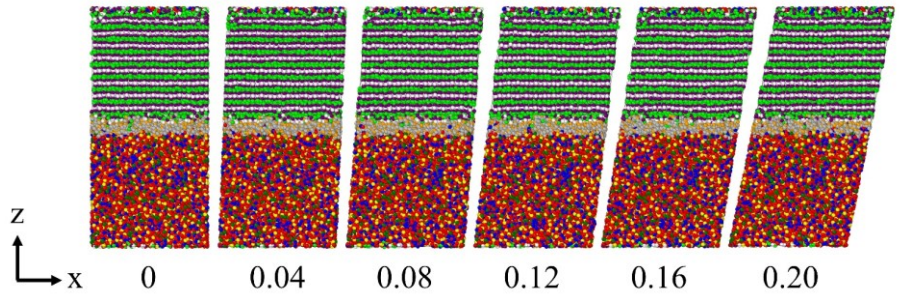

Figure 3.11 Shear test in xz-plane of C-S-H (I)/H_2O (6.2 Å)/CH composite in z-direction.

Figure 2.20 - Figure 2.22 illustrate the shear evolution of C-S-H (I)/CH composite after relaxation to 25% and 20% strain with different orientations and configurations of spacing. All simulations were run with strain rate of 10^{-6} fs^{-1}. Stress-strain curves of C-S-H (I)/CH composite with different orientations and configurations of spacing can be observed in **Figure 2.23**. In the case of 1 Å vacuum spacing and 3.1 Å water spacing, the behaviour among different orientations seems to be the same except in y-direction which gives higher peaks stress. It indicates that orientation in y-direction provided a better interaction at the interface between C-

S-H (I) and CH supercells. In the case of 6.2 Å water spacing, the orientation of counterclockwise rotated in y-direction gives a higher peak stress. It appears that the bigger the spacing, the bigger the oscillation can be observed. Results indicate that orientations of two supercells and configurations of different spacing affected the stress-strain curves of C-S-H (I)/CH composite. As can be seen, 1 Å vacuum spacing gave the highest peak stress and peak strain. In contrast, 6.2 Å water spacing gave the lowest peak stress. Results of peak stress, peak strain, running time and file size are summarized in **Table 2.5**.

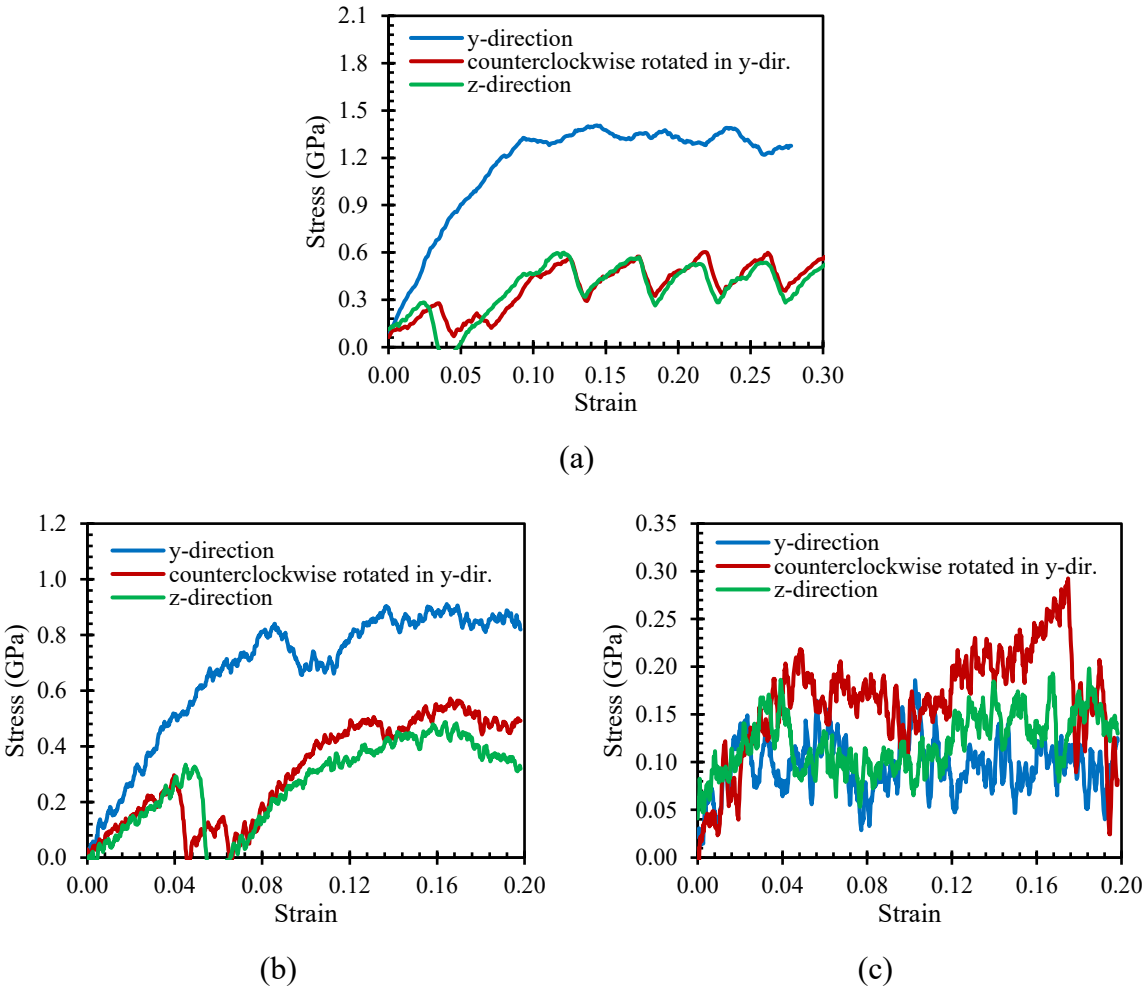

Figure 3.12 Stress-strain curves of shear tests with three orientations of C-S-H (I)/CH composite: (a) 1 Å vacuum spacing, (b) 3.1 Å water spacing and (c) 6.2 Å water spacing.

Table 3.4 Peak strain, peak stress, running time and file size of C-S-H (I)/CH composite.

Orientation	Spacing	Peak strain	Peak stress (GPa)	Running time (hr:min)	File size (MB)
y-direction	1 Å vacuum	0.14	1.41	72:00	213
	3.1 Å water	0.16	0.91	46:27	462
	6.2 Å water	0.10	0.19	47:34	481
Counterclockwise rotated in y-direction	1 Å vacuum	0.22	0.60	72:00	183
	3.1 Å water	0.17	0.57	45:58	420
	6.2 Å water	0.18	0.29	48:31	434
z-direction	1 Å vacuum	0.12	0.60	72:00	183
	3.1 Å water	0.16	0.49	44:58	413
	6.2 Å water	0.19	0.20	48:09	428

Figure 2.24 illustrates shear modulus of different orientation and configurations of spacing. The values of shear modulus obtained are quite similar except for orientation in y-direction. In y-direction, shear modulus are higher in all three configuration of spacing. The average shear modulus of three different orientations is summarized in **Table 2.6**. In the case of 1 Å vacuum spacing, shear modulus was found to be 12.6 GPa for C-S-H (I)/CH composite. When 3.1 Å and 6.2 Å water spacing were placed in between the supercells, shear modulus decreased to 10.3 GPa and 5.7 GPa, respectively. To the authors' knowledge, shear test with C-S-H (I)/CH composite modelled with MD simulation was never done before. For the first time, shear modulus of C-S-H (I)/CH composite has been calculated. As a result, no literature value has been found for a sake of comparison.

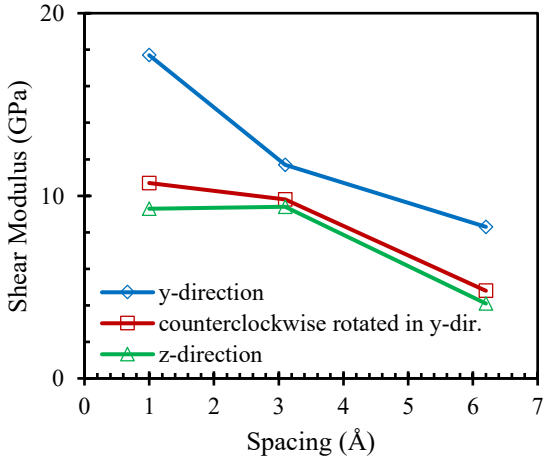

Figure 3.13 Curves of shear modulus and spacing between supercells with three orientations of C-S-H (I)/CH composite.

Table 3.5 Mean shear modulus of three orientations of C-S-H (I)/CH composite.

Composite	Shape	Spacing	G (GPa)
C-S-H (I)/CH	Cube	1 Å vacuum	12.6
		3.1 Å water	10.3
		6.2 Å water	5.7

3.5 Shear test of C-S-H (I)/AFt composite

3.5.1 Method

The methodology is similar to **Section 2.2**, unit cells of C-S-H (I) and AFt were replicated in x-, y-, and z-directions. C-S-H (I) and AFt unit cells were replicated 7 × 8 × 2 and 4 × 5 × 2 in x-, y- and z-directions. C-S-H (I) and AFt supercells were changed from monoclinic and trigonal supercells to orthogonal supercells in order to acquire the independent results to each direction. All MD simulations were done with ReaxFF force field in real units, three dimensions (3D) and periodic boundary condition (PPP). These supercells were relaxed in NPT ensemble with temperature of 300 K and pressure of 0 atm in all three directions for 50 ps.

Three different orientations were chosen as follows: (a) AFt supercell on top of C-S-H (I) supercell in z-direction, (b) AFt supercell on the side of C-S-H (I) supercell in y-direction, and (c) counterclockwise rotated AFt supercell around x-axis on the side of C-S-H (I) supercell in y-direction. Additionally, 1 Å vacuum, 3.1 Å water and 6.2 Å water spacing were placed between supercells. Relaxed supercells were put together with these different spacing in-between. C-S-H (I)/AFt composite was relaxed once again with NPT ensemble for another 50 ps. These supercells were counterclockwise rotated around x-axis in yz-plane. Bottom of these supercells were placed to the side of C-S-H (I) supercell. Timestep of these simulations was 0.25 fs. Final strain is comprised in between 25% to 20%.

For all simulations, either 24 or 48 visualization cores were used. The computer specifications were: supercomputer called “Liger”, 12-core Intel Xeon (Haswell) E5-2680v3 processors with 252 compute nodes (24 cores per node) and 14 visualization nodes (28 GPUs and 24 cores per node) and 36 608 GB compute memory.

3.5.2 Results and Discussion

The mechanical properties of C-S-H (I)/AFt composite have been obtained after calculating the stress-strain curves with different orientations and configurations of spacing.

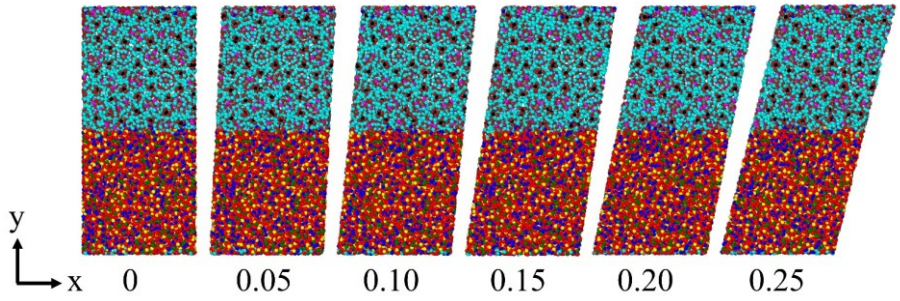

Figure 3.14 Shear test in xy-plane of C-S-H (I)/vacuum (1 Å)/AFt composite in y-direction.

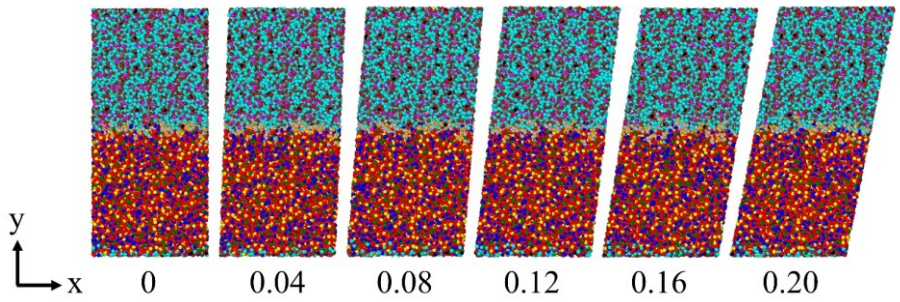

Figure 3.15 Shear test in xy-plane of C-S-H (I)/H_2O (3.1 Å)/AFt composite counterclockwise rotated in y-direction.

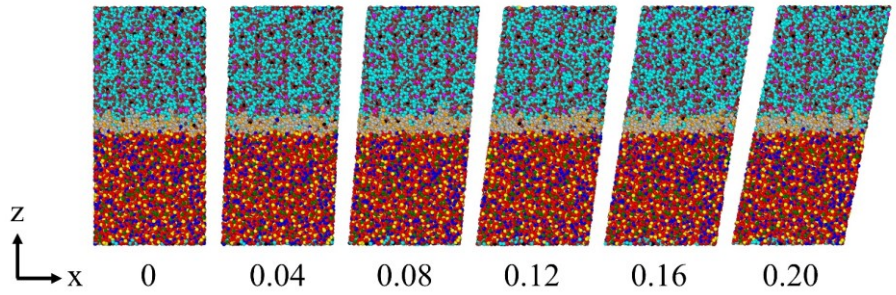

Figure 3.16 Shear test in xz-plane of C-S-H (I)/H_2O (6.2 Å)/AFt composite in z-direction.

Figure 2.32 - Figure 2.34 illustrate the direct tensile evolution of C-S-H (I)/AFt composite after relaxation to 25% and 20% strain with different orientations and configurations of spacing. All simulations were run with strain rate of 10^{-6} fs^{-1}. Stress-strain curves of C-S-H (I)/AFt composite with different orientations and configurations of spacing can be observed in **Figure 3.17**. The behaviour seems to be quite similar among different orientations except in the case of 1 Å vacuum spacing in y-direction. It appears that the bigger the spacing, the bigger the oscillation can be observed. Results indicate that orientations of two supercells and configurations of different spacing affected the stress-strain curves of C-S-H (I)/AFt composite

cube shape supercells. As can be seen, 1 Å vacuum spacing gave the highest peak stress and peak strain. In contrast, 6.2 Å water spacing gave the lowest peak stress and peak strain. Results of peak stress, peak strain, running time and file size are summarized in **Table 2.8**.

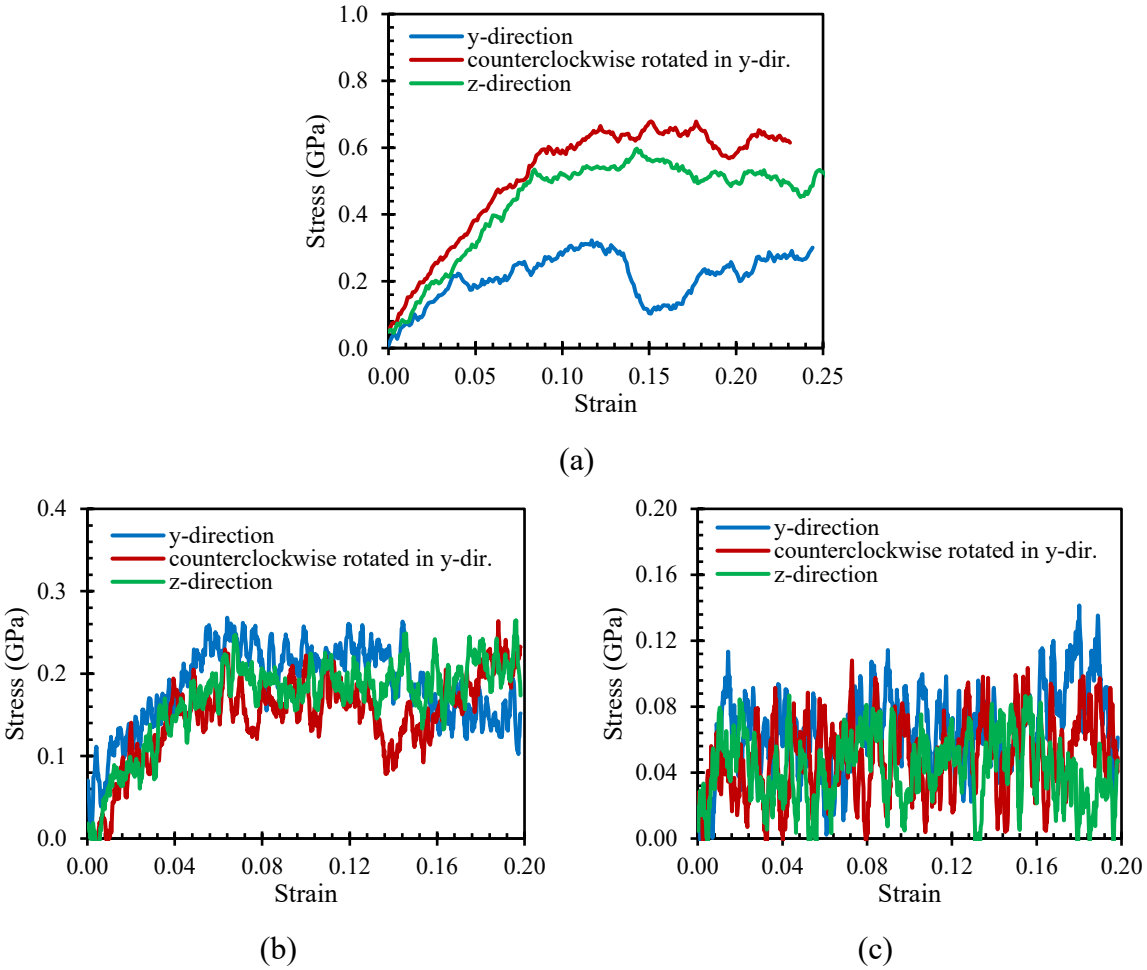

Figure 3.17 Stress-strain curves of shear tests with three orientations of C-S-H (I)/AFt composite: (a) 1 Å vacuum spacing, (b) 3.1 Å water spacing and (c) 6.2 Å water spacing.

Table 3.6 Peak strain, peak stress, running time and file size of C-S-H (I)/AFt composite.

Orientation	Spacing	Peak strain	Peak stress (GPa)	Running time (hr:min)	File size (MB)
y-direction	1 Å vacuum	0.12	0.32	72:00	198
	3.1 Å water	0.06	0.27	58:02	463
	6.2 Å water	0.18	0.14	60:03	487
Counterclockwise rotated in y-direction	1 Å vacuum	0.18	0.68	72:00	198
	3.1 Å water	0.19	0.26	59:30	481
	6.2 Å water	0.07	0.11	62:14	513
z-direction	1 Å vacuum	0.14	0.60	72:00	268
	3.1 Å water	0.20	0.27	54:25	549
	6.2 Å water	0.04	0.09	55:18	531

Figure 2.36 illustrates shear modulus of different orientation and configurations of spacing deduced from the stress-strain curves. The values of shear modulus are quite similar between different orientations. The average shear modulus of three different orientations is summarized in **Table 2.9**. In the case of 1 Å vacuum spacing, shear modulus was found to be 5.5 GPa. When 3.1 Å and 6.2 Å water spacing were placed in between the supercells, shear modulus decreased to 3.6 GPa and 5.8 GPa, respectively. To the authors' knowledge, shear test with C-S-H (I)/AFt composite modelled with MD simulation was never done before. For the first time, shear modulus of C-S-H (I)/AFt composite has been calculated. As a result, no literature value has been found for a sake of comparison.

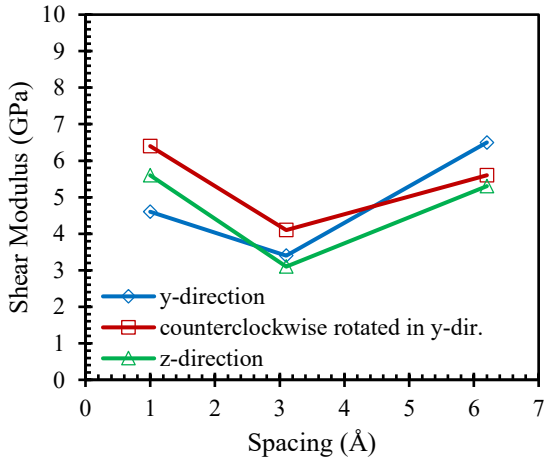

Figure 3.18 Curves of shear modulus and spacing between supercells with three orientations of C-S-H (I)/AFt composite.

Table 3.7 Mean shear modulus of three orientations of C-S-H (I)/AFt composite.

Composite	Shape	Spacing	G (GPa)
C-S-H (I)/AFt	Cube	1 Å vacuum	5.5
		3.1 Å water	3.6
		6.2 Å water	5.8

3.6 Shear test of AFt/CH composite

3.6.1 Method

Adapted from **Section 2.2**, unit cells of AFt and CH were replicated in x-, y-, and z-directions. AFt and CH unit cells were replicated 4 × 5 × 2 and 13 × 16 × 9 in x-, y- and z-directions. These supercells were changed from trigonal supercells to orthogonal supercells in order to acquire the independent results to each direction. All MD simulations were done with

ReaxFF force field in real units, three dimensions (3D) and periodic boundary condition (PPP). These supercells were relaxed in the NPT ensemble with temperature of 300 K and pressure of 0 atm in all three directions for 50 ps.

Three different orientations were chosen as follows: (a) CH supercell on top of AFt supercell in z-direction, (b) CH supercell on the side of AFt supercell in y-direction, and (c) counterclockwise rotated CH supercell around x-axis on the side of AFt supercell in y-direction. Additionally, 1 Å vacuum, 3.1 Å water and 6.2 Å water spacing were placed between supercells in our study. Relaxed supercells were put together with these different spacing in-between. AFt/CH composite was relaxed once again with NPT ensemble for another 50 ps. These supercells were counterclockwise rotated around x-axis in yz-plane. Bottom of these supercells were placed to the side of AFt supercell. Timestep of these simulations was 0.25 fs. Shear deformations were applied in either xy- or xz-planes coupled with relaxation in other directions. Final strain is comprised in between 25% to 20%.

For the simulations of AFt/CH composite cuboid shape supercells, 48 visualization cores were used. The computer specifications were as follows: supercomputer called “Liger”, 12-core Intel Xeon (Haswell) E5-2680v3 processors with 252 compute nodes (24 cores per node) and 14 visualization nodes (28 GPUs and 24 cores per node) and 36 608 GB compute memory.

For the simulations of AFt/CH composite cube shape supercells, we used 48 visualization cores. Here are the computer specifications that were used to run all simulations: supercomputer called “Liger”, 12-core Intel Xeon (Haswell) E5-2680v3 processors with 252 compute nodes (24 cores per node) and 14 visualization nodes (28 GPUs and 24 cores per node) and 36 608 GB compute memory.

3.6.2 Results and Discussion

Using the method described above, we obtained stress-strain curves with different orientations and configurations of spacing. Results are divided into two parts as follows: AFt/CH composite cuboid shape supercells and AFt/CH composite cube shape supercells.

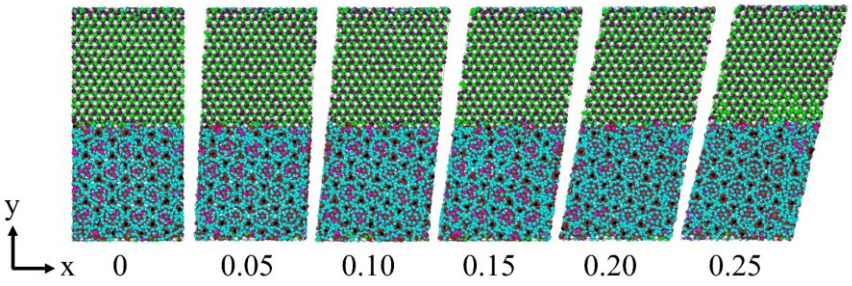

Figure 3.19 Shear test in xy-plane of AFt/vacuum (1 Å)/CH composite in y-direction.

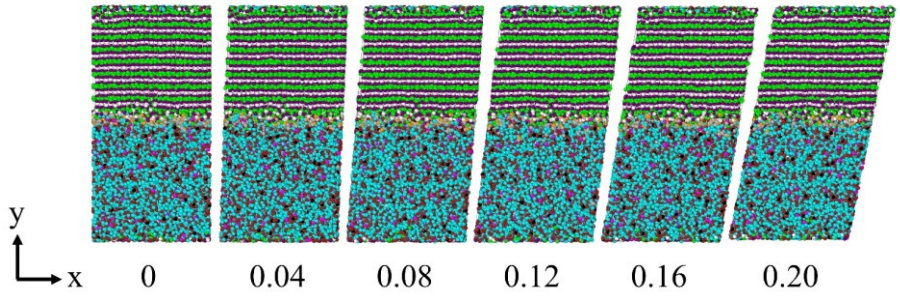

Figure 3.20 Shear test in xy-plane of AFt/H_2O (3.1 Å)/CH composite counterclockwise rotated in y-direction.

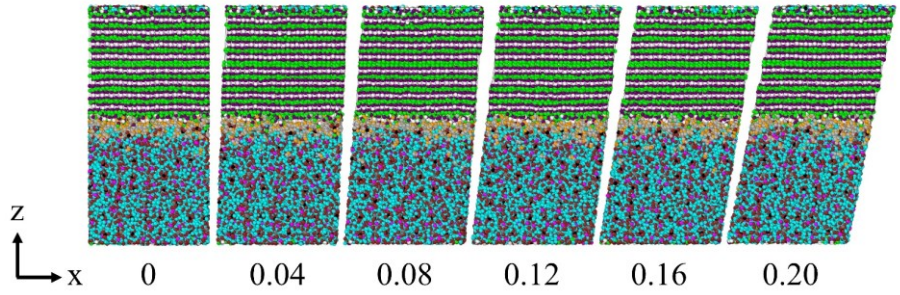

Figure 3.21 Shear test in xz-plane of AFt/H_2O (6.2 Å)/CH composite in z-direction.

Figure 2.43 - Figure 2.45 illustrate the direct tensile evolution of AFt/CH composite after relaxation to 25% and 20% strain with different orientations and configurations of spacing. All simulations were run with strain rate of 10^{-6} fs^{-1}. Stress-strain curves of AFt/CH composite with different orientations and configurations of spacing can be observed in **Figure 2.46**. In the case of 1 Å vacuum spacing, orientation in z-direction gives the peak stress and peak strain. The behaviour seems to be quite different in the case of 3.1 Å and 6.2 Å water spacing. It appears that the bigger the spacing, the bigger the oscillation can be observed. Results indicate that orientations of two supercells and configurations of different spacing affected the stress-strain curves of AFt/CH composite. As can be seen, 1 Å vacuum spacing gave the highest peak stress and peak strain. In contrast, 6.2 Å water spacing gave the lowest peak stress and peak strain. Results of peak stress, peak strain, running time and file size are summarized in **Table 2.11**.

3 Shear test of hydrated cement paste phases

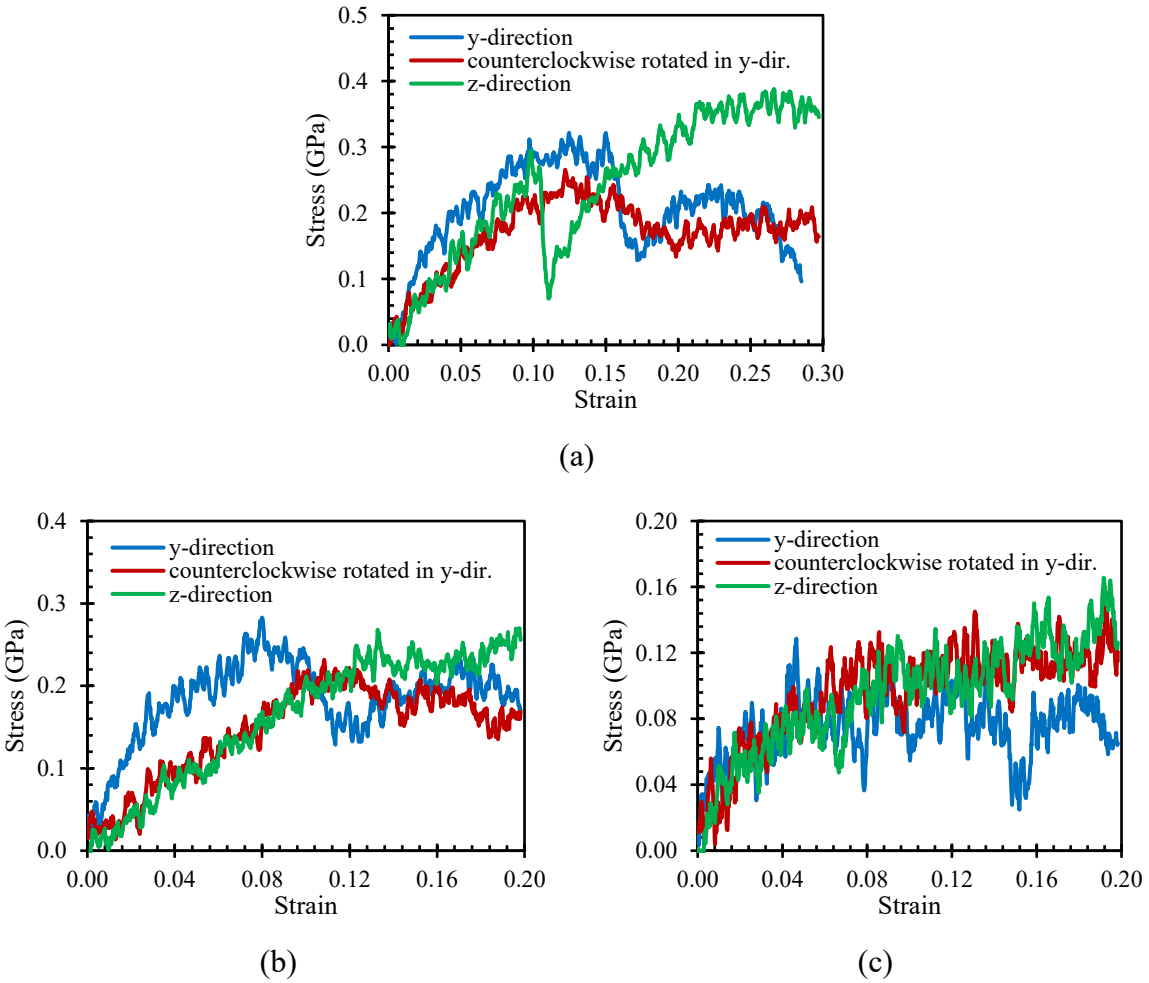

Figure 3.22 Stress-strain curves of shear tests with three orientations of AFt/CH composite: (a) 1 Å vacuum spacing, (b) 3.1 Å water spacing and (c) 6.2 Å water spacing.

Table 3.8 Peak strain, peak stress, running time and file size of AFt/CH composite.

Orientation	Spacing	Peak strain	Peak stress (GPa)	Running time (hr:min)	File size (MB)
y-direction	1 Å vacuum	0.13	0.32	51:06	330
	3.1 Å water	0.08	0.28	50:24	330
	6.2 Å water	0.05	0.13	35:20	354
Counterclockwise rotated in y-direction	1 Å vacuum	0.12	0.27	49:39	330
	3.1 Å water	0.11	0.23	33:47	344
	6.2 Å water	0.19	0.15	34:33	355
z-direction	1 Å vacuum	0.27	0.39	51:06	330
	3.1 Å water	0.20	0.27	50:24	330
	6.2 Å water	0.19	0.17	35:30	358

Figure 2.36 illustrates shear modulus of different orientation and configurations of spacing obtained from the stress-strain curves. The orientation in y-direction gives higher values of shear modulus compared to other orientations. The average shear modulus of three different orientations is summarized in **Table 2.9**. In the case of 1 Å vacuum spacing, shear modulus was found to be 3.4 GPa. When 3.1 Å and 6.2 Å water spacing was placed in between the supercells, shear modulus decrease to 2.8 GPa and 2.5 GPa, respectively. To the authors' knowledge, shear test with AFt/CH composite modelled with MD simulation was never done before. For the first time, shear modulus of AFt/CH composite has been calculated. As a result, no literature value has been found for a sake of comparison.

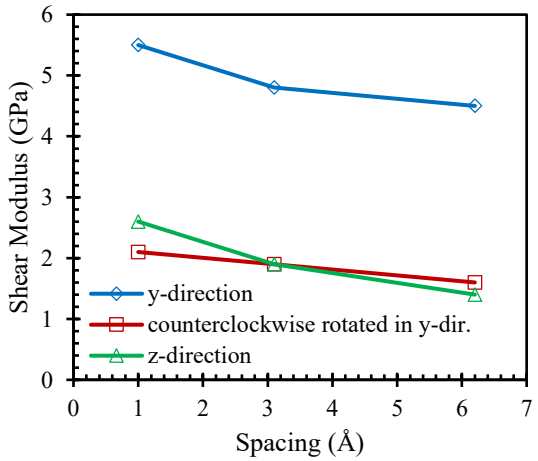

Figure 3.23 Curves of shear modulus and spacing between supercells with three orientations of AFt/CH composite.

Table 3.9 Mean shear modulus of three orientations of AFt/CH composite.

Composite	Shape	Spacing	G (GPa)
AFt/CH	Cube	1 Å vacuum	3.4
		3.1 Å water	2.8
		6.2 Å water	2.5

3.7 In summary

In this chapter, shear properties of different main hydrated cement paste phases (i.e., CH supercell, AFt supercell, C-S-H (I)/C-S-H (I) composite, C-S-H (I)/CH composite, C-S-H (I)/AFt composite and AFt/CH composite) were explored. By means of reactive molecular dynamics simulations, adhesion between these phases was taken into account with ReaxFF force field. Different cases of shear test were performed consisting of three different orientations and three different configurations of spacing with strain rate of 10^{-6} fs^{-1}. Results

indicate that stress-strain curves were affected by both orientations and configurations of spacing. More or less oscillation and bigger or smaller peak stress can be observed for different cases. These results can be utilized in the upper-scale simulation in **Chapter 5**. In the next chapter, we present another method to obtain Young's modulus and Poisson's ratio of the main hydrated cement paste composites using Voigt-Reuss-Hill (VRH) approximation.

4 Elastic constants of hydrated cement paste

Chapter 4 is partly adapted from our article published in Materials Today Communications. S. Hoeun, F. Bernard, F. Grondin, S. Kamali-Bernard, S.Y. Alam, Elastic constants of nano-scale hydrated cement paste composites using reactive molecular dynamics simulations to homogenization of hardened cement paste mechanical properties, Materials Today Communications. (2023) 106671. https://doi.org/10.1016/j.mtcomm.2023.106671.

4.1 Background

This chapter describes the methodology to calculate the mechanical properties of the composite phases between different main hydrated cement paste phases (i.e., C-S-H (I), CH and AFt) using MD simulations. Three main hydrated cement paste composites are modelled as follows: (a) C-S-H (I)/C-S-H (I) composite, (b) C-S-H (I)/CH composite and (c) C-S-H (I)/AFt composite. Results are divided into two cases: (1) cuboid shape and (2) cube shape supercells composites. Three different orientations and configurations of spacing were explored. Calculation of elastic constants are deduced from stress-strain curves obtained from deformation in six different directions. Then, Young's modulus and Poisson's ratio were calculated via Voigt-Reuss-Hill (VRH) approximation. Content of this chapter were arranged as follows: (4.2) material and method, (4.3) presentation of the numerical test, (4.4) results of composites composed of cuboid shape supercells, (4.4) results of composites composed of cube shape supercells and (4.6) in summary.

4.2 Materials and method

4.2.1 Representation of the hydrated cement microstructure

CH has a trigonal space group ($P\bar{3}m1$) with cell lengths of a = b = 3.589 Å and c = 4.911 Å at room temperature. It has cell angles (α, β, γ) = (90^0, 90^0, 120^0) and chemical formula: $Ca(OH)_2$. The CH unit cell was modelled following Desgranges et al. [42] as shown in **Figure 4.1a**, where white balls are Ca atoms, lime balls are H atoms, and purple balls are O atoms.

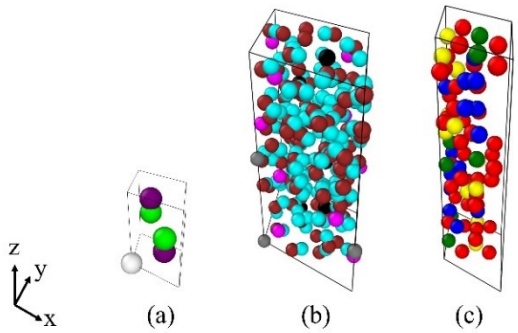

Figure 4.1 Unit cells of (a) calcium hydroxide, (b) ettringite and (c) tobermorite 11 Å in perspective view.

The ettringite (AFt) has a trigonal space group (P31c) with the chemical formula: $Ca_6[Al_2(SO_4)_3(OH)_{12}]\cdot 26H_2O$. AFt unit cell at 23 ºC was modelled following Goetz-Neunhoeffer and Neubauer [43] with cell angles $\alpha = 90^0$, $\beta = 90^0$, $\gamma = 120^0$, cell lengths (a, b, c) = (11.229 Å, 11.229 Å , 21.478 Å) and chemical formula: $Ca_6[Al_2(SO_4)_3(OH)_{12}]\cdot 26H_2O$ as shown in **Figure 4.1b**, where grey balls are Al atoms, magenta balls are Ca atoms, cyan balls are Ha toms, brown balls are O atoms, and black balls are S atoms.

One possible ordered of the structures of 11 Å natural tobermorite [44] is a monoclinic crystal system $P2_1$ with cell lengths (a, b, c) = (6.69 Å, 7.39 Å, 22.779 Å), cell angle $\gamma = 123.49^0$ and chemical formula: $(Ca_4Si_6O_{14}(OH)_4\cdot 2H_2O)$ as shown in **Figure 4.1c**, where green balls are Ca atoms, yellow balls are Si atoms, red balls are O atoms, and blue balls are H atoms. Fu [23] developed C-S-H cell, which long range is distorted, initially from tobermorite 11 Å and acquired the first amorphous tobermorite. We get the annealed amorphous structure, which is C-S-H (I) with calcium-to-silica (Ca/Si) ratio of 0.67, following his methodology.

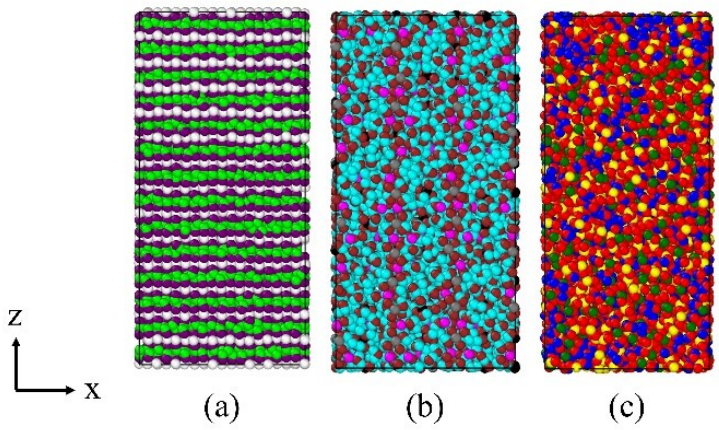

Figure 4.2 Supercells of calcium hydroxide, ettringite and C-S-H (I) after relaxation with NPT ensemble in xz plane: (a) supercell of 9×10×14 CH, (b) supercell of 3×3×3 AFt, and (c) supercell of 5×5×3 C-S-H (I).

In the case of composites composed of cuboid shape supercells, CH was replicated 9 times in x-direction, 10 times in y-direction, and 14 times in z-direction to get a larger cell (i.e., supercell CH) as shown in **Figure 4.2**. Ettringite and C-S-H (I) were likewise replicated 3×3×3 and 5×5×3 times in x-, y-, and z-directions, respectively. The replicated cells are called supercell AFt and C-S-H (I). These sizes of supercells were obtained for the sake of having similar lengths in all three dimensions. AFt was chosen as a reference because of its biggest size of unit cell among all three phases. In this way, it facilitated the replication of other phases. All colours of balls, which represent different types of atoms, remain the same in this chapter.

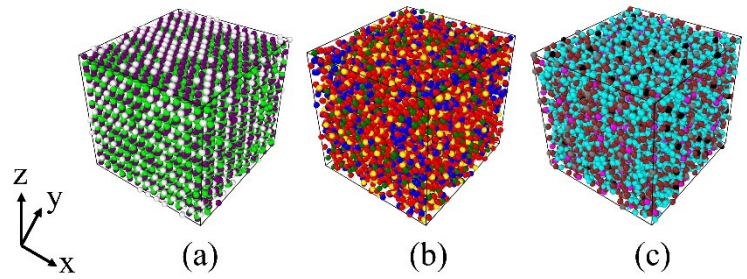

Figure 4.3 Calcium hydroxide, C-S-H (I) and ettringite supercells after relaxation with NPT ensemble in xz plane: (a) supercell of 13×16×9 CH, (b) supercell of 7×8×2 C-S-H (I), and (c) supercell of 4×5×2 AFt.

In the case of composites composed of cube shape supercells, the methodology was the same as that in the case of composites composed of cuboid shape supercells. The difference is the size of supercells, which made different shapes (i.e., cubic and cuboid). This difference was studied for investigating the effect of shape on the obtained results. In order to get CH supercell, the replication of CH unit cell was firstly done 13, 16 and 9 times in x-, y- and z-directions, respectively. Similar to CH, C-S-H (I) and AFt were replicated to have C-S-H (I) and AFt supercells with the sizes of 7×8×2 and 4×5×2 in x-, y- and z-directions, respectively as can be seen in **Figure 4.3**.

4.2.2 Molecular Dynamics and LAMMPS

A method for calculating equilibrium and transport characteristics of a classical many-body system is called molecular dynamics simulations. The term "classical" in this regard refers to the fact that nuclear motion of constituent particles complies with laws of classical mechanics. For many different types of materials, this is a great approximation [45]. MD simulations and actual experiments are remarkably similar in many ways. In experimental tests, one carries out the following steps. A sample of the content ones intends to investigate is prepared. One attaches this sample to a measuring device (such as a manometer, thermometer, or viscometer),

and then one measures the desired property for a predetermined period. Similar strategy was employed in MD simulations [45].

Large-scale Atomic/Molecular Massively Parallel Simulator is known by the acronym LAMMPS. Since the release of open source code of classical molecular dynamics simulator LAMMPS in 2004, it has gained popularity as a tool for particle-based modelling of materials at length scales varying from continuum to mesoscale to atomic. There are several reasons for its popularity. Firstly, it provides a wide range of particle interaction models for various materials. Secondly, it is the fact that it runs on all platforms from single CPU cores to the largest supercomputers with accelerators. Lastly, it gives users control over simulation details through the input script or by adding code for new interatomic potentials, constraints, diagnostics, or other features required for their models [46].

4.2.3 Force field

Force field is quite important in MD simulations and there are multiple force fields such as: Clay Force Field (ClayFF) [47] which is a Classical MD and Reactive Force Field (ReaxFF) [48] which is a Reactive MD. For ClayFF, it is compatible with CH and C-S-H, whereas ReaxFF could be used with CH, C-S-H and sulfoaluminate (AFm or AFt). In order to run ClayFF in LAMMPS, bonds between atoms are created at the beginning of the simulation. For ReaxFF, it is not required to create bonds between atoms at the start of simulation. Hence, it fits to model the composite between main cement paste phases, in particular the interaction at the interface. However, ReaxFF is time consuming compared to ClayFF.

In order to create a practical MD simulation of large scale reactive chemical systems, Van Duin et al. [48] developed ReaxFF for Hydrocarbons, which is a force field for reactive systems. ReaxFF utilized a general relationship between bond distance and bond order. Furthermore, it employed a general relationship between bond energy and bond order that led to proper dissociation of bonds in order to separate atoms. Other valence terms that presented in force field (angle and torsion) were defined in terms of same bond orders. Consequently, all these terms moved smoothly to zero as the bond break. In addition, Morse (van der Waals) and Coulomb potentials were also composed in ReaxFF in order to describe non-bonded interactions between all atoms.

The classical force fields were unable to characterize the chemical reactions that will be triggered by large deformations. Via Reactive Molecular Dynamics simulations using ReaxFF, this matter has been taken into account in the study of Hajilar and Shafei [49]. The classical MD harmonic bonds were replaced by bond orders and energies upon the interatomic distances.

While the bonded interactions were allowed to decay smoothly to zero, it could capture the bond breakage and formation with this approach. Such an approach has already been used in [50] for other cement nanocomposites and presented thus many advantages compared to the Classical Molecular Dynamics simulations for which constructions of model were more difficult [31,51].

For all atoms in system using a screened taper function, the van der Waals and non-bonded Columbic interactions were obtained. The charged equilibrium (Q_{Eq}) method set the atomic charges and was required to be updated at each time step. ReaxFF parameters could be found in Liu et al. [52]. ReaxFF separated the system energy up to different partial energy contributions as shown in **Eq. (1.5)** comparable to the empirical non-reactive force fields [48].

$$E_{system} = E_{bond} + E_{over} + E_{under} + E_{val} + E_{pen} + E_{tors} + E_{conj} + E_{vdWaals} + E_{Coulomb} \quad (4.1)$$

where E_{bond} is bond energy, E_{over} and E_{under} are energy penalty for over- and under-coordination of atoms, E_{val}, E_{pen}, E_{tors}, E_{conj}, $E_{vdWaals}$ and $E_{Coulomb}$ are valence angle, penalty, torsion, conjugation, Van der Waals and Coulomb energy, respectively.

4.3 Presentation of the numerical test

Several points will be discussed in this section. Those are elastic constants calculation via MD simulations and Young's modulus (E) and Poisson's ratio (ν) obtained from VRH approximation.

4.3.1 Model construction

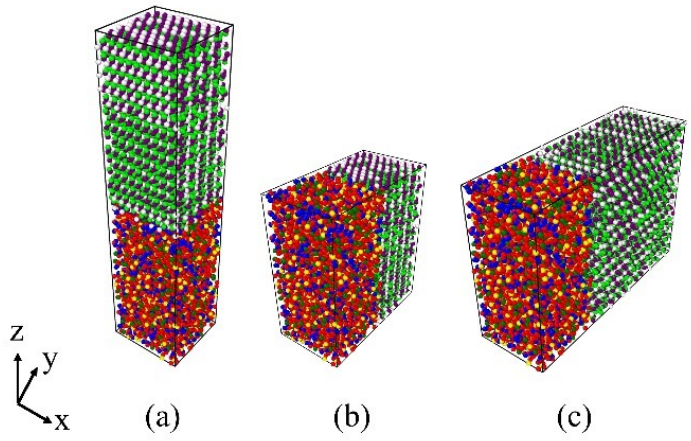

Figure 4.4 Orientation of C-S-H (I)/CH composite: (a) in z-direction, (b) in y-direction, and (c) counterclockwise rotated in y-direction (Cuboid shape supercells).

4 Elastic constants of hydrated cement paste

In the work of Liang [27], the unit cells of C-S-H and CH were replicated in order to get the believable results. Then the supercells were relaxed individually with NPT ensemble at 300 K and 0 Pa at x-, y- and z-directions. The relaxed supercells were placed together with the gaps of about 3 Å at the interface and relaxed again with NPT ensemble. These procedures are similar. Firstly, unit cells were replicated in x-, y- and z-directions, respectively. The simulation was modelled in 3D in LAMMPS with periodic boundary condition (PPP). Then they were changed to orthogonal cells to get independent results to each direction since unit cells of CH and AFt have trigonal space groups, and unit cell of C-S-H (I) has a monoclinic space group. The supercells were applied under energy minimization and relaxation with NPT ensemble for 50 ps with pressure of 0 atm and temperature of 300 K in x-, y- and z-directions. Finally, composite of different phases were constructed by placing supercell together following the same steps. It means that the composite was applied again under energy minimization and relaxation with NPT ensemble for 50 ps with the pressure of 0 atm and temperature of 300 K in x-, y- and z-directions.

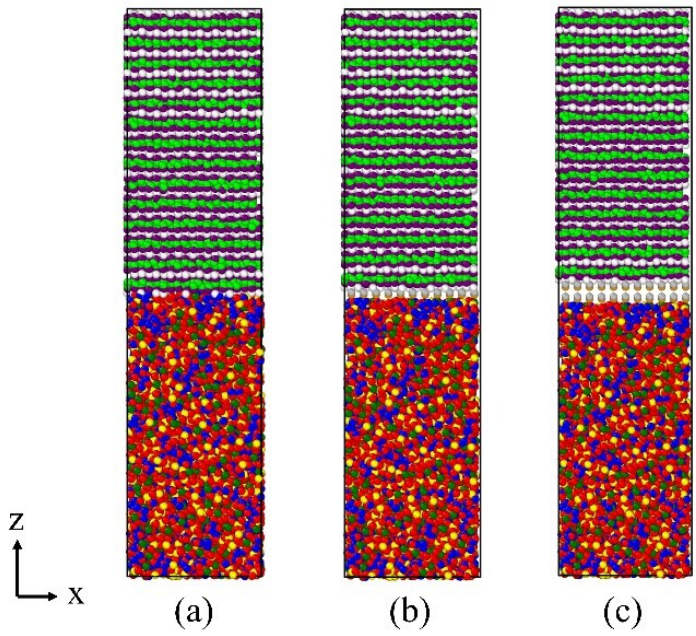

Figure 4.5 Configurations of C-S-H (I)/CH composite: (a) 1 Å vacuum spacing, (b) 3.1 Å water spacing, and (c) 6.2 Å water spacing in z-direction (Cuboid shape supercells).

Three orientations were decided due to the fact that Bonnaud et al. [26] studied three various orientation configurations of C-S-H particle pairs employed to investigate the interaction grand potential at the molecular level. They chose these orientations to take into account the effects of: (a) anisotropic in crystallography and geometry of C-S-H particles, and (b) different interaction forces among particles related to orientation. In addition, they moved the other

particle to compute the interaction grand potentials at different interparticle distance. They found different interparticle distances related to the minimum interaction grand potential minima. Subsequently, vacuum and different water spacing were imposed between supercells in our study. Zhu et al. [40] studied the hydrated surface properties of C-S-H via MD simulations and ReaxFF force field. They used SPC/E water model in their simulation. As a result, SPC/E water model was employed to model the 3.1 Å and 6.2 Å water spacing in this study. We have done three distinct orientations for composites: (a) supercell CH on top of supercell C-S-H (I) in z-direction, (b) supercell CH on the side of supercell C-S-H (I) in y-direction, and (c) counterclockwise rotated supercell CH around x-axis on the side of supercell C-S-H (I) in y-direction as shown in **Figure 2.2**. It should be noticed that in order to have a similar dimension in z-direction for the counterclockwise rotated case, the supercells of C-S-H (I), CH and AFt were replicated to 5 × 11 × 3, 9×22×14 and 3×7×3 in x-, y-, and z-directions, respectively. This procedure was only done for composites composed of cuboid shape supercells. Then, these supercells were counterclockwise rotated around x-axis in yz plane where bottom of these supercells were placed to the side of C-S-H (I) supercell. As could be seen in **Figure 4.5**, there are three different configurations: (a) 1 Å vacuum spacing was placed between supercell C-S-H (I) and CH, (b) 3.1 Å water spacing was placed between supercell C-S-H (I) and CH, and (c) 6.2 Å water spacing was placed between supercell C-S-H (I) and CH. In water layer between two supercells, silver balls are H atoms, and orange balls are O atoms.

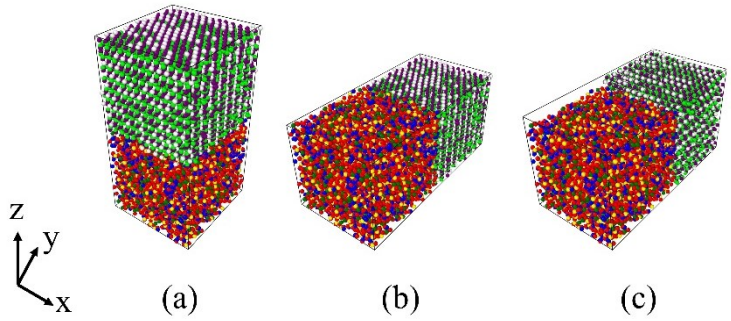

Figure 4.6 Orientation of C-S-H (I)/CH composite: (a) in z-direction, (b) in y-direction, and (c) counterclockwise rotated in y-direction (Cube shape supercells).

In the case of composites composed of cube shape supercells, the methodology was the same as that in the case of composites composed of cuboid shape supercells. There were three orientations and configurations as shown respectively in **Figure 4.6** and **Figure 4.7**. The difference was the third orientation. Unlike in the case of composites composed of cuboid shape supercells, it did not require to change the size of the counterclockwise rotated supercells in y-direction. Lengths in all directions were already similarly the same because of the cubic shape.

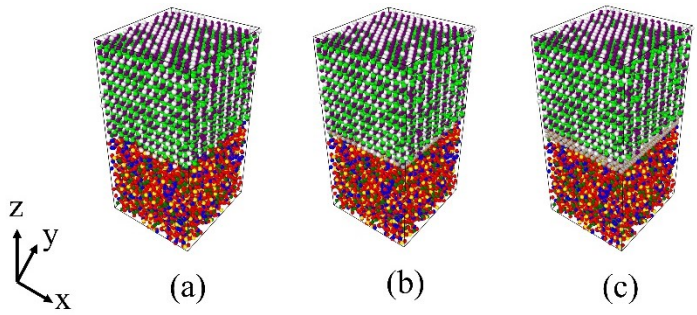

Figure 4.7 Configurations of C-S-H (I)/CH composite: (a) 1 Å vacuum spacing, (b) 3.1 Å water spacing, and (c) 6.2 Å water spacing in z-direction (Cube shape supercells).

4.3.2 Elastic constants calculation and VRH approximation

At nanoscale, element cells are anisotropic. Their elastic constitutive behaviour is governed by their elastic stiffness matrix. The components of the $[D^{el}]$ in **Eq. (4.2)** matrix are called "elastic constants". The total numbers of independent elastic components depend on crystal structure.

$$\begin{pmatrix}\sigma_{11}\\ \sigma_{22}\\ \sigma_{33}\\ \sigma_{23}\\ \sigma_{13}\\ \sigma_{12}\end{pmatrix} = [D^{el}] \begin{pmatrix}\varepsilon_{11}\\ \varepsilon_{22}\\ \varepsilon_{33}\\ \varepsilon_{23}\\ \varepsilon_{13}\\ \varepsilon_{12}\end{pmatrix} \tag{4.2}$$

In the work of Claverie et al. [8], they chose two methods to find elastic properties of solids:

(1) For time integration methods, Equilibrium Molecular Dynamics (EMD) or Non-Equilibrium Molecular Dynamics (NEMD) simulations are used to compute the deformation of the simulation box while controlling the stress or vice versa.

(2) For static optimization methods, a small strain ($\Delta\varepsilon_j$) is applied negatively and positively in each direction (j) while it is generally applied at 0 K:

$$C_{ij}^{+} = -\frac{\sigma_i(\Delta\varepsilon_j) - \sigma_i(0)}{\Delta\varepsilon_j}$$
$$C_{ij}^{-} = \frac{\sigma_i(\Delta\varepsilon_j) - \sigma_i(0)}{\Delta\varepsilon_j} \tag{4.3}$$

Eftekhari and Mohammadi [53] investigated on the numerical study of enhanced mechanical properties of C-S-H reinforced using the embedded carbon nanotube (CNT) in its molecular structure. The uniaxial and shear deformations were introduced in six independent directions

(axial x, y, z and shear xy, xz, yz) of the simulation box with a constant velocity of 1 Å/ps in an NVT ensemble after the system was in the equilibrium state. From applied strain, pressure of the system was obtained. Accordingly, the corresponding stress-strain response was acquired once the full application of deformation is reached. Then, they calculated the elastic constants of the models from the initial linear part of the obtained stress-strain curves.

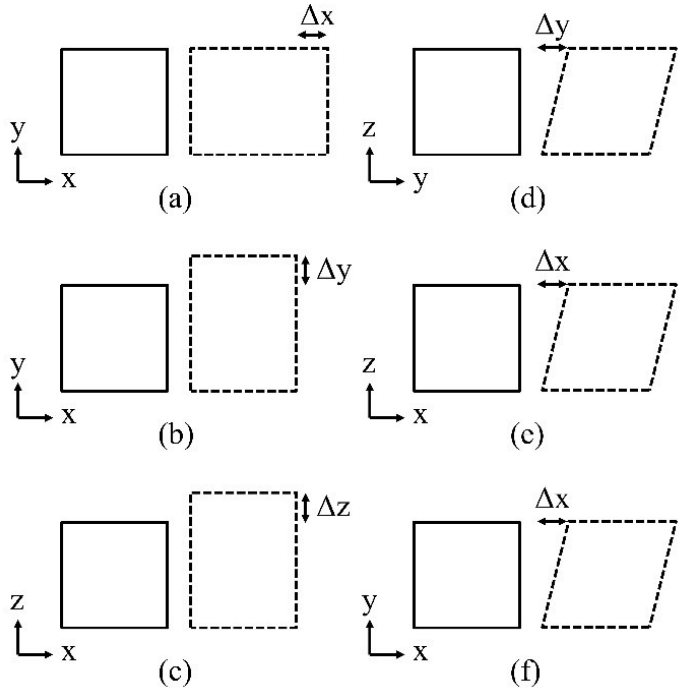

Figure 4.8 Six deformation directions: (a) tensile in x-direction, (b) tensile in y-direction, (c) tensile in z-direction, (d) shear in yz-direction, (e) shear in xz-direction, and (f) shear in xy-direction.

In our study, deformations on six different directions were performed once at a time as shown in **Figure 4.8** while relaxing with NPT (temperature of 300 K and pressure of 0 atm) in directions whose values of elastic constants equalled to zero. For example, in the space group of trigonal, C_{51} and C_{61} are equalled to zero. Thus, we relaxed with NPT ensemble in xz- and xy-directions. **Figure 4.9** shows deformation in z-direction with the C-S-H (I)/H_2O (6.2 Å)/AFt composite. However, it just shows how deformation was applied. To calculate the elastic constants, it only requires a small deformation. A strain of 1%, at this scale, seems to be a good compromise between an accurate determination of the slope in the stress-strain curve and an acceptable calculation time. We used strain rate of 10^{-6} fs^{-1} or 10^{-5} fs^{-1} for all simulations in this study. The study of sensitivity on the strain rate was carried out with direct tension test simulations. This study made us retain the strain rate of 10^{-6} fs^{-1} and 10^{-5} fs^{-1} for the calculation of elastic constants. This choice was made on the one hand by determining the velocity from which the results in term of stress-strain curve no longer evolved, and on the other hand by checking the stability conditions for VRH approximation. The results of elastic constants were

likewise obtained from the initial linear part of the obtained stress-strain curves by $C_{ij} = \delta\sigma_i/\delta\varepsilon_j$ $(i,j = 1,2,3,4,5,6)$ where $\sigma_1 = \sigma_{xx}, \sigma_2 = \sigma_{yy}, \sigma_3 = \sigma_{zz}, \sigma_4 = \sigma_{yz}, \sigma_5 = \sigma_{xz}$ and $\sigma_6 = \sigma_{xy}$. Finally, the elastic constants values were averaged along the symmetric matrix.

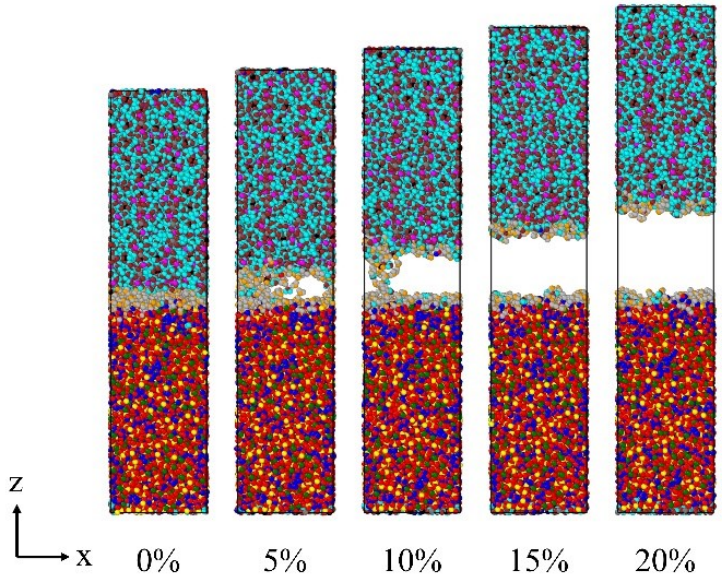

Figure 4.9 Direct tension test in z-direction in xz plane from the state after NPT relaxation to 20% strain with C-S-H (I)/H_2O (6.2 Å)/AFt composite (Cuboid shape supercells).

With elastic constants, it was possible to calculate Young's modulus (E_{VRH}) and Poisson's ratio (ν_{VRH}) via Voigt-Reuss-Hill (VRH) approximation scheme. It should be noted that calculations are not the same for different space groups.

For monoclinic space group (i.e., C-S-H (I)), calculations of shear modulus and bulk modulus of Reuss and Voigt bounds are as follows [54]:

$$G_V = \frac{1}{15}[C_{11} + C_{22} + C_{33} + 3(C_{44} + C_{55} + C_{66}) - (C_{12} + C_{13} + C_{23})] \tag{4.4}$$

$$\begin{aligned} G_R = 15\{4[&(C_{33}C_{55} - C_{35}^2)(C_{11} + C_{22} + C_{12}) + (C_{23}C_{55} \\ &- C_{25}C_{35})(C_{11} - C_{12} - C_{23}) \\ &+ (C_{13}C_{35} - C_{15}C_{33})(C_{15} + C_{25}) \\ &+ (C_{13}C_{55} - C_{15}C_{35})(C_{22} - C_{12} - C_{23} - C_{13}) \\ &+ (C_{13}C_{25} - C_{15}C_{23})(C_{15} - C_{25}) + f] / \Omega \\ &+ 3[g/\Omega + (C_{44} + C_{66})/(C_{44}C_{66} - C_{46}^2)]\}^{-1} \end{aligned} \tag{4.5}$$

$$B_V = [C_{11} + C_{22} + C_{33} + 2(C_{12} + C_{13} + C_{23})] / 9 \tag{4.6}$$

$$\begin{aligned} B_R = \Omega[&(C_{33}C_{55} - C_{35}^2)(C_{11} + C_{22} - 2C_{12}) \\ &+ (C_{23}C_{55} - C_{25}C_{35})(2C_{12} - 2C_{11} - C_{23}) \\ &+ (C_{13}C_{55} - C_{15}C_{33})(C_{15} - 2C_{25}) \\ &+ (C_{13}C_{55} - C_{15}C_{35})(2C_{12} + 2C_{23} - C_{13} - 2C_{22}) \\ &+ 2(C_{13}C_{25} - C_{15}C_{23})(C_{25} - C_{15}) + f]^{-1} \end{aligned} \tag{4.7}$$

$$\begin{aligned} f = {} & C_{11}(C_{22}C_{55} - C_{25}^2) - C_{12}(C_{12}C_{55} - C_{15}C_{25}) \\ & + C_{15}(C_{12}C_{25} - C_{15}C_{22}) + C_{25}(C_{23}C_{35} - C_{25}C_{33}) \end{aligned} \tag{4.8}$$

$$g = C_{11}C_{22}C_{33} - C_{11}C_{23}^2 - C_{22}C_{13}^2 - C_{33}C_{12}^2 + 2C_{12}C_{13}C_{23} \tag{4.9}$$

$$\begin{aligned} \Omega = 2[&C_{15}C_{25}(C_{33}C_{12} - C_{13}C_{23}) + C_{15}C_{35}(C_{22}C_{13} - C_{12}C_{23}) \\ &+ C_{25}C_{35}(C_{11}C_{23} - C_{12}C_{13})] - [\, C_{15}^2(C_{22}C_{33} - C_{23}^2) \\ &+ C_{25}^2(C_{11}C_{33} - C_{13}^2) + C_{35}^2(C_{11}C_{22} - C_{12}^2)] \; + gC_{55} \end{aligned} \tag{4.10}$$

The VRH estimation of the two moduli correspond to the arithmetic mean values:

$$B_H = (B_V + B_R) \,/\, 2 \tag{4.11}$$

$$G_H = (G_V + G_R) \,/\, 2 \tag{4.12}$$

The Young's modulus and Poisson's ratio can now be estimated:

$$E = \frac{9BG}{3B + G} \tag{4.13}$$

$$\nu = \frac{3B - 2G}{2(3B + G)} \tag{4.14}$$

There are seven mechanical stability conditions to respect for monoclinic space group [54]:

$$C_{ii} > 0, (i = 1,2,3,4,5,6) \tag{4.15}$$

$$(C_{44}C_{66} - C_{46}^2) > 0 \tag{4.16}$$

$$(C_{33}C_{55} - C_{35}^2) > 0 \tag{4.17}$$

$$(C_{22} + C_{33} - 2C_{23}) > 0 \tag{4.18}$$

$$[C_{11} + C_{22} + C_{33} + 2(C_{12} + C_{13} + C_{23})] > 0 \tag{4.19}$$

$$[C_{22}(C_{33}C_{55} - C_{35}^2) + 2C_{23}C_{25}C_{35} - C_{23}^2C_{55} - C_{25}^2C_{33}] > 0 \tag{4.20}$$

$$\begin{aligned}\{2[&C_{15}C_{25}(C_{33}C_{12} - C_{13}C_{23}) + C_{15}C_{35}(C_{22}C_{13} - C_{12}C_{23}) \\ &+ C_{25}C_{35}(C_{11}C_{23} - C_{12}C_{13})] - [C_{15}^2(C_{22}C_{33} - C_{23}^2) \\ &+ C_{25}^2(C_{11}C_{33} - C_{13}^2) + C_{35}^2(C_{11}C_{22} - C_{12}^2)] + gC_{55}\} > 0\end{aligned} \tag{4.21}$$

For trigonal space group (i.e., CH and AFt), calculations of shear and bulk moduli of Voigt and Reuss bounds are as follows [55]:

$$G_V = \frac{(C_{11} + C_{22} + C_{33}) - (C_{12} + C_{23} + C_{31}) + 3(C_{44} + C_{55} + C_{66})}{15} \tag{4.22}$$

$$G_R = \frac{15}{4(S_{11} + S_{22} + S_{33}) - 4(S_{12} + S_{23} + S_{31}) + 3(S_{44} + S_{55} + S_{66})} \tag{4.23}$$

$$B_V = \frac{C_{11} + C_{22} + C_{33} + 2(C_{12} + C_{23} + C_{31})}{9} \tag{4.24}$$

$$B_R = \frac{1}{S_{11} + S_{22} + S_{33} + 2(S_{12} + S_{23} + S_{31})} \tag{4.25}$$

$$\begin{aligned}S_{11}=&(C_{11}C_{33}C_{44} - C_{33}C_{14}^2 - C_{44}C_{13}^2)/(\ C_{33}C_{44}C_{11}^2 - 2C_{11}C_{33}C_{14}^2 - \\ &C_{33}C_{44}C_{12}^2 - 2C_{12}C_{33}C_{14}^2 - 2C_{11}C_{44}C_{13}^2 + 2C_{12}C_{44}C_{13}^2 + 4C_{13}^2C_{14}^2)\end{aligned} \tag{4.26}$$

$$\begin{aligned}S_{12} = -(&C_{12}C_{33}C_{44} + C_{33}C_{14}^2 - C_{44}C_{13}^2)/(\ C_{33}C_{44}C_{11}^2 - 2C_{11}C_{33}C_{14}^2 \\ &- C_{33}C_{44}C_{12}^2 - 2C_{12}C_{33}C_{14}^2 - 2C_{11}C_{44}C_{13}^2 + 2C_{12}C_{44}C_{13}^2 \\ &+ 4C_{13}^2C_{14}^2)\end{aligned} \tag{4.27}$$

$$S_{13} = -\frac{C_{13}}{C_{11}C_{33} + C_{12}C_{33} - 2C_{13}^2} \tag{4.28}$$

$$S_{14} = -\frac{C_{14}}{C_{11}C_{44} - C_{12}C_{44} - 2C_{14}^2} \tag{4.29}$$

$$S_{33} = \frac{C_{11} + C_{12}}{C_{11}C_{33} + C_{12}C_{33} - 2C_{13}^2} \tag{4.30}$$

$$S_{44} = \frac{C_{11} - C_{12}}{C_{11}C_{44} - C_{12}C_{44} - 2C_{14}^2} \tag{4.31}$$

$$S_{66} = 2(S_{11} - S_{12}) \tag{4.32}$$

Results should be respected by these three following mechanical stability conditions [55]:

$$C_{11} > |C_{12}| \tag{4.33}$$

$$(C_{11} + C_{12})C_{33} - 2C_{13}^2 > 0 \tag{4.34}$$

$$(C_{11} - C_{12})C_{44} - 2C_{14}^2 > 0 \tag{4.35}$$

4.4 Results of composites composed of cuboid shape supercells

4.4.1 Elastic constant, Young's modulus, and Poisson's ratio

4.4.1.1 Calcium-silicate-hydrates

Table 4.1 Elastic constants (in GPa) of C-S-H (I)/C-S-H (I) in y-direction.

Spacing	1Å vacuum	3.1 Å water	6.2 Å water
C_{11}	71.9	59.9	68.4
C_{22}	82.9	55.6	45.8
C_{33}	76.3	62.1	67.9
C_{44}	20.9	14.0	11.8
C_{55}	19.2	17.6	18.8
C_{66}	20.8	11.4	7.6
C_{12}	36.3	28.3	15.3
C_{13}	32.4	28.9	31.7
C_{15}	4.5	1.5	4.9
C_{23}	37.4	27.8	14.7
C_{25}	-1.4	2.5	-1.7
C_{35}	-2.4	-1.1	1.9
C_{46}	1.2	-0.5	-2.5

Table 4.1 and **Table 4.2** shows elastic constants of C-S-H (I)/C-S-H (I) composite with monoclinic space group following procedure on **section 4.3.2**. Thirteen elastic constants values were calculated for orientation in y- and in z-directions. Elastic constants of counterclockwise

rotated in y-direction could be found in **Table 4.3**. Young's modulus and Poisson's ratio of this composite are shown in **Figure 4.1**.

Table 4.2 Elastic constants (in GPa) of C-S-H (I)/C-S-H (I) in z-direction.

Spacing	1 Å vacuum	3.1 Å water	6.2 Å water
C_{11}	78.6	72.1	70.9
C_{22}	83.1	80.6	71.6
C_{33}	70.9	65.6	24.7
C_{44}	20.7	17.5	11.6
C_{55}	19.4	15.1	5.6
C_{66}	19.6	21.9	18.9
C_{12}	45.7	38.6	35.6
C_{13}	39.0	36.1	14.0
C_{15}	0.4	-0.01	1.9
C_{23}	40.5	36.7	16.6
C_{25}	2.4	-0.04	2.7
C_{35}	0.9	0.6	-2.3
C_{46}	-0.01	4.4	-0.4

Table 4.3 Elastic constants (in GPa) of C-S-H (I)/C-S-H (I) counterclockwise rotated in y-direction.

Spacing	1 Å vacuum	3.1 Å water	6.2 Å water
C_{11}	74.6	69.5	61.3
C_{22}	73.3	61.9	34.7
C_{33}	70.7	67.1	63.0
C_{44}	17.7	13.2	3.9
C_{55}	21.8	16.6	16.2
C_{66}	19.2	13.8	1.2
C_{12}	39.3	33.9	18.1
C_{13}	33.3	33.4	30.7
C_{15}	1.0	-1.3	3.5
C_{23}	37.6	33.6	18.1
C_{25}	-0.9	0.9	2.3
C_{35}	-2.2	0.6	1.3
C_{46}	0.4	0.5	0.3

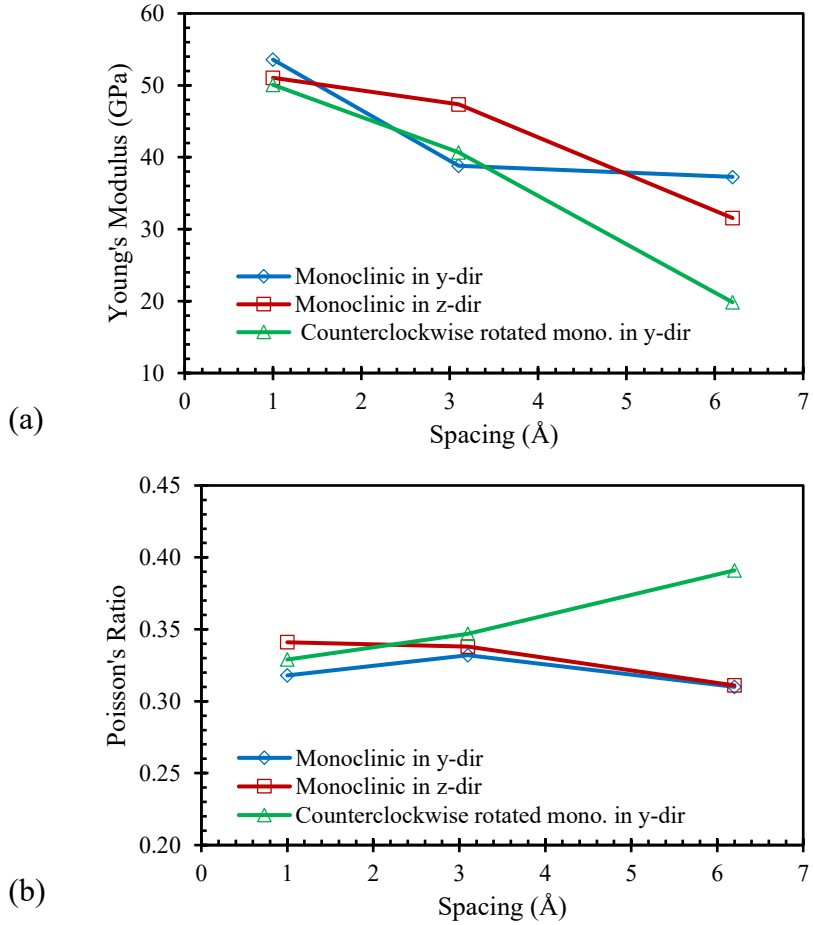

Figure 4.10 Curves of (a) Young's modulus, (b) Poisson's ratio and spacing between supercells with three different orientations of C-S-H (I)/C-S-H (I) composite.

4.4.1.2 Calcium-silicate-hydrates/portlandite

For C-S-H (I)/CH composite, calculation of elastic constants was also followed by **section 4.3.2**. However, sixteen elastic constants values were calculated as a result of combination of monoclinic and trigonal space group. **Table 4.4** and **Table 4.5** shows the results in y-, and in z-directions with different spacing of vacuum and water between C-S-H (I)/CH composite. In addition, **Table 4.6** shows results of elastic constants of C-S-H (I)/CH composite where supercell CH was counterclockwise rotated around x-axis in y-direction on the side of supercell C-S-H (I). Young's modulus and Poisson's ratio of C-S-H (I)/CH composite were calculated by both monoclinic space group and trigonal space group as shown in **Figure 4.11** because C-S-H (I) has a monoclinic space group, and CH has a trigonal space group.

Table 4.4 Elastic constants (in GPa) of C-S-H (I)/CH in y-direction.

Spacing	1 Å vacuum	3.1 Å water	6.2 Å water
C_{11}	85.5	71.4	74.4
C_{22}	76.7	69.5	57.3
C_{33}	50.9	48.0	52.6
C_{44}	9.8	9.8	5.3
C_{55}	15.3	11.9	12.6
C_{66}	21.2	18.9	7.2
C_{12}	36.9	29.6	28.3
C_{13}	28.5	26.8	26.8
C_{15}	-0.1	-0.1	0.4
C_{23}	30.9	28.4	24.7
C_{25}	2.0	1.6	4.7
C_{35}	-0.1	-0.4	3.9
C_{46}	-1.2	1.9	-2.6
C_{14}	-0.2	-0.6	-5.9
C_{24}	11.6	5.4	3.2
C_{56}	-2.3	-2.8	-2.7

Table 4.5 Elastic constants (in GPa) of C-S-H (I)/CH in z-direction.

Spacing	1 Å vacuum	3.1 Å water	6.2 Å water
C_{11}	72.7	71.5	71.8
C_{22}	72.1	74.9	63.5
C_{33}	42.5	37.5	24.9
C_{44}	7.0	7.6	4.9
C_{55}	9.5	7.8	2.3
C_{66}	19.9	18.1	15.6
C_{12}	31.8	43.1	36.3
C_{13}	22.7	24.2	18.2
C_{15}	-1.5	4.5	2.2
C_{23}	22.2	18.8	16.0
C_{25}	0.7	1.8	-3.5
C_{35}	0.2	0.6	-1.8
C_{46}	1.4	-0.3	0.1
C_{14}	-9.4	-6.9	-3.5
C_{24}	2.6	7.7	4.6
C_{56}	-6.1	-8.6	-4.4

Table 4.6 Elastic constants (in GPa) of C-S-H (I)/CH counterclockwise rotated in y-direction.

Spacing	1 Å vacuum	3.1 Å water	6.2 Å water
C_{11}	79.7	72.6	71.1
C_{22}	37.2	42.5	34.2
C_{33}	67.9	70.3	69.3
C_{44}	7.1	7.3	4.3
C_{55}	18.7	19.4	19.9
C_{66}	6.3	7.6	7.5
C_{12}	20.4	19.5	19.9
C_{13}	43.1	38.1	36.4
C_{15}	0.5	0.02	0.4
C_{23}	21.4	20.6	19.4
C_{25}	0.6	2.4	-0.1
C_{35}	-1.04	0.2	-3.1
C_{46}	0.3	-1.1	0.8
C_{14}	8.8	3.0	7.9
C_{24}	2.8	-2.7	3.5
C_{56}	6.5	2.9	5.7

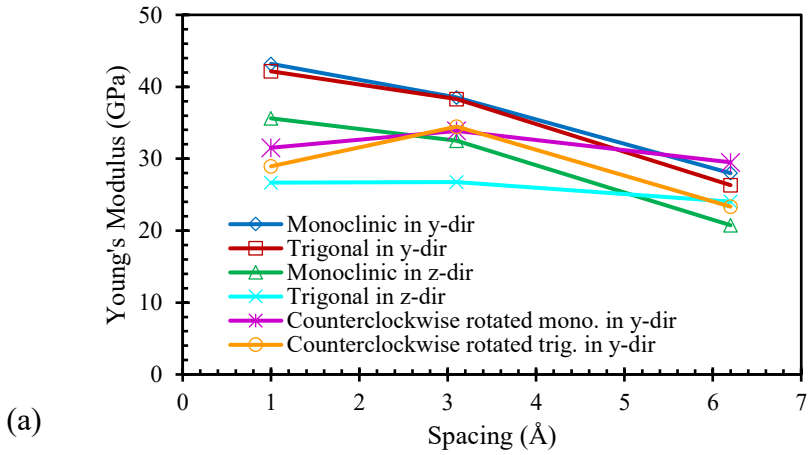

(a)

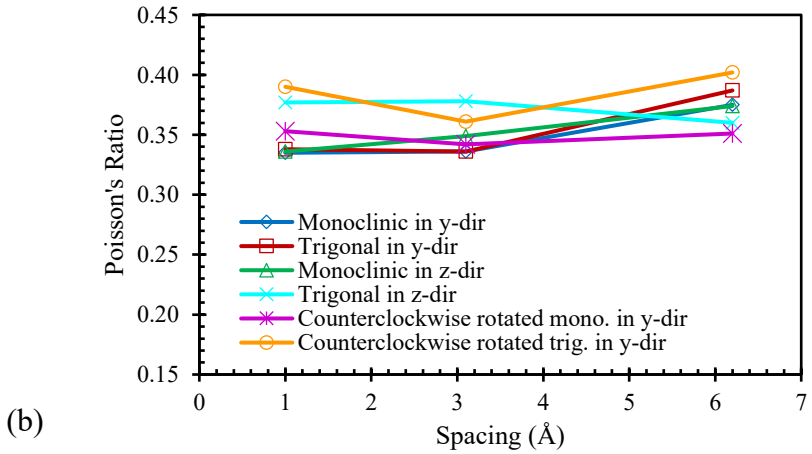

(b)

Figure 4.11 Curves of (a) Young's modulus, (b) Poisson's ratio and spacing between supercells with three different orientations of C-S-H (I)/CH composite.

4.4.1.3 Calcium-silicate-hydrates/ettringite

In the case of calcium-silicate-hydrates/ettringite, elastic constants of C-S-H (I)/AFt composite were also calculated following **section 4.3.2**. Since AFt has also a trigonal space group, Young's modulus were calculated by both monoclinic and trigonal space group. **Table 4.7** and **Table 4.8** shows the results of elastic constants in y- and z-directions. Additionally, **Table 4.9** shows the results of elastic constants of C-S-H (I)/AFt composite where AFt supercell was counterclockwise rotated in y-direction. The results of Young's modulus and Poisson's ratio of this composite could be found in **Figure 4.12**.

Table 4.7 Elastic constants (in GPa) of C-S-H (I)/AFt in y-direction.

Spacing	1 Å vacuum	3.1 Å water	6.2 Å water
C_{11}	39.4	37.7	34.9
C_{22}	25.1	28.1	14.2
C_{33}	50.7	46.8	42.4
C_{44}	4.6	2.8	7.2
C_{55}	14.0	10.0	8.4
C_{66}	4.9	5.1	6.6
C_{12}	13.7	13.4	4.5
C_{13}	20.0	16.5	13.5
C_{15}	2.2	3.5	-7.3
C_{23}	15.9	13.8	5.5
C_{25}	-0.2	-0.4	-6.6
C_{35}	1.9	1.6	-5.3
C_{46}	0.8	0.01	-2.1
C_{14}	-3.3	3.6	-4.3
C_{24}	-2.4	-1.3	-1.8
C_{56}	1.6	0.8	-2.5

Table 4.8 Elastic constants (in GPa) of C-S-H (I)/AFt in z-direction.

Spacing	1 Å vacuum	3.1 Å water	6.2 Å water
C_{11}	44.8	45.0	43.2
C_{22}	50.5	42.3	41.7
C_{33}	48.8	35.2	24.4
C_{44}	10.0	5.3	2.1
C_{55}	8.1	1.9	2.5
C_{66}	10.6	11.8	12.6
C_{12}	22.9	23.7	20.4
C_{13}	19.2	19.4	12.2
C_{15}	0.1	-1.5	2.8
C_{23}	23.3	17.6	11.1
C_{25}	1.0	0.4	-1.9
C_{35}	3.2	-1.5	-2.2
C_{46}	1.2	-0.1	-0.01
C_{14}	2.0	2.6	-0.3
C_{24}	4.3	-1.1	2.8
C_{56}	-0.2	-0.2	-1.6

Table 4.9 Elastic constants (in GPa) of C-S-H (I)/AFt counterclockwise rotated in y-direction.

Spacing	1 Å vacuum	3.1 Å water	6.2 Å water
C_{11}	40.6	33.4	39.5
C_{22}	47.7	38.0	38.4
C_{33}	42.1	36.9	41.4
C_{44}	7.9	6.8	8.3
C_{55}	9.3	9.4	8.8
C_{66}	8.1	3.8	4.7
C_{12}	19.7	17.0	16.7
C_{13}	22.3	20.5	18.9
C_{15}	0.9	0.2	-0.1
C_{23}	18.9	16.7	14.1
C_{25}	-0.9	0.7	1.7
C_{35}	0.5	-1.7	0.3
C_{46}	-1.2	-0.7	0.8
C_{14}	1.9	-1.1	-1.1
C_{24}	0.8	0.4	-2.5
C_{56}	-0.7	-0.7	0.1

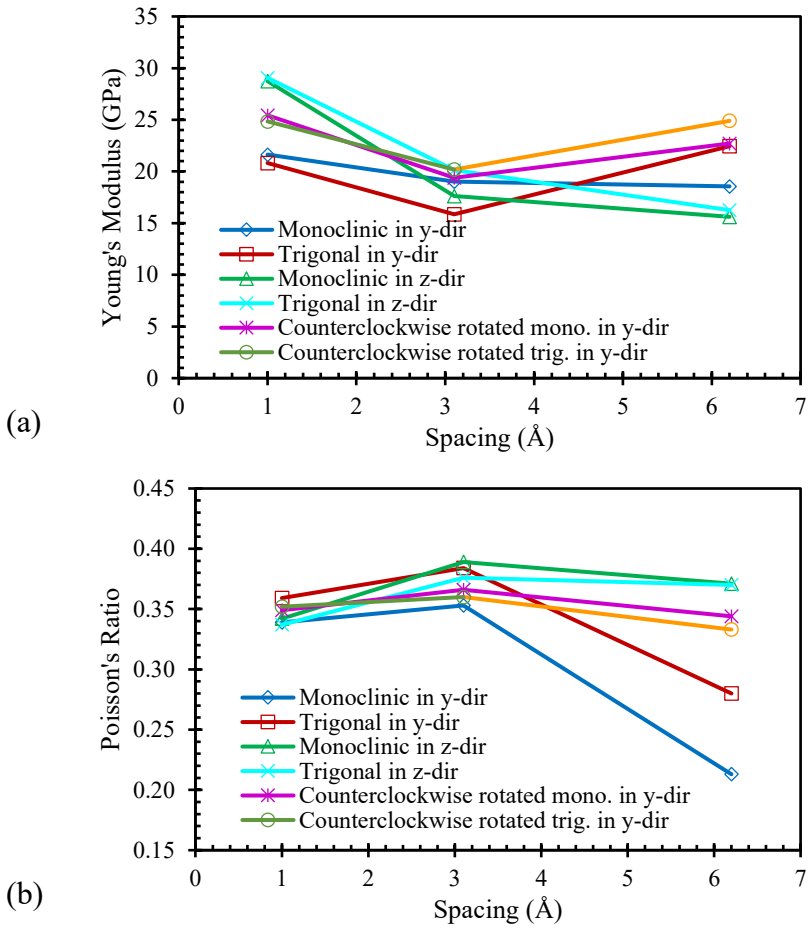

Figure 4.12 Curves of (a) Young's modulus, (b) Poisson's ratio and spacing between supercells with three different orientations of C-S-H (I)/AFt composite.

4.4.2 Discussion

In the case of composites composed of cuboid shape supercells, all Reactive Molecular Dynamics simulations to obtain elastic constants values were done with strain rates of 10^{-6} fs^{-1} or 10^{-5} fs^{-1}. With the values of elastic constants, VRH approximation makes it possible to obtain Young's modulus and Poisson's ratio of main hydrated cement paste phases composites. Young's modulus and Poisson's ratio of C-S-H (I)/C-S-H (I) composite with 1 Å vacuum spacing were found to be 51.6 GPa and 0.33, respectively. When the spacing increases up to 3.1 Å and 6.2 Å, with water molecules in between the two phases, the Young's modulus decreased and was equal to 42.3 GPa and 29.6 GPa, respectively. The value of 42.3 GPa might be compared to the result obtained by Bonnaud et al. [26] (i.e., mean value of 40.1 GPa). Both results are in good agreement. Thus, even if the force fields between atoms are different and the procedure is totally different as Bonnaud et al. evaluated the mean forces and interaction Grand Potential between C-S-H nanoparticles through Grand canonical Monte Carlo simulations.

To the authors' knowledge, simulations of C-S-H (I)/CH composite were only done by Liang [27]. In their study, they placed CH phase about 3 Å on top of C-S-H phase. They found the Young's modulus to be about 40 GPa. Compared to their results, C-S-H (I)/CH composite results with 1 Å vacuum spacing with trigonal and monoclinic space group were 32.6 GPa and 36.8 GPa, respectively. The result of monoclinic space group seems to be much closer to the result obtained by Liang than the one with trigonal space group. The methods to obtain Young's modulus are different. They calculated the values of Young's modulus from stress-strain curve of uniaxial tensile test. In our study, VRH approximation was used. As could be seen, different orientations in y-, in z-, and counterclockwise in y-directions gave different values of Young's modulus and Poisson's ratio. Space group and spacing of vacuum and water also led to quite different results.

For the first time, Young's modulus and Poisson's ratio of C-S-H/AFt composites have been calculated. Considering a monoclinic space group, Young's modulus of this composite decreased from 25.3 to 19 GPa when the interlayer spacing grew up from 1 Å to 6.2 Å. Poisson's ratio also decreased, from 0.34 to 0.31. In the same time, considering a trigonal space group, Young's modulus presented a minimal value of 18.7 GPa for a spacing of 3.1 Å. Poisson's ratio still decreases from 0.35 to 0.33. No literature value has been found for a sake of comparison.

For spacing between supercells equalled to 3.1 Å, Young's modulus of C-S-H (I)/C-S-H (I), C-S-H (I)/CH and C-S-H (I)/AFt were respectively equal to 42.3 GPa, 34.1 GPa and 18.7 GPa. All these values of Young's modulus and Poisson's ratio were averaged among three orientations. Note that, for the two last ones, mean values between trigonal and monoclinic space groups have been provided.

4.5 Results of composites composed of cube shape supercells

4.5.1 Elastic constant, Young's modulus, and Poisson's ratio

4.5.1.1 Calcium-silicate-hydrates

The results of elastic constants of different orientations, different configurations and different composites are summarized in **Table 4.10 - Table 4.18**. By using obtained values of elastic constants, it was possible to calculate Young's modulus and Poisson's ratio using Voigt-Reuss-Hill (VRH) approximation as shown in **Figure 4.13 - Figure 4.15**.

Table 4.10 Elastic constants (in GPa) of C-S-H (I)/C-S-H (I) in y-direction.

Spacing	1 Å vacuum	3.1 Å water	6.2 Å water
C_{11}	85.4	78.8	66.8
C_{22}	77.7	57.9	37.0
C_{33}	84.3	71.9	67.3
C_{44}	18.2	16.8	4.1
C_{55}	22.5	19.7	20.1
C_{66}	21.3	12.9	3.4
C_{12}	40.0	34.4	20.4
C_{13}	45.4	39.8	28.5
C_{15}	3.6	-1.1	-2.6
C_{23}	38.0	30.8	19.1
C_{25}	3.2	-1.9	-1.9
C_{35}	3.5	-0.2	0.5
C_{46}	1.5	-1.4	0.8

Table 4.11 Elastic constants (in GPa) of C-S-H (I)/C-S-H (I) in z-direction.

Spacing	1 Å vacuum	3.1 Å water	6.2 Å water
C_{11}	81.6	74.5	65.9
C_{22}	85.5	74.8	61.3
C_{33}	83.8	66.2	23.8
C_{44}	19.9	20.6	1.5
C_{55}	18.9	12.9	1.4
C_{66}	22.4	20.7	21.3
C_{12}	43.8	37.9	28.2
C_{13}	44.8	37.3	17.6
C_{15}	1.6	-0.5	0.7
C_{23}	46.0	36.3	15.2
C_{25}	2.1	-2.6	1.1
C_{35}	-1.2	-1.3	2.1
C_{46}	0.6	1.9	-0.9

Table 4.12 Elastic constants (in GPa) of C-S-H (I)/C-S-H (I) counterclockwise rotated in y-direction.

Spacing	1 Å vacuum	3.1 Å water	6.2 Å water
C_{11}	68.3	63.0	56.0
C_{22}	64.1	53.6	35.1
C_{33}	38.0	33.2	31.8
C_{44}	11.6	10.1	4.4
C_{55}	13.3	9.5	11.6
C_{66}	17.7	15.4	2.7
C_{12}	28.7	24.9	17.7
C_{13}	21.5	15.8	13.4
C_{15}	1.8	1.5	-2.3
C_{23}	23.9	18.2	7.9
C_{25}	-0.3	1.9	-1.4
C_{35}	0.8	2.6	-0.8
C_{46}	0.6	-1.1	-0.7

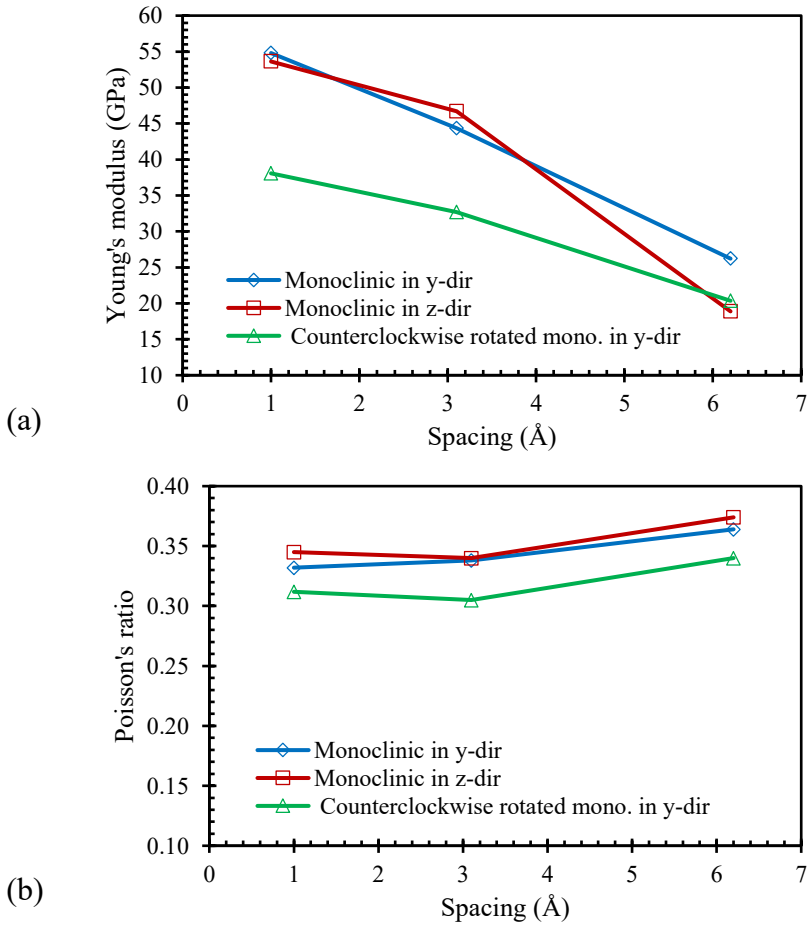

Figure 4.13 (a) Young's modulus, (b) Poisson's ratio in relation with spacing of C-S-H (I)/C-S-H (I) composites.

4.5.1.2 Calcium-silicate-hydrates/portlandite

Table 4.13 Elastic constants (in GPa) of C-S-H (I)/CH in y-direction.

Spacing	1 Å vacuum	3.1 Å water	6.2 Å water
C_{11}	83.3	79.9	63.6
C_{22}	82.4	68.8	39.1
C_{33}	56.3	52.1	45.1
C_{44}	6.3	6.4	3.8
C_{55}	11.5	13.0	9.5
C_{66}	21.2	13.5	6.2
C_{12}	38.4	36.1	21.1
C_{13}	30.9	33.6	24.0
C_{15}	2.4	-0.7	-2.4
C_{23}	28.3	27.2	11.8
C_{25}	3.4	2.4	-0.7
C_{35}	1.2	3.1	-2.3
C_{46}	1.1	1.0	-3.7
C_{14}	-7.3	-5.3	-6.0
C_{24}	7.4	3.1	-2.5
C_{56}	-2.7	-0.1	-0.9

Table 4.14 Elastic constants (in GPa) of C-S-H (I)/CH in z-direction.

Spacing	1 Å vacuum	3.1 Å water	6.2 Å water
C_{11}	83.3	79.9	63.6
C_{22}	82.4	68.8	39.1
C_{33}	56.3	52.1	45.1
C_{44}	6.3	6.4	3.8
C_{55}	11.5	13.0	9.5
C_{66}	21.2	13.5	6.2
C_{12}	38.4	36.1	21.1
C_{13}	30.9	33.6	24.0
C_{15}	2.4	-0.7	-2.4
C_{23}	28.3	27.2	11.8
C_{25}	3.4	2.4	-0.7
C_{35}	1.2	3.1	-2.3
C_{46}	1.1	1.0	-3.7
C_{14}	-7.3	-5.3	-6.0
C_{24}	7.4	3.1	-2.5
C_{56}	-2.7	-0.1	-0.9

Table 4.15 Elastic constants (in GPa) of C-S-H (I)/CH counterclockwise rotated in y-direction.

Spacing	1 Å vacuum	3.1 Å water	6.2 Å water
C_{11}	83.3	79.9	63.6
C_{22}	82.4	68.8	39.1
C_{33}	56.3	52.1	45.1
C_{44}	6.3	6.4	3.8
C_{55}	11.5	13.0	9.5
C_{66}	21.2	13.5	6.2
C_{12}	38.4	36.1	21.1
C_{13}	30.9	33.6	24.0
C_{15}	2.4	-0.7	-2.4
C_{23}	28.3	27.2	11.8
C_{25}	3.4	2.4	-0.7
C_{35}	1.2	3.1	-2.3
C_{46}	1.1	1.0	-3.7
C_{14}	-7.3	-5.3	-6.0
C_{24}	7.4	3.1	-2.5
C_{56}	-2.7	-0.1	-0.9

(a)

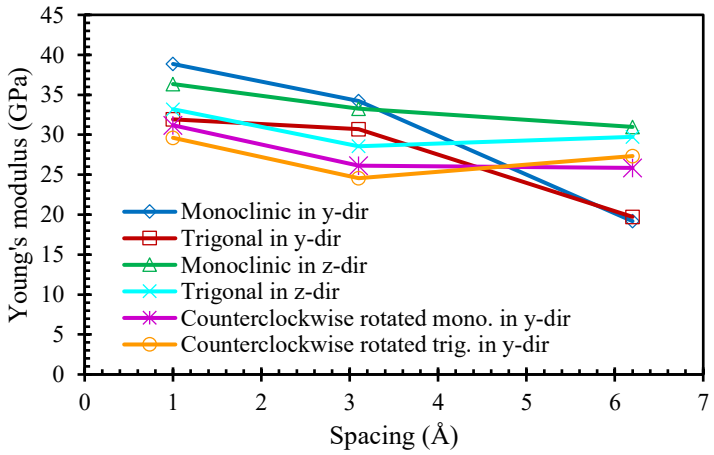

(b)

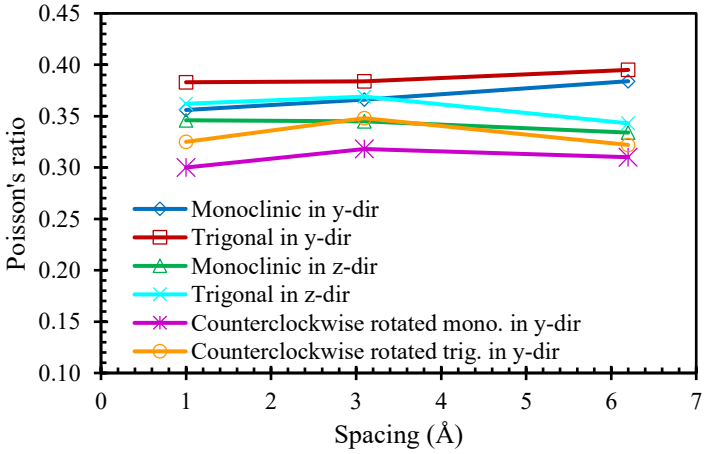

Figure 4.14 (a) Young's modulus, (b) Poisson's ratio in relation with spacing of C-S-H (I)/CH composite.

4.5.1.3 Calcium-silicate-hydrates/ettringite

Table 4.16 Elastic constants (in GPa) of C-S-H (I)/AFt in y-direction.

Spacing	1 Å vacuum	3.1 Å water	6.2 Å water
C_{11}	49.9	46.9	40.8
C_{22}	28.9	31.0	23.9
C_{33}	58.0	57.7	55.1
C_{44}	4.0	4.0	2.5
C_{55}	9.8	11.5	9.2
C_{66}	6.4	2.2	2.3
C_{12}	19.6	15.9	14.1
C_{13}	22.9	22.7	21.6
C_{15}	1.6	0.5	1.6
C_{23}	18.4	17.5	16.8
C_{25}	1.6	0.5	0.6
C_{35}	-0.1	-0.7	2.7
C_{46}	0.4	-0.6	-1.6
C_{14}	0.7	-1.2	1.8
C_{24}	2.3	1.2	-0.6
C_{56}	-1.3	-0.3	0.4

Table 4.17 Elastic constants (in GPa) of C-S-H (I)/AFt in z-direction.

Spacing	1 Å vacuum	3.1 Å water	6.2 Å water
C_{11}	50.8	51.6	42.5
C_{22}	45.4	44.2	44.9
C_{33}	50.4	41.1	21.2
C_{44}	4.9	6.6	2.7
C_{55}	8.5	5.4	3.9
C_{66}	10.1	8.5	10.8
C_{12}	24.7	23.5	22.9
C_{13}	21.6	19.5	11.5
C_{15}	1.8	0.9	1.2
C_{23}	23.5	19.3	14.4
C_{25}	-2.1	1.9	2.9
C_{35}	0.5	-2.0	1.9
C_{46}	-0.6	-0.2	-0.4
C_{14}	0.7	-1.7	-0.1
C_{24}	1.5	-1.7	0.6
C_{56}	0.8	-0.9	-0.7

Table 4.18 Elastic constants (in GPa) of C-S-H (I)/AFt counterclockwise rotated in y-direction.

Spacing	1 Å vacuum	3.1 Å water	6.2 Å water
C_{11}	51.8	47.6	42.9
C_{22}	51.8	39.9	27.6
C_{33}	45.0	39.6	43.3
C_{44}	7.1	4.3	1.9
C_{55}	11.2	8.1	10.2
C_{66}	8.1	7.4	0.1
C_{12}	20.8	18.6	12.9
C_{13}	23.9	22.6	24.1
C_{15}	0.4	-0.2	1.7
C_{23}	23.4	17.9	13.2
C_{25}	2.1	0.4	-1.5
C_{35}	0.3	-0.6	-0.02
C_{46}	-1.3	0.4	-0.1
C_{14}	0.1	1.5	1.9
C_{24}	-1.7	2.9	0.6
C_{56}	-1.3	-1.6	-0.02

(a)

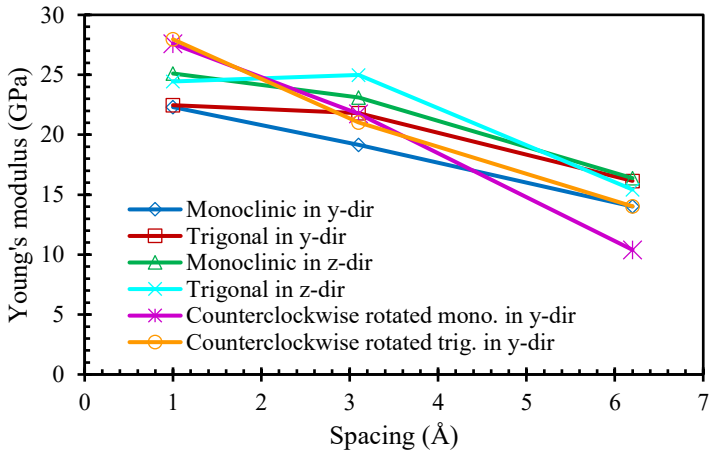

(b)

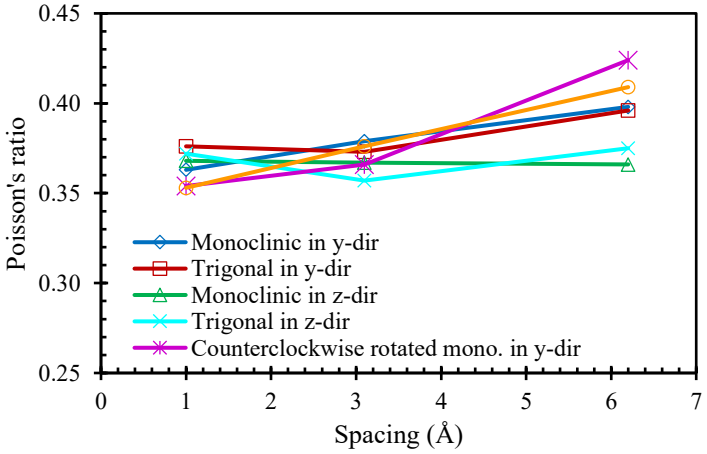

Figure 4.15 (a) Young's modulus, (b) Poisson's ratio in relation with spacing of C-S-H (I)/AFt composite.

4.5.2 Discussion

In the case of composites composed of cube shape supercells, all Reactive Molecular Dynamics simulations to obtain elastic constants values were done with strain rates of 10^{-6} fs^{-1}. Young's modulus and Poisson's ratio of C-S-H (I)/C-S-H (I) composite were respectively 48.8 GPa and 0.33 in the case of 1 Å vacuum spacing. When 3.1 Å and 6.2 Å water spacing were placed, Young's modulus dropped to the values of 41.2 GPa and 21.8 GPa, respectively.

Young's modulus of C-S-H (I)/CH composite obtained using VRH approximation with trigonal and monoclinic space groups were respectively 31.6 and 35.5 GPa in the case of 1 Å vacuum spacing. It seems that Young's modulus obtained by monoclinic space group is much closer to result obtained by Liang [27] compared to trigonal space group. It should be noticed that the methods to obtain Young's modulus are not the same. In their study, the values were obtained from stress-strain curves of uniaxial tensile test along z-direction. VRH approximation was utilized. It can be seen in **Figure 4.13** - **Figure 4.15** that different orientations and configurations could lead to different results.

For the first time, Young's modulus and Poisson's ratio of C-S-H (I)/AFt composite has been obtained. In the case of monoclinic space group, when interlayer spacing increased from 1 Å to 6.2 Å, Young's modulus of this composite dropped from 24.9 GPa to 13.6 GPa. Poisson's ratio otherwise increased from 0.36 to 0.39. In the case of trigonal space group, Young's modulus dropped from 24.9 GPa to 15.2 GPa and Poisson's ratio increased from 0.37 to 0.39 which are quite close to results obtained by monoclinic space group. For the sake of comparison, no literature value could be found.

Young's modulus and Poisson's ratio were averaged among three different orientations. Considering spacing between supercells equalled to 3.1 Å, Young's modulus of C-S-H (I)/C-S-H (I), C-S-H (I)/CH and C-S-H (I)/AFt composites are as follows: 41.2 GPa, 29.6 GPa and 21.9 GPa, respectively. For the last two values, they were obtained from mean values between trigonal and monoclinic space groups.

4.6 In summary

In this chapter, elastic constants of different hydrated cement phase composites were found via MD simulations. ReaxFF force field was used in all simulations with strain rate of 10^{-6} fs^{-1}. Three different composites were formed by placing three different phases together. Those composites are as follows: (a) C-S-H (I)/C-S-H (I) composite, (b) C-S-H (I)/CH composite and (c) C-S-H (I)/AFt composite. Three different orientations and three different configuration of spacing were studied. Results are divided into two cases: (1) cuboid shape and (2) cube shape

supercells composites. By deforming in six different directions, stress-strain curves were obtained. Elastic constants were then deduced from these stress-strain curves. Young's modulus and Poisson's ratio were finally calculated via Voigt-Reuss-Hill approximation. It can be seen that shape of supercells (i.e., cuboid shape and cube shape supercells composites) could affect value of Young's modulus and Poisson's ratio of cement paste composites. Results obtained in this chapter are served for the calculation of Young's modulus and Poisson's ratio of a simplified hardened cement paste in the next chapter using homogenization scheme, i.e., Mori-Tanaka scheme.

5 Elastic properties of hardened cement paste

5.1 Background

This chapter describes the method to obtain the mechanical properties of the hardened cement paste by taking into account the mechanical properties of different main hydrated cement paste phases using MD simulations. This includes calculation of Young's modulus and Poisson's ratio of a simplified hardened cement paste (HCP) using the homogenization scheme (i.e., Mori-Tanaka scheme). With results of Young's modulus and Poisson's ratio obtained via Voigt-Reuss-Hill approximation in previous chapter, it is now possible to calculate Young's modulus and Poisson's ratio of a simplified HCP. A preliminary result obtained from a tensile test of a simplified HCP via Discrete Element Method (DEM) was investigated in this chapter too. The tensile test at the microscale was done using the results of mechanical properties obtained in previous chapters. This chapter consists of the following sections: (5.2) Multi-scale Modelling of Computational Concrete, (5.3) Homogenization of simplified hardened cement paste, (5.4) tensile test of hardened cement paste and (5.5) in summary.

5.2 Multi-scale Modelling of Computational Concrete

Many researchers from all over the world have faced a challenge to simulate the properties and performances of hardened cement-based materials. To have a better understanding of the material and optimization of its properties and to improve its performances, numerical and analytical models have been developed in the last two decades. Concrete properties are related to its microstructure at many length scales ranging from nanometres to millimetres and centimetres. Moreover, it is too difficult to be presented correctly by analytical models. Therefore, using a numerical approach provides several advantages. It could be considered as the sole approach to represent the microstructure and to predict the properties [56].

Consequently, Bernard and Kamali-Bernard [56] have developed the platform called Multi-scale Modelling of Computational Concrete (MuMoCC). This platform used different modelling methods developed based on a multi-scale approach at INSA Rennes. It should be noticed that input at higher scale were used by output at lower scale in MuMoCC approach.

Four various scales have been studied for cementitious materials [57]:

- Nanoscale in which element cells of different components of hardened cement paste are studied. This scale was previously studied by PhD students, Fu [24] and Claverie [58], by mean of MD or DFT simulation.
- Microscale in which hardened cement paste as a complex and heterogeneous porous material are considered. Calcium-Silicate-Hydrate (C-S-H), Portlandite (CH), Ettringite (AFt), and Monosulfoaluminate (AFm) are the main solid phases. The Representative Element Volume (REV) of hydrated cement paste has been simulated using CEMHYD3D software, which was developed by National Institute of Standards and Technology (NIST) in USA. This REV has been meshed in order to use in Finite Element Method (FEM) framework to study the mechanical and physical behaviour of cement paste.
- Sub-mesoscale in which mortal scale is investigated. This scale takes into account the smallest fraction of particle size distribution bonded by homogeneous cement paste with air voids and porosity.
- Mesoscale in which concrete is studied. It refers to the largest aggregates embedded in a matrix of mortar. FEM has been used another time for both sub-mesoscale and mesoscale.

5.3 Homogenization of simplified hardened cement paste

5.3.1 Materials and method

Phase composition of hardened cement paste (HCP) with water-to-cement (w/c) ratio of 0.4 was used. We supposed that cement paste was well hydrated. Thus few unhydrated phases should be present. Then we considered a simplified hardened cement paste without taking into account unhydrated phases.

Volume percentages of those phases are as follows [59]:

- C-S-H phase represented by C-S-H (I) of 53%
- CH phase of 19%
- Sulfoaluminate phase represented by AFt of 10%
- Capillary porosity of 18%.

Moreover, C-S-H gel includes low-density (LD) C-S-H about 70% and high-density (HD) C-S-H about 30% with gel porosity of 35% and 24%, respectively [57].

In the study of Fu et al. [6], they investigated the elastic modulus assessment of LD and HD C-S-H through Mori-Tanaka and self-consistent schemes. They found that self-consistent scheme could be utilized to acquire Young's modulus no more than porosity volume fraction of 50%. And yet, Mori-Tanaka scheme could be utilized to acquire Young's modulus more than porosity volume fraction of 50%. In this study, Mori-Tanaka scheme was chosen to calculate Young's modulus because porosity volume fraction of C-S-H (I)/nanoporosity is equal to 70%. Details of Mori-Tanaka homogenization procedure of simplified HCP are given in **Figure 5.1**. Firstly, Mori-Tanaka homogenization scheme was applied on C-S-H (I) referred to matrix and nanoporosity referred to inclusion. Then C-S-H (I)/nanoporosity referred to matrix and C-S-H (I)/CH referred to inclusion were taken into account. Additionally, Mori-Tanaka scheme were applied on C-S-H (I)/nanoporosity/CH matrix referred to matrix and C-S-H (I)/AFt referred to inclusion. Finally, solid phase (i.e., matrix of C-S-H (I)/nanoporosity/CH/AFt) and capillary porosity referred to inclusion were taken into account in order to get a simplified HCP.

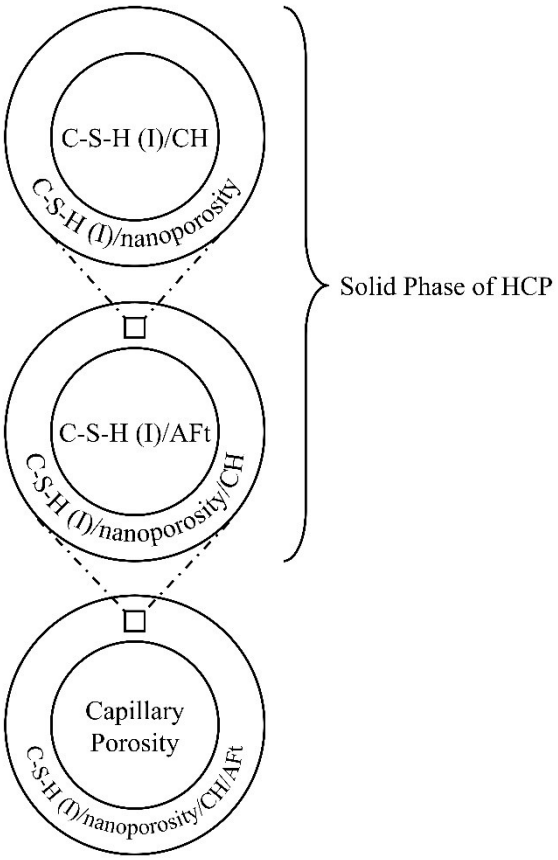

Figure 5.1 Scheme of homogenization procedure of simplified hardened cement paste.

In order to calculate shear and bulk moduli of homogenous matrix, following equations of Mori-Tanaka scheme could be used [32]:

$$K = \frac{\sum_r f_r k_r \left[1 + \alpha_s \left(\frac{k_r}{k_s} - 1\right)\right]^{-1}}{\sum_r f_r \left[1 + \alpha_s \left(\frac{k_r}{k_s} - 1\right)\right]^{-1}} \tag{5.1}$$

$$G = \frac{\sum_r f_r g_r \left[1 + \beta_s \left(\frac{g_r}{g_s} - 1\right)\right]^{-1}}{\sum_r f_r \left[1 + \beta_s \left(\frac{g_r}{g_s} - 1\right)\right]^{-1}} \tag{5.2}$$

where f_r is volume fraction of matrix, α_s and β_s coefficients are given by:

$$\alpha_s = \frac{3k_s}{3k_s + 4g_s} \tag{5.3}$$

$$\alpha_s = \frac{3k_s}{3k_s + 4g_s} \tag{5.4}$$

where g_r and g_s are shear modulus, k_r and k_s are bulk modulus of matrix and inclusion, respectively:

$$g_{r,s} = \frac{E_{r,s}}{2(1 + \mu_{r,s})} \tag{5.5}$$

$$k_{r,s} = \frac{E_{r,s}}{3(1 - 2\mu_{r,s})} \tag{5.6}$$

Shear and bulk moduli of water are 2.2 and 0 GPa, respectively. Poisson's ratio of water is equal to 0.5.

5.3.2 Homogenization of composites composed of cuboid shape supercells

5.3.2.1 Results

In order to calculate the homogenization of simplified HCP, the values of Young's modulus and Poisson's ratio were averaged among the three orientations: in y-, in z-, and counterclockwise rotated in y-directions. The results are summarized in **Table 5.1.**

Table 5.1 Mean Young's modulus and Poisson's ratio of three orientations.

Composite	Space Group	Spacing	E (GPa)	υ
C-S-H (I)/C-S-H (I)	Monoclinic	1 Å vacuum	51.6	0.33
		3.1 Å water	42.3	0.34
		6.2 Å water	29.6	0.34
C-S-H (I)/CH	Monoclinic	1 Å vacuum	36.8	0.34
		3.1 Å water	34.9	0.34
		6.2 Å water	26.1	0.37
	Trigonal	1 Å vacuum	32.6	0.37
		3.1 Å water	33.2	0.36
		6.2 Å water	24.6	0.38
C-S-H (I)/AFt	Monoclinic	1 Å vacuum	25.3	0.34
		3.1 Å water	18.7	0.37
		6.2 Å water	18.9	0.31
	Trigonal	1 Å vacuum	24.9	0.35
		3.1 Å water	18.7	0.37
		6.2 Å water	21.2	0.33

Following scheme on **Figure 5.1** and **Eqs. (5.1) - (5.6)**, Young's modulus and Poisson's ratio of homogenization of simplified HCP were obtained (see **Figure 5.2)**.

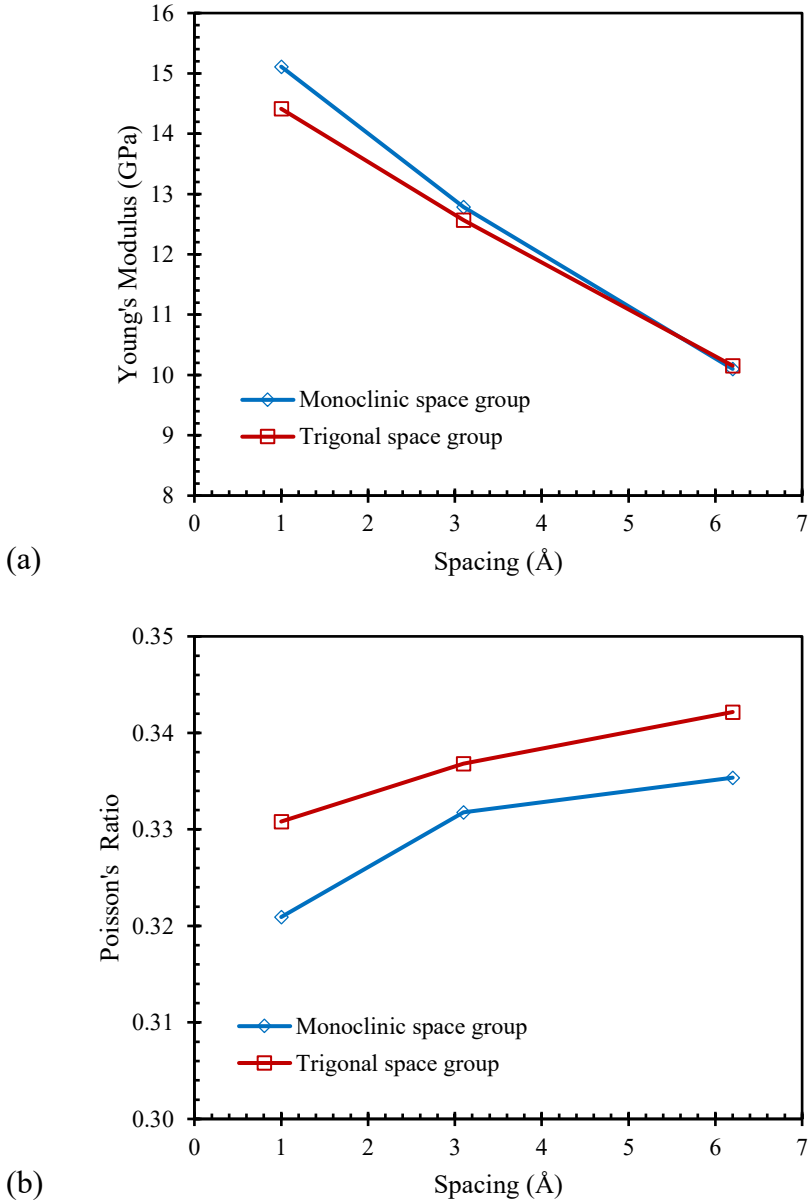

Figure 5.2 Curves of (a) Young's modulus, and (b) Poisson's ratio with different spacing of two different space groups using Mori-Tanaka scheme with simplified HCP.

5.3.2.2 Discussion

In the case of composites composed of cuboid shape supercells, we used results obtained from Reactive Molecular Dynamics simulations with strain rates of 10^{-6} fs^{-1} or 10^{-5} fs^{-1}. For spacing between supercells equalled to 3.1 Å, Young's modulus of C-S-H (I)/C-S-H (I), C-S-H (I)/CH and C-S-H (I)/AFt were respectively equal to 42.3 GPa, 34.1 GPa and 18.7 GPa. All these values of Young's modulus and Poisson's ratio obtained from **Chapter 4** were averaged among three orientations. Note that, for the two last ones, mean values between trigonal and monoclinic space groups have been provided.

These results enabled the calculation of homogenization of simplified HCP via Mori-Tanaka scheme as shown in **Figure 5.2a**. The results ranged from 10.1 GPa to 15.1 GPa and from 0.32 to 0.34 for Young's modulus and Poisson's ratio, respectively. It should be noticed that results in this study were obtained from a simplified hardened cement paste without taking into account unhydrated phases and including only three main hydrated cement phases (i.e., AFt, CH and C-S-H (I)). As a result, it is not easy to compare with results of normal hardened cement paste. Especially, taking into account the unhydrated phases might increase the values of Young's modulus since their Young's modulus are very high.

5.3.3 Homogenization of composite composed of cube shape supercells

5.3.3.1 Results

Young's modulus and Poisson's ratio were averaged among three different orientations as shown in **Figure 5.3**. With the results of Young's modulus and Poisson's ratio of different composites, it was possible to calculate Young's modulus and Poisson's ratio of simplified HCP using Mori-Tanaka scheme. The results are summarized in **Table 5.2**.

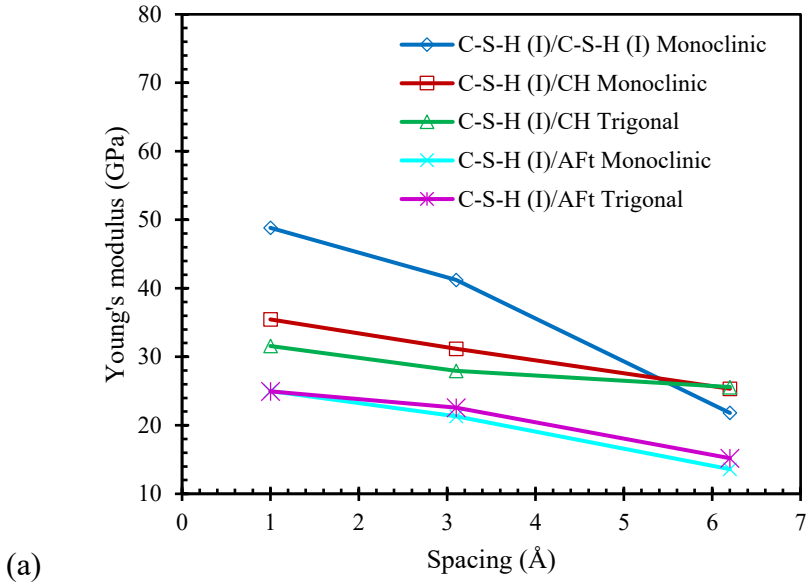

(a)

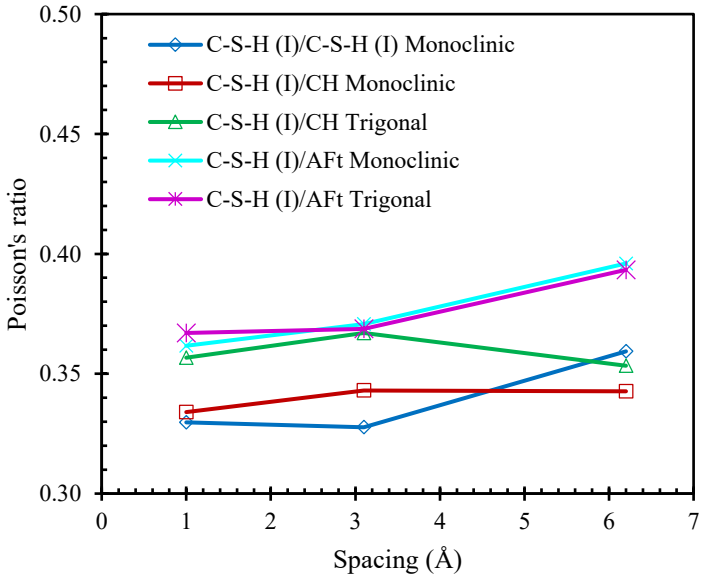

(b)

Figure 5.3 Mean (a) Young's modulus, (b) Poisson's ratio in relation with spacing of three orientations.

Table 5.2 Young's modulus and Poisson's ratio of simplified HCP via Mori-Tanaka scheme.

Group	Spacing	E (GPa)	υ
Monoclinic	1 Å vacuum	14.6	0.32
	3.1 Å water	12.6	0.33
	6.2 Å water	8.1	0.36
Trigonal	1 Å vacuum	13.9	0.33
	3.1 Å water	12.3	0.34
	6.2 Å water	8.4	0.36

5.3.3.2 Discussion

In the case of composites composed of cube shape supercells, all Reactive Molecular Dynamics simulations to obtain elastic constants values were done with strain rates of 10^{-6} fs^{-1}. As can be seen in **Figure 5.3**, Young's modulus and Poisson's ratio obtained from **Chapter 4** were averaged among three different orientations. Considering spacing between supercells equalled to 3.1 Å, Young's modulus of C-S-H (I)/C-S-H (I), C-S-H (I)/CH and C-S-H (I)/AFt are as follows: 41.2 GPa, 29.6 GPa and 21.9 GPa, respectively. For the last two values, they were obtained from mean values between trigonal and monoclinic space groups.

As could be seen in **Table 5.2**, Young's modulus and Poisson's ratio ranged from 8.1 GPa to 14.6 GPa and 0.32 to 0.36, respectively. Nevertheless, the obtained results in this study were calculated using a simplified hardened cement paste taking into account only three main hydrated cement paste phases (i.e., CH, C-S-H (I) and AFt) without considering unhydrated phases. It should be possible to use this method to calculate Young's modulus and Poisson's ratio of a normal hardened cement paste by calculating elastic constants of different composites with other hydrated and unhydrated phases.

5.4 Tensile test of hardened cement paste

5.4.1 Model construction

In order to create a virtual microstructure of hydrated cement paste, it is necessary to have all input parameters of the cementitious materials. Virtual Cement and Concrete Testing Laboratory (VCCTL) was chosen to create this virtual microstructure. Following the same methodology proposed by Rhardane et al. [12], cement paste with a water-to-binder ratio of 0.4 was obtained from ordinary Portland cement (CEM I 52.5 N). **Table 5.3** summarizes the mineral compositions of the cement for input parameters in VCCTL. The size of Representative Elementary Volume (REV) was 200 × 200 × 200 μm^3, which is the same size used in the work of Rhardane et al. [12]. The REV of cement paste is controlled by resolution of 1 μm^3 microstructure voxels. Default values in VCCTL were utilized for mix properties. For curing conditions, isothermal and sealed saturation conditions with temperature of 20°C were applied. Since we would like to have a simplified of hardened cement paste (HCP) taking into account only the main hydrated cement paste phases (i.e., C-S-H (I), CH and AFt), we used microstructure image at the degree of hydration of 65.9% with hydration duration of 28 days.

Table 5.3 Mineral composition of cement (values represent mass fractions) **[12]**.

	Primary constituents of cement							Secondary constituents	
Cement pastes	Clinker phases						Sulfates	Calcium carbonate	Limestone
Label	C_3S	C_2S	C_3A	C_4AF	$K\bar{S}$	$N\bar{S}$	$C\bar{S}H_x$		
CEM-N1	72.2	9.4	9.4	7.3	1.3	0.3	4.2	1	1

The image of hydrated microstructure obtained from VCCTL was a data file containing a list of numbers that represents different types of phases of hydrated and unhydrated phases. We supposed that cement paste was well hydrated. Therefore, few unhydrated phases should be present. Then we considered a simplified HCP taking into account only the three main hydrated phases similar to **Section 5.3**.

Volume percentages of those phases are as follows:

- C-S-H phase represented by C-S-H (I) of 49.4%
- CH phase of 18.2%
- Sulfoaluminate phase represented by AFt of 8.5%
- Saturated porosity of 16.4%
- Self-desiccated porosity of 7.5%.

The microstructure image was selected from the middle section along x-direction of the 3D model obtained from VCCTL as shown in **Figure 5.4**. By replacing the hydrated and unhydrated phases as shown in **Table 5.4**, a simplified HCP was obtained with the volume percentages mentioned earlier. **Figure 5.5a** illustrates the microstructure image of simplified HCP after replacing with main hydrated cement paste phases in Excel with the same size as the REV microstructure, i.e., 200 × 200 μm². Particle Flow Code (PFC) program was chosen to model DEM simulations. Rock test's example code provided by PFC was used to model the direct tension test. The simplified HCP microstructure were then imported to PFC as different groups to represent each phase as shown in **Figure 5.5b**.

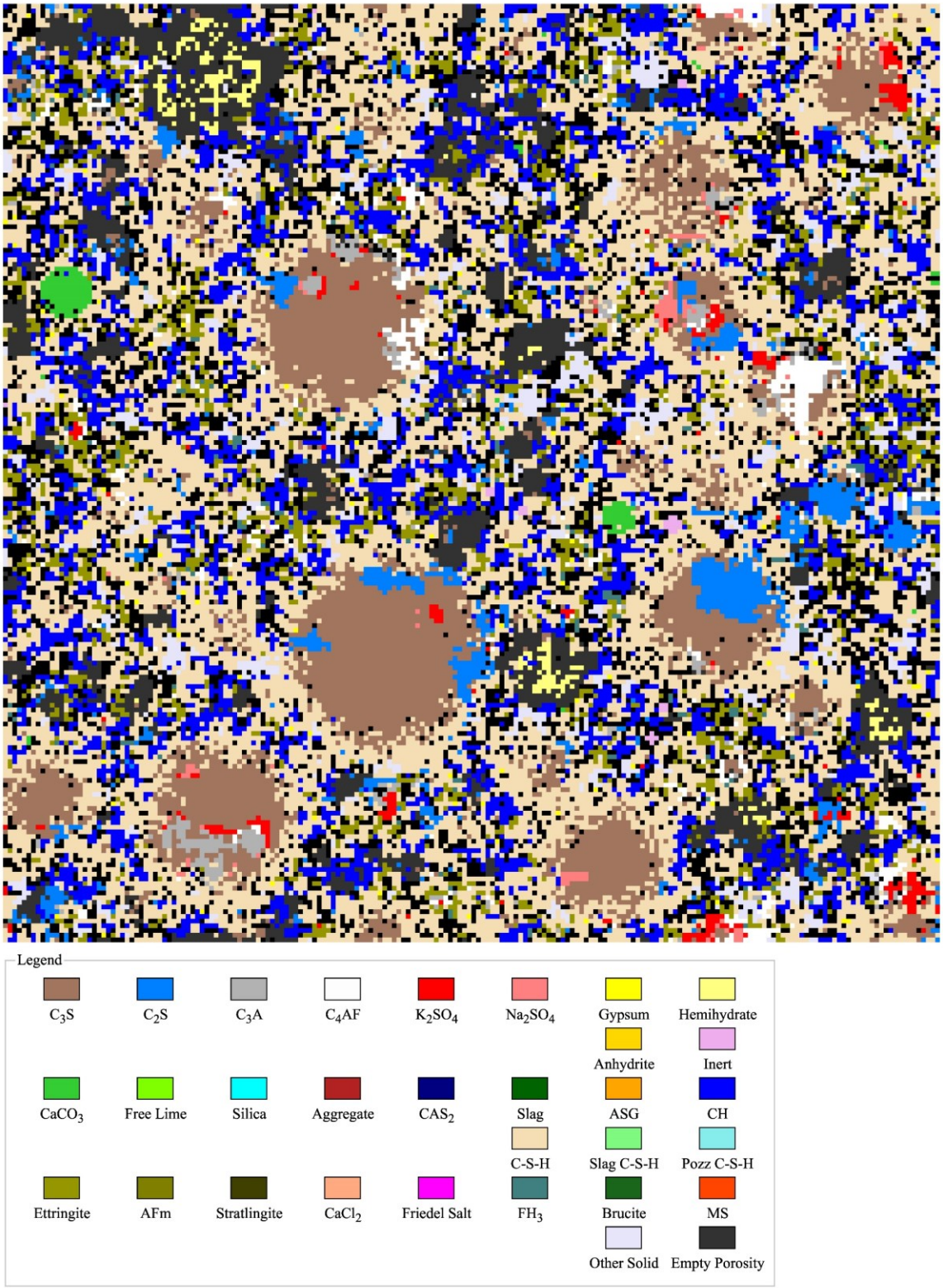

Figure 5.4 Microstructure image of hardened cement paste obtained from VCCTL.

Table 5.4 Surface area fraction of other phases replaced by C-S-H (I), CH and AFt.

Initial phase	Replaced phase	Surface area fraction
C_3S (alite)	C-S-H (I)	11.6%
C_2S (belite)	C-S-H (I)	2.9%
C_3AH_6 (hydrogarnet)	CH	3.7%
C_4AF (felite)	CH	1.5%
$Fe(OH)_3$	CH	0.4%
$CaCO_3$ (generic limestone)	CH	0.4%
AFt with Fe substitution	AFt	1.8%
C_3A (cubic form)	AFt	0.9%
K_2SO_4 (arcanite)	AFt	0.7%
$CaSO_4 \cdot 0.5H_2O$	AFt	0.6%
Na_2SO_4 (thenardite)	AFt	0.3%
Inert filler	AFt	0.1%
Secondary gypsum	AFt	0.1%

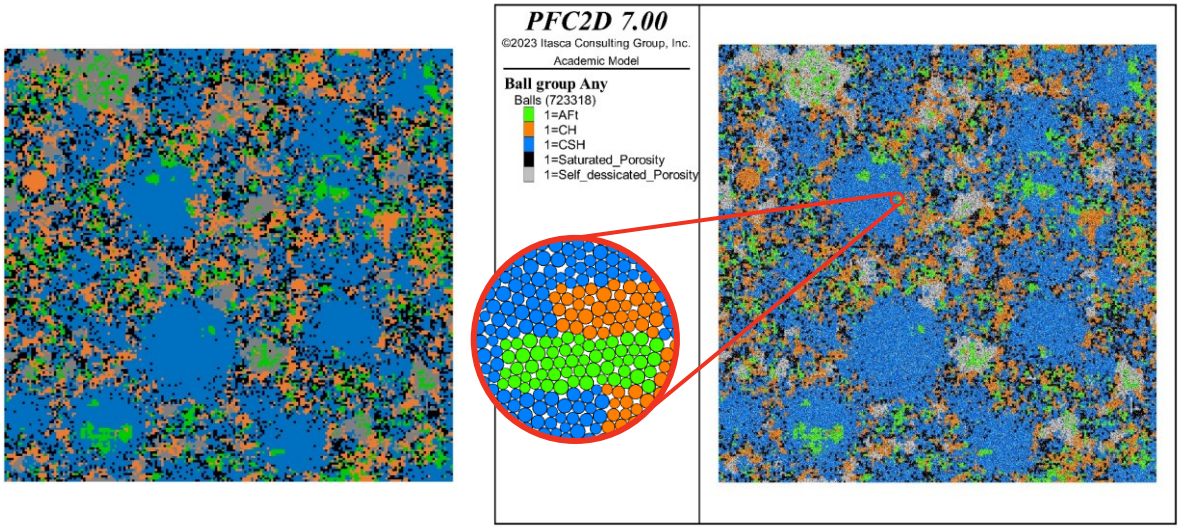

(a) (b)

Figure 5.5 Microstructure image of simplified hardened cement paste: (a) replaced by main hydrated cement phases in Excel and (b) imported to PFC.

Zhu et al. [60] developed an exponential softening model that represents well the constitutive behaviour of cementitious material. In the model at a contact point, micro-mechanical parameters consists of normal and shear spring constants (k_n, k_s), normal and shear bonds (S_n, S_s) and friction coefficient (μ). The relative displacements (u_n, u_s) was used to include the

softening behavior of a quasi-brittle material. We used this softening model to model the simplified hardened cement paste microstructure. In accordance with a damage law proposed by Jirásek and Bauer [61], normal and shear bond are supposed to decrease exponentially at a contact point after the peak tensile loading. Since damage parameters in normal and shear direction have the same value, there is only one damage parameter (D_f) [62,63]:

$$D_f = \max\left(D_f^n, D_f^s\right) = \begin{cases} 0 & u_{n,s} \le u_e^{n,s} \\ 1 - \dfrac{u_e^{n,s}}{u_{n,s}} \exp\left(-\dfrac{u_{n,s} - u_e^{n,s}}{u_f^{n,s} - u_e^{n,s}}\right) & u_{n,s} > u_e^{n,s} \end{cases} \tag{5.7}$$

where $u_{n,s}$ represents the relative normal or shear displacement between two particles, $u_e^{n,s}$ the displacement corresponding to elastic limit in normal or shear directions, $u_f^{n,s}$ the displacement parameter that controls the slope of softening curve in normal or shear direction.

The bond force in normal or shear directions is given by the following expression [60]:

$$F_{n,s} = (1 - \mathrm{D_f})\mathrm{k_{n,s}} u_{n,s} = \begin{cases} k_{n,s} u_{n,s} & u_{n,s} \le u_e^{n,s} \\ k_{n,s} u_e^{n,s} \exp\left(-\dfrac{u_{n,s} - u_e^{n,s}}{u_f^{n,s} - u_e^{n,s}}\right) & u_{n,s} > u_e^{n,s} \end{cases} \tag{5.8}$$

The reduced normal and shear strength can then be calculated at a certain damage condition as follows [60]:

$$\begin{aligned} s_{n,sof} &= \left(1 - D_f\right) k_n u_n \\ s_{s,sof} &= \left(1 - D_f\right) k_s u_s \end{aligned} \tag{5.9}$$

Bond fails either in tension or shear in this softening model. Shear strength is increased by the slip contributed by compression when the particles are in compression [60]:

$$S'_{s,sof} = \mu\langle -F_n \rangle + S_{s,sof} \tag{5.10}$$

where $S_{s,sof}$ represents the softening shear strength, $\langle \cdot \rangle$ Macaulay brackets.

For in-plane loadings, the ellipsoidal failure envelope is implemented here in this model [60]:

$$\left(\frac{F_n}{S_n}\right)^2 + \left(\frac{F_s}{S_s}\right)^2 = 1 \tag{5.11}$$

Therefore, the above equation establishes the softening model. Seven parameters (i.e., $k_n, k_s, S_n, S_s, u_f^n, u_f^s$ and μ control the behaviour of this softening model.

As mentioned earlier, we used the code available in PFC example (i.e., rock test). Firstly, a sample with effective modulus of 24.03 GPa [64] and density of 1950 kg/m³ [65] was created. The boundary of the simulation box was -100 μm and 100 μm both in x- and y-directions. Then, 773318 balls with radius ranging from 0.1 μm to 0.15 μm were generated inside the 200 × 200 μm² simulation box. Next, we calmed and solved the system to reach equilibrium. After that, those balls were assigned to different group of phases based on the microstructure image of simplified hardened cement paste. Capillary porosity was represented by saturated porosity and self-desiccated porosity. The following step was to create sample with the softening model contacts. k_n and k_s are Young's modulus and shear modulus, respectively.

S_n and S_s are calculated from the following equation [66]:

$$S_n = 2Rt\sigma_n \tag{5.12}$$

where $2Rt$ is the tributary area for each bond, $t = 1$ is the thickness in 2D. $R = (0.1 + 0.15)/2 = 0.125$ μm is the average radius of balls.

μ_f^n and μ_f^s are calculated from the following equation [66]:

$$\mu_f^n = \frac{S_n}{2k_n} + \frac{2\bar{R}tG_f}{S_n} \tag{5.13}$$

where G_f is the fracture energy.

We have chosen cube shape supercells with ReaxFF force field except for CH supercell, strain rate 10^{-6} fs^{-1} and 3.1 Å water spacing in z-direction for composites as follows:

- 10 × 10 × 10 CH supercell with ClayFF force field
- 4 × 5 × 2 AFt supercell
- C-S-H (I)/C-S-H (I) composite
- C-S-H (I)/CH composite
- C-S-H (I)/AFt composite
- AFt/CH composite.

Fracture energy was calculated from the area under stress and displacement curves after peak stress. **Figure 5.8** and **Figure 5.9** shows the curves of stress and displacement.

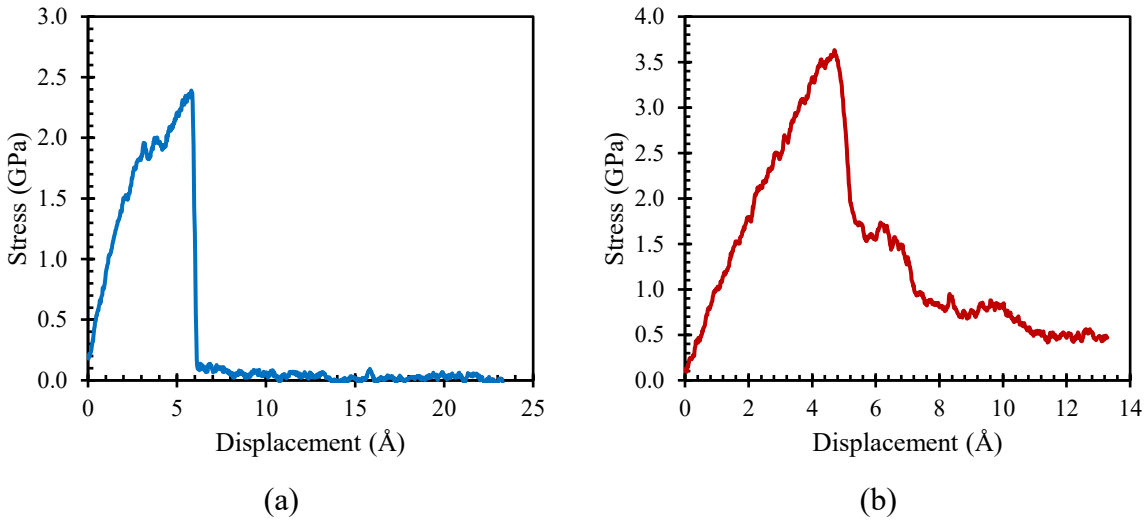

Figure 5.6 Stress and displacement curves: (a) CH supercell and (b) AFt supercell.

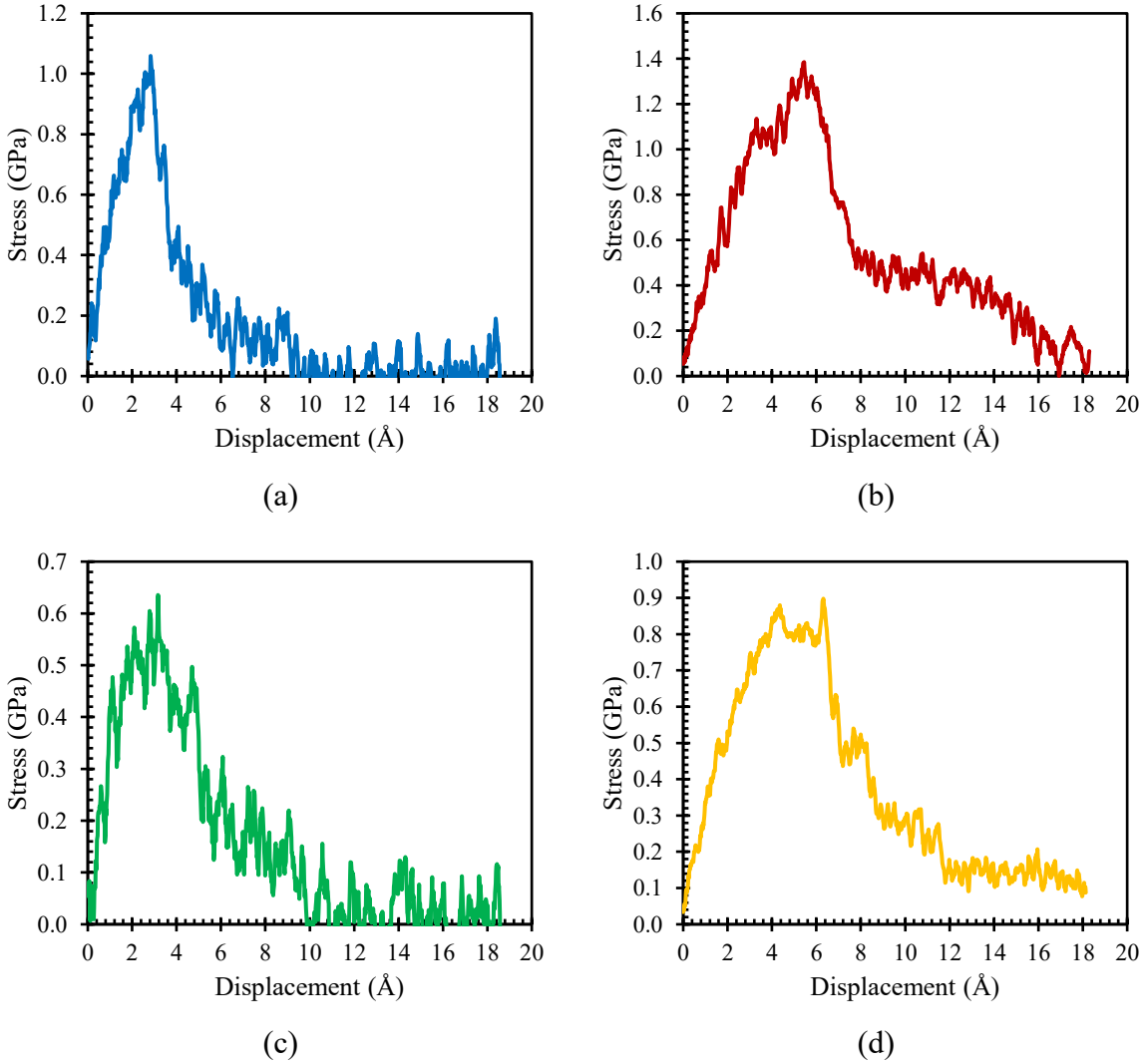

Figure 5.7 Stress and displacement curves: (a) C-S-H (I)/C-S-H (I), (b) C-S-H (I)/CH, (c) C-S-H (I)/AFt and (d) AFt/CH composites.

Then, we reset the ball displacements and the linear contact forces. We calmed and solved the system to reach equilibrium once again. Top and bottom grips with the height of 2 μm were respectively formed at the lower and upper parts of the sample. A direct tension test was then performed by moving the top grip upward and moving the bottom grip downward with velocity ranging from 50 m/s to 0.2 m/s. Stress is calculated by creating a single measurement circle covering all balls. The strain is calculated by observing the displacement of bottom and top grips. The axial strain was deduced from the relative displacement of the two grips particles divided by the initial distance between them. The properties of different phases are summaries in **Table 5.5**. These properties were obtained from the MD simulations in the previous chapters. Since stress-strain curves of shear test did not show the post-peak part, fracture energy could not be calculated. Therefore, u_f^s supposed to be the same as u_f^n. Friction coefficient supposed to be 0.5 for all cases. Capillary porosity were calculated by 1/100 of the average values of each parameters.

Table 5.5 Softening model properties of different hydrated cement paste phases.

Phase	k_n (GPa)	k_s (GPa)	S_n (N)	S_s (N)	u_f^n (μm)	u_f^s (μm)	μ
CH	33.3	4.6	598	115	0.009	0.009	0.5
AFt	37.1	5.4	908	183	0.012	0.012	0.5
C-S-H (I)/C-S-H (I)	48.5	12.1	265	120	0.0029	0.0029	0.5
C-S-H (I)/CH	31.1	9.4	348	123	0.006	0.006	0.5
C-S-H (I)/AFt	40.4	3.1	158	68	0.0022	0.0022	0.5
AFt/CH	24.0	1.9	225	68	0.005	0.005	0.5
Capillary porosity	0.4	0.1	4.2	1.1	0.00006	0.00006	0.5

5.4.2 Results and discussion

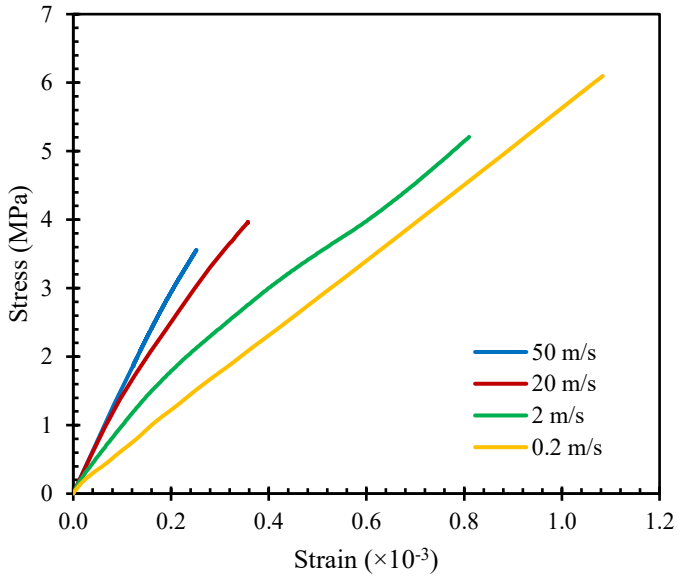

Figure 5.8 Stress-strain curve of tensile test of simplified HCP.

Figure 5.8 shows the stress-strain curve of the tensile test of simplified HCP with different velocities ranging from 50 m/s to 0.2 m/s. Stresses should reach the peak at the end of simulation because one condition in the simulation was imposed that the test will stop when stress falls below 50% of the peak stress. Peak stress, peak strain and Young's modulus are summarized in **Table 5.6**. Results are found to be similar with experimental results of Rhardane et al. [12] (i.e., tensile strength of 7.66 MPa and Young's modulus of 17.4 GPa) and also results obtained via homogenization scheme in the previous section. However, for velocities of 2 m/s and 0.2 m/s, the values of Young's modulus found are small. **Figure 5.9** to **Figure 5.12** illustrate the fracture of simplified HCP at different strains and velocities. The fractures were moved to the right side 20 μm for the ease of observation. As can be seen, the fracture can be observed around the grips for the case of 50 m/s and 20 m/s. With the decrease of velocities to 2 m/s and 0.2 m/s, fractures begin to show across the sample. Parameter study should give a better result. It should be noted that these preliminary results were obtained from the simplified HCP consisting of only main hydrated cement paste phases. It should give a better result by taking into account all hydrated and unhydrated phases.

Table 5.6 Softening model properties of different hydrated cement paste phases.

Velocity	Peak strain ($\times 10^{-3}$)	Peak stress (MPa)	E (GPa)
50 m/s	0.25	3.56	15.3
20 m/s	0.36	3.96	13.1
2 m/s	0.81	5.21	7.27
0.2 m/s	1.08	6.10	5.49

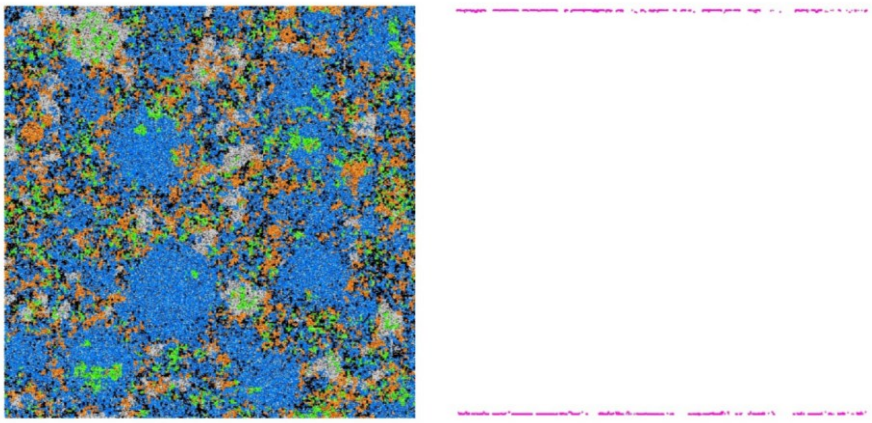

Figure 5.9 Fracture at the strain of 0.25×10^{-3} with velocity of 50 m/s.

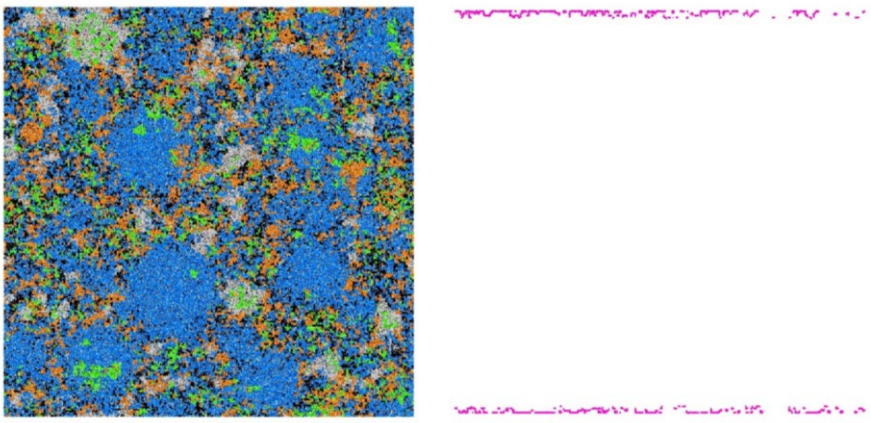

Figure 5.10 Fracture at the strain 0.36×10^{-3} of with velocity of 20 m/s.

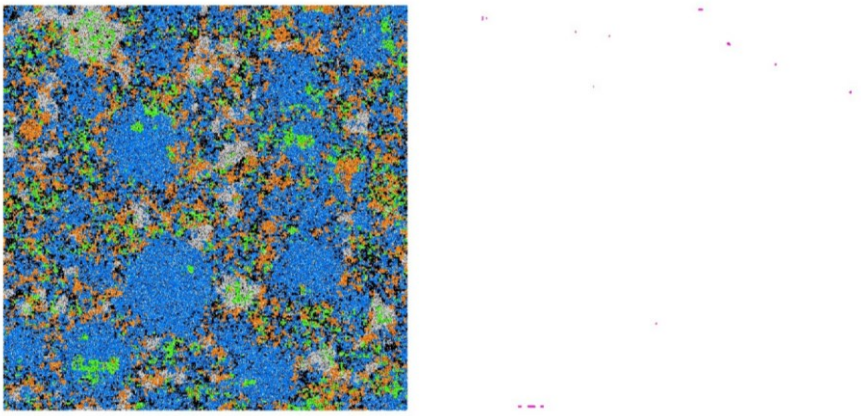

Figure 5.11 Fracture at the strain of 0.81×10^{-3} with velocity of 2 m/s.

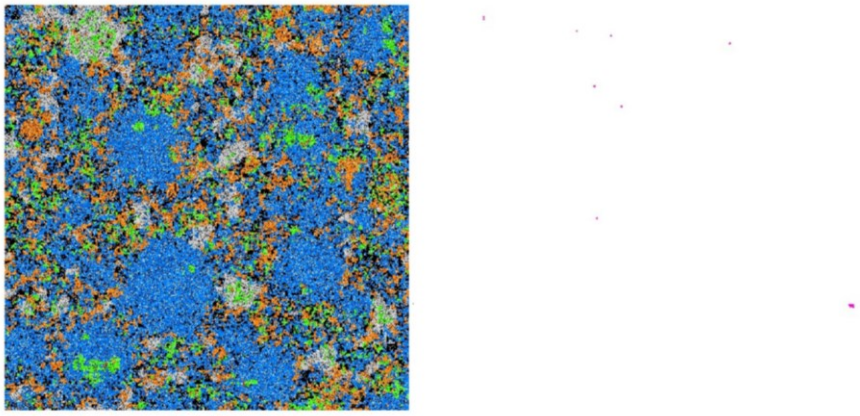

Figure 5.12 Fracture at the strain of 1.08×10^{-3} with velocity of 0.2 m/s.

5.5 In summary

This chapter consists of the mechanical properties calculation of a simplified hardened cement paste via Mori-Tanaka homogenization scheme and via DEM simulations using PFC. In the case of Mori-Tanaka homogenization scheme, it can be seen that the shape of supercells could affect the value of Young's modulus and Poisson's ratio of cement paste composites. Therefore, it led to slightly different results of Young's modulus of a simplified hardened cement paste. On the condition of paying attention to the simulation and calculation procedures as well as to the formulas of VRH approximation, which must all be adapted to the crystallographic groups, this work could be continued in order to take into account other secondary phases of the cementitious matrices (anhydrous phases, gypsum, different forms of hydrated calcium aluminates...) and to obtain a more precise estimate of the mechanical properties of hydrated cement pastes. In the case of DEM simulations using PFC, we performed

a tensile test and obtained a preliminary result of stress-strain curves from which Young's modulus, peak stress and peak strain could be deduced. It should be noted that these values were calculated from simplified hardened cement paste taking into account only the main hydrated cement paste phases. It might be possible to use this method to obtain normal hardened cement paste by calculating mechanical properties of different composites with other hydrated and unhydrated phases. This study might contribute to make it possible the bridge of achieving transition from molecular scale to continuous microscopic scale. In the next chapter, general conclusion and perspective could be observed.

Conclusion and perspective

General conclusion

The aim of this PhD thesis was to investigate the mechanical properties of different phases of hydrated cement paste required for the multi-scale modelling. The numerical simulations, i.e., Molecular Dynamics (MD) simulations at the nano-scale, could be used to obtain these properties. The grasp of the adhesion properties between different hydrated cement paste phases is important because the rupture of the adhesion between these phases is responsible for the damage of the material and the micro-cracking even more than the rupture of the phases themselves (inter-phase and not intra-phase ruptures). The adhesion between the main hydrated cement paste phases of C-S-H (I), CH and AFt was taken into account by means of Reactive MD simulations with ReaxFF force field. The combination of two different main phases of hydrated cement paste was called cement paste composite in this study. For the composites, three different orientations and configurations of spacing were imposed. Those orientations are as follows: (a) one phase on top of other phase in z-direction, (b) one phase on the side of other phase in y-direction, and (c) counterclockwise rotated phase around x-axis on the side of other phase in y-direction. On the other hand, those configurations are as follows: (a) 1 Å vacuum spacing, (b) 3.1 Å water spacing and (c) 6.2 Å water spacing. The spacing was placed in-between the two phases. The results are divided into two groups such as cuboid shape and cube shape supercells composites.

In **Chapter 1**, tensile tests were performed to obtain the mechanical properties of these main hydrated cement paste phases. Different size and strain rate were explored for the sensitive analysis. In general, it is evident from the results that C-S-H (I) phase has the highest peak stress, followed by CH and AFt phases. Strain rate of 10^{-6} fs^{-1} was chosen in this study. Finally, we would like to favour the CH supercells of 9 × 10 × 14 and 13 × 16 × 9 in x-, y- and z-directions with Young's modulus of 33.9 GPa and 33.1 GPa, respectively. For AFt supercells, 3 × 3 × 3 and 4 × 5 × 2 are the chosen sizes with Young's modulus of 33.8 GPa and 37.1 GPa, respectively. For C-S-H (I) supercells, 5 × 5 × 3 and 7 × 8 × 2 are the chosen sizes with Young's modulus of 56 GPa and 56.4 GPa, respectively.

In **Chapter 2**, tensile tests were not only applied on the individual phases but also the composite of the main phases. These simulations provided the stress-strain curves of the

composite phases. Therefore, peak stress, peak strain and Young's modulus could be calculated from the stress-strain curves. For cement paste composite, C-S-H (I)/C-S-H (I) composite has the highest peak stress, followed by C-S-H (I)/CH, C-S-H (I)/AFt and AFt/CH composites. For configuration of spacing, 1 Å vacuum spacing has the highest peak stress, followed by 3.1 Å and 6.2 Å water spacing. All rupture appeared at the interface of composite indicating that vacuum and water spacing made the interaction between main hydrated cement phases weaker and initiated the rupture. Finally, we obtained peak stress, peak strain and Young's modulus of the main hydrated cement paste phases.

In **Chapter 3**, shear test was performed on the composites composed of the main hydrated cement paste phases in order to obtain the shear behaviour. Different cases of shear test were performed consisting of three different orientations and three different configurations of spacing. It should be noticed that stress-strain curves were affected by both orientations and configurations of spacing. In the case of composites composed of cube shape supercells, shear modulus of C-S-H (I)/C-S-H (I), C-S-H (I)/CH, C-S-H (I)/AFt and AFt/CH are as follows: 10.6 GPa, 10.3 GPa, 3.6 GPa and 2.8 GPa, respectively. These values are the mean value of spacing (3.1 Å) among different orientations. Our results provide a mean for further studies in the upper scale, i.e., micro-scale of cement-based materials.

In **Chapter 4**, elastic constants of composite hydrated cement paste phases were calculated using the molecular dynamics software called LAMMPS. The effort was focused here on the adhesion between the different main phases of the hydrated cement paste. Their elastic constants were calculated from the slope of stress-strain curves with 1% strain in six different deformations of composite supercells. The elastic constants could be used to calculate homogenized Young's modulus and Poisson's ratio via Voigt-Reuss-Hill approximation. Two different methods were used to calculate Young's modulus and Poisson's ratio depending on space group (i.e., monoclinic and trigonal space groups). For the mean value of spacing (3.1 Å) the Young's modulus of C-S-H (I)/C-S-H (I), C-S-H (I)/CH and C-S-H (I)/AFt were found to be respectively equal to 42.3 GPa, 34.1 GPa and 18.7 GPa. These values were obtained in the case of composites composed of cuboid shape supercells. In the case of composites composed of cube shape supercells, Young's modulus of C-S-H (I)/C-S-H (I), C-S-H (I)/CH and C-S-H (I)/AFt are as follows: 41.2 GPa, 29.6 GPa and 21.9 GPa, respectively.

In **Chapter 5**, it was also possible to obtain Young's modulus and Poisson's ratio of simplified hardened cement paste with homogenization scheme (i.e., Mori-Tanaka scheme). In the case of composites composed of cube shape supercells, results were found in range between 10.1 GPa and 15.1 GPa, and between 0.32 and 0.34 for Young's modulus and Poisson's ratio,

respectively. Nonetheless, Young's modulus and Poisson's ratio were found to be respectively in a range of 8.1 - 14.6 GPa and 0.32 - 0.36 in the case of composites composed of cube shape supercells. Moreover, tensile test was performed on a simplified hardened cement paste with Discrete Element Method via PFC. We obtained a preliminary result with a similar result to Rhardane et al. [12] as well as the results of Young's modulus obtained via homogenization scheme. The values of tensile strength and Young's modulus are found to be 3.56 – 6.10 MPa and 5.49 – 15.3 GPa, respectively.

In conclusion, this PhD thesis demonstrates the feasibility of using MD simulations in order to obtain the mechanical properties of interphases of the main hydrated cement paste phases. Moreover, our study provides also the methodology to access the mechanical properties of simplified hardened cement paste by means of homogenization scheme and DEM simulations. Therefore, this PhD thesis subject makes it possible to create the bridge of achieving the transition from the molecular scale to the continuous microscopic scale.

Perspective

Future work should include the development of ReaxFF force field that will be optimized for all the hydrated cement paste phases because ReaxFF developed for ettringite was used in this study. Mechanical properties of C-S-H (II) with Ca/Si of 1.7 should also be included in the study. Because of the time constraints, only C-S-H (I) with Ca/Si of 0.67 was studied in this work. It should be noted that these values were calculated from simplified hardened cement paste taking into account only the main hydrated cement paste phases. It might be possible to use this method to obtain normal hardened cement paste by calculating mechanical properties of different composites with other hydrated and unhydrated phases. Shear test was performed as a pure shear deformation. Therefore, friction coefficient was not taken into account for DEM simulations. It would be good to model the shear test where friction coefficient could be calculated. Our results are encouraging and should be validated with the experiment such as scanning force microscopes (SFM) to study the adhesion between hydrated cement paste. Lastly, development of methodology for low carbon concrete and simulation of creep will be conducted.

References

[1] D. Keinde, S. Kamali-Bernard, F. Bernard, I. Cisse, Effect of the interfacial transition zone and the nature of the matrix-aggregate interface on the overall elastic and inelastic behaviour of concrete under compression: a 3D numerical study, European Journal of Environmental and Civil Engineering. 18 (2014) 1167–1176. https://doi.org/10.1080/19648189.2014.896757.

[2] D. Lau, W. Jian, Z. Yu, D. Hui, Nano-engineering of construction materials using molecular dynamics simulations: Prospects and challenges, Composites Part B: Engineering. 143 (2018) 282–291. https://doi.org/10.1016/j.compositesb.2018.01.014.

[3] K. Ioannidou, Mesoscale Structure and Mechanics of C-S-H, in: W. Andreoni, S. Yip (Eds.), Handbook of Materials Modeling: Applications: Current and Emerging Materials, Springer International Publishing, Cham, 2020: pp. 1–15. https://doi.org/10.1007/978-3-319-50257-1_127-1.

[4] H.F.W. Taylor, Cement chemistry, 2. ed., Repr, Telford, London, 1997.

[5] A.E. Moore, H.F.W. Taylor, Crystal structure of ettringite, Acta Cryst B. 26 (1970) 386–393. https://doi.org/10.1107/S0567740870002443.

[6] J. Fu, S. Kamali-Bernard, F. Bernard, M. Cornen, Comparison of mechanical properties of C-S-H and portlandite between nano-indentation experiments and a modeling approach using various simulation techniques, Composites Part B: Engineering. 151 (2018) 127–138. https://doi.org/10.1016/j.compositesb.2018.05.043.

[7] F. Bernard, S. Kamali-Bernard, W. Prince, 3D multi-scale modelling of mechanical behaviour of sound and leached mortar, Cement and Concrete Research. 38 (2008) 449–458. https://doi.org/10.1016/j.cemconres.2007.11.015.

[8] J. Claverie, S. Kamali-Bernard, J.M.M. Cordeiro, F. Bernard, Assessment of mechanical, thermal properties and crystal shapes of monoclinic tricalcium silicate from atomistic simulations, Cement and Concrete Research. 140 (2021) 106269. https://doi.org/10.1016/j.cemconres.2020.106269.

[9] X. Gao, Y. Wei, W. Huang, Effect of individual phases on multiscale modeling mechanical properties of hardened cement paste, Construction and Building Materials. 153 (2017) 25–35. https://doi.org/10.1016/j.conbuildmat.2017.07.074.

[10] S. Kamali-Bernard, F. Bernard, Effect of tensile cracking on diffusivity of mortar: 3D numerical modelling, Computational Materials Science. 47 (2009) 178–185. https://doi.org/10.1016/j.commatsci.2009.07.005.

[11] A. Rhardane, S. Al Haj Sleiman, S.Y. Alam, F. Grondin, A quantitative assessment of the parameters involved in the freeze–thaw damage of cement-based materials through numerical modelling, Construction and Building Materials. 272 (2021) 121838. https://doi.org/10.1016/j.conbuildmat.2020.121838.

[12] A. Rhardane, F. Grondin, S.Y. Alam, Development of a micro-mechanical model for the determination of damage properties of cement pastes, Construction and Building Materials. 261 (2020) 120514. https://doi.org/10.1016/j.conbuildmat.2020.120514.

References

[13] T. Honorio, P. Guerra, A. Bourdot, Molecular simulation of the structure and elastic properties of ettringite and monosulfoaluminate, Cement and Concrete Research. 135 (2020) 106126. https://doi.org/10.1016/j.cemconres.2020.106126.

[14] T. Honorio, Monte Carlo Molecular Modeling of Temperature and Pressure Effects on the Interactions between Crystalline Calcium Silicate Hydrate Layers, Langmuir. (2019). https://doi.org/10.1021/acs.langmuir.8b04156.

[15] E. Del Gado, K. Ioannidou, E. Masoero, A. Baronnet, R.J.-M. Pellenq, F.-J. Ulm, S. Yip, A soft matter in construction – Statistical physics approach to formation and mechanics of C–S–H gels in cement, Eur. Phys. J. Spec. Top. 223 (2014) 2285–2295. https://doi.org/10.1140/epjst/e2014-02264-1.

[16] Y. Zhou, D. Hou, H. Manzano, C.A. Orozco, G. Geng, P.J.M. Monteiro, J. Liu, Interfacial Connection Mechanisms in Calcium–Silicate–Hydrates/Polymer Nanocomposites: A Molecular Dynamics Study, ACS Appl. Mater. Interfaces. 9 (2017) 41014–41025. https://doi.org/10.1021/acsami.7b12795.

[17] H. Manzano, J.S. Dolado, A. Ayuela, Elastic properties of the main species present in Portland cement pastes, Acta Materialia. 57 (2009) 1666–1674. https://doi.org/10.1016/j.actamat.2008.12.007.

[18] H. Manzano, E. Masoero, I. Lopez-Arbeloa, H.M. Jennings, Shear deformations in calcium silicate hydrates, Soft Matter. 9 (2013) 7333–7341.

[19] P.C. Hewlett, Lea's Chemistry of Concrete and Cement, Elsevier, Oxford, 1998.

[20] L. Desgranges, D. Grebille, G. Calvarin, G. Chevrier, N. Floquet, J.-C. Niepce, Hydrogen thermal motion in calcium hydroxide: Ca(OH)2, Acta Cryst B. 49 (1993) 812–817. https://doi.org/10.1107/S0108768193003556.

[21] A. Stukowski, Visualization and analysis of atomistic simulation data with OVITO–the Open Visualization Tool, Modelling Simul. Mater. Sci. Eng. 18 (2009) 015012. https://doi.org/10.1088/0965-0393/18/1/015012.

[22] F. Goetz-Neunhoeffer, J. Neubauer, Refined ettringite (Ca6Al2(SO4)3(OH)12·26H2O) structure for quantitative X-ray diffraction analysis, Powder Diffraction. 21 (2006) 4–11. https://doi.org/10.1154/1.2146207.

[23] J. Fu, F. Bernard, S. Kamali-Bernard, Assessment of the elastic properties of amorphous calcium silicates hydrates (I) and (II) structures by molecular dynamics simulation, Molecular Simulation. 44 (2018) 285–299. https://doi.org/10.1080/08927022.2017.1373191.

[24] J. Fu, Multiscale modeling and mechanical properties of typical anisotropic crystals structures at nanoscale, INSA Rennes, 2016. https://www.theses.fr/s121120.

[25] S.A. Hamid, The crystal structure of the 11Å natural tobermorite Ca2.25[Si3O7.5(OH)1.5] · 1H2O, Zeitschrift Für Kristallographie - Crystalline Materials. 154 (1981) 189–198. https://doi.org/10.1524/zkri.1981.154.3-4.189.

[26] P.A. Bonnaud, C. Labbez, R. Miura, A. Suzuki, N. Miyamoto, N. Hatakeyama, A. Miyamoto, K.J.V. Vliet, Interaction grand potential between calcium–silicate–hydrate nanoparticles at the molecular level, Nanoscale. 8 (2016) 4160–4172. https://doi.org/10.1039/C5NR08142D.

[27] Y. Liang, Mechanical and fracture properties of calcium silicate hydrate and calcium hydroxide composite from reactive molecular dynamics simulations, Chemical Physics Letters. 761 (2020) 138117. https://doi.org/10.1016/j.cplett.2020.138117.

[28] K. Ioannidou, R.J.-M. Pellenq, E.D. Gado, Controlling local packing and growth in calcium–silicate–hydrate gels, Soft Matter. 10 (2014) 1121–1133. https://doi.org/10.1039/C3SM52232F.

[29] E. Masoero, H.M. Jennings, F.J. Ulm, E. Del Gado, H. Manzano, R.J.M. Pellenq, S. Yip, Modelling cement at fundamental scales: From atoms to engineering strength and durability, Comput. Model. Concr. Struct. 1 (2014) 139–148.

[30] W. Sekkal, A. Zaoui, I. Shahrour, Stability and adhesion of calcite/montmorillonite assembly, American Mineralogist. 100 (2015) 516–521. https://doi.org/10.2138/am-2015-5068.

[31] W. Sekkal, A. Zaoui, Enhancing the interfacial bond strength of cement nanocomposite with carbonate nanostructure, Composites Part B: Engineering. 124 (2017) 111–119. https://doi.org/10.1016/j.compositesb.2017.05.057.

[32] S. Plimpton, Fast Parallel Algorithms for Short-Range Molecular Dynamics, Journal of Computational Physics. 117 (1995) 1–19. https://doi.org/10.1006/jcph.1995.1039.

[33] A.C.T. van Duin, S. Dasgupta, F. Lorant, W.A. Goddard, ReaxFF: A Reactive Force Field for Hydrocarbons, J. Phys. Chem. A. 105 (2001) 9396–9409. https://doi.org/10.1021/jp004368u.

[34] S. Hajilar, B. Shafei, Mechanical failure mechanisms of hydrated products of tricalcium aluminate: A reactive molecular dynamics study, Materials & Design. 90 (2016) 165–176. https://doi.org/10.1016/j.matdes.2015.10.089.

[35] R.T. Cygan, J.-J. Liang, A.G. Kalinichev, Molecular Models of Hydroxide, Oxyhydroxide, and Clay Phases and the Development of a General Force Field, J. Phys. Chem. B. 108 (2004) 1255–1266. https://doi.org/10.1021/jp0363287.

[36] S. Hajilar, B. Shafei, Assessment of structural, thermal, and mechanical properties of portlandite through molecular dynamics simulations, Journal of Solid State Chemistry. 244 (2016) 164–174. https://doi.org/10.1016/j.jssc.2016.09.026.

[37] L. Liu, A. Jaramillo-Botero, W.A. Goddard, H. Sun, Development of a ReaxFF Reactive Force Field for Ettringite and Study of its Mechanical Failure Modes from Reactive Dynamics Simulations, J. Phys. Chem. A. 116 (2012) 3918–3925. https://doi.org/10.1021/jp210135j.

[38] H. Manzano, A. Ayuela, A. Telesca, P.J.M. Monteiro, J.S. Dolado, Ettringite Strengthening at High Pressures Induced by the Densification of the Hydrogen Bond Network, J. Phys. Chem. C. 116 (2012) 16138–16143. https://doi.org/10.1021/jp301822e.

[39] J. Zhao, C. Sun, Q. Wang, X. Shen, L. Lu, Thermodynamic, mechanical, and electronic properties of ettringite and AFm phases from first-principles calculations, Construction and Building Materials. 350 (2022) 128777. https://doi.org/10.1016/j.conbuildmat.2022.128777.

[40] X. Zhu, A. Zaoui, W. Sekkal, Wettability and work of adhesion of water nanodroplet on (001) surface of cement paste, Cement and Concrete Research. 159 (2022) 106896. https://doi.org/10.1016/j.cemconres.2022.106896.

References

[41] D. Fan, S. Yang, Mechanical properties of C-S-H globules and interfaces by molecular dynamics simulation, Construction and Building Materials. 176 (2018) 573–582. https://doi.org/10.1016/j.conbuildmat.2018.05.085.

[42] L. Desgranges, D. Grebille, G. Calvarin, G. Chevrier, N. Floquet, J.-C. Niepce, Hydrogen thermal motion in calcium hydroxide: Ca(OH)2, Acta Cryst B. 49 (1993) 812–817. https://doi.org/10.1107/S0108768193003556.

[43] F. Goetz-Neunhoeffer, J. Neubauer, Refined ettringite (Ca6Al2(SO4)3(OH)12·26H2O) structure for quantitative X-ray diffraction analysis, Powder Diffraction. 21 (2006) 4–11. https://doi.org/10.1154/1.2146207.

[44] S.A. Hamid, The crystal structure of the 11Å natural tobermorite Ca2.25[Si3O7.5(OH)1.5] · 1H2O, Zeitschrift Für Kristallographie - Crystalline Materials. 154 (1981) 189–198. https://doi.org/10.1524/zkri.1981.154.3-4.189.

[45] D. Frenkel, B. Smit, Understanding Molecular Simulation: From Algorithms to Applications, Elsevier, 2001.

[46] A.P. Thompson, H.M. Aktulga, R. Berger, D.S. Bolintineanu, W.M. Brown, P.S. Crozier, P.J. in 't Veld, A. Kohlmeyer, S.G. Moore, T.D. Nguyen, R. Shan, M.J. Stevens, J. Tranchida, C. Trott, S.J. Plimpton, LAMMPS - a flexible simulation tool for particle-based materials modeling at the atomic, meso, and continuum scales, Computer Physics Communications. 271 (2022) 108171. https://doi.org/10.1016/j.cpc.2021.108171.

[47] R.T. Cygan, J.-J. Liang, A.G. Kalinichev, Molecular Models of Hydroxide, Oxyhydroxide, and Clay Phases and the Development of a General Force Field, J. Phys. Chem. B. 108 (2004) 1255–1266. https://doi.org/10.1021/jp0363287.

[48] A.C.T. van Duin, S. Dasgupta, F. Lorant, W.A. Goddard, ReaxFF: A Reactive Force Field for Hydrocarbons, J. Phys. Chem. A. 105 (2001) 9396–9409. https://doi.org/10.1021/jp004368u.

[49] S. Hajilar, B. Shafei, Mechanical failure mechanisms of hydrated products of tricalcium aluminate: A reactive molecular dynamics study, Materials & Design. 90 (2016) 165–176. https://doi.org/10.1016/j.matdes.2015.10.089.

[50] D. Hou, C. Wu, Q. Yang, W. Zhang, Z. Lu, P. Wang, J. Li, Q. Ding, Insights on the molecular structure evolution for tricalcium silicate and slag composite: From 29Si and 27Al NMR to molecular dynamics, Composites Part B: Engineering. 202 (2020) 108401. https://doi.org/10.1016/j.compositesb.2020.108401.

[51] D. Hou, J. Yu, P. Wang, Molecular dynamics modeling of the structure, dynamics, energetics and mechanical properties of cement-polymer nanocomposite, Composites Part B: Engineering. 162 (2019) 433–444. https://doi.org/10.1016/j.compositesb.2018.12.142.

[52] L. Liu, A. Jaramillo-Botero, W.A. Goddard, H. Sun, Development of a ReaxFF Reactive Force Field for Ettringite and Study of its Mechanical Failure Modes from Reactive Dynamics Simulations, J. Phys. Chem. A. 116 (2012) 3918–3925. https://doi.org/10.1021/jp210135j.

[53] M. Eftekhari, S. Mohammadi, Molecular dynamics simulation of the nonlinear behavior of the CNT-reinforced calcium silicate hydrate (C–S–H) composite, Composites Part A: Applied Science and Manufacturing. 82 (2016) 78–87. https://doi.org/10.1016/j.compositesa.2015.11.039.

[54] Z. Wu, E. Zhao, H. Xiang, X. Hao, X. Liu, J. Meng, Crystal structures and elastic properties of superhard Ir N2 and Ir N3 from first principles, Phys. Rev. B. 76 (2007) 054115. https://doi.org/10.1103/PhysRevB.76.054115.

[55] J. Fu, H. Bai, Z. Zhang, W. Lin, Elastic constants and homogenized moduli of manganese carbonate structure based on molecular dynamics and Reuss-Voigt-Hill methods, IOP Conf. Ser.: Mater. Sci. Eng. 423 (2018) 012046. https://doi.org/10.1088/1757-899X/423/1/012046.

[56] F. Bernard, S. Kamali-Bernard, Performance simulation and quantitative analysis of cement-based materials subjected to leaching, Computational Materials Science. 50 (2010) 218–226. https://doi.org/10.1016/j.commatsci.2010.08.002.

[57] F. Bernard, J. Fu, S. Kamali-Bernard, Multiscale modelling approach to determine the specific heat of cementitious materials, European Journal of Environmental and Civil Engineering. 23 (2019) 535–551. https://doi.org/10.1080/19648189.2018.1443157.

[58] J. Claverie, Molecular dynamics investigation of the mechanical, thermal and surface properties of tricalcium silicate and its early hydration, Universidade Estadual Paulista (Unesp), 2019. https://repositorio.unesp.br/handle/11449/191301 (accessed January 25, 2022).

[59] S. Kamali, Comportement et simulation des matériaux cimentaires en environnement agressifs: lixiviation et température, PhD Thesis, Cachan, Ecole normale supérieure, 2003.

[60] R. Zhu, S.Y. Alam, A. Loukili, Relevance of displacement softening model in discrete element method to investigate structural and grain size scaling effect, Theoretical and Applied Fracture Mechanics. 123 (2023) 103706. https://doi.org/10.1016/j.tafmec.2022.103706.

[61] M. Jirásek, M. Bauer, Numerical aspects of the crack band approach, Computers & Structures. 110–111 (2012) 60–78. https://doi.org/10.1016/j.compstruc.2012.06.006.

[62] J. Bobiński, J. Tejchman, Comparison of continuous and discontinuous constitutive models to simulate concrete behaviour under mixed-mode failure conditions, International Journal for Numerical and Analytical Methods in Geomechanics. 40 (2016) 406–435. https://doi.org/10.1002/nag.2411.

[63] J. Mazars, A description of micro- and macroscale damage of concrete structures, Engineering Fracture Mechanics. 25 (1986) 729–737. https://doi.org/10.1016/0013-7944(86)90036-6.

[64] X. Li, X. Gu, X. Xia, E. Madenci, X. Chen, Q. Zhang, Effect of water-cement ratio and size on tensile damage in hardened cement paste: Insight from peridynamic simulations, Construction and Building Materials. 356 (2022) 129256. https://doi.org/10.1016/j.conbuildmat.2022.129256.

[65] G. Skripkiunas, V. Sasnauskas, M. Daukšys, D.V. Palubinskaite, Peculiarities of hydration of cement paste with addition of hydrosodalite, Materials Science Poland. (2007) 627–635.

[66] H.-Z. Liu, J.-S. Lin, J.-D. He, H.-Q. Xie, Discrete elements and size effects, Engineering Fracture Mechanics. 189 (2018) 246–272. https://doi.org/10.1016/j.engfracmech.2017.11.019.

Titre : Influence de l'adhésion entre les principales phases cimentaires sur le comportement mécanique de la pâte de ciment hydratée

Mots clés : Modélisation multi-échelle, Pâte de ciment hydratées, Voigt-Reuss-Hill, homogénéisation, Dynamique Moléculaire, Méthode Eléments Discrets

Résumé : Cette thèse de doctorat porte sur la modélisation multi-échelle des propriétés mécaniques des matériaux cimentaires. L'objectif de cette thèse est d'obtenir les propriétés mécaniques des phases de pâte de ciment hydratées à l'échelle nanométrique à l'aide de simulations de Dynamique Moléculaire (DM). Les propriétés mécaniques de la pâte de ciment durcie à l'échelle microscopique ont ensuite été calculées à l'aide d'une méthode d'homogénéisation et de la Méthode Éléments Discrets (MED). En effet, les propriétés obtenues à l'échelle inférieure sont considérées comme les données d'entrée à l'échelle supérieure. À l'échelle nanométrique, le test de traction et le test de cisaillement ont été réalisés avec les principales phases de la pâte de ciment hydratées à l'aide de simulations DM. En conséquence, des propriétés mécaniques à l'échelle nanométrique ont été obtenues. Une autre approche pour obtenir le module de Young et le coefficient de Poisson a été réalisée via l'approximation de Voigt-Reuss-Hill. Avec la méthode d'homogénéisation (i.e., Mori-Tanaka), le module d'Young et le coefficient de Poisson d'une pâte de ciment durcie simplifiée ont été calculés. Enfin, une simulation MED a été réalisée avec un essai de traction d'une pâte de ciment durcie simplifiée en prenant en compte les propriétés mécaniques à l'échelle nanométrique. Cette thèse de doctorat contribue à créer le pont permettant de réaliser la transition de l'échelle moléculaire à l'échelle microscopique continue.

Title : Influence of adhesion between the main cement phases on the mechanical behaviour of hydrated cement paste

Keywords : Multi-scale modelling, hydrated cement paste, Voigt-Reuss-Hill, homogenization, Molecular Dynamics, Discrete Element Method

Abstract : This PhD thesis focuses on the multi-scale modelling of mechanical properties of cementitious materials. The aim of this PhD thesis is to obtain the mechanical properties of hydrated cement paste phases at nano-scale using Molecular Dynamics (MD) simulations. Mechanical properties of hardened cement paste at micro-scale were then calculated with homogenization scheme and Discrete Element Method (DEM). Indeed, properties obtained at the lower scale are considered as the input data at the upper scale. At nano-scale, tensile test and shear test were performed with main hydrated cement paste phases (i.e., calcium-silicate-hydrates, portlandite and ettringite) via MD simulations. As a result, mechanical properties at nano-scale were obtained. Another approach to obtain Young's modulus and Poisson ratio was done via Voigt-Reuss-Hill approximation. With homogenization scheme (i.e., Mori-Tanaka scheme), Young's modulus and Poisson's ratio of a simplified hardened cement paste were calculated. Finally, DEM simulation was done with tensile test of a simplified hardened cement paste by taking into account the mechanical properties at the nano-scale. This PhD thesis contributes to create the bridge of achieving the transition from the molecular scale to the continuous microscopic scale.